Studying the Dissociation Behaviour of Ionized Non-Covalent Complexes with a Cohesive Energetic and Structure Approach

Justin Beneteau Renaud

Thesis submitted to the

Faculty of Graduate and Postdoctoral Studies

in partial fulfillment of the requirements

for the Doctorate in Philosophy degree in Chemistry

Department of Chemistry

Faculty of Science

University of Ottawa,

Mitt liv har känts som några timmar,
vad ska man blir när man blir stor?
Det ena leder till det andra är allt jag vet.
De pratade om något underbart,
Nu är jag där och kan berätta.
Stort, större än jag någonsin trott,

Det snurrar i min skalle

- *Familjen*

Abstract

This research explores the links between the structure and dissociation energetics of ionized non-covalent complexes.

In chapter 3, a large series of similar non-covalent complexes were probed using electrospray tandem mass spectrometry (ESI-MS/MS) and RRKM modelling in order to identify any trends in the dissociation energetics based on charge state, overall size of the complex, or size of the substrate. Ion mobility spectrometry (IMS) in conjunction with molecular mechanics/molecular dynamics (MM/MD) was used to study the conformations of these non-covalent complexes in order to determine if the same trends identified in the energetics could be corroborated independently based on structure. The system of study consisted of varying lengths of the synthetic polymer, polymethylmethacrylate (PMMA) complexed with singly or doubly protonated diaminoalkanes (DAA) of varying length. The critical energies of dissociation (E_0) increased as the length of the polymer increased and was not significantly affected by the length of the singly protonated DAA substrates. The E_0 of dissociation of doubly protonated complexes was strongly influenced by the length of the DAA; longer DAA substrates had greater separation of charge which decreased coulombic repulsion within the complex resulting in higher E_0 values. MM/MD low energy structures of all complexes were validated with experimental IMS measurements and showed that the arrangement between the polymer and DAA were similar for different singly protonated DAAs. When doubly protonated, the length of DAA was the most important factor in determining the overall structure of the complex.

In chapter 4, a direct link is shown between the observed E_0 dissociation energies and the molecular conformations for eight different peptide–saccharide complexes containing either a tri-saccharide (d-(+)-raffinose and d-panose) or tetra-saccharide (stachyose and maltotetraose) with a small peptide (FLEEL and FLEEV). The E_0 values were highly related to the overall conformation adopted by the non-covalent complex in the gas phase. Complexes containing peptide FLEE(L/V) with the tri-saccharide raffinose or panose had similar E_0 of dissociation (~0.64 eV) and similar conformations based on MM/MD simulations and IMS drift times. Conversely, for complexes containing a FLEE(L/V) peptide with one of the isomeric tetra-saccharides; stachyose had a E_0 ~0.08 eV greater than maltotetraose. This difference of intermolecular interaction was also reflected by the IMS drift times; maltotetraose in complex with FLEEV or FLEEL had a 5.9% and 2.3% faster IMS drift time than stachyose respectively. This indicated that the molecular arrangement between maltotetraose and the peptides was more compact than the stachyose-peptide complexes.

In chapter 5, RRKM modelling of breakdown diagrams is not possible when the reactant ion signal is overlapped by other isobaric species. Trimeric, non-covalent complexes that contained two PMMA molecules and a doubly protonated DAA, $[(PMMA_a)(DAA+2H)(PMMA_b)]^{+2}$, have m/z signals that contain multiple different complexes having the same total number of polymer repeat units but differ in the length of the each polymer. In this situation, the applicability of using the simple kinetic method to gain insight into relative binding energies was explored. The major factors which determined the suitability of the kinetic method for this system were identified as the structural arrangement of the reactant ion complex, possible reverse activation barriers, and the evaluations of $\Delta(\Delta S^{\ddagger})$. MM/MD simulations coupled with IMS suggests that within the reactant ion, the DAA is almost equally shared between two PMMA oligomers and that the two PMMA oligomers interact predominately with the DAA, and not with each other. MS/MS of the trimeric reactant complexes proceeds by neutral loss of one polymer and is suggested to proceed with little or no reverse activation barrier based on the low coulombic repulsion factors. The IMS drift times of $[(PMMA_a)(DAA+2H)]^{+2}$ complexes that were generated directly by ESI-MS or by dissociation of a trimeric, $[(PMMA_a)(DAA+2H)(PMMA_b)]^{+2}$ complex were found to be identical. This provides some evidence that $\Delta(\Delta S^{\ddagger}) \approx \Delta(\Delta S)$ and using a statistical mechanics approach, $\Delta(\Delta S) \approx 0$. The effective temperature (T_{eff}) variable in the kinetic method expression was found to decrease as a function of the size of the trimeric complex, suggesting that the population distribution of the dissociating ensemble of complexes narrows as size increases. Overall, when RRKM fitting is not possible, the simple kinetic method could provide relative energetic ranking of competing dissociations reactions however the T_{eff} term contributed to the greatest uncertainty in obtaining absolute quantities.

Fitting MS/MS breakdown diagrams of non-covalent complexes with multiple dissociation channels is difficult due to the number of total fitting variables. Building from the simple kinetic method, chapter 6 shows that the relationship between the natural logarithm of competing fragment ions and reciprocal collision energy yields a branching relationship that allows for the sign of $\Delta(\Delta S^{\ddagger})$ and $\Delta(E_0)$ between the channels to be obtained. Furthermore, the relationships between the fitting variables of RRKM modelling are empirically related to the theoretical branching relationship characteristics. This allowed for the fitting variables of all dissociation channels to be expressed as a function of a single channel so that the theoretical branching relationship matches the experimental branching relationship. Using this method, RRKM fitting of a MS/MS breakdown diagram for APCI ionized anthracene determined the E_0 and $\Delta S^{\ddagger}$ was 4.69 ± 0.29 eV and -3 ± 17 J K^{-1}; 4.21 ±0.29 eV and -19 ±15 J $K^{-1;}$ and 4.81 ± 0.29 eV and 36 ±22 J K^{-1} for hydrogen loss, acetylene loss and diacetylene loss respectively. With one exception, these values are within experimental error of the iPEPICO derived energetic values.

In chapter 7, MS/MS of ammoniated triacylglycerides at multiple collision energies and computational analysis are used to explain the cause of uneven dissociation rates of the FAs from different positions on the glycerol backbone. The loss of sn-1 and sn-3 FAs are found to have lower activation energies than the loss of the sn-2 position FA, however the loss of the FA from the sn-2 position is more entropically favourable. Theoretical MS/MS breakdown curves were fit to experimental values using RRKM theory to estimate the E_0 of dissociation of FAs from the three glycerol positions. The E_0 values for cleavage from the sn-1 and sn-3 positions were found to be approximately 1.52 eV, while that for the sn-2 position was highly dependent on the identity of the FA at that position. Computational structures and energy analysis suggest that an important step in the dissociation of $[TAG+NH_4]^+$ is the loss of ammonia. In a model system, glyceryl tributyrate, the loss of NH_3 produced two distinct $[TAG+H]^+$ product structures sitting 148 kJ and 160 kJ in energy above the ammoniated structure. The $[TAG+H]^+$ structure that leads to the loss of the sn-1(3) is 12 kJ lower than the $[TAG+H]^+$ structure that leads to the loss of the sn-2 FA. From this, the loss of a neutral FA that follows sits only an additional 35–48 kJ above the $[TAG+H]^+$ structures.

In Chapter 8, singly deprotonated β-cyclodextrin monomers, $[(\beta\text{-CD-H}^+]^{-1}$, and doubly deprotonated dimers, $[(\beta\text{-CD})_2\text{-2H}^+]^{-2}$, are both present following ESI-MS and have the same monoisotopic m/z. Similar to chapter 5, this makes it difficult to generate an MS/MS breakdown diagrams that can be modelled with RRKM theory. IMS was used to mobility separate $[(\beta\text{-CD-H}^+]^{-1}$ and $[(\beta\text{-CD})_2\text{-2H}^+]^{-2}$ and was followed by MS/MS of the $[(\beta\text{-CycD})_2\text{-2H}^+]^{-2}$ ion. A second problem when generating a MS/MS breakdown diagram of non-covalent complexes that contain identical components is that the fragment ions could have an identical monoisotopic m/z as the reactant ion. MS/MS of $[(\beta\text{-CycD})_2\text{-2H}^+]^{-2}$ results in two $[(\beta\text{-CD-H}^+]^{-1}$ fragments. To overcome this, breakdown diagrams were then generated by monitoring the changes in the isotopic profile. The RRKM derived E_0 for dissociation of $[(\beta\text{-CycD})_2\text{-H+}]^{-1}$ and $[(\beta\text{-CycD})_2\text{-2H+}]^{-2}$ were 1.85 ± 0.11eV and 1.79 ± 0.09eV, respectively, corresponding to a slight decrease in complex stability due to increased charge-charge repulsion in the dianion.

Acknowledgements

The John Holmes Mass Spectrometry center is filled with very talented people who possess a love of mass spectrometry and related sciences:
Dr. Kazakoff, Dr. Mommers, Dr. Curtis, S. Overton, and Dr. John Holmes.
I am greatly thankful for their assistance in explaining concepts, fixing machines and their collaboration.

Being a member of the Mayer research group for 5 years has brought me into contact with a huge number of students that I am thankful to have worked with:
Dr. Abdulrahman Alhazmi, Dr. Eric Martineau, Dr. Yawei Lin, Dr. Ameneh Gholami, Dr. Barbara Francisco, Dr. Huayu Xue, Brandi West, Jenna Hamilton, Jeffrey Butson, Jaleh Halvachizadeh, Melanie Ouelette, Eduardo Solano, Alicia Sit, Jason Dimuzio, Alex Mungham, Dhiya Hassan, Julie Roy, Amanda Comeau, Kevin Berland, Peter Chen, Sabria Mohammad, Hajer Trabelsi, Moufida Weslati, Najla Benahmed and Nick Zinck.

I was also fortunate enough to have collaborated with inspiring scientists outside the Mayer group including Gleb Mironov, Dr. Maxim Berezovski and Dr. Ollie Hampe.

Most of all, I would like to thank my supervisor Dr. Paul Mayer. When I first arrived in his lab, I was a biochemist finishing his undergraduate degree with no intention of moving forward to graduate studies. After one summer, Dr. Mayer’s passion for scientific research inspired me to start a master’s degree, however I had no intention of going on to a PhD. After12 months of graduate work with Dr. Mayer, I began my PhD. The most important thing I’ve learned from Dr. Mayer is that mass spectrometry and scientific research is an unparalleled adventure and I’m thankful for being able to do my graduate studies under his supervision.

Table of Content

List of Figures

List of Tables

Abbreviations

E_0	*0K activation energy (eV)*
PDDA	*4,4'-(propane-1,3-diyl) dibenzoic acid*
α	*alpha (K eV^{-1})*
A	*Arrhenius parameter*
ATD	*Arrival time distribution (ms)*
AMBER	*Assisted model building with energy refinement*
AM1	*Austin Model 1*
APCI	*Atmospheric pressure chemical ionization*
BIRD	*Blackbody infrared radiative dissociation*
E_{com}	*Center of mass collision energy*
CID	*Collision Induced dissociation*
CD	*Cyclodextrin*
dT_{10}	*Decathymidine*
DOF	*Degrees of freedom*
DAG	*Diacylglyceride*
DAA	*Diaminoalkane*
DAB	*Diaminobutane*
DAD	*Diaminodecane*
DAH	*Diaminohexane*
Dc	*Direct current*
T_{eff}	*Effective temperature*
E_f	*Electric field*
ESI	*Electrospray ionization*
$\Delta H^{\ddagger}$	*Enthalpy of activation*
$\Delta S^{\ddagger}$	*Entropy of activation*
ECEEM	*Equilibrium capillary electrophoresis of equilibrium mixtures*
EHSS	*Exact hard sphere scattering*
Ω_{exp}	*Experimental collision cross section*
Ω_{theo}	*Theoretical collision cross section*
FTICR	*Fourier transform ion cyclotron resonance*
GAFF	*Generalized amber force field*
H-NOESY	*Hydrogen-nuclear overhauser effect spectroscopy*
Ibu	*Ibuprofen*
iPEPICO	*Imaging photoelectron photoion coincidence spectrometry*
T_i	*Initial temperature*
U	*Internal energy*
U_{dist}	*Internal energy distribution*

IVR	*intra-vibrational relaxation*
K	*Ion mobility*
IMS	*Ion mobility spectrometry*
E_{lab}	*Lab frame collision energy*
L	*Linoleic acid*
LC	*Liquid chromatography*
Mal	*Maltotetraose*
MS	*Mass spectrometry*
m/z	*Mass to charge ratio*
MALDI	*Matrix assisted laser desorption ionization*
MD	*Molecular dynamics*
MM	*Molecular mechanics*
NA	*Natural isotope abundance*
OA	*Observed isotope abundance*
O	*Oleic acid*
P	*Palmitic Acid*
Pan	*Panose*
PMMA	*Polymethylmethacrylate*
PA	*Proton affinity*
Raf	*Raffinose*
$\rho(E)$	*Reactant ion density of States*
Rf	*Radio frequency*
RRKM	*Rice–Ramsperger–Kassel–Marcus*
Sta	*Stachyose*
MS/MS	*Tandem mass spectrometry*
Ω_{theo}	*Theoretical collision cross section*
TCID	*Threshold collision induced dissociation*
TM	*Trajectory method*
TOF	*Time of flight*
$TS^{\ddagger}$	*Transition state*
$N^{\ddagger}$	*Transition state sum of states*
TWIMS	*Travelling wave ion mobility spectrometry*
TAG	*Triacylglyceride*
Z	*Partition coefficient*

Chapter 1: Introduction

Non-covalent complexes

The manner in which atoms within a molecule are arranged is a dominant factor that determines the behaviour and properties of matter. This molecular architecture is commonly thought of in a covalent sense; that is the sharing of electrons between atoms [1]. Molecular structure is also determined by non-covalent interactions which consist of a variety of electromagnetic interactions such as ionic, hydrogen bonding, dipole-dipole, induced-dipole, London dispersion force and π-π interactions. Intermolecular interactions are by definition non-covalent and hugely important to biological, synthetic and inorganic systems. In synthetic domains such as supramolecular chemistry, the control of subtle non-covalent interactions is used to form large chemical systems with unique characteristics [2]. Non-covalent interactions are important to many biological processes; signalling pathways, enzymatic activity, antibody/ligand binding, and drug action are only some of the many examples that involve non-covalent interactions. The conformations of non-covalent complexes are determined by the overall energetics of interaction and the strength of the interaction is determined by the conformation [3]; the structure and energetics of non-covalent complexes are inherently linked. The study of non-covalent interactions permeates many scientific fields, and is investigated with a number of techniques including mass spectrometry (MS).

Mass Spectrometry

At its core, MS measures the mass to charge ratio (m/z) of gas phase ions. MS has existed for more than 100 years, beginning with experiments demonstrating beams of positive ions, called anode rays, could be deflected by a magnetic field based on the ion's mass and charge [4-6]. Early MS instruments measured the m/z of gas phase ions solely based on ion beam deflection in a magnetic field [7, 8] however, variations of this [9] and new approaches to measure the m/z of ions followed [10-15].

Initially, MS analysis was used exclusively for volatile compounds ionized by electron impact. In the modern era, the development of soft ionization techniques has allowed much larger and non-volatile compounds to be ionized and promoted to the gas phase, greatly increasing the variety of chemical systems accessible to MS analysis. In 2002, Koichi Tanaka and John Bennett Fenn shared half of the Nobel Prize in chemistry for their respective works on soft ionization methods. Tanaka showed that large proteins or synthetic polymers dried within a mixture of glycerol and fine metal powder could be softly desorbed and ionized by irradiation with a nitrogen laser [16]. Although not awarded the Nobel Prize for their work, Karas and Hillenkamp developed a similar technique known as matrix assisted laser desorption ionization (MALDI) [17, 18] which unlike Tanaka's approach, continues to be very widely used. Fenn received the Nobel Prize for his work on electrospray ionization (ESI) [19, 20] which built on earlier work by others, notably Malcolm Dole [21]. ESI has a number of benefits which include the direct interfacing of the liquid phase and mass spectrometry, the formation of multiply charged ions and the ability to softly ionize intact non-covalent complexes.

Studying non-covalent complexes with mass spectrometry

Molecules that are easily protonated, deprotonated or permanently charged (i.e. quaternary amines) are generally ionized well with ESI. Some molecules lacking these functional groups can still be ionized effectively with ESI by forming non-covalent, electrostatic adducts with small charged molecules. For example, it has been shown that glycans can form stable non-covalent complexes with a nitrate anion (NO_3^-) at a tenfold increase in sensitivity vis à vis its deprotonated form [22]. Ionization of synthetic polymers routinely requires formation of non-covalent complexes (Reviewed in [23]) between the polymer and small cations including Ag^+ [24-26], Na^+ [26-28], K^+ [24, 26], Li^+ [25] and NH_4^+ [26, 29]. Larger non-covalent complexes, clusters [30] and molecular aggregates are commonly observed in ESI-MS as well. Many non-covalent complexes observed with ESI-MS can be the result of the electrospray ionization process and not representative of the solution phase associations; these complexes are considered non-specific interactions. However, many specific interactions which are known to occur in solution have been maintained during the ionization process [30, 31]. ESI based studies of non-covalent complexes are numerous and early examples include protein-substrate [32], protein-protein [30], DNA [33], DNA-substrate [34, 35], and host-guest complexes [36, 37]. ESI-MS not only has the ability to identify solution phase interactions between different biomolecules, but under careful conditions can also quantify the extent of solution phase binding ([38, 39], reviewed in [40]). This includes but not limited to maintaining low concentrations, using ESI compatible solutions that still maintain the native solution structure of the complex and making the ionization conditions as soft as possible.

Investigating non-covalent complex dissociation with tandem MS

Tandem MS (MS/MS) is a technique whereby an ion or charged complex is isolated and made to dissociate by increasing its internal energy and the m/z of fragment ions are measured. There are several MS/MS methods to activate ions including blackbody infrared radiative dissociation (BIRD), infrared multiphoton dissociation (IRMPD), electron transfer dissociation, electron capture dissociation, surface induced dissociation, and collision induced dissociation (CID). A well-known example outlining the utility of MS/MS is the dissociation of ionized peptides which allows for the amino acid sequence to be determined (reviewed in [41]). MS/MS of non-covalent complexes often leads to dissociation of the individual components prior to fragmentation of covalent bonds. In some cases, including the 800 kDa eukaryotic translation factor elF3, the manner by which dissociates allows for the arrangement of the subunits to be mapped [31]. In other instances, the manner in which a molecule within a non-covalent complex fragments is greatly influenced by the other molecule(s) within the complex. For example, poly(methylmethacrylate) (PMMA) complexed with Na^+ undergoes a free radical fragmentation along the polymer's backbone, resulting in a small number of low-mass product ions [42]. In contrast, PMMA in complex with protonated amines with appropriate proton affinity will undergo charge directed fragmentation along the side chains yielding a large number of high mass fragment ions [43]. Therefore, the use of different adducts in forming non-covalent complexes can aid in the characterization of the compound.

The fragment ions that are produced in MS/MS are determined by the dissociation reactions available to the reactant ion at or below its internal energy content. The relative intensity and the activation energies where a fragment ion appears is determined in part by its dissociation rate constant, which itself is a reflection of the dissociation reaction's thermochemistry. A number of MS/MS based techniques have been applied to measure absolute or relative interaction energetics of non-covalent complexes.

Threshold collision induced dissociation (TCID) allows for the absolute measurement of bond dissociation energies using a specialized guided ion beam apparatus. Ideally, the molecule or non-covalent complex [44] is ionized and thermalized [45, 46] and subsequently activated under single collision conditions. The intensity of the reactant and fragment ions are plotted as a function of kinetic energy (E_{lab}) and converted to a plot of absolute reaction cross sections as a function of center of mass collision energy (E_{com}). The reaction cross section represents the probability the dissociation will occur and is theoretically modelled to obtain the threshold dissociation energies [47, 48].

BIRD is a MS technique for determining the Arrhenius activation energies (E_a) and the Arrhenius parameters (A) of dissociation reactions, including the dissociation of non-covalent complexes [49, 50]. BIRD experiments are performed on a Fourier transform ion cyclotron resonance (FTICR) mass spectrometer as this type of instrument allows for ions to be trapped and stored for an extended period of time under very low pressures (10^{-10} mbar). In FTICR, ions are stored in three dimensions by a combination of a large magnetic field (radial direction) and small electric field (1-2 V). A Fourier transform converts the resulting time domain of the signal into the frequency domain, thereby providing the m/z ratios of the trapped ions [51]. The temperature of the ICR cell is controlled and acts as a blackbody emitting photons with energies that reflect its temperature. The ICR temperatures that are generally used for BIRD experiments have photon emissions with a maximum intensity in the infrared region. The infrared photons are absorbed by the stored ions. If the rate of energy exchange between the ions and the ICR cell is faster than the rate of dissociation, the stored ions have a Boltzmann distribution of energies [52] and accurate Arrhenius values can be obtained. The rate of dissociation at different temperatures is measured to generate an Arrhenius plot [49] where E_a is determined by:

$$\mathbf{ln(k) = -\frac{E_a}{R} \cdot \frac{1}{T} + lnA} \qquad \text{Equation 1-1}$$

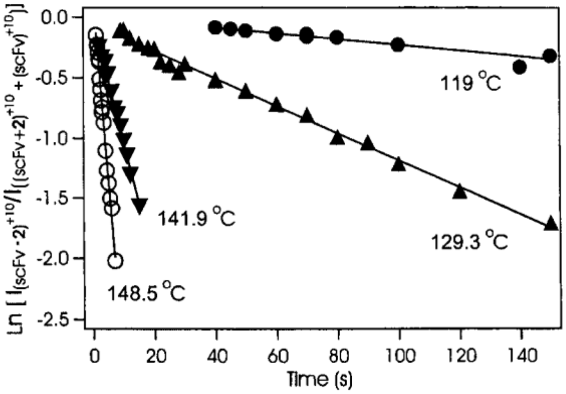

Figure 1-1 BIRD temperature dependent dissociation plot
Kitova and co-workers mapped the intermolecular interactions between a single chain fragment of an antibody and a series of tri-saccharides. [53]

Although able to measure accurate and absolute thermochemical values, techniques such as TCID and BIRD require specialized instrumentation which limits the extent of their use.

Most commercially available mass spectrometers are equipped to perform CID under multiple collision conditions. A rapid technique to assign relative kinetic stabilities is the $E_{1/2}$ method which compares the collision energies at which 50% of an ion or non-covalent complex ion dissociates [54]. Although fast and not requiring extensive modelling or calculations, care has to be taken when comparing $E_{1/2}$ values for different systems as it is greatly affected by the number of degrees of freedom (DOF) within the complex [55], and does separately consider entropic and enthalpic terms. Breakdown diagrams plot the relative intensities of the reactant and product ions as a function of collision energy (Figure 1-2).

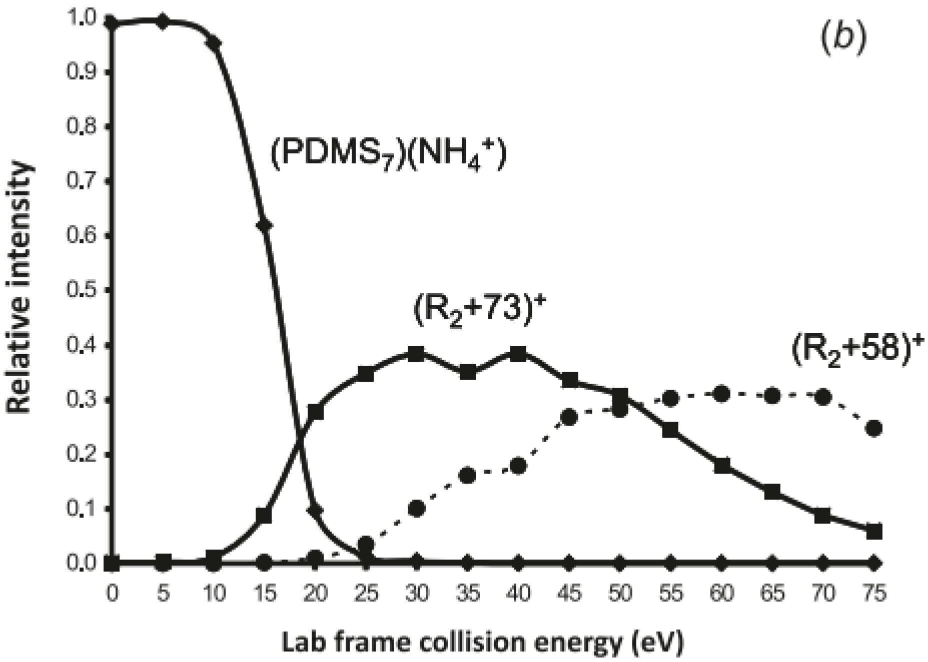

Figure 1-2 Breakdown diagram of ammoniated polydimethylsiloxane
Renaud and co-workers determined the onset of different fragmentation pathways of polydimethylsiloxane non-covalently bound to a variety of small cations[26]

The method used throughout this work to measure meaningful thermochemical values on unmodified, commercially available instruments takes kinetic shift, DOF, enthalpic and entropic contributions into account by modelling experimental breakdown diagrams with Rice, Ramsperger, Kassel and Marcus (RRKM) unimolecular rate theory. The shape and features of a breakdown diagram are influenced by a number of factors (Table 1-1).

Table 1-1 Major factors that influence the shape of MS/MS breakdown diagrams

• The time scale of the dissociation
• The initial internal energy distribution of the reactant ions before collisional activation
• The relationship of collision energy and the internal energy distribution of the reactant ion
• The unimolecular rate constants of all accessible dissociation channels.

The unimolecular rate constant (k(E)) was modelled in a statistical manner by Rice and Ramsperger [56, 57] and Kassel [58, 59] who treated a molecule as a collection of identical harmonic oscillators. For a dissociation reaction, the bond that is broken is the critical oscillator, and its reaction rate is determined by the internal energy content. This was later merged with transition state theory by Rice and Marcus [60] to give a more complete description:

$$\mathbf{k(E)} = \frac{\boldsymbol{\sigma} \mathbf{N^{\ddagger}(E-E_0)}}{\mathbf{h}\boldsymbol{\rho}\mathbf{(E)}} \qquad \text{Equation 1-2}$$

k(E) is the rate constant at internal energy E,
σ is the reaction degeneracy
$N^{\ddagger}(E-E_0)$ is the sum of states of the transition state between energies 0 and E - E_0,
h is Planck's constant, and
ρ(E) is the density of states of the reactant ion.

The $N^{\ddagger}(E-E_0)$ term represents the ways that energy can be arranged throughout the oscillators of the transition state ($TS^{\ddagger}$) structure at energy E-E_0. The ρ(E) term represents the number of ways energy can be arranged in the reactant ion at energy E + dE. The reaction can proceed through σ critical coordinate(s), and ρ(E) defines the possibility of the reaction getting lost in the phase space of the molecular ion and not dissociating. $N^{\ddagger}(E-E_0)$ and ρ(E) are calculated directly from the vibrational frequencies of the reactant ion and $TS^{\ddagger}$ structures using the appropriately named 'direct count method' developed by Beyer and Swinehart [61].

The entropy of activation ($\Delta S^{\ddagger}$) of the dissociation is also expressed within the RRKM equation 1-2 based on the differences in vibrational frequencies of the reactant ion and $TS^{\ddagger}$ ion by:

$$\boldsymbol{\Delta S^{\ddagger}} = \frac{\mathbf{U^{\ddagger}-U}}{\mathbf{T}} + \mathbf{k_B ln}\frac{\prod \mathbf{Z_i^{\ddagger}}}{\prod \mathbf{Z_i}} \qquad \text{Equation 1-3}$$

Z and $Z^{\ddagger}$ are the partition functions of the reactant and $TS^{\ddagger}$ vibrational frequencies respectively described as:

$$\boldsymbol{Z_i^{(\ddagger)}} = \frac{\mathbf{1}}{\mathbf{1-e^{\frac{hv_i}{k_B T}}}} \qquad \text{Equation 1-4}$$

T is temperature,
k_B is the boltzmann constant, and
v_i is the vibrational frequency of the oscillator

When the factors outlined in Table 1-1 are known, a theoretical MS/MS breakdown diagram can be generated. When all these values are not known, a number of theoretical breakdown curves can be generated by altering the RRKM variables to best reflect the experimental breakdown diagram.

As mentioned previously, the energetics of interaction and the structure of non-covalent complexes are inherently linked. Interpretation of energetic data obtained by MS/MS normally requires details into the structural nature of the reactant, $TS^‡$ and fragment.

Obtaining structural details of gas phase ions

There are relatively few experimental techniques that can elucidate the structure of gas phase ions. Infrared multiphoton dissociation (IRMPD) consequence spectroscopy operates by directing tunable infrared radiation into a cloud of stored ions. When the frequency of the radiation is in resonance with an ion's v=0, to v=1 vibrational mode transition, a photon is absorbed. The absorbed energy is quickly redistributed throughout the ion which allows other photons to be absorbed by the active vibrational mode. Multiple photon absorption will increase the internal energy of the ion until dissociation channels of the ion/complex become accessible. Examining the relationship between the frequency of radiation to the level of ion dissociation gives a consequence spectrum that can be compared to the vibrational modes of computationally derived structures (reviewed in [62]).

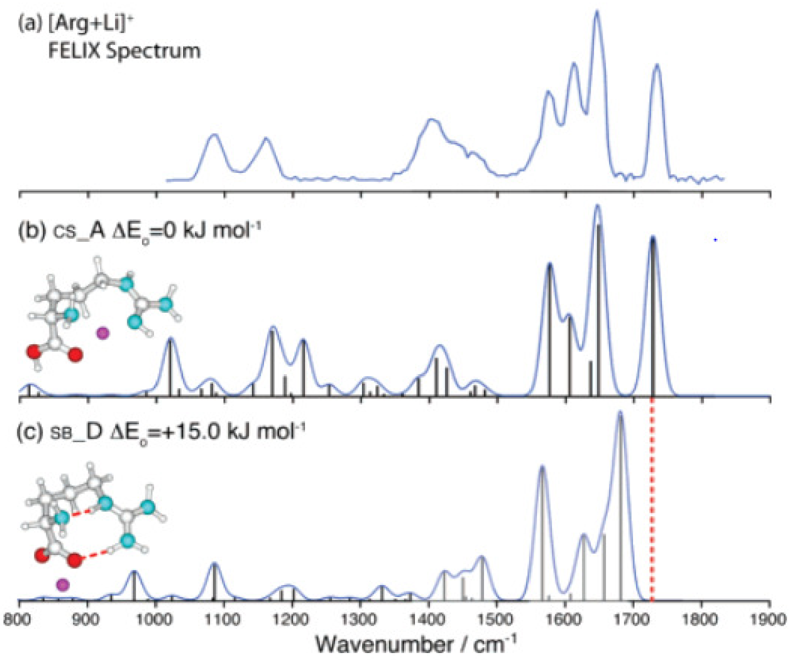

Figure 1-3 IRMPD consequence spectra of [Arg+Li]$^+$
Forbes et al. clearly show that (a) experimental IRMPD consequence spectrum of lithiated arginine corresponds to (b) theoretical low energy charge solvated structure and not (c) theoretical low energy salt bridge structure[63].

IRMPD of even larger ions including a 104 amino acid protein [64] can give signatures of higher order structure. However, in the opinion of this author, it is challenging to obtain detailed structural characteristics of large and intermediate sized ions with this method given the range and overlap of vibrational frequencies that can exist in very large molecules.

Ion mobility spectrometry

Ion mobility spectrometry (IMS) is a complementary technique to MS and provides direct insight into molecular structure by measuring an ion's collision cross section (Ω) to charge ratio (reviewed in [65]). Although IMS exists in a number of designs, the basic operation involves measuring the mobility of an ion being propelled by an electric field through a drift tube containing an obstructing buffer gas. The physical characteristics of the ion that determines its mobility (K) is described by the Mason equation:

$$\mathbf{K} = \frac{3}{16}\sqrt{\frac{2\pi}{\mu k_B T}} \cdot \frac{e}{N} \cdot \frac{z}{\Omega}$$ Equation 1-5 (Discussed in detail in [66])

μ is the reduced mass of the ion and neutral buffer gas
N is the number density of the buffer gas,
T is the temperature of the buffer gas,
e is the elementary charge ($1.60218\ 10^{-19}$ C),
z is the charge of the ion, and
Ω is the collision cross section.

An ion with a large Ω being propelled through a buffer gas will be impeded more than an ion with a small Ω and will therefore take longer to arrive at the detector. Knowledge of an ion's experimental cross section (Ω_{exp}) is often not sufficient to describe its molecular structure. However it does allow for the correctness of theoretical structures generated with computational methods to be either validated or refuted. This powerful combination of computational and ion mobility analysis has allowed for detailed structural analysis of many non-covalent complexes, including large protein complexes [67, 68] and to metal cationized synthetic polymers [69-72].

1.2 Summary of thesis objectives

As previously stated, the association between structure and interaction energetics of non-covalent complexes is inherently linked. When applicable, RRKM modelling of MS/MS breakdown diagrams of non-covalent complexes was used to obtain energetic data, while IMS in conjunction with computational methods were used to obtain structural data. The objective of this work was to develop an efficient approach to describe both the structure and energetics of non-covalent complexes in a cohesive manner.

1.3 References

1. Langmuir, I. THE ARRANGEMENT OF ELECTRONS IN ATOMS AND MOLECULES. Journal of the American Chemical Society 41, 868-934 (1919)
2. Lehn, J.-M. Supramolecular chemistry. Science 260, 1762-1763 (1993)
3. Bennett, W.S.; Steitz, T.A. Glucose-induced conformational change in yeast hexokinase. Procedings of the National Academy of Sciences of the United States of America 75, 4 (1978)
4. Wien, W. Untersuchungen über die electrische Entladung in verdünnten Gasen. Annalen der Physik 301, 440-452 (1898)
5. Thomson, J. J. XLVII. On rays of positive electricity. The London, Edinburgh, and Dublin Philosophical Magazine and Journal of Science 13, 561-575 (1907)
6. Thomson, J. Rays of Positive Electricity and their Application to Chemical Analysis. Journal of the Röntgen Society 10, 41-42 (1914)
7. Dempster, A. A new method of positive ray analysis. Physical Review 11, 316-325 (1918)
8. Aston, F. W. LXXIV. A positive ray spectrograph. The London, Edinburgh, and Dublin Philosophical Magazine and Journal of Science 38, 707-714 (1919)
9. Mattauch, J. A double-focusing mass spectrograph and the masses of N 15 and O 18. Physical Review 50, 617 (1936)
10. Lawrence, E. O., Method and apparatus for the acceleration of ions, 1934.
11. Stephens, W., in *Physical Review, Vol. 69*, American Physical Soc. MD 20740-3844 USA, 1946, pp. 691-691.
12. Paul, W., Steinwedel, H. Ein neues massenspektrometer ohne magnetfeld. Zeitschrift Naturforschung Teil A 8, 448 (1953)
13. Paul, W., Raether, M. Das elektrische massenfilter. Zeitschrift für Physik 140, 262-273 (1955)
14. Comisarow, M. B., Marshall, A. G. Fourier transform ion cyclotron resonance spectroscopy. Chemical physics letters 25, 282-283 (1974)
15. Makarov, A., in *Proceedings of the 48th ASMS conference on mass spectrometry and allied topics, Dallas, TX*, 1999.
16. Tanaka, K.; Waki, H.; Ido, Y.; Akita, S.; Yoshida, Y.; Yoshida, T., Matsuo, T. Protein and polymer analyses up to m/z 100 000 by laser ionization time of flight mass spectrometry. Rapid Communications in Mass Spectrometry 2, 151-153 (1988)

17. Karas, M.; Bachmann, D., Hillenkamp, F. Influence of the wavelength in high-irradiance ultraviolet laser desorption mass spectrometry of organic molecules. Analytical Chemistry 57, 2935-2939 (1985)

18. Karas, M., Hillenkamp, F. Laser desorption ionization of proteins with molecular masses exceeding 10,000 daltons. Analytical Chemistry 60, 2299-2301 (1988)

19. Yamashita, M., Fenn, J. B. Electrospray ion source. Another variation on the free-jet theme. The Journal of Physical Chemistry 88, 4451-4459 (1984)

20. Fenn, J. B.; Mann, M.; Meng, C. K.; Wong, S. F., Whitehouse, C. M. Electrospray ionization for mass spectrometry of large biomolecules. Science 246, 64-71 (1989)

21. Dole, M.; Hines, R.; Mack, L.; Mobley, R.; Ferguson, L., Alice, M. Gas phase macroions. Macromolecules 1, 96-97 (1968)

22. Harvey, D. J. Fragmentation of Negative Ions from Carbohydrates: Part 1. Use of Nitrate and Other Anionic Adducts for the Production of Negative Ion Electrospray Spectra from< i> N</i>-linked Carbohydrates. Journal of the American Society for Mass Spectrometry 16, 622-630 (2005)

23. Montaudo, G., Lattimer, R. P., *Mass spectrometry of polymers*, CRC Press, 2001.

24. Deery, M. J.; Jennings, K. R.; Jasieczek, C. B.; Haddleton, D. M.; Jackson, A. T.; Yates, H. T., Scrivens, J. H. A Study of Cation Attachment to Polystyrene by Means of Matrix-assisted Laser Desorption/Ionization and Electrospray Ionization-Mass Spectrometry. Rapid Communications in Mass Spectrometry 11, 57-62 (1997)

25. Chen, R., Li, L. Lithium and transition metal ions enable low energy collision-induced dissociation of polyglycols in electrospray ionization mass spectrometry. Journal of the American Society for Mass Spectrometry 12, 832-839 (2001)

26. Renaud, J.; Alhazmi, A. M., Mayer, P. M. Comparing the fragmentation chemistry of gas-phase adducts of poly (dimethylsiloxane) oligomers with metal and organic ions. Canadian Journal of Chemistry 87, 453-459 (2009)

27. Wong, S.; Meng, C., Fenn, J. Multiple charging in electrospray ionization of poly (ethylene glycols). The Journal of Physical Chemistry 92, 546-550 (1988)

28. Nielen, M. W., Buijtenhuijs, F. Polymer analysis by liquid chromatography/electrospray ionization time-of-flight mass spectrometry. Analytical Chemistry 71, 1809-1814 (1999)

29. Fouquet, T.; Humbel, S., Charles, L. Tandem mass spectrometry of trimethylsilyl-terminated poly (dimethylsiloxane) ammonium adducts generated by electrospray ionization. Journal of the American Society for Mass Spectrometry 22, 649-658 (2011)
30. Light-Wahl, K. J.; Schwartz, B. L., Smith, R. D. Observation of the noncovalent quaternary associations of proteins by electrospray ionization mass spectrometry. Journal of the American Chemical Society 116, 5271-5278 (1994)
31. Zhou, M.; Sandercock, A. M.; Fraser, C. S.; Ridlova, G.; Stephens, E.; Schenauer, M. R.; Yokoi-Fong, T.; Barsky, D.; Leary, J. A., Hershey, J. W. Mass spectrometry reveals modularity and a complete subunit interaction map of the eukaryotic translation factor eIF3. Proceedings of the National Academy of Sciences 105, 18139-18144 (2008)
32. Ganem, B.; Li, Y. T., Henion, J. D. Observation of noncovalent enzyme-substrate and enzyme-product complexes by ion-spray mass spectrometry. Journal of the American Chemical Society 113, 7818-7819 (1991)
33. Bayer, E.; Bauer, T.; Schmeer, K.; Bleicher, K.; Maier, M., Gaus, H.-J. Analysis of double-stranded oligonucleotides by electrospray mass spectrometry. Analytical chemistry 66, 3858-3863 (1994)
34. Gale, D. C.; Goodlett, D. R.; Light-Wahl, K. J., Smith, R. D. Observation of duplex DNA-drug noncovalent complexes by electrospray ionization mass spectrometry. Journal of the American Chemical Society 116, 6027-6028 (1994)
35. Gale, D. C., Smith, R. D. Characterization of noncovalent complexes formed between minor groove binding molecules and duplex DNA by electrospray ionization-mass spectrometry. Journal of the American Society for Mass Spectrometry 6, 1154-1164 (1995)
36. Lippmann, T.; Wilde, H.; Pink, M.; Schäfer, A.; Hesse, M., Mann, G. Host–Guest Complexes between Calix [4] arenes Derived from Resorcinol and Alkylammonium Ions. Angewandte Chemie International Edition in English 32, 1195-1197 (1993)
37. Ramanathan, R., Prokai, L. Electrospray ionization mass spectrometric study of encapsulation of amino acids by cyclodextrins. Journal of the American Society for Mass Spectrometry 6, 866-871 (1995)
38. Wang, W.; Kitova, E. N., Klassen, J. S. Influence of solution and gas phase processes on protein-carbohydrate binding affinities determined by nanoelectrospray Fourier transform ion cyclotron resonance mass spectrometry. Analytical Chemistry 75, 4945-4955 (2003)

39. Sun, J.; Kitova, E. N.; Wang, W., Klassen, J. S. Method for distinguishing specific from nonspecific protein-ligand complexes in nanoelectrospray ionization mass spectrometry. Analytical Chemistry 78, 3010-3018 (2006)

40. Daniel, J. M.; Friess, S. D.; Rajagopalan, S.; Wendt, S., Zenobi, R. Quantitative determination of noncovalent binding interactions using soft ionization mass spectrometry. International Journal of Mass Spectrometry 216, 1-27 (2002)

41. Hernandez, P.; Müller, M., Appel, R. D. Automated protein identification by tandem mass spectrometry: issues and strategies. Mass spectrometry reviews 25, 235-254 (2006)

42. Chaicharoen, K.; Polce, M. J.; Singh, A.; Pugh, C., Wesdemiotis, C. Characterization of linear and branched polyacrylates by tandem mass spectrometry. Analytical and bioanalytical chemistry 392, 595-607 (2008)

43. Alhazmi, A. M., Mayer, P. M. Protonating polymer oligomers in the gas phase to change fragmentation pathways. Journal of the American Society for Mass Spectrometry 20, 60-66 (2009)

44. Rodgers, M., Armentrout, P. Noncovalent metal–ligand bond energies as studied by threshold collision-induced dissociation. Mass spectrometry reviews 19, 215-247 (2000)

45. Schultz, R. H., Armentrout, P. A guided-ion beam study of the reactions of $N^+{}_4$ with H_2, HD, and D_2: An evaluation of pseudo-Arrhenius analyses of ion–molecule reaction systems. The Journal of chemical physics 96, 1046-1052 (1992)

46. Schultz, R. H.; Crellin, K. C., Armentrout, P. Sequential bond energies of iron carbonyl Fe (CO) x+ (x= 1-5): systematic effects on collision-induced dissociation measurements. Journal of the American Chemical Society 113, 8590-8601 (1991)

47. Armentrout, P., Beauchamp, J. Cobalt carbene ion: Reactions of Co^+ with C_2H_4, cyclo-$C_3H_{6,}$ and cyclo-C_2H_4O. The Journal of chemical physics 74, 2819-2826 (1981)

48. Aristov, N., Armentrout, P. B. Reaction mechanisms and thermochemistry of vanadium ions with ethane, ethene and ethyne. Journal of the American Chemical Society 108, 1806-1819 (1986)

49. Price, W. D.; Schnier, P. D., Williams, E. R. Tandem mass spectrometry of large biomolecule ions by blackbody infrared radiative dissociation. Analytical chemistry 68, 859-866 (1996)

50. Dunbar, R., McMahon, T. Activation of unimolecular reactions by ambient blackbody radiation. Science 279, 194-197 (1998)

51. Marshall, A. G.; Hendrickson, C. L., Jackson, G. S. Fourier transform ion cyclotron resonance mass spectrometry: a primer. Mass spectrometry reviews 17, 1-35 (1998)

52. Price, W. D., Williams, E. R. Activation of peptide ions by blackbody radiation: Factors that lead to dissociation kinetics in the rapid energy exchange limit. The Journal of Physical Chemistry A 101, 8844-8852 (1997)
53. Kitova, E. N.; Bundle, D. R., Klassen, J. S. Thermal dissociation of protein-oligosaccharide complexes in the gas phase: Mapping the intrinsic intermolecular interactions. Journal of the American Chemical Society 124, 5902-5913 (2002)
54. Wan, K. X.; Gross, M. L., Shibue, T. Gas-Phase Stability of Double-Stranded Oligodeoxynucleotides and Their Noncovalent Complexes With DNA-Binding Drugs As Revealed by Collisional Activation in an Ion Trap. J. Am. Soc. Mass Spectrom. 11, 7 (2000)
55. Gabelica, V., Pauw, E. D. Comparison between solution-phase stability and gas-phase kinetic stability of oligodeoxynucleotide duplexes. J. Mass Spectrom. 36, 5 (2001)
56. Rice, O. K., Ramsperger, H. C. Theories of unimolecular gas reactions at low pressures. Journal of the American Chemical Society 49, 1617-1629 (1927)
57. Rice, O. K., Ramsperger, H. C. Theories of Unimolecular Gas Reactions at Low Pressures. II. Journal of the American Chemical Society 50, 617-620 (1928)
58. Kassel, L. S. Studies in Homogeneous Gas Reactions. I. The Journal of Physical Chemistry 32, 225-242 (1928)
59. Kassel, L. Studies in homogeneous gas reactions. II. Introduction of quantum theory. The Journal of Physical Chemistry 32, 1065-1079 (1928)
60. Marcus, R., Rice, O. The Kinetics of the Recombination of Methyl Radicals and Iodine Atoms. The Journal of Physical Chemistry 55, 894-908 (1951)
61. Beyer, T., Swinehart, D. Algorithm 448: number of multiply-restricted partitions. Communications of the ACM 16, 379 (1973)
62. Fridgen, T. D. Infrared consequence spectroscopy of gaseous protonated and metal ion cationized complexes. Mass spectrometry reviews 28, 586-607 (2009)
63. Forbes, M. W.; Bush, M. F.; Polfer, N. C.; Oomens, J.; Dunbar, R. C.; Williams, E. R., Jockusch, R. A. Infrared spectroscopy of arginine cation complexes: direct observation of gas-phase zwitterions. The Journal of Physical Chemistry A 111, 11759-11770 (2007)
64. der Meer, L., Helden, G. Charge-state resolved mid-infrared spectroscopy of a gas-phase protein. Physical Chemistry Chemical Physics 7, 1345-1348 (2005)
65. Dugourd, P.; Hudgins, R.; Clemmer, D., Jarrold, M. High-resolution ion mobility measurements. Review of Scientific Instruments 68, 1122-1129 (1997)

66. Revercomb, H., Mason, E. Theory of plasma chromatography/gaseous electrophoresis. review. Analytical Chemistry 47, 970-983 (1975)

67. Ruotolo, B. T.; Benesch, J. L.; Sandercock, A. M.; Hyung, S.-J., Robinson, C. V. Ion mobility–mass spectrometry analysis of large protein complexes. Nature Protocols 3, 1139-1152 (2008)

68. Loo, J. A.; Berhane, B.; Kaddis, C. S.; Wooding, K. M.; Xie, Y.; Kaufman, S. L., Chernushevich, I. V. Electrospray ionization mass spectrometry and ion mobility analysis of the 20S proteasome complex. Journal of the American Society for Mass Spectrometry 16, 998-1008 (2005)

69. Wyttenbach, T.; von Helden, G., Bowers, M. T. Conformations of alkali ion cationized polyethers in the gas phase: polyethylene glycol and bis [(benzo-15-crown-5)-15-ylmethyl] pimelate. International journal of mass spectrometry and ion processes 165, 377-390 (1997)

70. Gidden, J.; Wyttenbach, T.; Jackson, A. T.; Scrivens, J. H., Bowers, M. T. Gas-phase conformations of synthetic polymers: poly (ethylene glycol), poly (propylene glycol), and poly (tetramethylene glycol). Journal of the American Chemical Society 122, 4692-4699 (2000)

71. Gidden, J.; Jackson, A. T.; Scrivens, J. H., Bowers, M. T. Gas phase conformations of synthetic polymers: poly (methyl methacrylate) oligomers cationized by sodium ions. International Journal of Mass Spectrometry 188, 121-130 (1999)

72. Gidden, J.; Bowers, M. T.; Jackson, A. T., Scrivens, J. H. Gas-phase conformations of cationized poly (styrene) oligomers. Journal of the American Society for Mass Spectrometry 13, 499-505 (2002)

Chapter 2: Methods of study

2.1.1 Electrospray ionization

In 2002, John B. Fenn shared the Nobel Prize for his work on electrospray ionization (ESI) [1, 2] which built on earlier work by others, notably Malcolm Dole [3]. ESI is a soft ionization technique that is a direct interface between a liquid phase and a mass spectrometer. Several reviews have appraised the current understanding of the ESI mechanism [4-7]. The electrospray phenomenon, which was first reported in 1749 [8], is the generation of a fine aerosol from a small liquid droplet in the presence a strong electric field (Figure 2-1).

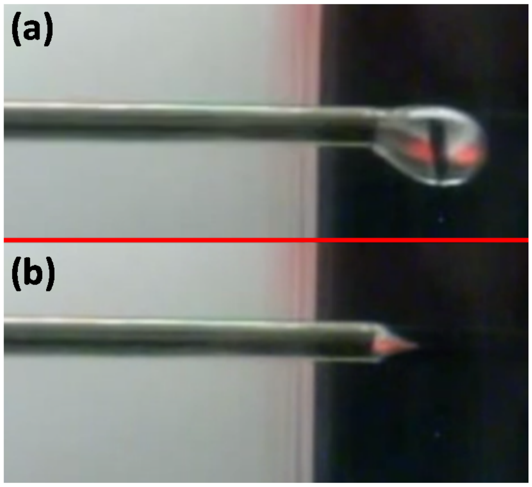

Figure 2-1 Formation of Taylor cone by applying high voltage to a metal capillary
Courtesy of Brandi J. West (2007)

The analytical use of ESI as an MS ionization source was established by Dole and co-workers who ionized a solution of large, intact polystyrene ions [9]. A conductive capillary held at voltages in the kV range is placed near a counter electrode. The aerosolized droplets formed by the electrospray contain either an excess of positive or negative charge depending on the polarity of analysis and are directed towards the entrance of the mass spectrometer by the electric field. The excess droplet charges are believed to originate at the metal capillary/liquid interphase from either oxidation or reduction reactions for positive or negative mode respectively (Figure 2-2) [10].

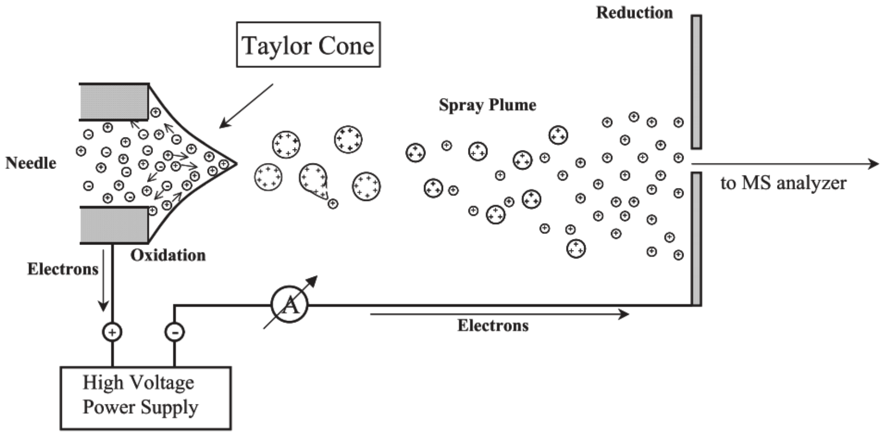

Figure 2-2 ESI as an electrolysis cell

Blades and co-workers showed that oxidation is occurring at the capillary/liquid interface by using a zinc capillary and detecting Zn^{2+} ions [10].

An additional source of charge within the droplets is due to the electrophoretic mobility of the ions. Grimm and co-workers showed that strong electrical fields could desorb and ionize molecules from neutral droplets [11]. Prior to this, Zhou and co-workers proposed that under a strong electric field, positive and negative ions will migrate to opposite ends of the droplet, leading to buildup of excess surface charge [12].

Two principle mechanistic models of outlining how the desolvated ions are formed are the charged residue (CR) model and the ion evaporation (IE) model although other explanations such as the chain ejection model have been put forward for the ionization of specific kinds of compounds [13].

In the CR model, the droplets shrink as the solvent molecules evaporate while the charge remains constant until the droplet reaches the Rayleigh stability limit:

$$\mathbf{q} = \mathbf{8\pi}\sqrt{\epsilon_0\ \boldsymbol{\gamma}\ \mathbf{R}^3} \qquad \text{Equation 2-1}$$

q is the charge on the droplet,
ϵ_0 is the electric permittivity of the medium,
γ is surface tension , and
R is the radius of the droplet

The Rayleigh stability limit occurs when the electrostatic repulsion is equal to the droplet's surface tension, after which the unstable droplet undergoes coulombic fission producing progeny droplets. The progeny droplets undergo successive shrinkage/fission cycles until a charged analyte remains. In the IE model, the evaporation of an ion occurs directly from the droplet. Similar to the CR model, the charged droplets shrink as the solvent evaporates. In order to relax the growing coulombic repulsion of the droplet, analyte molecules evaporate from the surface taking charge(s) with it.

2.1.2 Mass analysis

Quadrupole

In this work, the quadrupole arrangement was used as a ion filter to isolate ions for MS/MS and in some instances for mass analysis (Chapters 3,6). Detailed descriptions of the behaviour of trapped ions in quadrupoles and quadrupole ion traps is found in a review by Raymond E. March [14]. A quadrupole mass filter consists of four parallel rods in which adjustable direct current (dc) and radio frequency (rf) voltages are applied. The two rods opposite one another are paired and the two pairs have voltages of equal magnitude and opposite sign (Figure 2-3) and rf voltages that are 180° out of phase from one another. By convention, the plane of the rods is the Z axis, the horizontal is the X direction and the vertical Y direction.

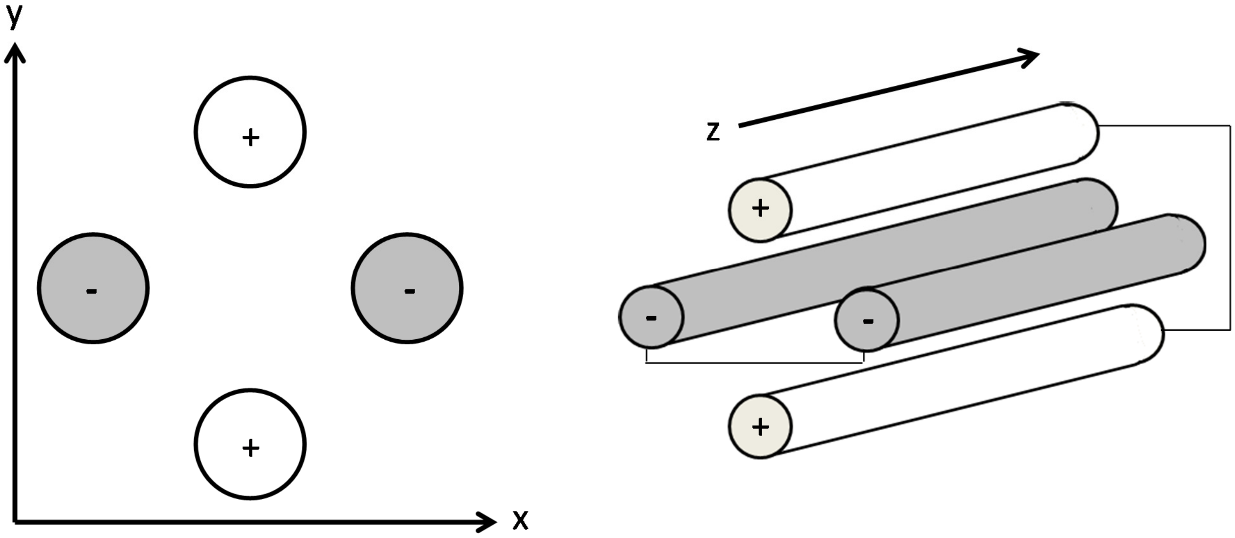

Figure 2-3 Quadrupole mass analyzer schematic

As a pair, the rods will act either as a low mass pass or high mass pass filter. The motion of the ions in the X and Y planes can be described by:

$$\frac{d^2x}{dt^2} = -\frac{\omega^2}{4}[a + 2q \cdot \cos(\omega t)]x$$ Equation 2-2

$$\frac{d^2y}{dt^2} = \frac{\omega^2}{4}[a + 2q \cdot \cos(\omega t)]y$$ Equation 2-3

With,

$$a = \frac{4eU}{\omega^2 r_0^2 m}$$ Equation 2-4

$$q = \frac{2eV}{\omega^2 r_0^2 m}$$ Equation 2-5

m and e are the mass and charge of the ion,
ω is the rf angular frequency,
U is the magnitude of the dc potential,
V is the magnitude of the rf potential, and
r_0 is the distance from the surface of the rod to the center of the axis.
When the rods are hyperbolic, the motion of the ions in the x, y and z directions will be completely independent

For negative ions, the X axis rod pair in Figure 2-3 is the high mass pass filter and has a stabilizing dc voltage and an rf voltage that is destabilizing to ions below a critical m/z threshold. The rf voltage oscillations will have the greatest effect on the motion of low m/z ions which stay in phase with the rf field with an increasingly large amplitude until they collide with a rod and are neutralized. In contrast, Y axis rod pair of Figure 2-3 is the low pass mass filter and has a de-stabilizing dc voltage and a corrective rf voltage. In this plane, the dc potential on the rods is opposite to the charge of the ions and therefore will have a defocusing effect. The oscillating rf voltage corrects the destabilizing effects of the dc voltage and will have the greatest effect of low m/z ions. The trajectories of ions above a critical m/z ratio will not be sufficiently rectified and will collide with a rod. The high mass and low mass pass together allow for only a specific range of m/z values to maintain stable trajectories and be transmitted across the quadrupole in the z-direction. When combinations of dc and rf voltages are scanned, the quadrupole will act as a mass analyzer. Hexapole arrangements have been commonly used in place of quadrupoles as collision/reaction cells for tandem MS experiments. Quadrupoles are better at focusing ions, however a hexapole arrangements has steeper potential wells which make them better at providing linear transmissions of ions across a range of collision energies [15].

Time of flight

Time of flight mass analyzers (TOF) determine the m/z ratio of ions by measuring the time ions require to travel a specific distance within a flight tube. The kinetic energy (E_k) of an ion in an electric field is:

$$\mathbf{E_k = zU} \qquad \text{Equation 2-6}$$

z is the charge of the ion and
U is the applied voltage.

The E_k of a body is related to its mass (m) and velocity (v) by:

$$\mathbf{E_k = \frac{1}{2} m v^2} \qquad \text{Equation 2-7}$$

Equation 2-4 can be written to express velocity as time (t) and distance (d) parameters:

$$\mathbf{E_k = \frac{1}{2} m \left(\frac{d}{t}\right)^2} \qquad \text{Equation 2-8}$$

Combining equations 2-3 and 2-5 gives:

$$\mathbf{zU = \frac{1}{2} m \left(\frac{d}{t}\right)^2} \qquad \text{Equation 2-9}$$

Equation 2-5 contains both m and z values and therefore can be re-organized as:

$$\mathbf{t = \frac{d}{\sqrt{2U}} \sqrt{\frac{m}{z}}} \qquad \text{Equation 2-10}$$

In TOF mass analysis, the length of ion trajectory and the applied voltage is known; therefore the time taken for an ion to travel to a detector can be related directly to the ion's m/z. Unlike a quadrupole, TOF analyzers allow for the m/z of ions to be measured without scanning; however, they cannot easily act as an ion filter. The above description is for a single dimension TOF. Most commercial TOF analyzers contain a reflectron, which adds complexity to ion trajectories. Reflectrons use an electrostatic field to reflect ions to the opposite end of a flight tube in a hyperbolic trajectory which increases the resolving power of a TOF by doubling the distance the ions travel to the detector and by correcting initial differences in the kinetic energy distributions of the ions [16]. In this work, the TOF mass analyzer was used in conjunction with a quadrupole that acted as either an ion filter or transmitter.

2.1.3 Collision induced dissociation

In separate experiments, K. R. Jennings [17] and Haddon and McLafferty [18] demonstrated the usefulness of inducing ion fragmentation though collisions with a neutral target gas although the phenomenon was known to exist much earlier [19]. In the activation step, the target molecule can be considered to be at rest in reference to the ion whose kinetic energy is described as the laboratory frame collision energy (E_{lab}). The center of mass collision energy (E_{com}) is defined classically as the maximum kinetic energy available to be transferred into the ions internal from a single collision:

$$\mathbf{E_{com} = E_{lab} \cdot z \frac{M_{target}}{M_{target} + M_{ion}}} \qquad \text{Equation 2-11}$$

M_{target} and M_{ion} are the masses of the target and ion respectively, and z is the charge state of the ion.

In almost all modern mass spectrometers, MS/MS is accomplished under multiple collision conditions. This is because greater energy deposition and product ion yields (specifically with higher mass ions) are achieved under multiple collision conditions [20]. The translational energy of the collision can be transferred into electronic, rotational and vibrational modes of the ion depending on the nature of the ion and the instrumental design. The lab frame collision energy sampled within this thesis and the multiple collisions conditions are expected to only transfer translational energy into ro-vibrational modes of the ion and not lead electronic excited states [20]. The internal energy deposited into an ion by a collision is quickly redistributed statistically throughout the molecule through intra-vibrational relaxation (IVR). A more complete explanation of the collisional activation process is found in reviews by McLuckey [20] and Poon and Mayer [21].

2.1.4 Ion mobility spectrometry

In its basic form, IMS consists of measuring the time required for an ion propelled by a electric field to move through a drift tube containing an opposing inert buffer gas. The mobility of an ion (K) is the ion's velocity divided by the strength of the electric field (E_f) and can be defined by:

$$\mathbf{K} = \frac{\mathbf{L}}{\mathbf{t_D \cdot E_f}}$$ Equation 2-12 (Discussed in detail in [22])

t_D time required for an ion to traverse a drift tube of length L

On type of ion mobility that is currently found on the commercial Waters Synapt mass spectrometer relies on using stacked ring electrode ion guides. Stacked ring electrode ion guides are a series of stacked disk shaped electrodes with a hole in the middle. Applying rf of opposite phases to consecutive disks produces a radially confining effective potential [23, 24].

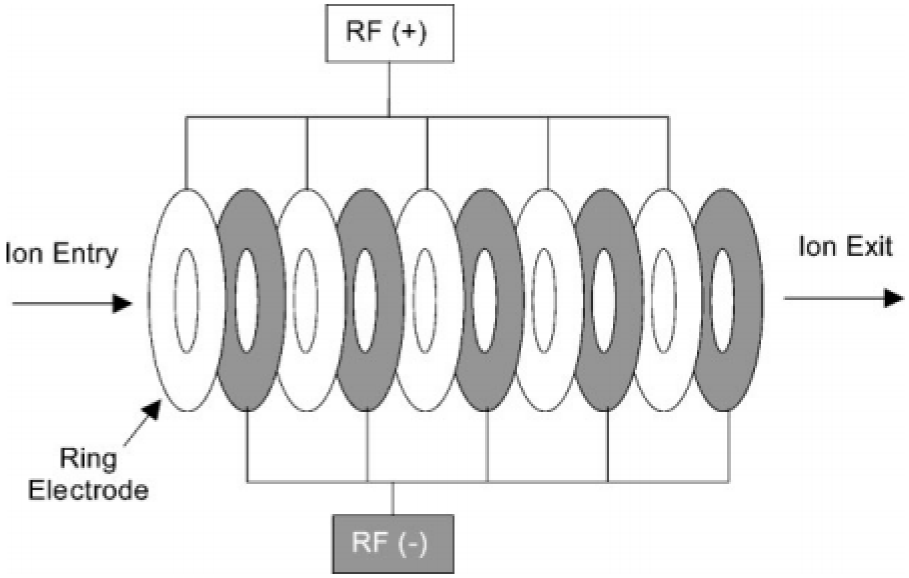

Figure 2-4 Stacked ring electrode ion guide schematic
Giles and co-workers showed that ions can be propelled through a series of stacked ring electrodes by applying a travelling wave voltage.[25]

Propelling ions through a stacked ring electrode ion guide is achieved by superimposing a travelling dc voltage on the radially confining rf voltage [26]. The height of the resulting potential waves can be controlled by the applied dc voltage while the speed of the wave is controlled by how quickly the dc voltage is switched to the adjacent stacked electrode. When the voltages of the waves are high, all ions will be transmitted together, even when their axial motion is opposed by a buffer gas. Larger ions make more collisions with the buffer gas and lowering the potential wave height allows them to roll over the apex of the waves into the next potential wave front. Smaller ions will roll over the travelling waves less frequently and therefore traverse the ion guide faster leading to mobility separation [25]. This ion motion is far more complex than what is seen in traditional ion mobility measurements taken in drift tubes with uniform electric fields, making it difficult to obtain the experimental collision cross section (Ω_{exp}) directly. Ω_{exp} values of many ions in helium have been measured on drift tube instruments and are available online; notably the Clemmer database [27]. Ions with known Ω_{exp} values on a travelling wave instrument show an exponential relationship with drift time defined as:

$$\boldsymbol{\Omega_{exp} = \frac{z \cdot e}{\sqrt{\mu}} \cdot A' \cdot t_D^B} \qquad \text{Equation 2-13 [27]}$$

The A’ and B values in equation 2-12 are instrumental constants that are sensitive to the specific conditions of the experiment including the travelling wave height, velocity and the buffer gas density. Although helium can used, the Synapt mass spectrometer is designed to use N_2 as the buffer gas. If all the instrumental settings are maintained, equation 2-12 can be used to measure the helium Ω_{exp} of ions based on their arrival times, even if the experiment uses N_2 buffer gas.

2.2.1 Theoretical MS/MS breakdown diagrams

A breakdown diagram is a plot of the relative intensity of the parent and each product ion as a function of collision energy. In order to generate a theoretical breakdown diagram the following details must be obtained:

- The timeframe of the dissociation reaction ($t_{reaction}$)
- The observed unimolecular rate constant (k_{obs})
- The internal energy distribution (U) at a given center of mass collision energy (E_{com})

Time frame of dissociation

The time frame of the dissociation reaction is dependent on the instrument used. In the Micromass triple quadrupole mass spectrometer (Chapters 3, 6) and the Waters QTOF instrument (Chapters 4, 5), the residence time of the ion in the collision hexapole is related to the collision energy:

$$\mathbf{t_{E_{lab}}} = \frac{\mathbf{l \times m}}{\mathbf{2 \cdot \sqrt{E_{lab}}}} \qquad \text{Equation 2-14}$$

l is the length of the collision cell,
m is the mass of the ion, and
E_{lab} is the laboratory frame collision energy.

In the Waters Synapt instrument, there are two collision cells – one immediately before the IMS cell and one after the IMS cell. When the IMS mode is active, the ion trap before the IMS cell releases stored ions as a packet. The ions are accumulated for the timeframe of an IMS scan (t_{IMS}) in addition to a scan delay (μ_{delay}). Since the ions are being accumulated, the average reaction time in the trap cell is:

$$\mathbf{t_{trap}} = \frac{\mathbf{t_{IMS}}}{\mathbf{2}} + \boldsymbol{\mu}_{\mathbf{delay}} \quad \text{Equation 2-15}$$

Ions can continue to fragment within the IMS cell and therefore for equation 2-15 to be accurate, the intensities of the reactant and product ions have to be extracted from their respective IMS arrival time distributions (ATD). Following the IMS cell in a Waters Synapt mass spectrometer is the transfer cell. The reaction time of the ions is related to the travelling wave velocity of the transfer cell (v_{wave}) and the length of the transfer cell ($l_{transfer}$):

$$\mathbf{t_{transfer}} = \frac{\mathbf{l_{transfer}}}{\mathbf{v_{wave}}} \quad \text{Equation 2-16}$$

It is possible for ions to dissociate prior to the entering the transfer cell, and in order for equation 2-16 to hold true, the intensities of the reactant and fragment ions must be extracted exclusively from the ATD of the reactant ion.

Obtaining the unimolecular rate constants

The RRKM unimolecular rate equation is:

$$\mathbf{k(E)} = \frac{\boldsymbol{\sigma}\mathbf{N^{\ddagger}(E-E_0)}}{\mathbf{h}\boldsymbol{\rho}\mathbf{(E)}} \qquad \text{Equation 2-17}$$

k(E) is the rate constant at internal energy E,
σ is the reaction degeneracy
$N^{\ddagger}(E-E_0)$ is the sum of states of the transition state between energies 0 and E - E_0,
h is Planck's constant, and
$\rho(E)$is the density of states of the reactant ion.

$N^{\ddagger}(E-E_0)$ and $\rho(E)$ are calculated with the direct count method developed by Beyer and Swinehart [28]. In this method, the harmonic oscillators are defined as having equally spaced energy levels of:

$$\mathbf{E_i} = \mathbf{n}\frac{\mathbf{v_i}}{\mathbf{c}} \qquad \text{Equation 2-18}$$

v_i and E_i are the frequency and energy of oscillator i respectively,
n is the state (0,1,2,3…), and
c is the speed of light

The energy scale of 0 and E_{max} is divided into discrete bins and the direct count algorithm counts the number of states in each bin by adding all the vibrational energy levels of all oscillators.

Observable unimolecular rate constant

The k(E) for the dissociation of the ion is the sum of the unimolecular rate constants of all the dissociation channels. For n dissociation channels:

$$\mathbf{k(E) = \sum k_n(E)} \qquad \text{Equation 2-19}$$

The timeframe available for ions to fragment in MS/MS is typically short. Product ions will only be observed when the reactant ion possesses additional internal energy above the critical energy of dissociation (E_0), in what is known as kinetic shift [29, 30]. The observed unimolecular rate constant (k_{obs}) of dissociation channel n is defined as:

$$\mathbf{k_{n(obs)} = \frac{\int_0^{t_{reaction}} e^{-kt} \cdot dt}{\int_0^{\infty} e^{-kt} \cdot dt} = 1 - e^{-k\, t_{reaction}}} \qquad \text{Equation 2-20}$$

$t_{reaction}$ is the maximum time frame of the dissociation reaction

Approximating the internal energy distribution

A major approximation of this method is describing the reactant ion population as a Boltzmann distribution. The normalized internal energy distribution at an effective temperature (T_{eff}) is described as:

$$\mathbf{U(E) = \frac{\frac{\rho(E)}{Z_{(Teff)}} \cdot e^{-E/R \cdot T_{eff}}}{\sum \frac{\rho(E)}{Z_{(Teff)}} \cdot e^{-\cdot E/R \cdot T_{eff}}}} \qquad \text{Equation 2-21}$$

Z is the partition function at T_{eff}:

$$\mathbf{Z(T_{eff}) = \prod \frac{1}{1-e^{\left(-v_i hc/k_B \cdot T_{eff}\right)}}} \qquad \text{Equation 2-22}$$

A second approximation is that relationship between the T_{eff} and E_{com} is linear:

$$\mathbf{T_{eff} = T_i + \alpha \cdot (E_{com})} \qquad \text{Equation 2-23}$$

T_i the initial temperature of the reactant ion

While there is no justification for a linear relationship between the internal energy distribution and E_{com}, given the small range of E_{com} collision energies sampled in this work, the approximation should lead to reliable relative results. One would not use such an oversimplification if a larger energy range fragmentation process was being explored.

Determining the extent of fragmentation at a defined E_{com}

The total amount reactant ion fragmentation ($\%F_{total}$) at internal energy E, is obtained by connecting $k_{obs}(E)$ and the U(E):

$$\mathbf{\%F_{total}(E) = k_{obs}(E) \times U(E)} \qquad \text{Equation 2-24}$$

When n dissociation channels are available, the % of each fragment at energy E is:

$$\mathbf{\%F_n(E) = \%F_{total}(E) \times \frac{k_n(E)}{k(E)}} \qquad \text{Equation 2-25}$$

Finally, the overall % of ion fragmentation at a given E_{com} is expressed as:

$$\mathbf{\%F_n(E_{com}) = \sum_0^{E_{max}} \%F_n(E)} \qquad \text{Equation 2-26}$$

Theoretical breakdown fitting

A complete theoretical breakdown diagram is obtained automatically by calculating equations 2-14 to 2-26 across all E_{com} values with a Fortran program written by Dr. Paul Mayer. The k(E) of each dissociation channel is changed by altering E_0 and the 1st eight vibrational frequencies of the transition state ($TS^{\ddagger}$); which determines the entropy of activations ($\Delta S^{\ddagger}$). The reactant ion internal energy distribution is set by altering the T_i and α found in equation 2-23. A python script generates thousands of breakdown curves by running the Fortran script across a defined range of variables and scoring the suitability of each theoretical breakdown as the absolute difference between the theoretical and experimental curves divided by the number of experimental points. An acceptable error level for each system is determined by visually inspecting fits to identify the maximum error that would still result with an acceptable fit. The error level of an acceptable fit is thus highly dependent on the quality of experimental breakdown diagram. The errors reported do not represent the absolute uncertainty which will be larger based on approximations of this model.

2.2.2 Molecular mechanics/ molecular dynamics

Obtaining theoretical structures of large molecules is often not feasible with quantum computational chemistry methods due to the expense in time needed. A much faster yet less accurate approach is Molecular mechanics/Molecular dynamics (MM/MD). The potential energy and forces within a molecule are defined by a force field based on classical mechanics. A simplified outline of an MD simulation is to use the initial positions of atoms to obtain the force constants. With these force expressions, the atoms are moved for a short time step after which new force parameters will be calculated and the atoms will be allowed to move again. This is repeated for the duration of the simulation.

AMBER force fields files and input structures

A widely used software for generating molecular force fields and running MD simulations is the Assisted Model Building with Energy Refinement (AMBER) package [31]. In this work, all AMBER input structures were generated using the Antechamber program which is used to classify the atom and bond types, calculate atomic charges and estimate force field parameters of the molecules that are absent [32]. The force field is a database of force constants for different atom types that have been calculated experimentally or with high level computational calculations. The generalized amber force field (GAFF) [33] used in this study was developed for organic compounds. The input files that contain the atom types, charges, connectivity and Cartesian coordinates are read into the xleap program. The components of non-covalent complexes were placed together in the xleap window. The xleap program produces two files – a topology file and an input coordinate file. The topology file contains all the information regarding the molecule's force field. The input coordinate file contains the initial Cartesian coordinates for all atoms within the complex. Throughout the simulation, the coordinates change, but the topology file is constant.

AMBER Simulated Annealing

All MD simulations in this work were completed with simulated annealing regime [34]. This began with an initial molecular minimization, followed by slow heating to 300K. The molecule was equilibrated at a constant temperature. These three initial steps ensured that the molecule is stable. After this, the molecule undergoes a series of drastic heating and then slow cooling cycles called simulated annealing (SA). SA endeavours to find the global minimum structure which could possibly be inaccessible had the simulations occurred at a constant temperature for an extended period of time. The structure of each SA cycle with the lowest MD energy was then used as the starting structure for the next SA cycle. Separately, this structure is cooled to 0K and minimized and saved for future potential energy comparisons. The MD potential energies of the structures are obtained from the force field. Based on how the force field is derived, there is a strong possibility that it does not accurately describe the ion, the simulation did not explore the global minimum, or the experimental gas phase structure is not the global minimum structure. In order to determine if the MD structure was plausible, its theoretical collision cross section (Ω_{theo}) was calculated and compared to the experimental cross section (Ω_{exp}).

2.2.3 Calculating the theoretical cross sections of computationally derived structures

There are three main approaches that are commonly used to calculate the Ω_{theo}. The projection approximation is a physical model where a fixed interaction radius is applied for the analyte and the buffer gas. The Ω_{theo} is the rotationally averaged cross section of numerous two-dimensional cutouts of a three-dimensional molecular structure [35]. The projection approximation method is fast and straight forward; however, it does not consider effects such as scattering angles and can underestimate the Ω_{exp}. The exact hard sphere scattering method (EHSS) does take ion-buffer scattering into account by modelling the ion as a series of overlapping hard spheres whose radii are the hard sphere collision distances [36]. Although some examples have showed the exact hard sphere scattering model is capable of obtaining accurate estimations of Ω_{exp} [37], other examples have found EHSS results in over estimations [38]. An important feature absent in the two previously discussed models is the effect of the long range potential between the ion and the buffer gas.

Measuring Ω_{theo} with MOBCAL

All collision cross sections were calculated using the open source MOBCAL software with the trajectory method (TM) [38]. The script was parallelized in order to increase speed, allowing for 25 independent calculations consisting of 1-50 structures each to be calculated simultaneously using 25 processors. The Ω_{theo} is the average of the collisional integral obtained over all possible geometries. The collision integral is:

$$\boldsymbol{\Omega_{theo}} = \frac{1}{8\pi^2}\int_0^{2\pi} d\,\theta \int_0^{\pi} d\varphi \sin\varphi \int_0^{2\pi} d\gamma \;\; \frac{\pi}{8}\left(\frac{\mu}{k_B T}\right)^3 \int_0^{\infty} dg \cdot e^{\mu g^2 / 2k_B T} \; g^5 \;\; \int_0^{\infty} db \cdot$$
$$2b\big(1 - \cos\varnothing(\theta, \varphi, \gamma, g, b)\big)$$

Equation 2-27

A more complete explanation of equation 2-27 is found in reference [38]. θ, φ, and γ define the angles between the buffer gas atom and the ion. The g value is the relative velocity and b is the impact parameter. The scatter angles, ø(θ,φ,γ,g,b,r) are calculated as a two body Leonard-Jones interaction and ion induced dipole interaction:

$$\Phi(\theta, \varphi, \gamma, b, r)$$
$$= 4\epsilon \sum_i^n \left[\left(\frac{\sigma}{r_i}\right)^{12} - \left(\frac{\sigma}{r_i}\right)^{6}\right] \; - \; \frac{\rho}{2}\left(\frac{ze}{n}\right)^2 \cdot \left[\left(\sum_i^n \frac{x_i}{r_i^3}\right)^2 + \left(\sum_i^n \frac{y_i}{r_i^3}\right)^2 + \left(\sum_i^n \frac{z_i}{r_i^3}\right)^2\right]$$

Equation 2-28

ϵ and σ are Lennard-Jones parameters obtained from experimental measurements which describe the depth of the well and coordinate where the potential interaction becomes positive respectively. The second term of equation 2-28 represents the ion induced dipole. ρ is the polarizability of the helium buffer gas, x_i,y_i,z_i, r_i define the positions of the atoms in the ion relative to the buffer gas, and n is the number of atoms. 250,000 Monte Carlo trajectories measured at 298K examined numerous orientations of the ion in order to determine the average mobility across all possible collision geometries [38] (Figure 2-5). The main disadvantage of the TM is it is computationally expensive and thus not suitable for very large ions. In this work, all reported Ω_{theo} are calculated using the TM method.

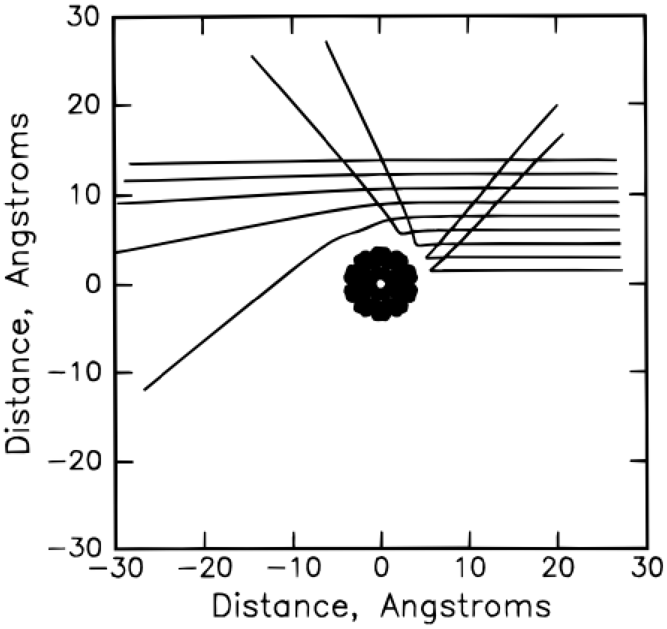

Figure 2-5 Representative plot of He-C_{60}^{+} trajectories with long range potentials Mesleh and co-workers applied a long range potential and induced dipole function to calculating Ω_{theo} of ions and He buffer gas [38]

2.3 References

1. Yamashita, M., Fenn, J. B. Electrospray ion source. Another variation on the free-jet theme. The Journal of Physical Chemistry 88, 4451-4459 (1984)
2. Fenn, J. B.; Mann, M.; Meng, C. K.; Wong, S. F., Whitehouse, C. M. Electrospray ionization for mass spectrometry of large biomolecules. Science 246, 64-71 (1989)
3. Dole, M.; Hines, R.; Mack, L.; Mobley, R.; Ferguson, L., Alice, M. Gas phase macroions. Macromolecules 1, 96-97 (1968)
4. Kebarle, P., Tang, L. From ions in solution to ions in the gas phase-the mechanism of electrospray mass spectrometry. Analytical Chemistry 65, 972A-986A (1993)
5. Kebarle, P., Peschke, M. On the mechanisms by which the charged droplets produced by electrospray lead to gas phase ions. Analytica Chimica Acta 406, 11-35 (2000)
6. Kebarle, P., Verkerk, U. H. Electrospray: from ions in solution to ions in the gas phase, what we know now. Mass Spectrometry Reviews 28, 898-917 (2009)
7. Crotti, S.; Seraglia, R., Traldi, P. Some thoughts on electrospray ionization mechanisms. Eur. J. Mass Spectrom 17, 85-99 (2011)
8. Nollet, J. A., Recherches sur les causes particulières des phénomènes électriques: et sur les effets nuisibles ou avantageux qu'on peut en attendre, Guerin, 1749.
9. Dole, M.; Mack, L.; Hines, R.; Mobley, R.; Ferguson, L., Alice, M. d. Molecular beams of macroions. The Journal of Chemical Physics 49, 2240-2249 (2003)
10. Blades, A. T.; Ikonomou, M. G., Kebarle, P. Mechanism of electrospray mass spectrometry. Electrospray as an electrolysis cell. Analytical Chemistry 63, 2109-2114 (1991)
11. Grimm, R. L., Beauchamp, J. Dynamics of field-induced droplet ionization: Time-resolved studies of distortion, jetting, and progeny formation from charged and neutral methanol droplets exposed to strong electric fields. The Journal of Physical Chemistry B 109, 8244-8250 (2005)
12. Zhou, S., Cook, K. D. A mechanistic study of electrospray mass spectrometry: charge gradients within electrospray droplets and their influence on ion response. Journal of the American Society for Mass Spectrometry 12, 206-214 (2001)

13. Konnermann, L., Ahadi, E., Rodriquez, AD., Vahidi, S., Unraveling the mechanism of electrospray ionization. Anal. Chem. 85, 2-9 (2012)

14. March, R. E. An introduction to quadrupole ion trap mass spectrometry. Journal of Mass Spectrometry 32, 351-369 (1997)

15. Chernushevich, I. V. Loboda, A. V.; Thomson, B. A., An introduction to quadrupole-time-of-flight mass spectrometry. J. Mass Spectrom. 36, 849-865 (2001)

16. Mamyrin, B.; Karataev, V.; Shmikk, D., Zagulin, V. The mass reflectron, a new non-magnetic time-of-flight mass spectrometer with high resolution. Zh. Eksp. Teor. Fiz 64, 82-89 (1973)

17. Jennings, K. R. Collision-induced decompositions of aromatic molecular ions. International Journal of Mass Spectrometry and Ion Physics 1, 227-235 (1968)

18. Haddon, W., McLafferty, F. Metastable ion characteristics. VII. Collision-induced metastables. Journal of the American Chemical Society 90, 4745-4746 (1968)

19. Aston, F. W. LXXIV. A positive ray spectrograph. The London, Edinburgh, and Dublin Philosophical Magazine and Journal of Science 38, 707-714 (1919)

20. McLuckey, S. A. Principles of collisional activation in analytical mass spectrometry. Journal of the American Society for Mass Spectrometry 3, 599-614 (1992)

21. Mayer, P. M., Poon, C. The mechanisms of collisional activation of ions in mass spectrometry. Mass spectrometry reviews 28, 608-639 (2009)

22. Revercomb, H., Mason, E. Theory of plasma chromatography/gaseous electrophoresis. review. Analytical Chemistry 47, 970-983 (1975)

23. Bahr, R., Gerlich, D., Teloy, E., Ring Electrode Ion Guide. E. Verh. Dtsch. Phys. Ges. (IV) 4, 343 (1969)

24. Luca, A.; Schlemmer, S.; Čermák, I., Gerlich, D. On the combination of a linear field free trap with a time-of-flight mass spectrometer. Review of Scientific Instruments 72, 2900-2908 (2001)

25. Giles, K.; Pringle, S. D.; Worthington, K. R.; Little, D.; Wildgoose, J. L., Bateman, R. H. Applications of a travelling wave-based radio-frequency-only stacked ring ion guide. Rapid Communications in Mass Spectrometry 18, 2401-2414 (2004)

26. Clemmer, D. Cross Section Database. Indiana University

27. Smith, D. P.; Knapman, T. W.; Campuzano, I.; Malham, R. W.; Berryman, J. T.; Radforda, S. E., Ashcrofta, A. E. Deciphering drift time measurements from travelling wave ion mobility spectrometry-mass spectrometry studies. cell [Equation (1)] 12, 13 (2009)
28. Beyer, T., Swinehart, D. Algorithm 448: number of multiply-restricted partitions. Communications of the ACM 16, 379 (1973)
29. Chupka, W. A. Effect of unimolecular decay kinetics on the interpretation of appearance potentials. The Journal of Chemical Physics 30, 191-211 (2004)
30. Lifshitz, C. Time-resolved appearance energies, breakdown graphs, and mass spectra: The elusive "kinetic shift". Mass Spectrometry Reviews 1, 309-348 (1982)
31. Case, D. A.; Darden, T.; Cheatham III, T. E.; Simmerling, C.; Wang, J.; Duke, R. E.; Luo, R.; Merz, K. M.; Pearlman, D. A., Crowley, M. AMBER 9. University of California, San Francisco (2006)
32. Wang, J.; Wang, W.; Kollman, P. A., Case, D. A. Antechamber: an accessory software package for molecular mechanical calculations. J. Am. Chem. Soc 222, U403 (2001)
33. Wang, J.; Wolf, R. M.; Caldwell, J. W.; Kollman, P. A., Case, D. A. Development and testing of a general amber force field. Journal of computational chemistry 25, 1157-1174 (2004)
34. Wilson, S. R., Cui, W. Applications of simulated annealing to peptides. Biopolymers 29, 225-235 (1990)
35. Mack Jr, E. Average cross-sectional areas of molecules by gaseous diffusion methods. Journal of the American Chemical Society 47, 2468-2482 (1925)
36. Shvartsburg, A. A., Jarrold, M. F. An exact hard-spheres scattering model for the mobilities of polyatomic ions. Chemical physics letters 261, 86-91 (1996)
37. Scarff, C. A.; Patel, V. J.; Thalassinos, K., Scrivens, J. H. Probing hemoglobin structure by means of traveling-wave ion mobility mass spectrometry. Journal of the American Society for Mass Spectrometry 20, 625-631 (2009)
38. Mesleh, M.; Hunter, J.; Shvartsburg, A.; Schatz, G., Jarrold, M. Structural information from ion mobility measurements: effects of the long-range potential. The Journal of Physical Chemistry 100, 16082-16086 (1996)

Chapter 3: A comprehensive evaluation of using RRKM modelling to obtained meaningful relative energetics for the dissociation of non-covalent complexes

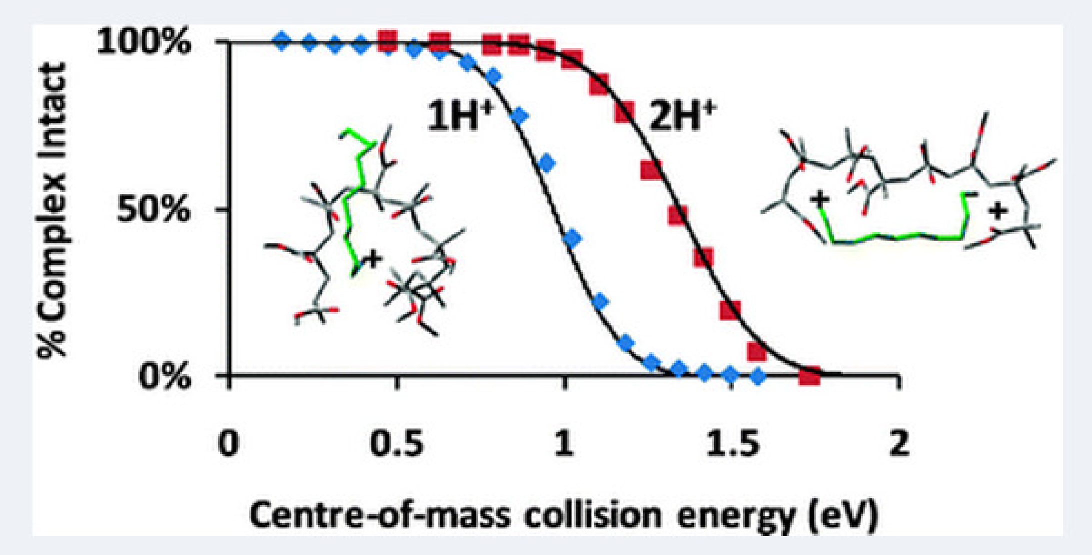

3.1 Objectives

- Implement program to automatically model breakdown diagrams of non-covalent complexes with RRKM unimolecular rate theory

- Validate the energetic terms extracted by RRKM modelling of breakdown diagrams using model complexes

- Define the factors that influence the relationship between collision energy and T_{eff} of similar non-covalent complexes; α

- Validate the accuracy of AMBER MM/MD-SA structural analysis of polymer-amine non-covalent complexes with IMS

3.2 Chapter acknowledgements

J.B Renaud thanks:

- Dr. Abulrahman M. Alhazmi for his assistance in interpretation of synthetic polymer mass spectrometry and tandem mass spectrometry.

- Dr. Eric Martineau for teaching MM/MD-SA concepts.

- Gleb Mironov for assistance with IMS measurements

3.3 Introduction

Previous studies from our research group have demonstrated how the kinetic parameters of 0K activation energy (E_0) and the entropy of activation ($\Delta S^{\ddagger}$) can be extracted from variable energy collision induced dissociation (CID) breakdown diagrams using Rice–Ramsperger–Kassel–Marcus (RRKM) theory [1], which inherently takes into account not only the number of vibrational degrees of freedom (DOF), but also their different vibrational frequencies [2].

Frequently, it is necessary to explain energetic observations based on molecular structure which can be investigated using molecular dynamics (MD). MD is a computational method used in this study for the identification of low energy conformations of molecular systems. When conclusions are being drawn directly from results obtained from MD simulations, it is necessary that the conformations obtained are an accurate reflection of the molecular structures present in the chemical environment of interest. For gas phase structures, ion-mobility spectrometry (IMS) can be used to measure the molecule's experimental collision cross section (Ω_{exp}). The Ω_{exp} is a value that describes the average, low resolution gas phase structure of an ion and can be compared with the theoretical collision cross section (Ω_{theo}) of MD-derived structures. With the incorporation of ion-mobility cells within many modern mass spectrometers, its use as an analytical technique is rapidly increasing. Likewise, the use of IMS to validate computationally derived structures is also becoming common practice and is leading to a greater confidence level being placed on MD simulation results.

This study aims to connect energetics obtained with RRKM theory with the results of conformational analysis, and to identify the links and trends that exist between these two properties. This was accomplished by examining a series of more than fifty non-covalent complexes consisting of a synthetic polymer of varying lengths with a singly or doubly protonated diaminoalkanes.

Materials

Polymethylmethcrylate (PMMA) Mw: 1460, Mw/Mn : 1.07; was purchased from Polymer Laboratories (Amherst, MA, USA). PMMA concentrations of 0.1 mg L^{-1} were mixed in a 1:1 ratio with either diamino(butane, hexane or decane) of concentration 0.1 mg L^{-1} in methanol. Formic acid was added to give a final solution of 0.1% formic acid. Cross section calibrants, ubiquitin, myoglobin and lysozme were purchased from Sigma-Aldrich, (St. Louis).

Electrospray ionization mass spectrometry (ESI-MS/MS)

A Micromass Quattro LC (Waters Micromass, Manchester, UK) triple quadrupole mass spectrometer equipped with a Z-spray source was used to carry out the electrospray ionization tandem mass spectrometry (ESI-MS/MS). Sample solutions were introduced via syringe pump at a flow rate of 40 μL min^{-1}. The sample cone voltage was set to 40 V. CID was carried out with argon at a gas pressure of 1×10^{-3} mbar (1 bar = 100 kPa), and laboratory frame collision energies (E_{lab}) ranging from 0 to 100 eV (specific settings are included in figure caption) recorded for 30 seconds at each collision energy step. The resolution of the first quadrupole was set to unit mass resolution (15 in the Masslynx software) for all experiments. The resolution of the final quadrupole was held constant at 12 to increase the sensitivity of the ESI-MS/MS experiments. All collision energies reported in this paper are center-of-mass (E_{com}) energies and derived from E_{lab} using the equation:

$$\mathbf{E_{com}} = \mathbf{z} \cdot \mathbf{E_{lab}} \left(\frac{\mathbf{M_{Ar}}}{\mathbf{M_{Ar}} + \mathbf{M_{ion}}} \right) \qquad \text{Equation 3-1}$$

The harmonic vibrations of PMMA were obtained from a previous study [3]. The vibrational frequencies of singly and doubly protonated 1,4-diaminobutane, 1,6-diaminohexane and 1,10-diaminodecane were calculated by geometry optimizations followed by frequency calculation at the AM1 theory using the Gaussian 03 suite of programs [4]. As the interaction between a protonated amine and the polymer is expected to be similar for all systems in the study, the intra-complex vibrational frequencies (librational modes) between the two components of the complex were approximated using the vibrational frequencies calculated between protonated 1-butylamine and PMMA at the AM1 level of theory.

The vibrational frequencies of the transition state were approximated by removing one oscillator from reactant ion (21 cm^{-1}, the critical oscillator), and altering the first 8 vibrational frequencies (Table 3-1).

Table 3-1 Harmonic vibrational frequencies used in the RRKM modeling of $[PMMA_n][DAA+mH]^{+m}$ complexes

	Harmonic vibrational frequencies (cm^{-1})
Monomer modes	17, 90, 113, 117, 129, 192, 222, 267, 306, 444, 549, 604, 781, 816, 847, 852, 954, 979, 1007, 1012, 1015, 1075, 1123, 1133, 1140, 1141, 1148, 1150, 1150, 1154, 1179, 1188, 1194, 1281, 1700, 2498, 2540, 2541, 2543, 2546, 2553, 2560, 2615, 2618, 2618
Librational modes	13, 21, 40, 79, 112, 113
Diaminobutane(H^+) modes	59, 69, 109, 163, 163, 245, 372, 404, 550, 759, 816, 874, 919, 1019, 1058, 1073, 1143, 1185, 1200, 1213, 1220, 1223, 1254, 1264, 1319, 1330, 1344, 1356, 1365, 1382, 1391, 1399, 1402, 1469, 1638, 1646, 1654, 1728, 2963, 2977, 3012, 3025, 3035, 3044, 3079, 3099, 3216, 3223, 3351, 3435, 3475,
Diaminohexane(H^+) modes	38, 45, 83, 95, 95, 115, 164, 236, 239, 309, 406, 528, 544, 748, 774, 825, 900, 934, 978, 1037, 1056, 1074, 1163, 1181, 1183, 1197, 1204, 1208, 1226, 1228, 1229, 1252, 1257, 1264, 1303, 1328, 1336, 1348, 1360, 1373, 1382, 1387, 1396, 1404, 1405, 1407, 1436, 1469, 1638, 1646, 1654, 1731, 2963, 2978, 3003, 3016, 3025, 3030, 3039, 3047, 3075, 3084, 3096, 3104, 3217, 3224, 3351, 3427, 3470,
Diaminodecane(H^+) modes	18, 24, 44, 45, 59, 77, 89, 103, 112, 116, 118, 164, 212, 214, 233, 322, 400, 433, 516, 540, 571, 740, 750, 767 794, 833, 882, 934, 970, 983, 1023, 1049, 1056, 1075, 1167, 1176, 1179, 1188, 1191, 1197, 1203, 1207, 1208, 1213, 1221, 1223, 1232, 1234, 1235, 1235, 1248, 1264, 1267, 1269, 1288, 1311, 1325, 1332, 1350, 1350, 1365, 1376, 1383, 1387, 1395, 1401, 1403, 1404, 1406, 1408, 1409, 1410, 1426, 1447, 1456, 1469, 1638, 1647, 1655, 1732, 2963, 2979, 3000, 3004, 3010, 3018, 3025, 3026, 3032, 3038, 3041, 3048, 3074, 3077, 3082, 3088, 3094, 3100, 3104, 3107, 3217, 3225, 3352, 3421, 3466,
Diaminobutane($2H^+$) modes	62, 80, 113, 164, 167, 169, 367, 404, 546, 760, 817, 919, 1017, 1053, 1062, 1069, 1181, 1192, 1215, 1217, 1222, 1238, 1261, 1262, 1271, 1275, 1331, 1351, 1366, 1385, 1387, 1397, 1411, 1424, 1639, 1639, 1643, 1644, 1648, 1648, 2948, 2949, 2999, 3013, 3013, 3020, 3068, 3084, 3180, 3180, 3195, 3196, 3326, 3328
Diaminohexane($2H^+$) modes	44, 50, 87, 99, 99, 118, 164, 166, 239, 307, 402, 526, 539, 750, 776, 825, 899, 976, 1033, 1049, 1058, 1068, 1178, 1181, 1197, 1198, 1199, 1207, 1227, 1229, 1239, 1240, 1253, 1269,

	1269, 1270, 1313, 1338, 1355, 1368, 1382, 1390, 1392, 1397, 1398, 1404, 1413, 1436, 1643, 1643, 1644, 1644, 1649, 1649, 2957, 2957, 2999, 3010, 3020, 3020, 3023, 3034, 3071, 3078, 3089, 3099, 3200, 3200, 3207, 3207, 3338, 3339
Diaminodecane(2H$^+$) modes	24, 25, 46, 50, 59, 80, 90, 106, 114, 117, 120, 164, 164, 212, 212, 320, 396, 431, 510, 540, 569, 742, 753, 769, 796, 833, 881, 932, 979, 1018, 1044, 1055, 1057, 1058, 1174, 1178, 1180, 1185, 1188, 1202, 1203, 1203, 1204, 1211, 1219, 1221, 1225, 1234, 1234, 1235, 1246, 1254, 1266, 1266, 1266, 1272, 1294, 1315, 1333, 1346, 1359, 1369, 1382, 1387, 1390, 1395, 1396, 1399, 1400, 1405, 1405, 1407, 1408, 1421, 1441, 1451, 1641, 1641, 1645, 1645, 1653, 1653, 2961, 2961, 3000, 3003, 3009, 3016, 3023, 3023, 3024, 3030, 3036, 3041, 3073, 3075, 3079, 3085, 3091, 3097, 3102, 3106, 3214, 3214, 3215, 3215, 3347, 3347

The internal energy distribution as a function of center of mass collision energy was approximated through the use of an effective temperature (T_{eff}) designation in the equation:

$$\mathbf{T_{eff} = 300\ K +\ \boldsymbol{\alpha} E_{com}} \qquad \text{Equation 3-2}$$

Where 300 K represents the initial temperature of the ions, and α which has units of K eV^{-1} is altered during the fitting procedure to reflect the effect a given collision energy will have upon the effective internal energy distribution. This approximation was used in previous work with Aβ-peptide/substrate complexes [1]. While there is no justification for a linear relationship between the internal energy distribution and E_{com}, given the small range of E_{com} collision energies sampled in this study, the approximation should lead to reliable relative results. One would not use such an oversimplification if the fragmentation of a polymer ion itself was being explored. In addition, since each of the complexes is chemically similar, the trends observed in the fitted parameters should be well represented.

The three variables; E_0, $\Delta S^{\ddagger}$ and α are altered in an automated manner using an in-house Python/ Fortran hybrid program and the score of each fit was assigned based the absolute difference between the relative intensity of experimental data to the relative intensity at the same collision energy on the theoretical breakdown curve divided by the number of data points in the set. The different combinations of E_0, $\Delta S^{\ddagger}$ and α that resulted in a fitting error no less than 0.05% above best scoring combination were averaged together, and standard deviation taken from this set of combinations. The listed uncertainty does not take into account the limitations of the model used and thus are to be viewed as lower limits.

In the interpretation of the value of α, the vibrational heat capacity (C_{vib}) was calculated using the statistical mechanical equation:

$$\mathbf{C_{vib} = k \sum \left(\frac{hv_i}{kT}\right)^2 \frac{e^{hv_i/kT}}{\left(e^{hv_i/kT-1}\right)^2}} \qquad \text{Equation 3-3}$$

Ion mobility spectrometry

Experimental cross sections (Ω_{exp}) of all complexes were measured following protocol of D.P. Smith et al.[5] using myoglobin, ubiquitin and lysozyme tryptic peptides calibrants to relate arrival time distribution to molecular cross-sections. A Beckman PA 800 capillary electrophoresis machine (Beckman Coulter inc., USA) was used to infuse analytes into Waters Synapt G2 HDMS mass spectrometer (Waters Corp., USA) via Micromass Capillary Electrophoresis Sprayer (Micromass UK Limited, UK) by applying constant pressure of 1 psi. Make up solution consisted 50:50 methanol:water mixture, with 0.1% formic acid introduced at a flow rate of 0.7 μL min^{-1}.

Molecular dynamics/ molecular modeling simulated annealing (MD/MM-SA)

The AMBER9 [6] program suite using the Generalized AMBER force field (GAFF) [7] was used to study the conformations of the complexes. Equilibration and annealing dynamics were performed for 60 different complexes in total; PMMA oligomers (7-16 repeat units) with diamino(butane/hexane/decane) in both the $1H^+$ and $2H^+$ state. Minimized energy conformations of the PMMA/diaminoalkane complex were briefly equilibrated for 20 ps (time step 1 fs) at 300 K before undergoing 2000 cycles of simulated annealing [8] (each 18.25 ps total, 0.5 fs time step) starting with drastic heating from 300 K to 800 K over 1.25 ps and equilibrated for 2 ps. This was followed by cooling increments of 100 K over 1 ps with 2 ps of equilibration at each temperature until 300 K. The lowest energy conformation of each simulated annealing cycle was then selected as the starting structure for the next cycle of simulated annealing. After each cycle, the low energy conformation was cooled to 0 K over 2 ps, minimized and potential energy measured. Theoretical cross sections of the 50 lowest structures sampled (< 6.3 kJ from the lowest structure energy) were measured using the trajectory method in the MOBCAL program [9, 10].

IMS validation/MD refinement

In cases where the theoretical cross section (Ω_{theo}) did not coincide well with the Ω_{exp}, a refined MD-SA regime was employed consisting of a second round of MD-SA. Within the 50 lowest energy conformations identified during the first 2000 cycles of MD-SA, the conformation having a theoretical cross section closest to the experimental cross section was equilibrated at 300K for 400 ps (1 fs time step). This was followed by 1000 cycles of MD-SA using the same regime as the first round and the new lowest energy conformations therein identified. A new conformation was deemed to be a refined structure if: (1) the theoretical cross section is closer to experimental cross section and (2) the MD potential energy is the new global minimum (lower than first round low energy conformation(s)

For brevity, diaminoalkane, 1,4-diaminobutane, 1,6-diaminohexane, 1,10-diaminodecane and dihydrogen terminated poly(methylmethacrylate) will be denoted as DAA, DAB, DAH, DAD and PMMA respectively.

IMS MD-SA conformational analysis

Conclusions that are solely based upon MD results can be precarious based on the reliability the computational regime employed. Therefore, IMS was used to obtain Ω_{exp} which were then compared to the theoretical cross sections (Ω_{theo}) obtained from the MD structures using the trajectory method in MOBCAL. Ω_{exp} measurements cannot directly confirm the validity of a theoretical structure, however it can be used to refute theoretical structures.

Shown in Figure 3-2, Ω_{theo} obtained from the MD-SA regime of this study agree well with those measured experimentally. When Ω_{theo} did not coincide within experimental error of the Ω_{exp}, it suggests that the low energy MD structure is most likely not accurate. A second round of MD-SA starting from a low energy conformation that was the closest to Ω_{exp} led to structures that not only had an overall lower energy, but also a more appropriately matched $\Omega_{theo(refined)}$ to Ω_{exp}. For example, following the initial 2000 cycles of MD-SA, the complex of $[PMMA_{12}][DAB+2H]^{+2}$ had a MD potential energy of 565.6 ± 4.6 kJ mol^{-1} yet the Ω_{theo} was overestimated by 18.9%. After MD refinement, the MD potential energy was lowered to 558.7 ± 0.8 kJ mol^{-1} and the refined Ω_{theo} became only 7.4% larger than Ω_{exp} (Figure 3-1b).

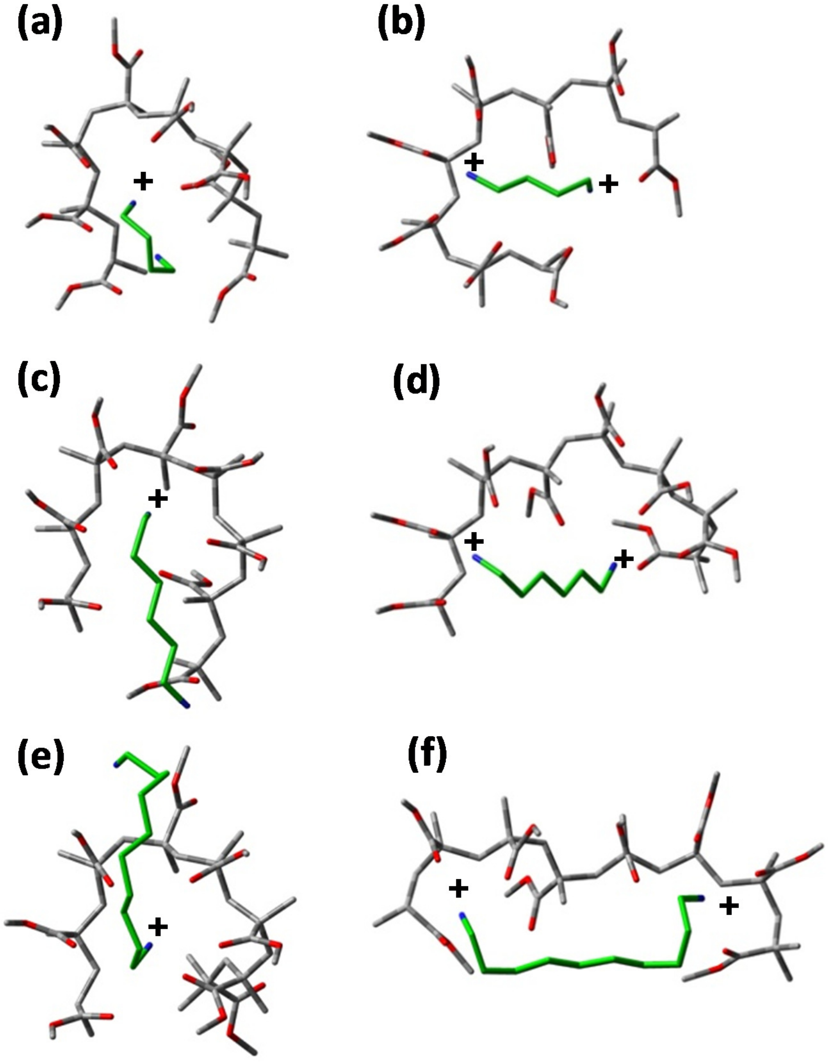

Figure 3-1 Lowest energy conformations of [DAA][PMMA$_8$] obtained using MD-SA Lowest Energy Conformations obtained using MD-SA for a) [PMMA$_8$][DAB+H]$^{+1}$, b) [PMMA$_8$][DAB+2H]$^{+2}$, c) [PMMA$_8$][DAH+H]$^{+1}$, d) [PMMA$_8$][DAH+2H]$^{+2}$, e) [PMMA$_8$][DAD+H]$^{+1}$ and f) [PMMA$_8$][DAD+2H]$^{+2}$.

Due to the good correlation between Ω_{exp} and Ω_{theo}, the level of confidence that can be assigned to observations drawn from the MD conformations is increased. The low energy conformers of complexes between PMMA and singly protonated diaminoalkanes show a tendency for the protonated amine to reside predominantly near the center of the PMMA, which adopts a ‘horseshoe’ structure (Figure 3-1a,c,e). This allows for the attractive electrostatic forces between the protonated amine and the carbonyl oxygens of the PMMA side-chains to be maximized. When the length of PMMA is of either small or intermediate size (7-12 units), the complexes are fairly rigid as the interaction of singly protonated alkylamine with the center of the PMMA chain is highly favourable. As the length of the PMMA increases, the structure becomes less confined and different conformations are observed where the protonated amine is able to interact with different positions of the PMMA chain, not just those from the terminal units. In all cases, the overall conformation was not affected in an evident way by the length of the substrate, meaning complexes containing DAB, DAH or DAD all had very similar conformations.

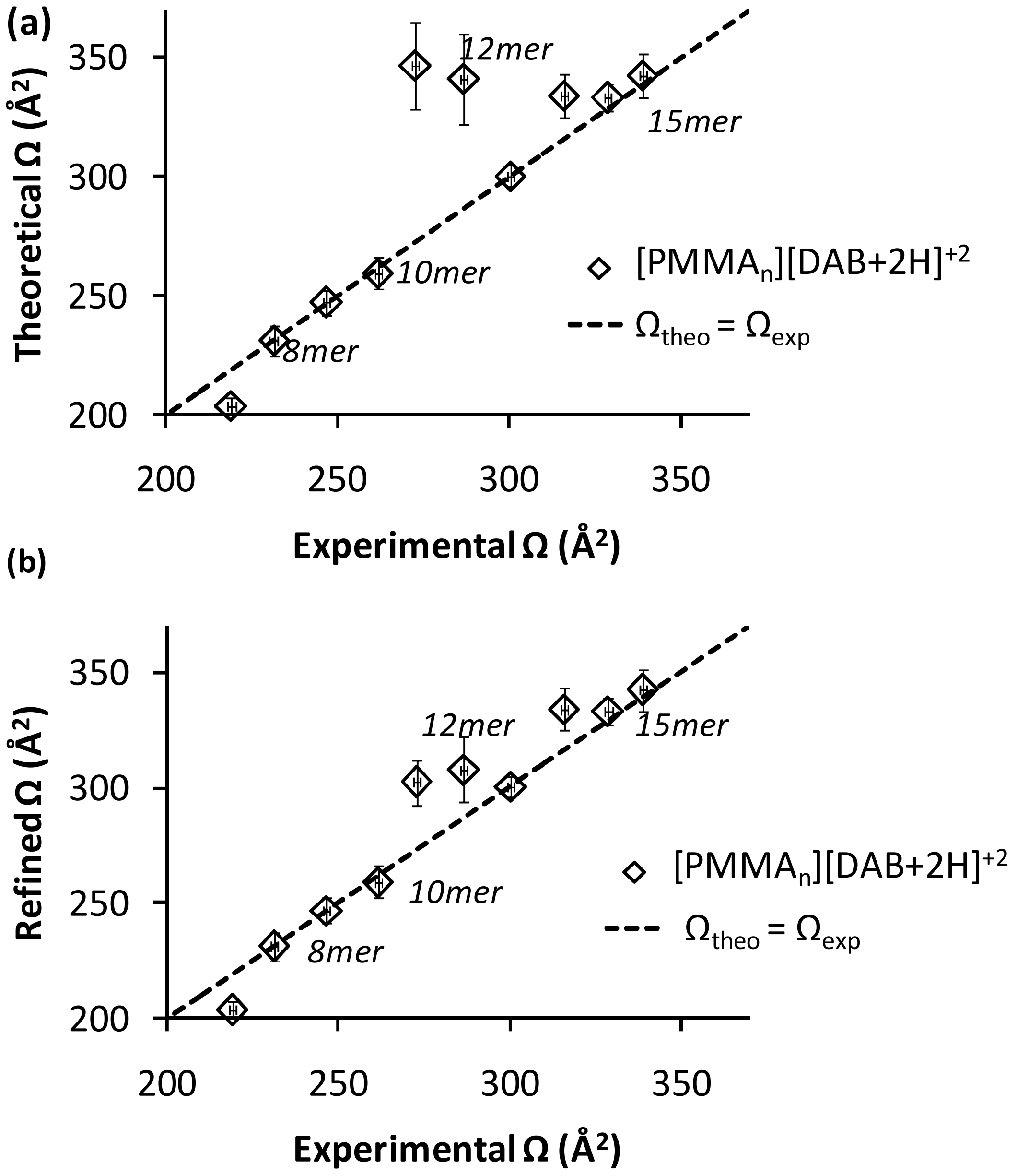

Figure 3-2 Ω_{theo} vs. Ω_{exp} of $[PMMA_n][DAB+2H]^{+2}$.

Dashed diagonal is for Ω_{theo}= $\Omega_{exp,}$. a) Ω_{theo} values obtained from 1st round, low energy MD structures using trajectory method (MOBCAL). b) Ω_{theo} obtained from 2nd MD round (refined).

In contrast, the doubly charged complexes, $[PMMA_n][DAA+2H]^{+2}$ (Figure 3-1b,d,f), have an overall structure that is dictated by the DAA, which is protonated on both terminal ends and adopts a linear arrangement that maximizes charge separation. Secondary to the separation of charges, the PMMA adopts a conformation around the DAA in a manner that maximizes interaction between carbonyl oxygens on the PMMA side-chains and the protonated amines. When the DAA is sufficiently short or polymer sufficiently long, a ‘horseshoe’ conformation is adopted similar to the corresponding +1 species occurs; one protonated site interacts with the central units of the PMMA oligomer, while the second protonated site interacts with the carbonyl oxygens of the terminal groups. If the DAA is larger and polymer of short/intermediate length (Figure 3-1d,f) a parallel arrangement between the DAA and polymer is seen where each protonation site of the DAA interacts with opposite terminal ends of the PMMA (Figure 3-2b). The overall trend based on the effects of charge state upon conformation is that as the length of the DAA increases, so do the differences between the conformations of singly and doubly protonated species. Similarly, the same observation was verified based on Ω_{exp} measurements.

Figure 3-3 shows that charge has the smallest effect on cross section when the shortest substrate, DAB, is complexed to a 10-mer of PMMA, while charge affects the cross section of the PMMA complex with the longest, DAD, to a greater extent. In addition to supporting MD observations, this observations strongly supports that the site of protonation within the complexes is on the amine sites of the DAA.

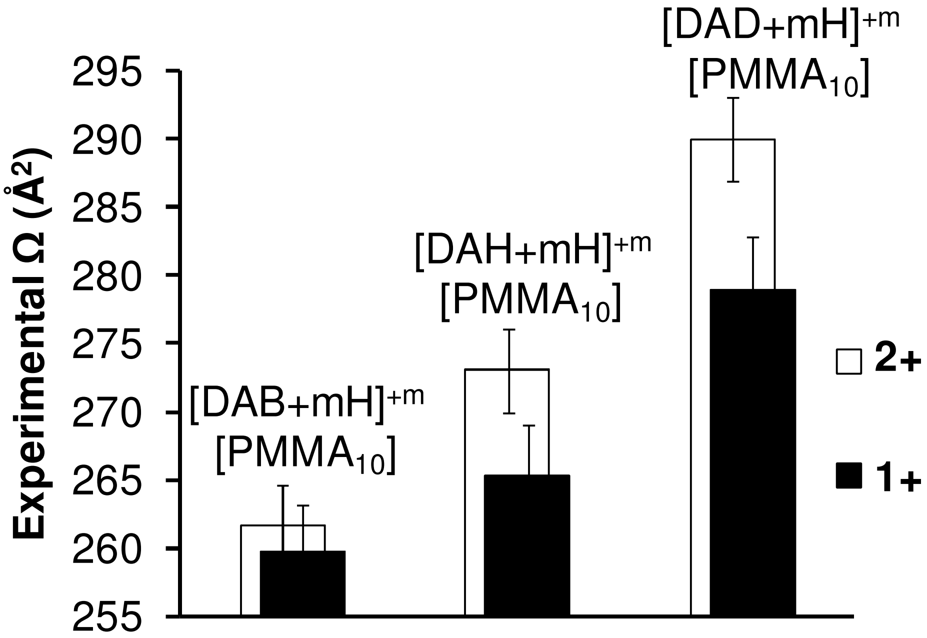

Figure 3-3 Experimental cross sections of [PMMA$_{10}$][DAB+$_m$H]$^{+m}$, [PMMA$_{10}$][DAH+$_m$H]$^{+m}$ and [PMMA$_{10}$][DAD+$_m$H]$^{+m}$
In black, singly protonated (m =1), in white, doubly protonated (m =2).

MS/MS, RRKM energetic analysis.

The range of E_{com} collision energies used for this study, was relatively narrow (0.65-1.9 eV) and dissociation of all the $[PMMA_n][DAA+mH]^{+m}$ complexes resulted in a single dominant dissociation pathway. Doubly charged complexes, $[PMMA_n][DAA+2H]^{+2}$, resulted in the expected partitioning of charges after dissociation, with one proton being retained by the DAA, and the other leaving with the PMMA oligomer where characteristic $PMMA+H^+$ fragmentation products were observed (Figure 3-4a). MS/MS of $[PMMA_n][DAA+2H]^{+2}$ generates two signals from a single reactant ion, therefore the breakdown diagrams were constructed using only the intensity of the $DAA+H^+$ signal relative to that of the reactant complex ion. Singly charged complexes; $[PMMA_n][DAA+1H]^{+1}$ dissociated with PMMA leaving as the neutral, and the diaminoalkane substrates retaining the proton (Figure 3-4b). The substrates used all have gas phase proton affinities ~ 1000 kJ mol^{-1} [11], which indicates that all the PMMA oligomers sampled have gas phase proton affinities of lower values. It should be noted that in cases where the substrate has a lower proton affinity (i.e. glycine, 886.5 kJ mol^{-1}) it is possible for the PMMA oligomer to retain the proton after dissociation, and to undergo unique, charge directed side-chain fragmentation [12].

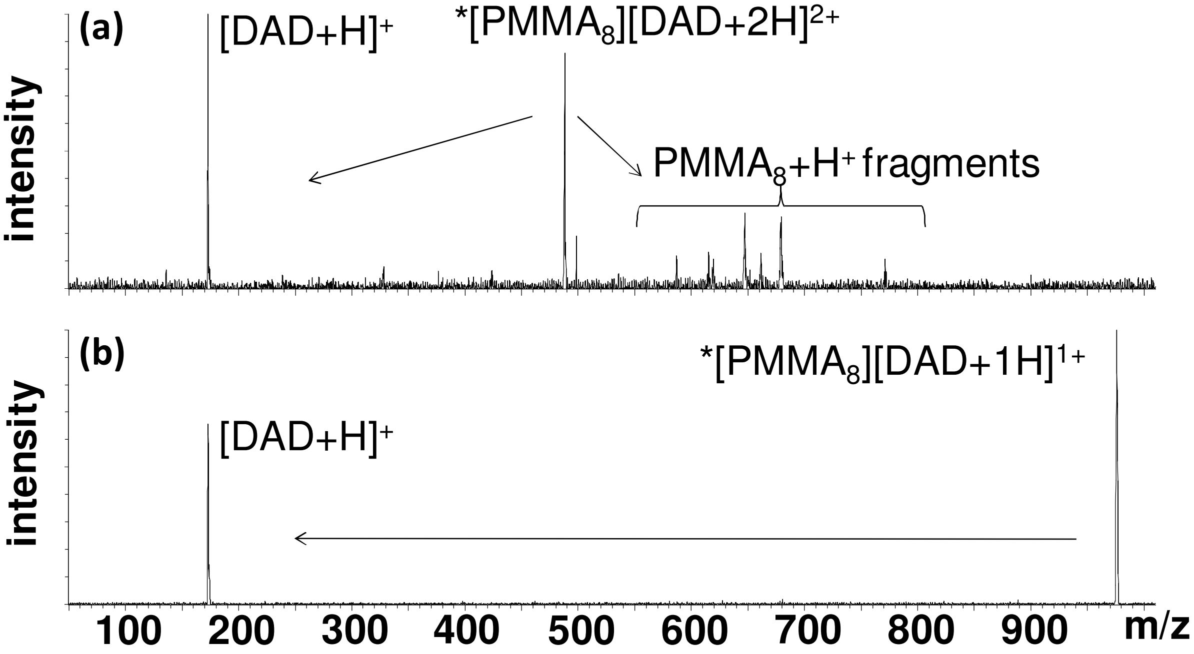

Figure 3-4 Collision-induced dissociation mass spectra of a) $[PMMA_8][DAD+2H]^{+2}$ and b) $[PMMA_8][DAD+1H]^{+1}$

Obtained at E_{com} of 1.26 ev and 0.95 ev respectively. In both cases, only 1 dissociation pathway exists under these experimental parameters. See experimental procedures for conditions.

Fitting of the experimental breakdown diagrams results in values for E_0, $\Delta S^{\ddagger}$ and α (Figure 3-5).

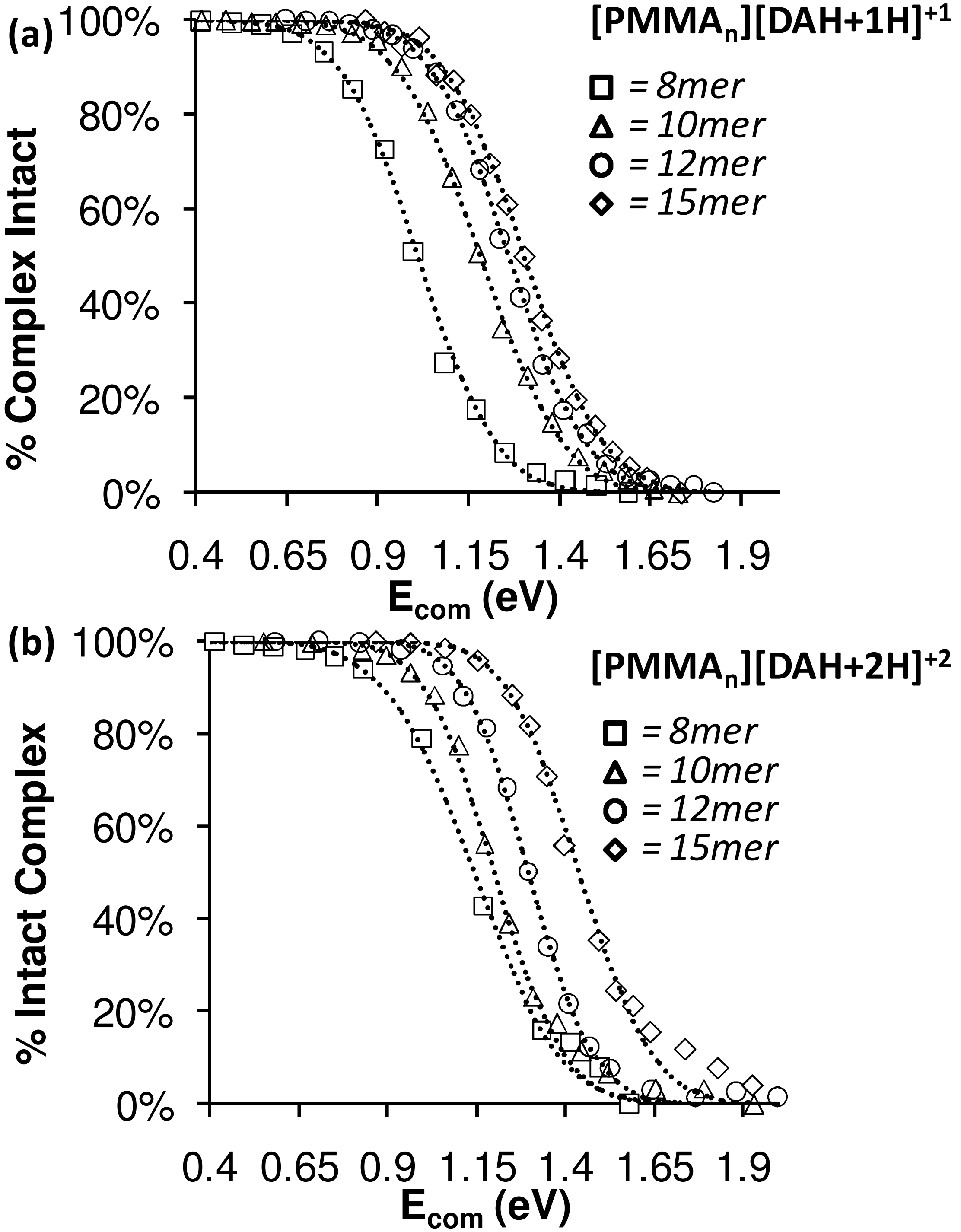

Figure 3-5 Breakdown Diagrams of a) [PMMA$_n$][DAH+1H]$^{+1}$ and b) [PMMA$_n$][DAH+2H]$^{+2}$ Experimental measurements obtained from CID of DAH complexed with PMMA units of 8mer(□), 10mer(Δ), 12mer(○) and 15mer(◊). Dotted lines obtained by theoretical fitting using RRKM.

Table 3-2 RRKM determined E_0 and $\Delta S^{\ddagger}$ for dissociation of $[PMMA_n][DAA+1H]^{+1}$ complexes

	$[PMMA_n][DAB+1H]^{1+}$			$[PMMA_n][DAH+1H]^{1+}$			$[PMMA_n][DAD+1H]^{1+}$		
n	E_0 (eV)	$\Delta S^{\ddagger}$ ($J\ K^{-1}$)	α ($K\ eV^{-1}$)	E_0 (eV)	$\Delta S^{\ddagger}$ ($J\ K^{-1}$)	α ($K\ eV^{-1}$)	E_0 (eV)	$\Delta S^{\ddagger}$ ($J\ K^{-1}$)	α ($K\ eV^{-1}$)
7	0.81±0.02	-63±7	421±16	0.91±0.01	-67±7	444±25	0.87±0.01	-73±3	458±13
8	0.85±0.01	-52±6	380±14	1.01±0.01	-30±5	336±9	1.03±0.01	-32±4	378±10
9	0.96±0.02	-27±7	348±13	1.13±0.02	-24±10	351±22	1.02±0.01	-35±4	357±11
10	1.01±0.01	-1±4	291±5	1.1±0.01	-10±4	281±5	1.1±0.03	-15±10	319±17
11	1.11±0.02	16±9	284±12	1.21±0.02	0±11	297±18	1.18±0.02	-3±6	317±7
12	1.15±0.02	26±4	232±7	1.32±0.01	22±5	278±8	1.22±0.01	26±6	250±9
13	1.30±0.01	48±9	254±6	1.31±0.02	42±8	236±9	1.31±0.03	34±10	262±11
14	1.35±0.02	76±7	214±9	1.40±0.03	43±7	255±10	1.36±0.02	62±5	211±13
15	1.43±0.03	99±2	190±11	1.38±0.04	70±11	209±6	1.43±0.01	80±2	195±10

Table 3-3 RRKM determined E_0 and $\Delta S^{\ddagger}$ for dissociation of $[PMMA_n][DAA+2H]^{+2}$ complexes

	$[PMMA_n][DAB+2H]^{2+}$			$[PMMA_n][DAH+2H]^{2+}$			$[PMMA_n][DAD+2H]^{2+}$		
n	E_0 (eV)	$\Delta S^{\ddagger}$ ($J\ K^{-1}$)	α ($K\ eV^{-1}$)	E_0 (eV)	$\Delta S^{\ddagger}$ ($J\ K^{-1}$)	α ($K\ eV^{-1}$)	E_0 (eV)	$\Delta S^{\ddagger}$ ($J\ K^{-1}$)	α ($K\ eV^{-1}$)
8	0.63±0.01	-90 ± 5	395±27	0.94±0.02	-77±5	428±30	1.22±0.03	-62±11	410±24
9	0.78±0.01	-56±4	348±12	1.32±0.02	0±9	378±14	1.43±0.02	-20±14	352±32
10	1.02±0.02	10±7	269±7	1.46±0.02	45±7	301±9	1.64±0.02	14±13	360±25
11	1.35±0.04	44±13	328±13	1.53±0.03	48±9	303±9	1.76±0.03	40±11	325±17
12	1.47±0.05	94±14	279±14	1.76±0.06	80±18	300±16	1.89±0.05	75±16	313±18
13	1.66±0.05	133±15	257±7	1.82±0.04	105±10	264±6	1.97±0.07	104±23	278±19
14	1.67±0.06	173±14	194±3	1.95±0.04	128±13	246±9	2.17±0.07	153±20	251±10
15	1.77±0.02	223±6	184±4	1.99±0.03	229±8	205±15	2.17±0.02	173±6	224±23

Figure 3-6 shows that E_0 for both singly and doubly protonated complexes increases as the length of the PMMA within the complex increases. Increasing the length of the polymer from small to intermediate size will allow more hydrogen bonds between the PMMA carbonyl oxygens and the amine hydrogens. Once the number intermolecular hydrogen bonds is maximized, complex stability could continue to increase with increasing polymer size due to attractive charge-dipole interactions. The distance relationship for a charge-dipole interactions is $1/\text{distance}^2$. Observed in the case of the +2 system is evidence for a plateau of the PMMA length dependence of E_0 which is due to PMMA repeat units that begin to be too far to have a noticeable additive impact upon the complex stability. If extrapolated further, it could be expected that for much larger PMMA oligomers, an increase in PMMA length would have very little or no effect upon the E_0 of dissociation.

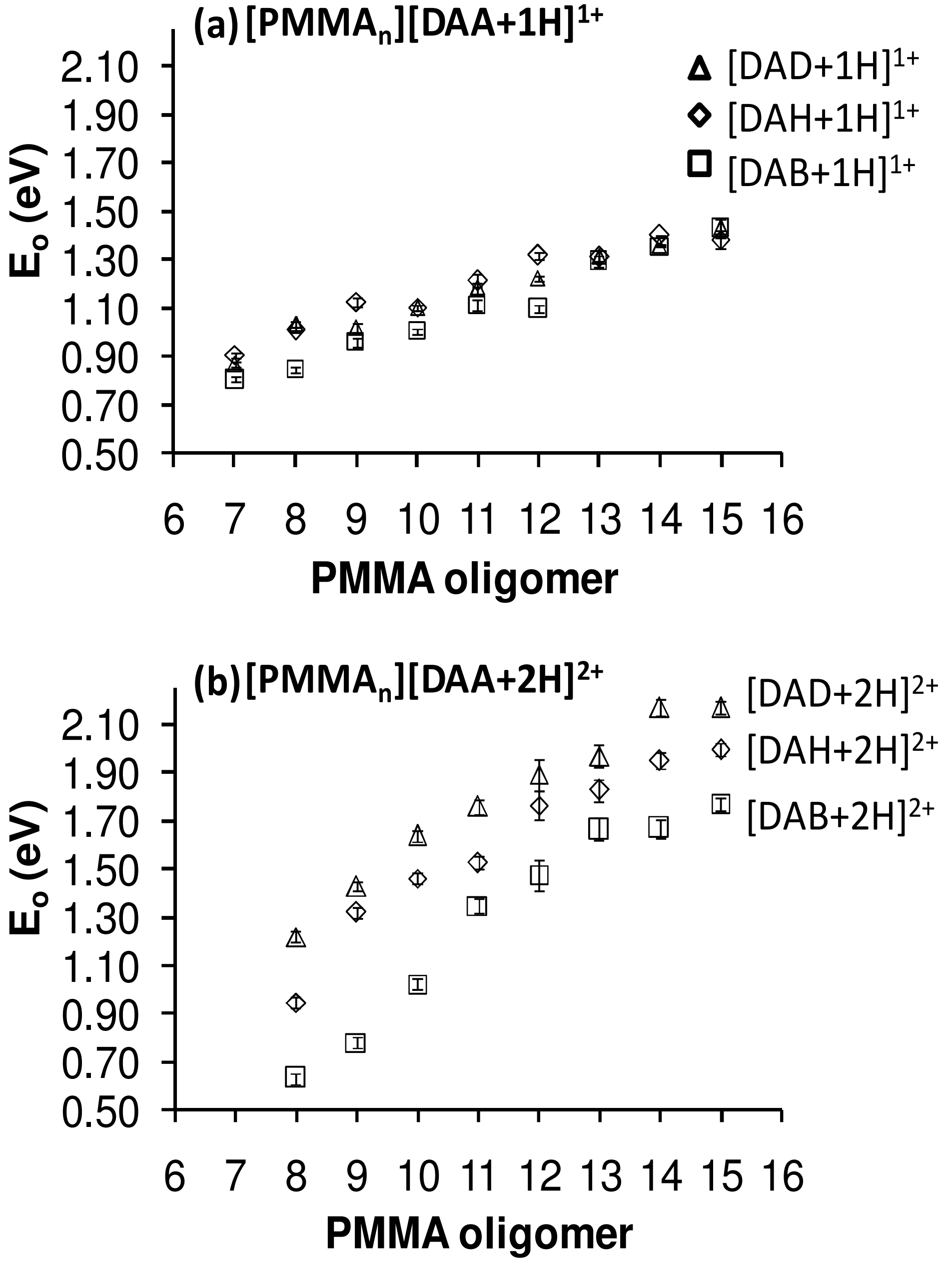

Figure 3-6 E_0 of a) singly and b) doubly protonated [DAA][PMMA] complexes

a) Singly protonated complexes; $[PMMA_n][DAB+1H]^{+1}$ (□), $[PMMA_n][DAH+1H]^{+1}$ (◊), $[PMMA_n][DAD+1H]^{+1}$ (Δ) and b) doubly protonated complexes; $[PMMA_n][DAB+2H]^{+2}$ (□), $[PMMA_n][DAH+2H]^{+2}$ (◊), $[PMMA_n][DAD+2H]^{+2}$ (Δ). E_0 values represent values which resulted in the best fit of experimental breakdown diagrams with theoretical breakdown curve obtained through RRKM.

The identity of the DAA substrate does not greatly affect E_0 when the complex is singly protonated; ($[PMMA_n][DAA+1H]^{+1}$) (Figure 3-6a). In contrast, the opposite is true for the doubly protonated species $[PMMA_n][DAA+2H]^{+2}$ (Figure 3-6b). $[PMMA_n][DAB+2H]^{+2}$ complexes have the lowest activation energy for a given PMMA size due to the increase of repulsive forces that are a result of the closer proximity of the charge bearing sites. Likewise, the longest substrate complexe, $[PMMA_n][DAD+2H]^{+2}$ has much higher E_0 values for a given PMMA size because repulsive forces between charges are minimized. Similar to the conformational analysis, this provides evidence for the site of protonation within the complex to be on the amines.

Previous studies using CID based techniques to probe gas phase binding energies, have showed that often a multiply charged complex that dissociates into two charged fragments will have a lower stability in comparison to the singly charged species [13]. In this system, however, multiple charging of the complex can lead to either a stabilizing or de-stabilizing effect. For $[PMMA_n][DAB+mH]^{+m}$, multiple charging leads to an initial decrease in complex stability until a tipping point where the PMMA oligomers contain >10 units (Figure 3-7a). The E_0 of $[PMMA_8][DAB+1H]^{+1}$ and $[PMMA_8][DAB+2H]^{+2}$ are 0.85 ± 0.01eV and 0.63 ± 0.01eV respectively. As chain length increases, the multiple charge leads to increased stabilization ($[PMMA_{15}][DAB+1H]^{+1}$; 1.43 ± 0.03eV and $[PMMA_{15}][DAB+2H]^{+2}$; 1.77 ± 0.02 eV). Although the charges are in close proximity to each other, there is an increase in the electrostatic attractive forces between the DAA and the polymer and increasing the length of the polymer will eventually lead to attractive electrostatic forces outweighing the repulsive. $[PMMA_n][DAD+2H]^{+2}$ complexes consistently showed multiple charging leading to complex stabilization vis à vis their singly protonated complement (Figure 3-7b). This is because the charge-charge repulsion within the [PMMA$_n$][DAD+2H]$^{+2}$ complexes is sufficiently low enough to always be outweighed but the added attractive forces that occur from having an additional charge.

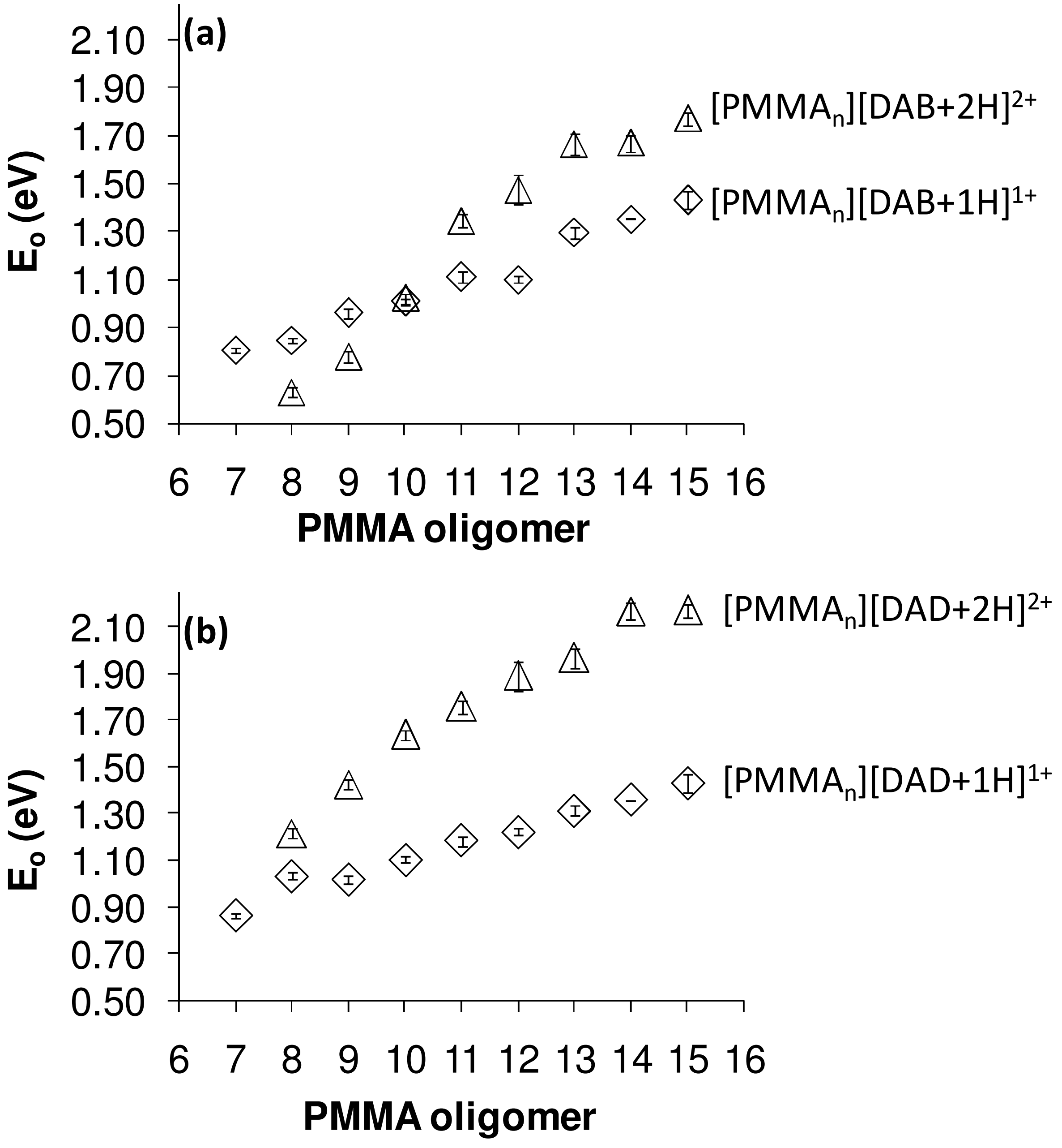

Figure 3-7 Effects of charge state on E_0 of [DAA][PMMA] complexes
Activation energies of a) [PMMA$_n$][DAB+1H]$^{+1}$ (◊),[PMMA$_n$][DAB+2H]$^{+2}$ (Δ) and b) [PMMA$_n$][DAD+1H]$^{+1}$ (◊),[PMMA$_n$][DAD+2H]$^{+2}$ (Δ).

The second kinetic value that was altered in order to fit experimental breakdown diagrams was $\Delta S^{\ddagger}$. Altering this value predominately changes the slope of the breakdown curve (whereas, E_0 is largely responsible for the onset location of the curve).

Figure 3-8 shows that both singly and doubly protonated, $[PMMA_n][DAA+mH]^{+m}$ complexes have an increasing $\Delta S^{\ddagger}$ coinciding with an increase in polymer size. The greatest difference was observed between the $\Delta S^{\ddagger}$ of the singly and doubly charged complexes; the doubly protonated complexes had a steeper slope of $\Delta S^{\ddagger}$ increase in comparison with its corresponding singly charged species. The presence of the two charges holds the oligomer chains more rigidly than a single charge site, and therefore the transition state of dissociation leading to two singly-charged products, which may be quite late in the reaction coordinate, is accompanied by a greater relative increase in entropy.

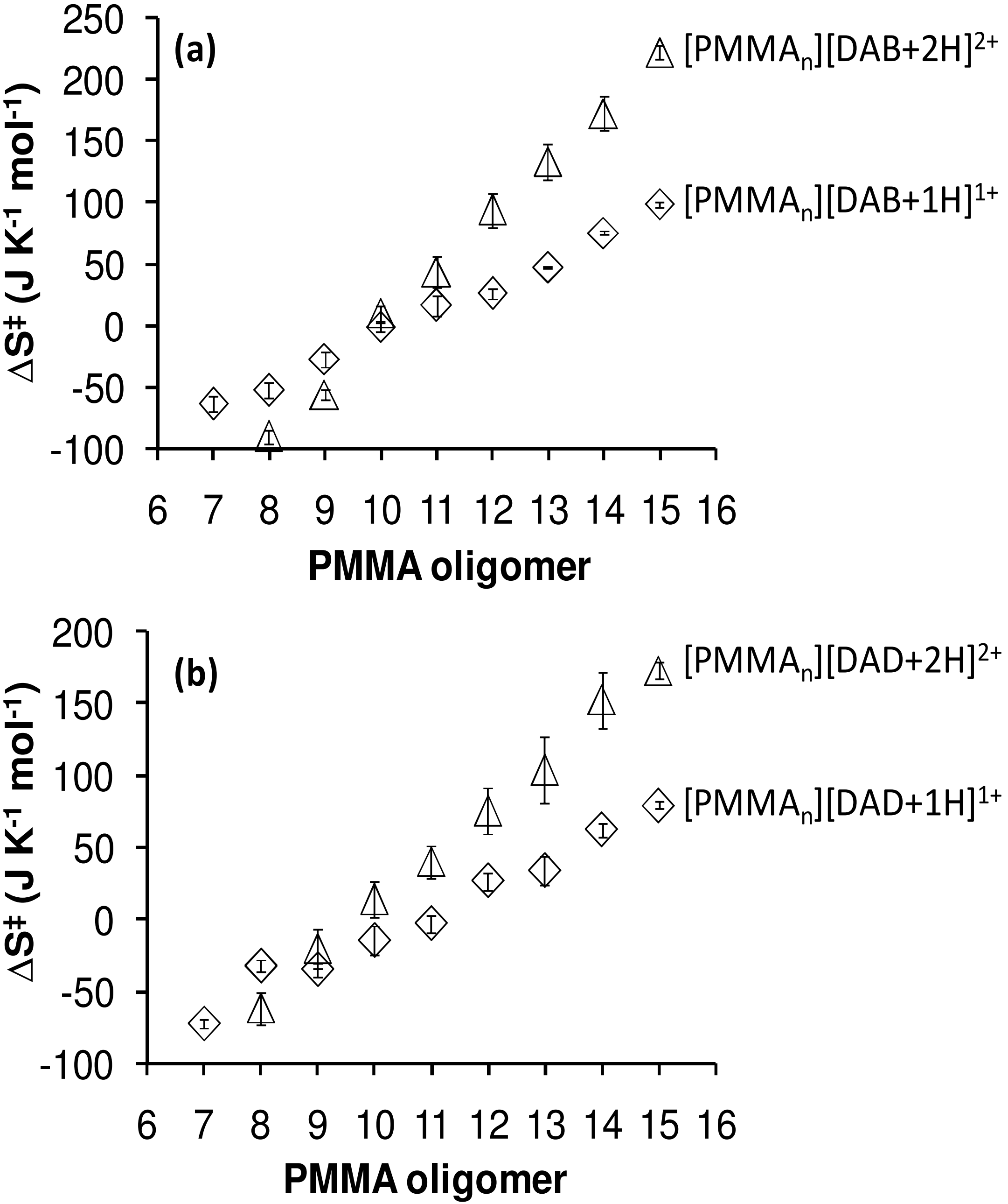

Figure 3-8 Effect of charge state on $\Delta S^{\ddagger}$ of [DAA][PMMA] complexes ($\Delta S^{\ddagger}$) of a) [PMMA$_n$][DAB+1H]$^{]+1}$ (◊),[PMMA$_n$][DAB+2H]$^{+2}$ (Δ) and b) [PMMA$_n$][DAD+1H]$^{+1}$ (◊),[PMMA$_n$][DAD+2H]$^{+2}$ (Δ). $\Delta S^{\ddagger}$ values represent values which resulted in the best fit of experimental breakdown diagrams with theoretical breakdown curve obtained through RRKM.

On the meaning of α

The final variable that was necessary to adjust was α, corresponding to the relationship between the effective internal energy distribution, and center-of-mass collision energy. In a previous study that used a similar RRKM protocol to extract energetic data from complexes between the Aβ-40 peptide and drug candidates, the α values were similar for all complexes (~200 K eV^{-1}) [1] whereas values obtained in this study ranged from 195-458 K eV^{-1}. This is because the overall Aβ-40 peptide complexes were quite similar to each other, whereas, the presently studied complexes cover a much wider range of cross section and degrees of freedom. Unlike E_0 and $\Delta S^{\ddagger}$, both singly and doubly protonated complexes show a similar negative slope of α over increasing polymer length (Figure 3-9)

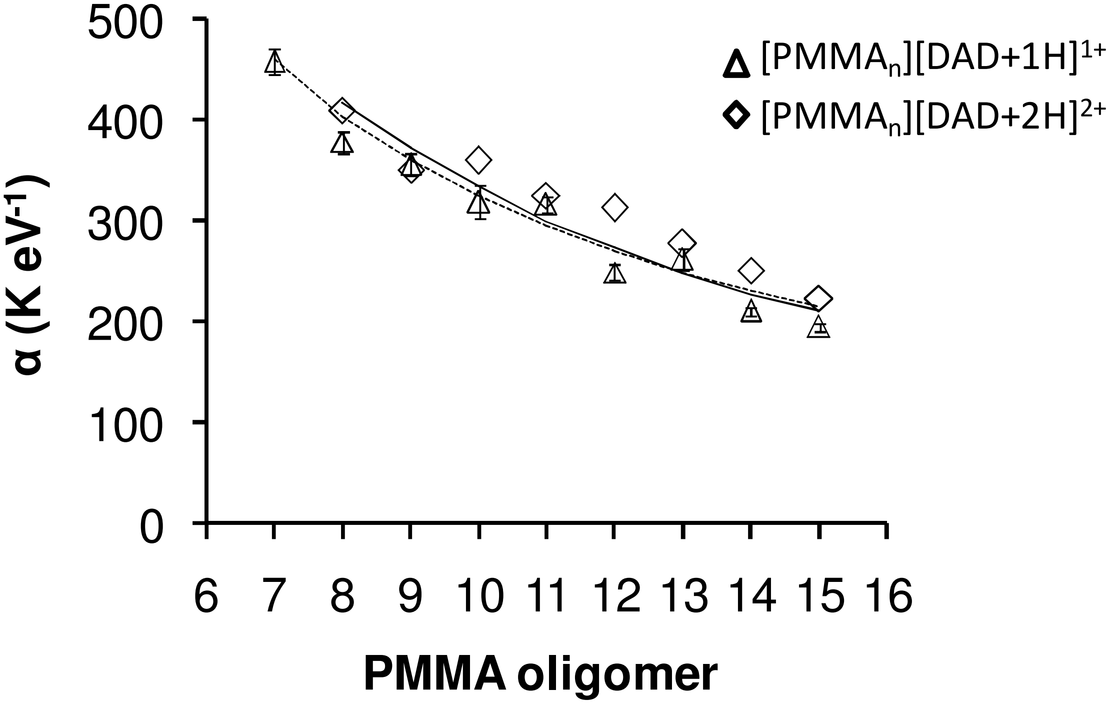

Figure 3-9 Best fit α of singly and doubly protonated [PMMA][DAD] complexes α values resulting in best fit of experimental breakdown diagrams by theoretical RRKM curves for $[PMMA_n][DAD+1H]^{+1}$ (Δ) and $[PMMA_n][DAD+2H]^{+2}$ (◊). Under experimental conditions this molecular system can be described by Eq.5 with b=2.23x 10^{-3}. Dashed and Solid lines represent theoretical alpha values for $[PMMA_n][DAD+1H]^{+1}$ and $[PMMA_n][DAD+2H]^{+2}$ respectively.

In essence, α describes the deposition of energy from a collision event into the effective internal energy of the ion, thus the difference in α between a corresponding singly or doubly charged complex of this size should not be significant. The variable α is a parameter that actually accounts for several molecular and instrumental properties, including the number of collision events (collision gas density, ion cross section) and the ability for a unit of collision energy to increase the effective temperature. Using the above properties, a theoretical curve that accurately described the α values of this system was found using the following relation:

$$\boldsymbol{\alpha} = \mathbf{b}\frac{\Omega}{\mathbf{C_{vib}}^{2}} \qquad \text{Equation 3-4}$$

b is an instrumental constant,
Ω is the experimentally measured cross section and
C_{vib} is the vibrational heat capacity of the reactant ion complex,

The b constant ($2.23\mathrm{x}\ 10^{-3}$) will be changed by different instrumental settings (i.e. pressure) and would also be different for dissimilar complexes; however, when instrumental settings throughout an experiment are maintained and the complexes are similar, b should be a constant throughout. As the sizes of the complexes increase, so do the cross sections, and accordingly the number of collision events that can lead to an overall increase in internal energy. Yet because the trend of α with increasing size is actually a decrease, the ability of each collision to increase the effective internal energy of larger complexes is reduced. This is due to the vibrational heat capacity of the ion, which increases with the addition of more oscillators. The reason that the heat capacity is square could be because the initial temperature is fixed within this model. Presumably as the ions are ionized and enter through the sampling cone into the ion guide, they are undergoing collisions with neutral gases. Larger ions will have a lower T_i than smaller ions due to the differences in heat capacity. By artificially fixing T_i, the α value will compensate in order to best reflect the effective internal energy distribution at a given collision energy, explaining why C_v in equation 3-4 is squared. The α values reported for similar complexes in our previous study on the Aβ-40 peptide also show the same dependence upon the number of oscillators [1].

3.6 Conclusions

Similar to previous reports, in gas phase complexes, electrostatic interactions are the dominant force and can determine the overall stability and conformation of the complexes. MD is a powerful and widely used tool to investigate molecular structure; however, many classic regimes of MD necessitate the assignment of charge site. In many cases, such as this study, the charge bearing site(s) are apparent but in other cases involving more complex systems, it could become more difficult. In this example, the location of the charges would greatly affect the overall conformation and energetics, and the location of charges was confirmed on two fronts; through MS/MS and IMS. For all DAA substrates, multiple charges will cause coulombic repulsion to lower the complex stability, however, additional charged hydrogen bonds, and charge-dipole interactions will increase complex stability. This causes the 'tipping' point effect where additional charge will lead to greater complex stability after certain length of polymer is achieved. The tipping point occurs first for DAD and last for DAB because the coulombic repulsion in the DAB complexes is much higher than the DAD complexes.

3.7 References

1. Mayer, P. M., Martineau, E. Gas-phase binding energies for non-covalent Aβ-40 peptide/small molecule complexes from CID mass spectrometry and RRKM theory. Physical Chemistry Chemical Physics 13, 5178-5186 (2011)
2. Marcus, R. A., Rice, O. K. The Kinetics of the Recombination of Methyl Radicals and Iodine Atoms. J. Phys. Chem. 55, 894-908 (1951)
3. Casey, J.; Alhazmi, A., Mayer, P. M. Conformation effects on the dissociation of ionized polymers. Eur. J. Mass Spectrom. 11, 557-563 (2005)
4. Frisch, M. J.; Trucks, G. W.; Schlegel, H. B.; Scuseria, G. E.; Robb, M. A.; Cheeseman, J. R.; Montgomery, J. A.; Vreven, T.; Kudin, K. N.; Burant, J. C.; Millam, J. M.; Iyengar, S. S.; Tomasi, J.; Barone, V.; Mennucci, B.; Cossi, M.; Scalmani, G.; Rega, N.; Petersson, G. A.; Nakatsuji, H.; Hada, M.; Ehara, M.; Toyota, K.; Fukuda, R.; Hasegawa, J.; Ishida, M.; Nakajima, T.; Honda, Y.; Kitao, O.; Nakai, H.; Klene, M.; Li, X.; Knox, J. E.; Hratchian, H. P.; Cross, J. B.; Bakken, V.; Adamo, C.; Jaramillo, J.; Gomperts, R.; Stratmann, R. E.; Yazyev, O.; Austin, A. J.; Cammi, R.; Pomelli, C.; Ochterski, J. W.; Ayala, P. Y.; Morokuma, K.; Voth, G. A.; Salvador, P.; Dannenberg, J. J.; Zakrzewski, V. G.; Dapprich, S.; Daniels, A. D.; Strain, M. C.; Farkas, O.; Malick, D. K.; Rabuck, A. D.; Raghavachari, K.; Foresman, J. B.; Ortiz, J. V.; Cui, Q.; Baboul, A. G.; Clifford, S.; Cioslowski, J.; Stefanov, B. B.; Liu, G.; Liashenko, A.; Piskorz, P.; Komaromi, I.; Martin, R. L.; Fox, D. J.; Keith, T.; Laham, A. M. A.; Peng, C. Y.; Nanayakkara, A.; Challacombe, M.; Gill, P. M. W.; Johnson, B.; Chen, W.; Wong, M. W.; Gonzalez, C., Pople, J. A. Gaussian 03, Revision C.02. Gaussian Inc, Wallingford CT (2004)
5. Smith, D. P.; Knapman, T. W.; Campuzano, I.; Malham, R. W.; Berryman, J. T.; Radford, S. E., Ashcroft, A. E. Deciphering drift time measurements from travelling wave ion mobility spectrometry-mass spectometry studies. Eur. J. Mass Spectrom. 15, 113-130 (2009)
6. Case, D. A.; Darden, T. A.; III, T. E. C.; Simmerling, C. L.; Wang, J.; Duke, R. E.; Luo, R.; Merz, K. M.; Pearlman, D. A.; Crowley, M.; Walker, R. C.; Zhang, W.; Wang, B.; Hayik, S.; Roitberg, A.; Seabra, G.; Wong, K. F.; Paesani, F.; Wu, X.; Brozell, S.; Tsui, V.; Gohlke, H.; Yang, L.; Tan, C.; Mongan, J.; Hornak, V.; Cui, G.; Beroza, P.; Mathews, D. H.; Schafmeister, C.; Ross, W. S., Kollman, P. A. AMBER 9. University of California, San Francisco, CA (2006)
7. Wang, J.; Wolf, R. M.; Caldwell, J. W.; Kollman, P. A., Case, D. E. Development and Testing of a General Amber Force Field. J. Comput. Chem. 25, 1157-1174 (2004)

8. Wilson, S. R., Cui, W. Applications of Simulated Annealing to Peptides. Biopolymers 29, 10 (1990)
9. Mesleh, M. F.; Hunter, J. M.; Shvartsburg, A. A.; Schatz, G. C., Jarrold, M. F. Structural Information from Ion Mobility Measurements: Effects of the Long-Range Potential. J. Phys. Chem. 100, 16082-16086 (1996)
10. Jarrold., M. J. Online: http://www.indiana.edu/ nano/Software/mobcaltxt.
11. Hunter, E. P., Lias, S. G. Evaluated Gas Phase Basicities and Proton Affinities of Molecules: An Update. J. Phys. Chem. Reference Data 27, 243 (1998)
12. Alhazmi, A. M., Mayer, P. M. Protonating Polymer Oligomers in the Gas Phase to Change Fragmentation Pathways. J. Am. Soc. Mass Spectrom. 20, 60-66 (2009)
13. Vinokur, N., Ryzhov, V. Using collision-induced dissociation with corrections for the ion number of degrees of freedom for quick comparisons of relative bonding strength. J. Mass Spectrom. 39, 1268-1274 (2004)

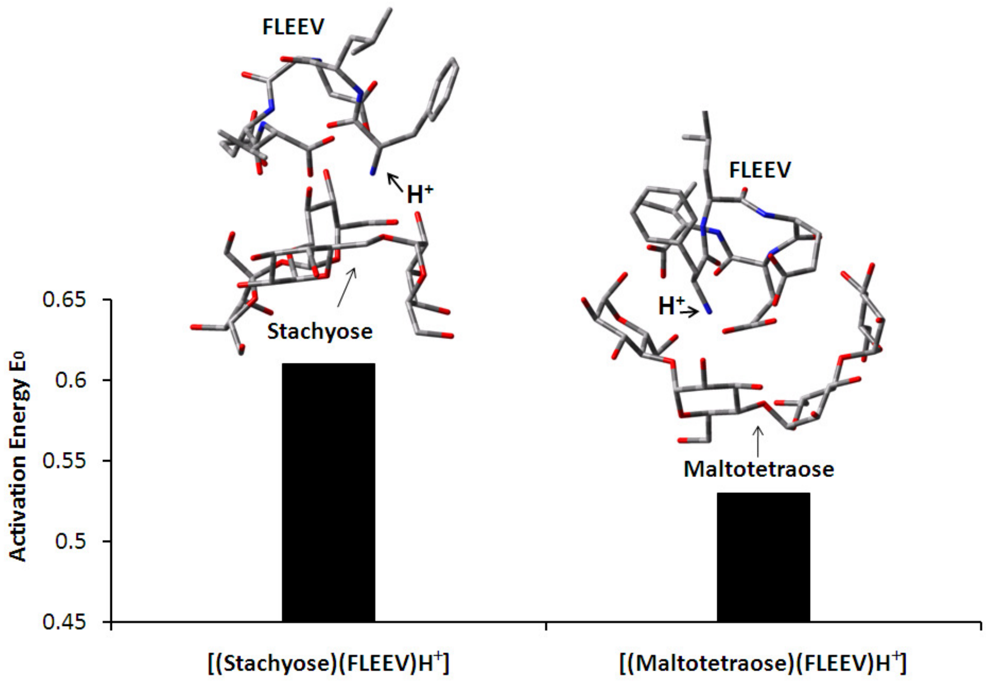
FLEEV
H+
Stachyose
FLEEV
H+
Maltotetraose
0.65
0.6
0.55
0.5
0.45
Activation Energy E0
[(Stachyose)(FLEEV)H+]
[(Maltotetraose)(FLEEV)H+]

4.1 Objectives

- Apply the methods in Chapter 3 to a more complex, chemical system
- Determine the sensitivity of RRKM modelling to differentiate small binding differences of isomeric saccharides to small peptides
- Connect energetic measurements with structural data obtained by IMS and MM/MD

4.2 Chapter acknowledgements

J. B. Renaud thanks:

- Amanda Comeau for assistance with collecting experimental data
- Gleb Mironov for kinetic capillary electrophoresis data

4.3 Introduction

In many examples, electrospray ionization mass spectrometry (ESI-MS) can provide a good approximation of the solution phase behaviour of non-covalent complexes [1, 2], but quite often, non-covalent complexes detected in the gas phase with MS do not necessarily represent their concentrations in solution. Non-covalent complexes that do not exist in solution be formed by the ESI process and the intensities of non-covalent complexes that are known to be specific can be over represented by additional non-specific interactions. Discrepancies between interactions observed in the gas phase and solution phase can be attributed to the ionization process, different structures accessible to a complex in the gas phase and the absence of solvent molecules that could normally be involved in the solution phase binding network. A particular challenge that arises when studying non-covalent saccharide/peptide (or protein) complexes is their propensity for non-specific interactions: peptides contain ample sites for protonation while carbohydrates have many sites that are accessible for hydrogen bonding. Klassen and co-workers have conducted many detailed mass spectrometry based studies of the interactions between carbohydrates and proteins [3-8], including non-specific interactions [9, 10]. This group also studied the gas-phase properties of these non-specific interactions with blackbody infrared radiative dissociation (BIRD), where in some examples, the non-specific complexes were found to be more kinetically stable in the gas phase than the specific interaction [6].

The extent of non-specific interaction is concentration dependent, but of interest are other contributing factors. Binding energetics and molecular conformation are fundamentally linked [11], especially when binding is mediated by hydrogen-bonds. The distance and directionality between the hydrogen-bond acceptor and donor is important to the overall interaction energy. If two similar saccharides have the same dissociation energy from a given peptide host, the complexes should be expected to have a similar conformation, or at least a range of conformations with an equal extent of hydrogen bonding. In contrast, if two similar saccharides have very different dissociation energies from a host, those complexes should exhibit molecular conformations with distinct hydrogen bonding arrangements.

The purpose of this study is to provide a direct conformational explanation for the gas-phase stabilities of non-specific saccharide/peptide complexes and the intensities of these complexes observed in an ESI-MS spectrum. This was accomplished using eight non-covalent complexes containing one of two peptides (FLEEL, FLEEV) and one of four saccharides (raffinose, D-panose, stachyose, maltotetraose). Raffinose and D-panose are isomeric tri-saccharides while stachyose and maltotetraose are isomeric tetra-saccharides. The two similar peptides, FLEEL and FLEEV were chosen because of their high similarity and therefore, any relative trends observed in the FLEEL complexes should also be present in the FLEEV complexes.

Materials

Phe-Leu-Glu-Glu-Leu (FLEEL), Phe-Leu-Glu-Glu-Val (FLEEV) peptides, saccharides (D-(+)- D-panose, maltotetraose, and stachyose hydrate) were purchased from Sigma Aldrich. Raffinose pentahydrate was purchased from Eastman Kodak Co. Peptide solutions in methanol:water:formic acid (40:40:10) of 1.5×10^{-4} M were mixed with an equamolar ratio of saccharide in a methanol:water (50:50) solution.

Kinetic Capillary Electrophoresis

All experiments were performed independently using a PA800plus Pharmaceutical Analysis CE system. Before each experiment, the capillary was thoroughly rinsed by 75 psi pressure with: 0.1 M HCl for 3 min, 0.1 M NaOH for 3 min, ddH_2O for 3 min, 2.5 mM tris-acetate buffer/1 % formic acid for 5 min, and the incubation/run buffer containing the saccharide for 2 min. Equilibrium mixtures of peptides and saccharides were prepared in the incubation buffer with saccharide concentrations of 1 and 2 mM with 10 μM or 30 μM peptide mixtures. All solutions were filtered through 0.22-μm pore size membrane filters (Millipore, Nepean, ON, Canada). The bare-silica capillary was purchased from Polymicro (Phoenix, AZ, USA).The equilibrium mixture consisting of the peptide and saccharide was injected into the capillary from the inlet end by a pressure pulse of 10 s × 1 psi. An electric field of 329 V/cm was applied for the separation with the anode at the injection end of the capillary. Incubation buffers were 12.5 mM tris-acetate or 1% formic acid.

ESI-MS, ESI-MS/MS

ESI-MS measurements were performed on a Waters Q-TOF 1 with MassLynx 4.1 for analysis and data processing. The mobile phase consisted of 50% methanol and 50% acetonitrile at a flow rate of 30 $\mu L \cdot min^{-1}$. The source temperature was 80°C and the desolvation temperature was set to 150°C. The capillary voltage was 3 kV and the cone voltage was 45 V. All mass spectra were averages of 30 scans (0.9 scan/s) from m/z 100 to 1500 in positive ion mode. The collision gas for collision-induced dissociation (CID) was argon at a pressure reading of 14 psi. Breakdown diagrams were constructed at energy intervals of 1 eV (E_{lab}) beginning at energies yielding no intensities and finishing after the reactant ion was completely dissociated. All collision energies reported in this paper are center-of-mass (E_{com}) energies

Ion mobility spectrometry

Experimental cross sections (Ω_{exp}) of all complexes were measured in a manner similar to that used by D.P. Smith et al.[12] however, the calibrants used to relate arrival time distribution to molecular cross-sections were doubly protonated complexes between different oligomers (7-16) of poly(methylmethacrylate) and diamino(butane/hexane/decane) for a total of 30 points between 219 $Å^2$and 370 $Å^2$ measured in a previous study done by our research group [13]. These complexes are secondary calibrants and were used because they are stable for long periods of time and provide multiple data points over a small cross-section range in a single experiment. Their cross-sections were initially calculated using the tryptic peptides of myoglobin, ubiquitin and lysozyme. A Beckman PA 800 capillary electrophoresis (Beckman Coulter inc., USA) was used to infuse analytes into a Waters Synapt G2 HDMS mass spectrometer (Waters Corp., USA) via a Micromass Capillary Electrophoresis Sprayer (Micromass UK Limited, UK) by applying a constant pressure of 1 psi. The mobile phase consisted 50:50 methanol:water mixture, introduced at a flow rate of 0.7 μL min^{-1}.

Extraction of activation parameters from breakdown diagrams using RRKM theory

The method used to generate a theoretical breakdown curve and fit it to experimental values has been described in detail elsewhere [14]. The internal energy distribution as a function of center-of-mass collision energy (E_{com}) was approximated through the use of an effective temperature (T_{eff}) designation in the equation

$$\mathbf{T_{eff} = 300K + \alpha E_{com}} \quad \text{Equation 4-1}$$

Where 300 K represents the initial temperature of the ions, and α which has units of K eV^{-1} and is altered during the fitting procedure to reflect the effect a given collision energy will have upon the effective internal energy distribution.

The three variables; E_0, $\Delta S^{\ddagger}$ and α were altered in an automated manner using an in-house Python/Fortran hybrid program and the score of each fit was assigned based the absolute separation between the E_{com} of experimental data points and the E_{com} of the point on the theoretical curve with the same % dissociation as experimental (in units of eV) divided by the number of data points in the set. The different combinations of E_0, $\Delta S^{\ddagger}$ and α that resulted in a score no less than 0.05% below the best scoring combination were averaged together, and standard deviation taken from this set of combinations. The listed uncertainty does not take into account the limitations of the model used and thus are to be viewed as lower limits.

Molecular mechanic/molecular dynamics simulated annealing (MD/MM-SA)

The AMBER9 [15] program suite using the Generalized AMBER force field (GAFF) [16] was used to study conformations of the complexes. Minimized energy conformations of the peptide/saccharide complexes were briefly equilibrated for 20 ps (time step 1 fs) at 300K before undergoing 2000 cycles of simulated annealing [17] (each 18.25 ps total, 0.5 fs time step) starting with drastic heating from 300 K to 800 K over 1.25 ps and equilibrated for 2 ps. This was followed by cooling increments of 100 K over 1 ps with 2 ps of equilibration at each temperature, until 300 K was reached. The lowest energy conformation of each simulated annealing cycle was then selected to undergo subsequent rounds of simulated annealing. After each cycle, the low energy conformation was cooled to 0 K over 2 ps, minimized and potential energy measured. Theoretical cross sections (Ω_{theo}) of the 50 lowest structures sampled (all being < 6.3 kJ from the lowest structure energy) were measured using the trajectory method [18] in the MOBCAL program [19]. The trajectory method functions through averaging the orientations of a set of coordinates and calculating their interactions with a theoretical helium buffer gas, taking into account long range interactions, scattering and multiple collisions.

4.6 Results and discussion

For brevity, saccharides D-(+)-raffinose, D-panose, stachyose, and maltotetraose will be written as Raf, Pan, Sta and Mal, respectively. All experiments were undertaken with eight systems in total, non-covalent complexes between one of the four saccharides and one of the two peptides (FLEEL and FLEEV). Two similar peptides were used in order to add confidence to any observations and measurements, and thus unless necessary, only figures of complexes with one of the peptides are shown.

Validation of non-specific interactions using kinetic capillary electrophoresis

Evaluation of solution phase interactions between the saccharides and peptides was performed using the ECEEM technique [20]. Due to the difference in the charges of peptides (positive in 1 % formic acid, pH 2.2 and negative in 12.5 mM tris-acetate, pH 7.8) and sugars (being neutral at the same pH), their respective electrophoretic velocities will not be equal. If the formation of a complex between a peptide and a sugar occurs, a shift in the migration time of the peptide towards the arithmetical mean of the migration times of the free peptide and free sugar would be observed, with the extent of the shift being representative of the extent of the solution phase interaction. No shifts were observed under the analyte concentrations used, which indicates that the peptides and saccharides do not interact strongly in solution and thus any ESI-MS signals are considered to be non-specific.

ESI-MS

Mixtures of peptides and Raf, Pan, Sta, or Mal were analyzed with ESI-MS and all [(saccharide)(FLEE(L/V))+H$^+$] complexes were observed (Figure 4-1).

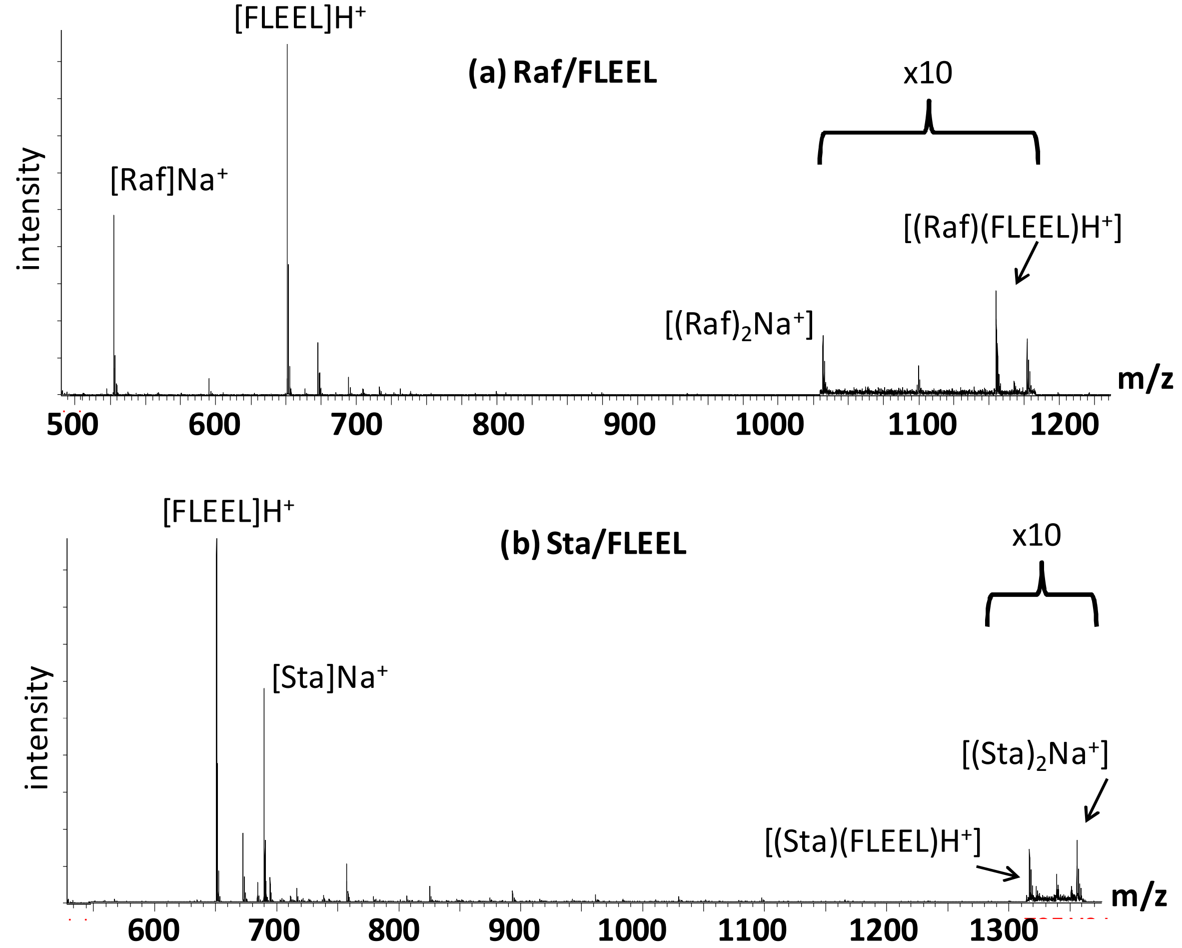

Figure 4-1 Example mass spectra of [(saccharide)(FLEEL)H$^+$] mixtures.
ESI+ mass spectra of mixtures for 1.5×10^{-4} M FLEEL peptide with1.5×10^{-4} M saccharide; (a) Raf and (b) Sta.

In this portion of the study, the goal was to investigate the relative ion abundance of the isomeric complexes. The intensity of the unbound saccharides, unbound peptides, saccharide dimers and saccharide/peptide complexes were measured as the sum of intensities of the proton and sodium bound complexes. These saccharides and peptides were shown not to interact in solution and therefore, any complexes were very likely formed in the ionization process and do not reflect any differences in solution phase binding affinities. At molar ratios of 1:1 saccharide:FLEEL, the percentage of bound peptide over total peptide was equal within experimental error for all saccharides studied (~ 11%), with the exception of complexes with Pan, which were found to be slightly higher than the experimental error of the percentage of peptide bound to tetra-saccharides Mal and Sta (Figure 4-2). The similarities of intensities suggests that the energy required to dissociate these gas-phase complexes is below that obtained by the complexes during the electrospray process after they have been formed. A difference in intensity was observed when comparing the percentage of saccharide in the dimer state over the total amount of saccharide; (dimer intensity)/(dimer + unbound + complexed intensity). Here a small, yet significant difference in intensity was observed between tri-saccharide dimers and tetra-saccharide dimers, suggesting there is a difference in the binding energetics of dimerization. This difference could be due to a different structural arrangement between the two homo-saccharides within the dimer complex, and likewise a different level of energetic interaction.

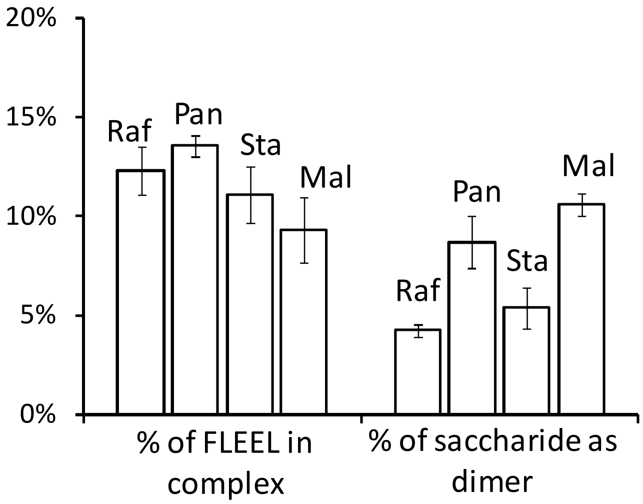

Figure 4-2 Relative [(saccharide)(FLEEL)+H^+] complex intensities in normal mass spectrum. Percentage of peptide within complex and saccharide observed as a dimer. The averages of 6 injections for the [(saccharide)(FLEEL)] complex intensities over total peptide intensities (unbound and complex) were measured. Percentage of saccharides observed as dimers were measured by taking intensity of dimer over total saccharide signal; unbound, complex, dimer. For all instances, intensities are the sum of sodiated and protonated signals.

MS/MS, RRKM energetic analysis

For all eight complexes, the dominant dissociation pathway consisted of the loss of neutral saccharide, leaving protonated FLEEL or FLEEV peptide (Figure 4-3).

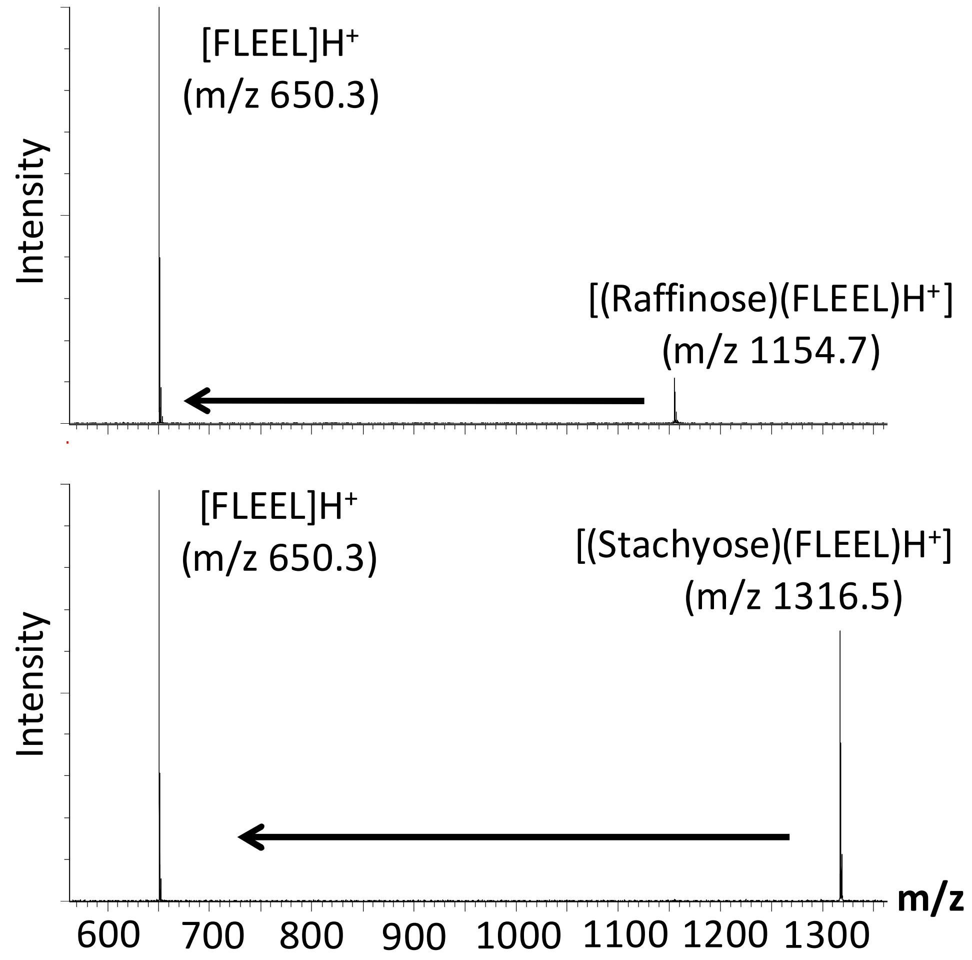

Figure 4-3 Example tandem mass spectra of [(Raf)(FLEEL)H$^+$] and [(Sta)(FLEEV)H$^+$] complexes
CID mass spectra of (a) [(Raf)(FLEEL)H$^+$] and (b) [(Sta)(FLEEL)H$^+$]. All [(saccharide)(FLEEL)H$^+$] complexes underwent loss of neutral saccharide as the sole, initial dissociation pathway

The intensities of the ions and dissociation products were recorded as a function of E_{com} beginning at energies prior to dissociation and ending when the reactant ion complex was completely dissociated (Figure 4-4).

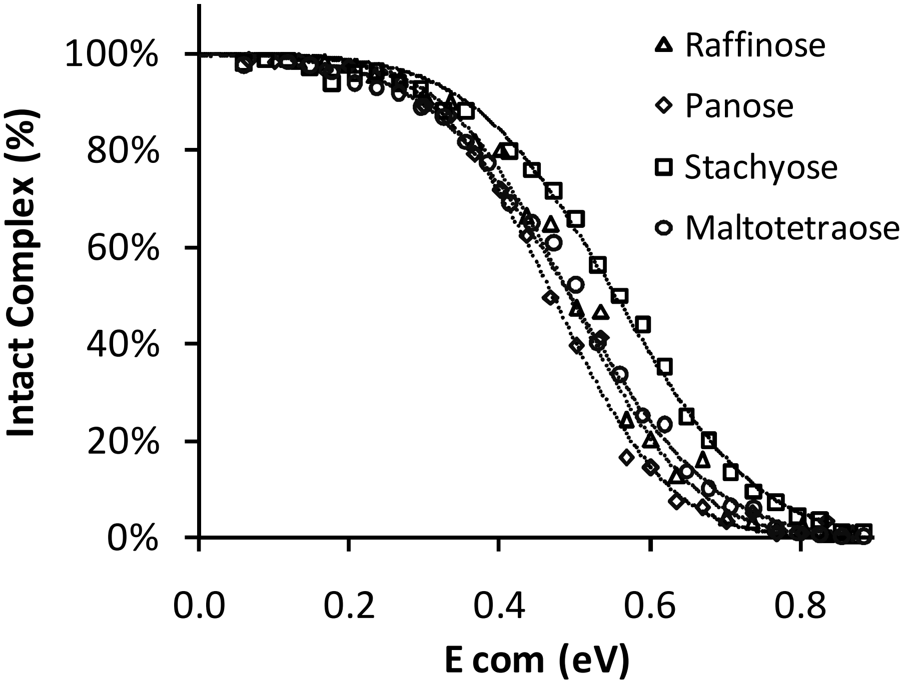

Figure 4-4 RRKM fitted breakdown diagrams of [(saccharide)(FLEEL)H^+] Breakdown diagrams of [(saccharide)(FLEEL)H^+] measured as a function of center-of-mass collision energy (E_{com}). Experimental measurements obtained from protonated peptides complexed with raffinose(Δ), panose(◊), stachyose(□) and maltotetraose(○). Dotted lines obtained by theoretical fitting using RRKM.

It is often not possible to extract even qualitative rankings of dissociation energies solely based on a breakdown diagram, as the shape and onset of the curves are not only determined by activation energy, but also by the entropy of activation, $\Delta S^{\ddagger}$, the molecular cross section (number of collision events) and the nature and number of the degrees of freedom, the latter affecting the relative reactant ion and transition state density and sums-of-states. In Figure 4-4, the breakdown diagrams of FLEEL complexes containing

Sta and Mal are shifted to higher E_{com} relative to those which contain Raf and Pan yet, through RRKM fitting, the E_0 values for the dissociation of Raf, Pan and Sta in proton bound complexes with FLEEL are similar

Table **4-1**).

Table 4-1 [(saccharide)(peptide)H^+] E_0 and $\Delta S^\ddagger$ of dissociation

	FLEEL			FLEEV		
	E_0 (eV)	$\Delta S^\ddagger$ (J K^{-1} mol^{-1})	α (K eV^{-1})	E_0 (eV)	$\Delta S^\ddagger$ (J K^{-1} mol^{-1})	α (K eV^{-1})
Raf	0.64 ± 0.01	-62 ± 5	389 ± 13	0.56 ± 0.02	-82 ± 5	383 ± 13
Pan	0.63 ± 0.02	-65 ± 8	429 ±24	0.48 ± 0.01	-80 ± 3	296 ± 9
Sta	0.66 ± 0.01	-52 ± 2	310 ± 12	0.61 ± 0.01	-69 ±5	341 ± 16
Mal	0.57 ± 0.01	-70 ± 3	335 ± 11	0.53 ± 0.03	-63 ± 9	251 ± 12

Interestingly, [(Mal)(FLEEL)H^+] has an E_0 value of 0.57 eV, lower than the 0.64 eV, 0.63 eV and 0.66 eV of Raf, Pan and Sta, respectively. As the role of electrostatic forces are chief in gas phase interactions, this difference between Mal complexes and those containing Raf, Pan and Sta could be due to decreased interaction between the protonated site of the peptide and the saccharide oxygens or likewise, the saccharide adopting a conformation with an increased number of 'self' hydrogen bonds. One large deviation between the results obtained with the FLEEL and FLEEV saccharide complexes are that in the FLEEV complexes, Pan shows the lowest E_0 (0.48 eV) which is below its isomeric complement raffinose at 0.56 eV. For the [(Pan)(FLEEV)H^+] complex, the α value is 296 ± 9 which is much lower than what should be expected based on findings in Chapter 3. Therefore, a lower quality of the experimental breakdown diagram for [(Pan)(FLEEV)H^+] is most likely responsible for the discrepancy in RRKM derived energetics.

The observed relative ESI-MS intensities cannot be directly related to the calculated E_0 values for the different complexes. For example, although [(Mal)(FLEEL)H^+] has a 0.09eV E_0 than [(Sta)(FLEEL)H^+](Table 4-1), we do not see a decrease in its ESI-MS intensity (Figure 4-2) outside of experimental error. This could mean that under the current electrospray conditions, the energy required for dissociation is above that experienced by the complexes in the source. If the source conditions were harsher, a difference in the ESI-MS intensities of Sta and Mal complexes with the peptide might be expected.

MM/MD-SA and IMS conformational complex analysis.

A specific energetic interaction between a host and ligand can generate a change in conformation, just as the conformation of a complex can determine the magnitude of the energetics of the interaction. Direct comparison of the arrival time distributions (ATD) of isomers is possible as the momentum effects arising from different masses are absent. Arrival times of the sodiated saccharide, sodiated saccharide dimer and saccharide-peptide complex are shown for FLEEL and FLEEV systems in Figure 4-5 and Figure 4-6, respectively.

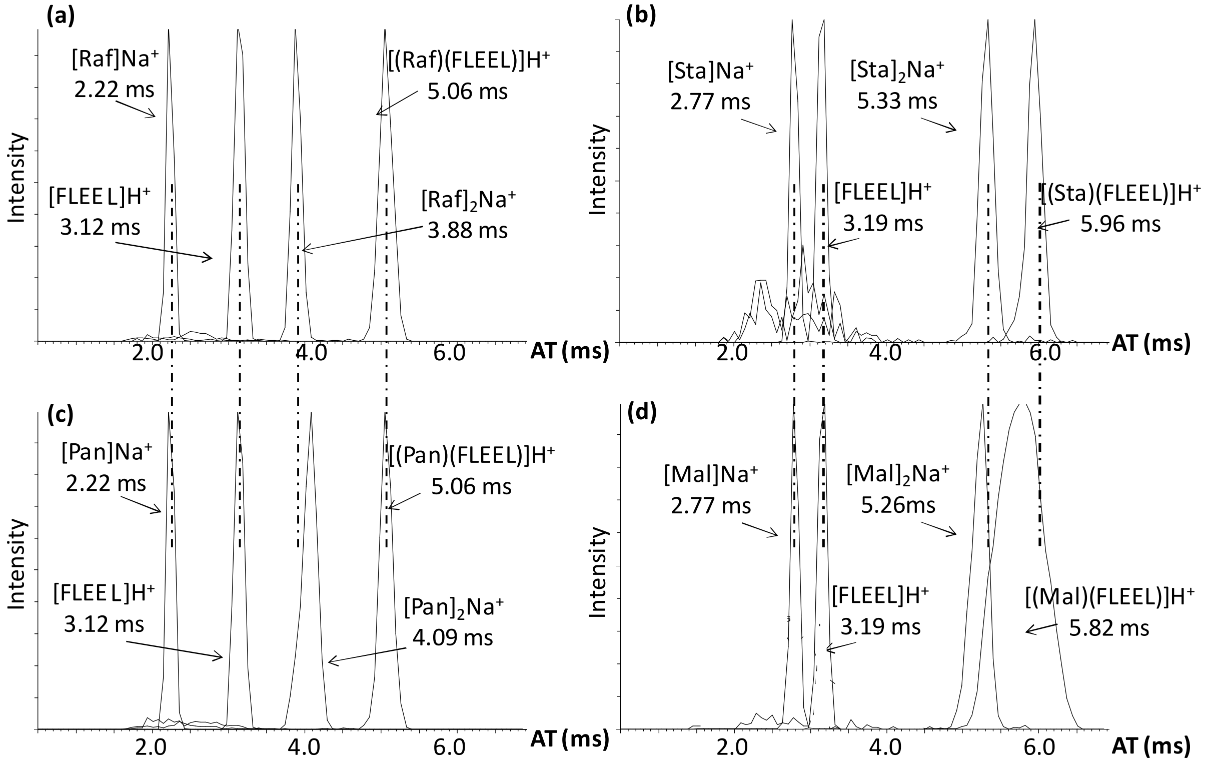

Figure 4-5 Ion mobility spectra of [(saccharide)(FLEEL)H^+]
Arrival time distributions (ATD) of [(saccharide)(FLEEL)H^+] complexes. Also shown are ATD of sodiated saccharides, protonated peptide and sodiated saccharide dimers FLEEL and (a) Raf, (b) Pan, (c) Sta and (d) Mal.

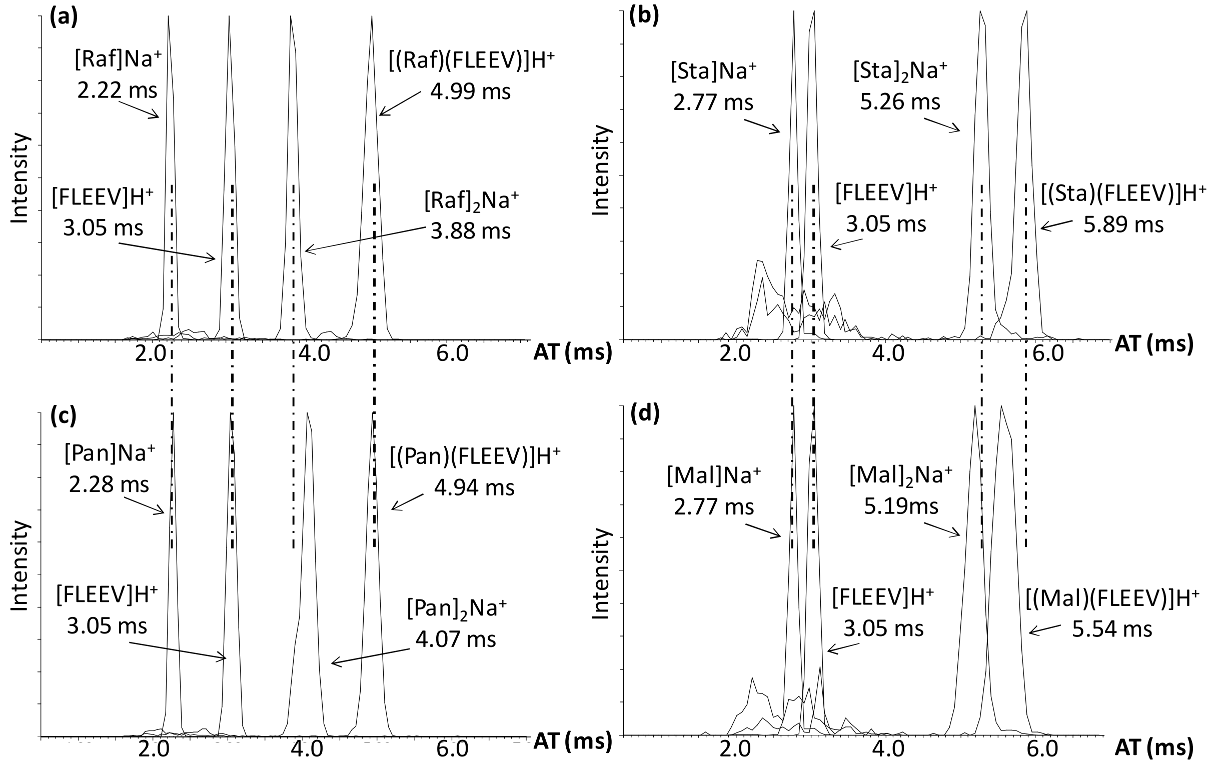

Figure 4-6 Ion mobility spectra of [(saccharide)(FLEEV)H^+]
Arrival time distributions (ATD) of [(saccharide)(FLEEV)H^+] complexes. Also shown are ATD of sodiated saccharides, protonated peptide and sodiated saccharide dimers FLEEV and (a) Raf, (b) Pan, (c) Sta and (d) Mal.

Table 4-2 summarizes the arrival times of the various complexes. The individual, sodiated isomeric pairs have very similar ATDs: 2.22 ms for (Raf)Na^+ and (Pan)Na^+ respectively and 2.77ms for both (Sta)Na^+ and (Mal)Na^+. There is a small difference between the ATD of sodiated Raf and Pan in the FLEEV solution (Pan ATD = 2.28ms) which could be due to small instrumental effects. When complexed with the FLEEV peptide, a slight difference is observed when comparing the [(Raf)(FLEEV)H^+] and [(Pan)(FLEEV)H^+] ATDs (Figure 4-6a,c) but a 6% change in ATD is observed with [(Sta)(FLEEV)H^+]and [(Mal)(FLEEV)H^+] (Figure 4-6 b,d). This same observation is present within the FLEEL/saccharide complexes, with those containing Raf and Pan having the same ATD of 5.06 ms while those with Sta and Mal have ATDs of 5.96 and 5.82 ms respectively. Noticeable in Figure 4-5d is that the ATD of [(Mal)(FLEEV)H^+] is much broader than all the other complexes. This could be the result of a wider distribution of conformations present or because of lower overall ion intensity. As these two complexes are isomeric, the different ATDs are attributed solely to differences of Ω_{exp}. Also listed are the ATDs of the sodiated saccharide dimers, where differences between all saccharide dimers are apparent. The difference in ATD of $[(Raf)_2Na^+]$ and $[(Pan)_2Na^+]$ are between 4.9% and 5.4% while the differences in ATD of $[(Sta)_2Na^+]$ and $[(Mal)_2Na^+]$ are between 1% and 1.3%. This suggests that although the unbound, sodiated isomeric saccharides have non-distinguishable ATDs, the bonding network that exists within the dimer state is different, and could potentially be used as a means to determine the identity of a saccharide.

Table 4.2 Summary of arrival time distributions

	Arrival time (ms)
$[FLEEL]H^+$	3.16 ± 0.03
$[FLEEV]H^+$	3.05
$[Raf]Na^+$	2.22
$[Pan]Na^+$	2.25 ± 0.03
$[Raf]_2Na^+$	3.88
$[Pan]_2Na^+$	4.08 ± 0.01
$[(Raf)(FLEEL)]H^+$	5.06
$[(Pan)(FLEEL)]H^+$	5.06
$[(Raf)(FLEEV)]H^+$	4.99
$[(Pan)(FLEEV)]H^+$	4.94
$[Sta]Na^+$	2.77
$[Mal]Na^+$	2.77
$[Sta]_2Na^+$	5.30 ± 0.04
$[Mal]_2Na^+$	5.23 ± 0.03
$[(Sta)(FLEEL)]H^+$	5.96
$[(Mal)(FLEEL)]H^+$	5.82
$[(Sta)(FLEEV)]H^+$	5.89
$[(Mal)(FLEEV)]H^+$	5.54

The IMS findings explain the RRKM E_0 values for complex dissociation. $[(Raf)(FLEEL)H^+]$ and $[(Pan)(FLEEL)H^+]$ have very similar ATDs and E_0 values; 0.64 eV and

0.63 eV respectively. [(Sta)(FLEEL)H$^+$] and [(Mal)(FLEEL)H$^+$] have different ATDs and different E_0 values; 0.66 eV and 0.57 eV respectively. This again is evidence of the relationship between conformation and energetics. In order to further probe this conformational difference, the structures were studied using a MM/MD-SA approach (Figure 4-7).

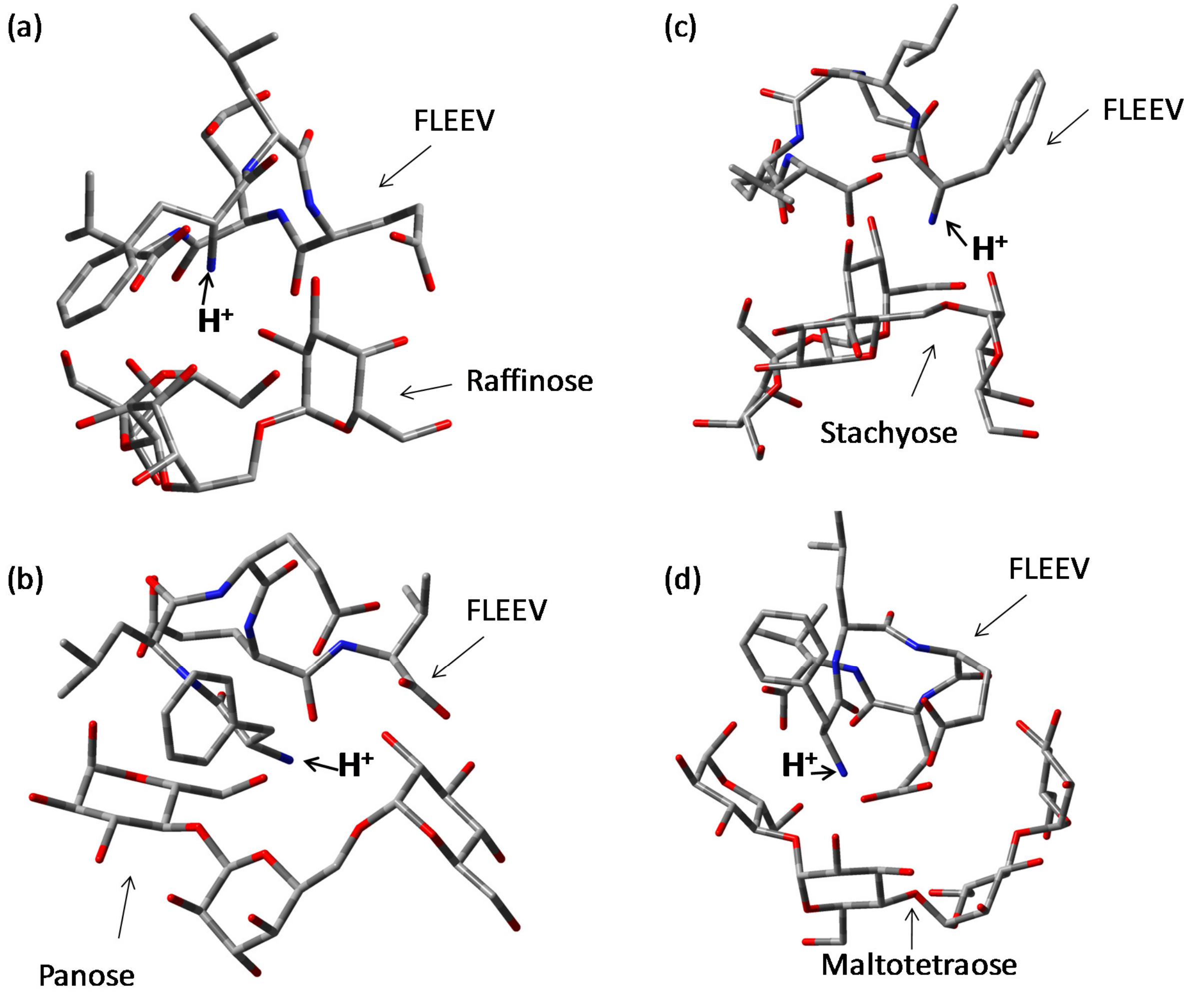

Figure 4-7 Low energy MD conformations of [(saccharide)(FLEEV)H$^+$]
Lowest energy conformations of obtained using MD-simulated annealing (SA) for (FLEEL)H$^+$ complexes with (a) Raf, (b) Pan, (c) Sta and (d) Mal. Site of protonation was assigned to N-terminus nitrogen of peptide.

In the low energy MD structures, the polar saccharide orients its oxygen atoms to interact with the protonated N-terminal of the peptide, maximizing the number of ionic hydrogen bonds.

[(Raf)(FLEEV)H$^+$] and [(Pan)(FLEEV)H$^+$] complexes are quite similar in structure, but a major change in conformation is evident between the [(Sta)(FLEEV)H$^+$] and [(Mal)(FLEEV)H$^+$] complexes. For [(Sta)(FLEEV)H$^+$] (Figure 4-7c), the Sta adopts a 'concave' conformation towards the peptide, and interaction is focused on the protonated N-terminal of the peptide and the central moieties of the saccharide. Conversely, [(Mal)(FLEEV)+H$^+$] (Figure 4-7d) adopts a 'convex' conformation towards the peptide, and appears to form limited ionic hydrogen bonds with the protonated N-terminal and also neutral hydrogen bonds with other portions of the peptide. These same conformational features are also present in the corresponding saccharide/FLEEL complexes. While each hydrogen bond adds to the overall dissociation energy of the complex, ionic hydrogen bonds are stronger than neutral hydrogen bonds and if the stability of a complex is based predominately upon hydrogen bonds, the presence of a few ionic hydrogen bonds could lead to greater stabilization than many neutral hydrogen bonds.

MM/MD-SA is a powerful tool in connecting energetic measurements with conformational properties, but unless confirmed experimentally, MM/MD-SA results may not be representative of the true conformations present in the experiment. Therefore, it is beneficial to compare the Ω_{exp} with Ω_{theo} of MM/MD-SA structures. Figure 4-8 shows the Ω_{exp} and Ω_{theo} of all eight complexes; in all cases, the Ω_{theo} underestimates Ω_{exp}.

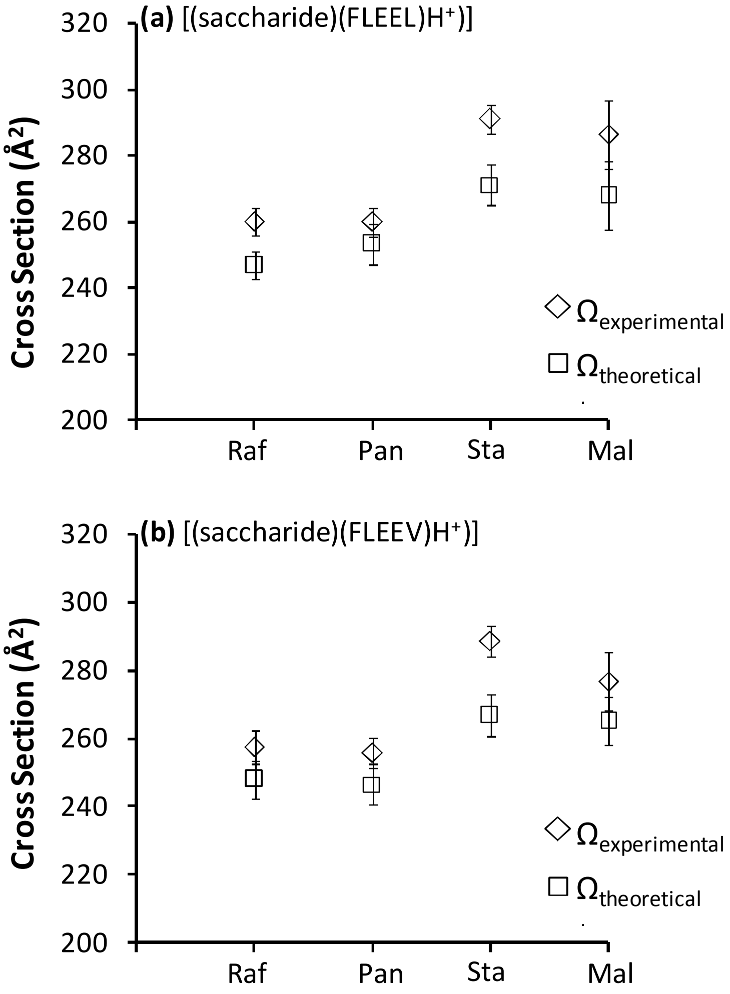

Figure 4-8 Experimental and theoretical cross sections of saccharide peptide complex Experimental cross sections (◊) and theoretical cross sections (□) for (a) [(saccharide)(FLEEL)+H^+] and (b) [(saccharide)(FLEEV)+H^+] complexes.

This underestimation could be the result of the fact that the calibrants used to correlate ATD with cross section were secondary calibrants. However, the relative trends between the two measurements are very similar; for example, theoretical and experimental cross sections for both FLEEL and FLEEV complexes identify the [(Sta)(FLEEV)+H^+] complex as being larger than [(Mal)(FLEEV)H^+]. This attests to the effective identification of low-energy conformations of small-mid size non-covalent complexes using MM/MD-SA.

4.7 Conclusions

Non-specific interactions between peptides FLEEL and FLEEV with Raf, Pan, Sta and Mal were examined with ESI-MS, MS/MS, IMS and MM/MD-SA. Differences in E_0 for the dissociation of saccharide/peptide complexes could not be directly related to the proportion of bound to unbound peptide observed using ESI-MS. However, differences in E_0 were found to be highly correlated with the structure of the complexes as calculated with MD and measured with IMS. Complexes containing tri-saccharides exhibited similar E_0 values and also similar conformations, however the tetra-saccharide containing complexes were found to have different E_0 values of dissociation and likewise, different conformations.

4.8 References

1. Richard D. Smith; Karen J. Light-Wahl; Brian E. Winger, Loo, J. A. Preservation of non-covalent associations in electrospray ionization mass spectrometry: Multiply charged polypeptide and protein dimers. Org. Mass Spectrom. 27, 10 (1992)
2. Burkitt, W. I.; Derrick, P. J.; Lafitte, D., Bronstein, I. Protein-ligand and protein-protein interactions studied by electrospray ionization and mass spectrometry. Biochem Soc. Trans. 31, 4 (2003)
3. Kitova, E. N.; Bundle, D. R., Klassen, J. S. Evidence for the Preservation of Specific Intermolecular Interactions in Gaseous Protein−Oligosaccharide Complexes. J. Am. Chem. Soc. 124, * (2002)
4. Kitova, E. N.; Wang, W.; Bundle, D. R., Klassen, J. S. Retention of Bioactive Ligand Conformation in a Gaseous Protein−Trisaccharide Complex. J. Am. Chem. Soc. 124, * (2002)
5. Kitova, E. N.; Bundle, D. R., Klassen, J. S. Thermal Dissociation of Protein−Oligosaccharide Complexes in the Gas Phase: Mapping the Intrinsic Intermolecular Interactions. J. Am. Chem. Soc. 124, 11 (2002)
6. Wang, W.; Kitova, E. N., Klassen, J. S. Influence of Solution and Gas Phase Processes on Protein−Carbohydrate Binding Affinities Determined by Nanoelectrospray Fourier Transform Ion Cyclotron Resonance Mass Spectrometry. Anal. Chem. 75, 10 (2003)
7. Kitova, E. N.; Kitov, P. I.; Paszkiewicz, E.; Kim, J.; Mulvey, G. L.; Armstrong, G. D.; Bundle, D. R., Klassen, J. S. Affinities of Shiga toxins 1 and 2 for univalent and oligovalent Pk-trisaccharide analogs measured by electrospray ionization mass spectrometry Glycobiology 17, 10 (2007)
8. Dingle, T.; Wee, S.; Mulvey, G. L.; Greco, A.; Kitova, E. N.; Sun, J.; Lin, S.; Klassen, J. S.; Palcic, M. M.; Ng, K. K. S., Armstrong, G. D. Functional properties of the carboxy-terminal host cell-binding domains of the two toxins, TcdA and TcdB, expressed by Clostridium difficile. Glycobiology 18, 8 (2008)
9. Wang, W.; Kitova, E. N., Klassen, J. S. Nonspecific Protein Carbohydrate Complexes Produced by Nanoelectrospray Ionization. Factors Influencing Their Formation and Stability. Anal. Chem. 77, 11 (2005)
10. Sun, J.; Kitova, E. N.; Wang, W., Klassen, J. S. Method for Distinguishing Specific from Nonspecific Protein Ligand Complexes in Nanoelectrospray Ionization Mass Spectrometry. Anal. Chem. 78, 8 (2006)

11. Babine, R. E., Bender, S. L. Molecular Recognition of Protein−Ligand Complexes: Applications to Drug Design. Chem. Rev. 97, 113 (1997)

12. Smith, D. P.; Knapman, T. W.; Campuzano, I.; Malham, R. W.; Berryman, J. T.; Radford, S. E., Ashcroft, A. E. Deciphering drift time measurements from travelling wave ion mobility spectrometry-mass spectometry studies. Eur. J. Mass Spectrom. 15, 17 (2009)

13. Renaud, J. B.; Martineau, E.; Mironov, G. G.; Berezovski, M. V., Mayer, P. M. The collaborative role of molecular conformation and energetics in the binding of gas-phase non-covalent polymer/amine complexes. PCCP Accepted Oct (DOI:10.1039/C1CP22936B), (2011)

14. Mayer, P. M., Martineau, E. Gas-phase binding energies for non-covalent Ab-40 peptide/small molecule complexes from CID mass spectrometry and RRKM theory. Phys. Chem. Chem. Phys. 13, 8 (2011)

15. Case, D. A.; Darden, T. A.; III, T. E. C.; Simmerling, C. L.; Wang, J.; Duke, R. E.; Luo, R.; Merz, K. M.; Pearlman, D. A.; Crowley, M.; Walker, R. C.; Zhang, W.; Wang, B.; Hayik, S.; Roitberg, A.; Seabra, G.; Wong, K. F.; Paesani, F.; Wu, X.; Brozell, S.; Tsui, V.; Gohlke, H.; Yang, L.; Tan, C.; Mongan, J.; Hornak, V.; Cui, G.; Beroza, P.; Mathews, D. H.; Schafmeister, C.; Ross, W. S., Kollman, P. A. AMBER 9. University of California, San Francisco, CA (2006)

16. Wang, J.; Wolf, R. M.; Caldwell, J. W.; Kollman, P. A., Case, D. E. Development and Testing of a General Amber Force Field. J. Comput. Chem. 25, 17 (2004)

17. Wilson, S. R., Cui, W. Applications of Simulated Annealing to Peptides. Biopolymers 29, 10 (1990)

18. Mesleh, M. F.; Hunter, J. M.; Shvartsburg, A. A.; Schatz, G. C., Jarrold, M. F. Structural Information from Ion Mobility Measurements: Effects of the Long-Range Potential. J. Phys. Chem. 100, 4 (1996)

19. Jarrold, M. J. Online: http://www.indiana.edu/ nano/Software/mobcaltxt.

20. Mironov, G. G.; Okhonin, V.; Gorelsky, S. I., Berezovski, M. V. Revealing Equilibrium and Rate Constants of Weak and Fast Noncovalent Interactions. Anal. Chem. 83, 6 (2011)

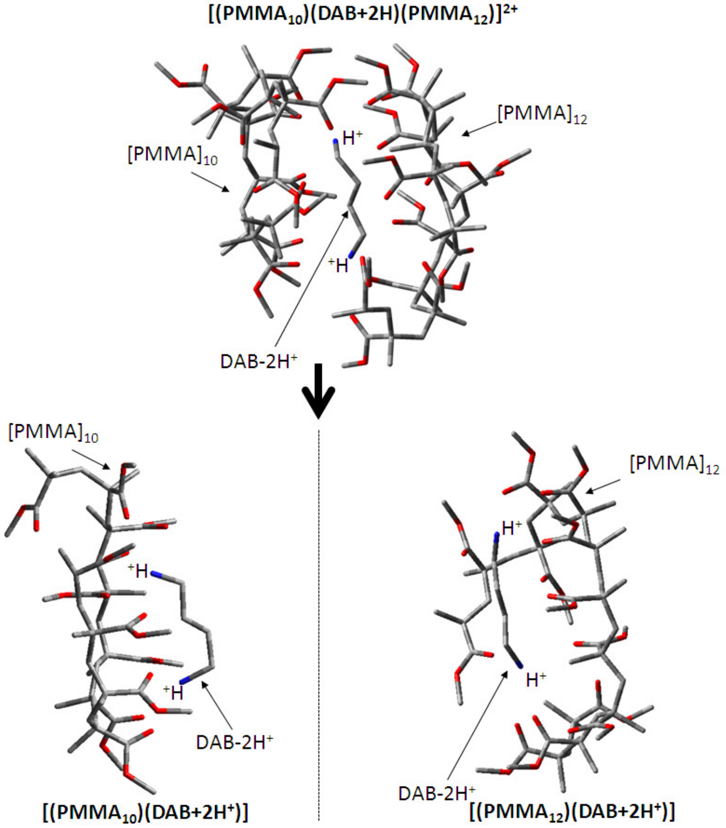
[(PMMA10)(DAB+2H)(PMMA12)]2+
[PMMA]12
H+
[PMMA]10
+H
DAB-2H+
[PMMA]10
+H
+H
DAB-2H+
[(PMMA10)(DAB+2H+)]
[PMMA]12
H+
H+
DAB-2H+
[(PMMA12)(DAB+2H+)]

5.1 Objectives

- Explore the utility of applying the kinetic method to measure the relative affinity of macromolecules for polyatomic substrates when other MS/MS based methods are not possible
- Evaluate the suitability using the simple kinetic method on larger systems and identify the factors that lead to the greatest uncertainty

5.2 Chapter acknowledgements

J.B Renaud thanks:
- Dr. Sharon Curtis for insightful commentary

5.3 Introduction

At the heart of the kinetic method is the Eyring-Polanyi equation for unimolecular dissociation:

$$\mathbf{k} = \frac{\mathbf{k_B T}}{\mathbf{h}} \cdot \mathbf{e}^{-\Delta \mathbf{H}^{\ddagger}/\mathbf{RT}} \cdot \mathbf{e}^{\Delta \mathbf{S}^{\ddagger}} \qquad \text{Equation 5-1}$$

k is the rate constant,
k_B is the Boltzmann constant,
T is the temperature, h is Planck's constant,
$\Delta H^{\ddagger}$ is the enthalpy of activation,
R is the gas constant, and
$\Delta S^{\ddagger}$ is the entropy of activation.

This links the observed rate constant to the reaction activation energy and entropy. When one considers the dissociation of a complex consisting of two molecules, A and B, sharing a charged substrate, such as a proton, metal ion, alkyl cation or an electron, the competing dissociation channels of the complex can be illustrated as:

$$\mathbf{A(substrate) + B \overset{(1)}{\leftarrow} Complex \overset{(2)}{\rightarrow} B(substrate) + A} \qquad \text{Equation 5-2}$$

The relative rate constants for channels 1 and 2 can then be expressed as:

$$\mathbf{ln}\left(\frac{\mathbf{k_1}}{\mathbf{k_2}}\right) = -\frac{\left(\Delta \mathbf{H}_1^{\ddagger} - \Delta \mathbf{H}_2^{\ddagger}\right)}{\mathbf{RT}} - \frac{\Delta(\Delta \mathbf{S}^{\ddagger})}{\mathbf{R}} \qquad \text{Equation 5-3}$$

$\Delta H_1^{\ddagger}$ and $\Delta H_2^{\ddagger}$ are the enthalpy of activation for channels 1 and 2, respectively, and $\Delta(\Delta S^{\ddagger})$ is the difference in the activation entropies between the two channels.

This difference in enthalpies of activation, provided there is no reverse-energy barrier in the dissociation reactions, can be equated to differences in the desired thermodynamic property of the two molecules (proton affinities, metal ion affinities, etc…).

When the dissociation of this complex is observed in the mass spectrometer, the relative peak intensities (I_1/I_2) of the two possible product ions are related to the relative rate constants of the two processes, and thus the equation can be re-written as:

$$\mathbf{ln}\left(\frac{I_1}{I_2}\right) = -\frac{\left(\Delta H_1^{\ddagger} - \Delta H_2^{\ddagger}\right)}{RT} - \frac{\Delta(\Delta S^{\ddagger})}{R} \qquad \text{Equation 5-4}$$

When the system involves a gas-phase complex in the high-vacuum of a mass spectrometer, it is generally not possible to associate a particular temperature to the experiment, unless special measures are taken such as those related to high pressure mass spectrometry [1, 2] or blackbody infrared radiative dissociation (BIRD) experiments [3-6]. Thus the temperature in the above equation is replaced by an "effective" temperature, T_{eff}:

$$\mathbf{ln}\left(\frac{I_1}{I_2}\right) = -\frac{\left(\Delta H_1^{\ddagger} - \Delta H_2^{\ddagger}\right)}{RT_{eff}} - \frac{\Delta(\Delta S^{\ddagger})}{R} \qquad \text{Equation 5-5}$$

Vekey and Drahos have related this effective temperature to the description of the internal energy distribution of the population of dissociating ensemble of complexes [7] "as it is clearly not related to the internal energy distribution of the entire ensemble of dissociating and non-dissociating complexes".

Extraction of the $\Delta H_1^{\ddagger}$ - $\Delta H_2^{\ddagger}$ term in the equation 5-5 requires information on the $\Delta(\Delta S^{\ddagger})$ term. The simplest assumption to make is that the similarity of the two competing channels means that their respective activation entropies are similar, and thus $\Delta(\Delta S^{\ddagger}) \approx 0$. Using this assumption allows one to directly relate the relative peak intensities for the two dissociation pathways to the difference in thermodynamic $\Delta H_1^{\ddagger}$ - $\Delta H_2^{\ddagger}$. This simplest version of the kinetic method has been used extensively to determine proton affinities [8-10] as well as relative affinities for interesting substrates such as halogen cations [11] and isocyanate cations [12].

Often the approximation of $\Delta(\Delta S^{\ddagger}) \approx 0$ is not true [13] and led to extended kinetic methods which are able to assess the entropic contribution [14]. Wesdemiotis and co-workers [15, 16] measured the PA of different peptides by first measuring the natural logarithm of the branching ratio between the peptide of study (B), and numerous references bases that were structurally similar amongst themselves (B_i). Plotting $\ln(B/B_i)$ over the known proton affinities of the reference bases gives a line for which the slope is equal to $1/RT_{eff}$ and the intercept is the apparent gas phase basicity $(GB^{app})/RT_{eff}$ at that given T_{eff}. Doing this at different collision conditions then allowed for a second plot of $(GB^{app})/RT_{eff}$ vs. $1/RT_{eff}$ which allows for the PA and the entropy of protonation to be calculated via the slope and intercept, respectively. Armentrout pointed out that there is a flaw of this method based on the correlation between the apparent free energy term and the T_{eff}. Armentrout suggested that a more appropriate treatment for the extended method would be obtained by plotting $\ln(B/B_i)$ over $[PA(B_i) - PA^{avg}(B_i)]$ [17]. The intercept is now $GB^{app}(B\text{-}PA^{avg}(B_i))$ and the slope would remain $1/RT_{eff}$. When the intercept and slope are obtained at different collision conditions and plotted, the slope of the second plot now becomes PA(B) – PA avg (B_i) and the $\Delta(\Delta S^{\ddagger})$ term is obtained from the intercept [17, 18]. It is also possible to attempt to define the $\Delta(\Delta S^{\ddagger})$ term in terms of $\Delta(\Delta S)$. If one assumes that the effective transition states for the two dissociation reactions lie close to the products (i.e. are "late" transition states"), then $\Delta(\Delta S^{\ddagger})$ can be replaced by the more easily obtainable, $\Delta(\Delta S)$ which can be approximated from standard statistical mechanical equations. Grabowy and Mayer explored this relationship in simple acetonitrile - alcohol proton-bound complexes with a simplified version of variational transition state theory [19]. As the alcohol grew in complexity from methanol and ethanol to n- and iso-propanol, they found this relationship broke down, with $\Delta(\Delta S^{\ddagger})$ and $\Delta(\Delta S)$ being different in the latter two cases by upwards of 45 J K^{-1} mol^{-1}.

The kinetic method has been applied to intermediate sized systems, to determine the effect of chain length upon the PA of poly-(glycines)$_n$ from n = 2-10 [20], the proton affinity of protonated peptides [21], as well as the effects of amino acid residue position upon the gas phase acidities of tetra- and penta-peptides [22, 23]. Of interest to this study is assessing the ability of the kinetic method to be applied to larger systems and to systems where the relative binding energy is for a polyatomic substrate.

Complexes studied by the kinetic method normally consist of two molecules, for which relative thermochemical information will be obtained, bridged by a substrate. In order for true relative thermochemical values to be extracted from the relative abundance of two competing dissociation channels, the vast majority of intra-complex interaction should only be between each competing molecule and the substrate. This is indeed the most likely arrangement of many examples of proton and metal bound pairs. As the size of these complexes increase, this arrangement might not remain true. For example, if it were possible to form an intact complex consisting of two non-interacting and unique biological receptors with one drug candidate in a complex, the drug would almost certainly not be completely interacting with both active site pockets simultaneously. Thus, any kinetic method measurements of these complexes would not point to the true relative affinity of each receptor for the drug.

For larger complexes and polyatomic substrates, the major topics that arise and explored herein are:

a) The suitability of the reactant ion complex for kinetic method measurements

b) The presence of a reverse activation barrier

c) The evaluation of $\Delta(\Delta S^{\ddagger})$

d) The interpretation of a relative substrate affinity ladder.

Inherent in the first question is the need for structural information to ensure that the relative activation energies of the competing channels reflects the desired relative binding affinity and not contributions from other non-desired interactions occurring within the complex. A major limitation in the evaluation of $\Delta(\Delta S^{\ddagger})$, which one could normally do with the extended versions of the kinetic method, is the general lack of reference compounds with known binding energies for polyatomic substrates.

We have investigated the use of the simple kinetic method to obtain meaningful binding energies of macromolecules for polyatomic substrates using model trimeric complexes consisting of two poly(methylmethacrylate) oligomers bound to a doubly protonated diaminoalkane, denoted $[(PMMA_a)(DAA+2H)(PMMA_b)]^{2+}$. If the questions about the applicability of the kinetic method listed above could be answered, it should be possible to construct a relative affinity allowing the effects of polymer length, and substrate structure upon binding affinity to be explored.

Chemicals and reagents

PMMA (Mw: 1460, Mw/Mn : 1.07) was purchased from Polymer Laboratories (Amherst, MA, USA). PMMA concentrations of 0.1 mg L^{-1} were mixed in a 1:1 ratio with either diamino(butane, hexane or decane) in methanol. Formic acid was added to give a final solution of 0.1% formic acid. Cross section calibrants, ubiquitin, myoglobin and lysozme were purchased from Sigma, (St. Louis).

ESI-MS, MS/MS

Electrospray ionization mass spectrometry (ESI-MS) and tandem mass spectrometry (ESI-MS/MS) measurements were performed on a Waters Q-TOF 1 with MassLynx 4.1 for analysis and data processing. The mobile phase consisted of 50% methanol and 50% acetonitrile at a flow rate of 30 $\mu L \cdot min^{-1}$. The source temperature was 80˚C and the desolvation temperature was set to 150˚C. The capillary voltage was 3 kV and the cone voltage was 45 V. All mass spectra were averages of 30 scans (0.9 scan/s) from m/z 70 to 2000 in positive ion mode. The collision gas for collision-induced dissociation (CID) was argon at a pressure reading of 14 psi. ESI-MS/MS of $[(PMMA_a)(DAA+2H)(PMMA_b)]^{2+}$ complexes were obtained at intervals of 1 eV (E_{lab}) beginning at energies yielding fragments from both competitive dissociation pathways at intensities above three times the signal-to-noise and ending after the detection of secondary dissociation products. All collision energies reported in this paper are center-of-mass (E_{com}) energies and derived from E_{lab} using the equation:

$$\mathbf{E_{com}} = \mathbf{E_{lab}}\left(\frac{\mathbf{M_{Ar}}}{\mathbf{M_{Ar}+M_{ion}}}\right) \qquad \text{Equation 5-6}$$

Branching ratios across several collision energies were averaged and used to calculate thermochemical values. The errors reported are not absolute and instead represent only the minimum error arising from the standard deviation of branching ratios measured at different energy intervals.

Ion mobility spectrometry

Experimental cross sections of all complexes were measured using tryptic peptides of myoglobin, ubiquitin and lysozyme as calibrants. A Beckman PA 800 capillary electrophoresis (Beckman Coulter Inc., USA) was used to infuse analytes into a Waters Synapt G2 HDMS mass spectrometer (Waters Corp., USA) via a Micromass Capillary Electrophoresis Sprayer (Micromass UK Limited, UK) by applying a constant pressure of 1 psi. The mobile phase consisted 50:50 methanol:water mixture, introduced at a flow rate of 0.7 μL min^{-1}. Drift times of dissociation products were obtained by mass selecting in the first quadrupole and CID in the trap of the tri-wave.

Molecular mechanic/molecular dynamics simulated annealing (MD/MM-SA)

The AMBER9 program suite [24] using the Generalized AMBER force field (GAFF) [25] was used to study conformations of the complexes and the neutral polymer. Minimized energy conformations of the polymer/polyamine complexes were briefly equilibrated for 20ps (time step 1fs) at 300K before undergoing 2000 cycles of simulated annealing [26] (each 18.25 ps total, 0.5 fs time step) starting with drastic heating from 300 K to 800 K over 1.25 ps and equilibrated for 2 ps. This was followed by cooling increments of 100 K over 1 ps with 2 ps of equilibration at each temperature until 300 K was reached. The lowest energy conformation of each simulated annealing cycle was then selected to undergo subsequent rounds of simulated annealing. After each cycle, the low energy conformation was cooled to 0 K over 2 ps, minimized and potential energy measured. Theoretical cross sections of the 50 lowest structures sampled (all being < 6.3 kJ from the lowest structure energy) were measured using the trajectory method [27] in the MOBCAL program [28].

Relative binding energies were approximated by equilibrating the lowest energy MM/MD-SA structure identified above for 5 ns, (2 fs time-step) at 300K. Relative binding was taken to be the difference of [$PMMA_n(DAA+2H)^{+2}$ + $PMMA_{n-1}$] and [$PMMA_{n-1}(DAA+2H)^{+2}$ + $PMMA_n$]. Furthermore, a curve of best fit was assigned to an additive plot of the relative MM/MD potential energy as a function of oligomer length.

Theoretical Δ(ΔS) calculations

Δ(ΔS) values for the dissociation reactions were calculated by taking into account translational, rotational and vibrational contributions using statistical mechanics [19]. Vibrational frequencies were obtained from previous studies [29] but given the similarity between the repeating units of the PMMA oligomers, the $\Delta(\Delta S_{vib})$ equated to 0. $\Delta(\Delta S_{rot})$ was calculated using the three moments of inertia derived from the lowest energy MM/MD structures.

5.5 Results and discussion

For brevity, diaminoalkane, 1,4-diaminobutane, 1,6-diaminohexane, 1,10-diaminodecane and dihydrogen terminated poly(methylmethacrylate) will be denoted as DAA, DAB, DAH, DAD and PMMA respectively.

The System of Study

Analysis of synthetic polymers with mass spectrometry is a common practice [30] and as most synthetic polymers are neutral, a charge is generally provided through adduction with a metal cation, or a protonated amine [31]. In this study, PMMA was cationized through complexation with a doubly protonated diaminoalkane; $[(PMMA_n)(DAA+2H)]^{2+}$ (Figure 5-1 a).

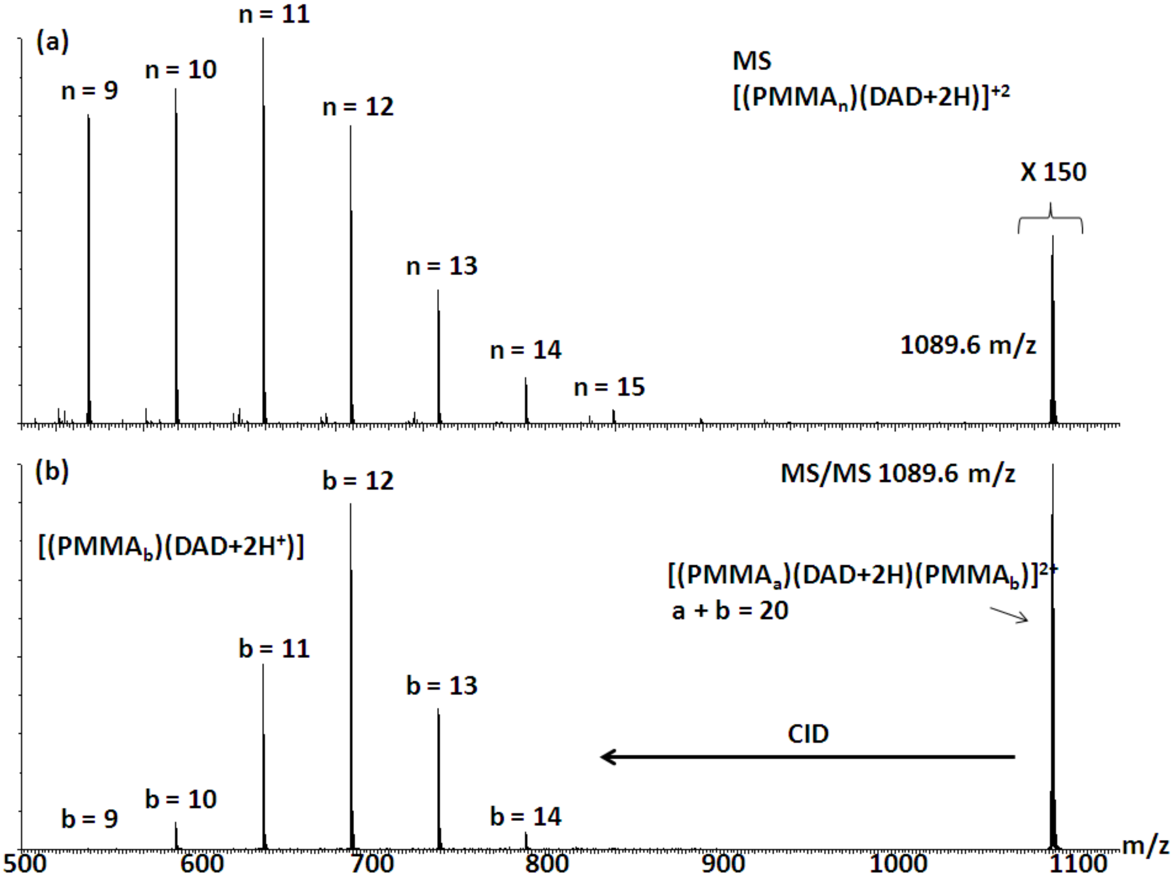

Figure 5-1 ESI (a) MS and (B) MS/MS of $[(PMMA_a)(DAA{+}2H)(PMMA_b)]^{+2}$ (a) ESI-MS of a solution containing 0.1 mg L^{-1} PMMA and equamolar DAD. The main distribution observed is $[(PMMA_n)(DAD{+}2H)]^{2+}$, at higher masses the distribution continues but is shifted by m/z 1 which represents $[(PMMA_a)(DAA{+}2H)(PMMA_b)]^{2+}$. (b) MS/MS of m/z 1089.6; $[(PMMA_a)(DAA{+}2H)(PMMA_b)]^{2+}$ where a + b = 20. Dissociation of the trimeric species shows that the reactant ion ensemble is actually composed of multiple combinations of polymer oligomers with summed repeat units equal to 20.

As the $[(PMMA_n)(DAA{+}2H)^{2+}]$ series increases in length, the isotopic distribution begins to deviate from the theoretical distribution and is eventually shifted completely by 2 mass units (Figure 5-2). This mass shift occurs because of the emergence of a trimeric; $[(PMMA_a)(DAA{+}2H)(PMMA_b)]^{2+}$. This trimeric complex differs in mass from the two-component complex $[(PMMA_n)(DAA{+}2H)]^{2+}$ because of two additional hydrogen atoms as endgroups.

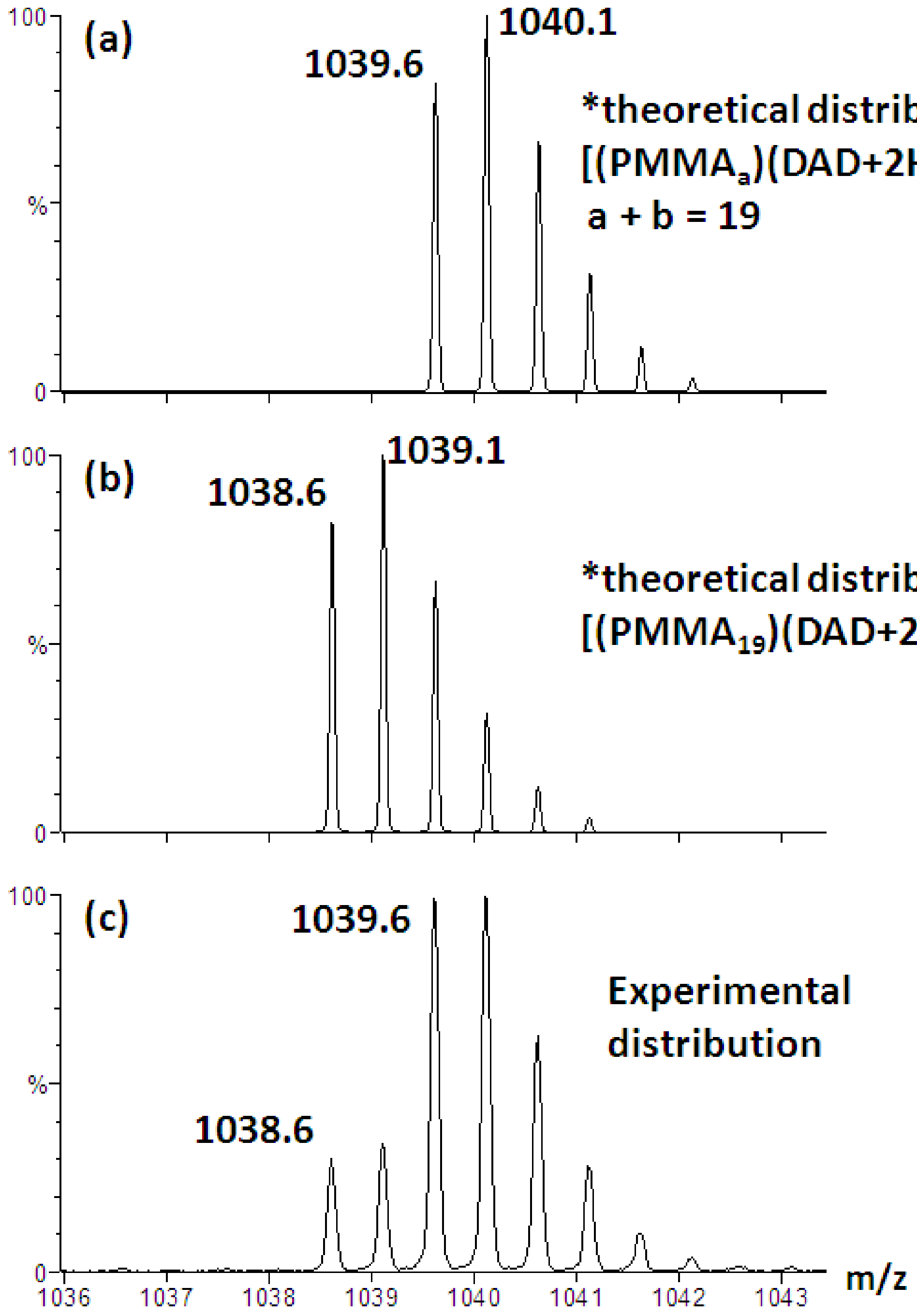

Figure 5-2 Theoretical isotopic distributions of PMMA complexes (a) trimeric species containing DAD and 2 PMMA oligomers, whose summed repeat units is 19 and (b) single PMMA oligomer containing 19 repeat units complexed with DAD. (c) the experimental isotopic distribution observed which shows the presence of both types of complexes. The 2 Da (1 m/z) difference observed between (a) and (b) arises from (b) having 2 additional hydrogen endgroups.

The presence of this $[(PMMA_a)(DAA+2H)(PMMA_b)]^{2+}$ complex is confirmed by collision-induced dissociation (CID) where the loss of one neutral PMMA oligomer, leaving a $[(PMMA_b)(DAA+2H)]^{2+}$ dissociation product, is observed. Figure 5-1b, shows that there are several $[(PMMA_b)(DAA+2H)]^{2+}$ dissociation products with different lengths of b, demonstrating that the reactant ion population is composed of several distinct combinations of different sized oligomers each resulting in the same mass. Many kinetics-based approaches, including fitting a breakdown diagram with a theoretical RRKM derived breakdown curve [32, 33] would not be applicable in this case, owing to the reactant ion being a composite of several distinct species. However, the kinetic method can be used to obtain insight into the energetic properties of these systems providing there are two competing dissociation channels.

Assessing the suitability of the reactant ion complex for kinetic method measurements

$[(PMMA_a)(DAA+2H)(PMMA_b)]^{2+}$ could dissociate to either (1) $[(PMMA_a)(DAA+2H)]^{2+}$ + $(PMMA_b)$ or (2) $[(PMMA_b)(DAA+2H)^{2+}$ + $(PMMA_a)$. This is interesting as there are two possible dissociation channels upon CID; however, very rarely are both observed (Figure 5-1b). In this system, both channels are observed only for complexes containing PMMA oligomers of very similar length; $[(PMMA_a)(DAA+2H)(PMMA_b)]^{2+}$ when $|b - a| \leq 2$. For example, in Figure 5-1b, the total number of PMMA repeat units is 20 and $[(PMMA_b)(DAA+2H)]^{2+}$ product ions are observed for $9 \leq b \leq 14$. The fragment ions $[(PMMA_9)(DAA+2H)]^{2+}$ and $[(PMMA_{11})(DAA+2H)]^{2+}$ are competing product ions from the same parent ion because their repeat units sum to 20. MM/MD-SA of the trimeric complexes identified low energy conformations by which the doubly protonated diaminoalkane substrate is ‘sandwiched’ between the two PMMA oligomers and appears to be very equally shared between the two polymers. Examples of this are shown in Figure 5-3 and Figure 5-4.

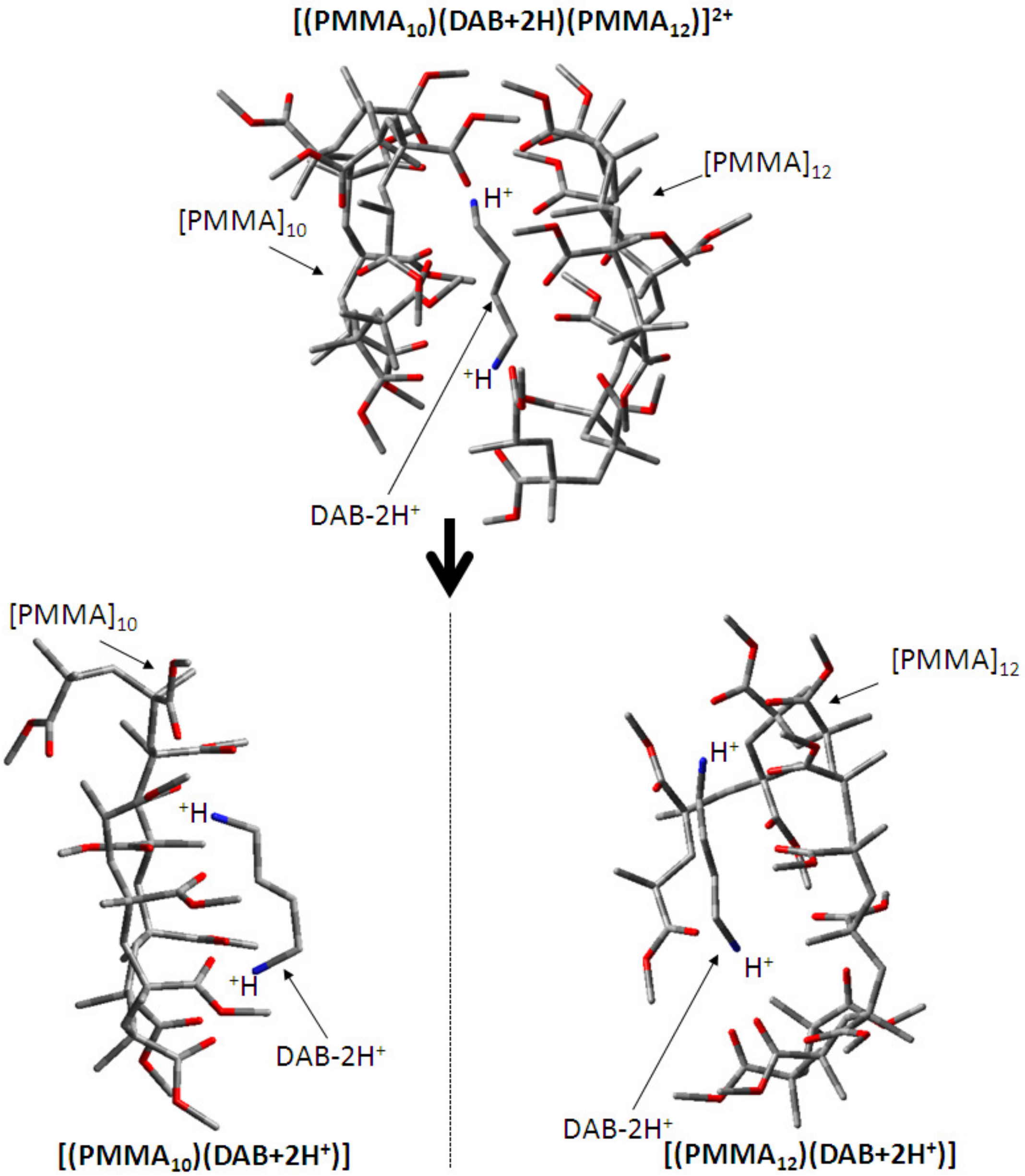

Figure 5-3 Low energy MD structures of[(PMMA$_{10}$)(DAB+2H)(PMMA$_{12}$)]^2 complexes (a) Low energy conformations of [(PMMA$_{10}$)(DAB+2H)(PMMA$_{12}$)]$^{2+}$ obtained by MM/MD-SA. The lowest energy structures were ones in which the di-protonated amine was equally shared by both polymeric species.(b) Low energy conformations of dissociation products possible from both channels.

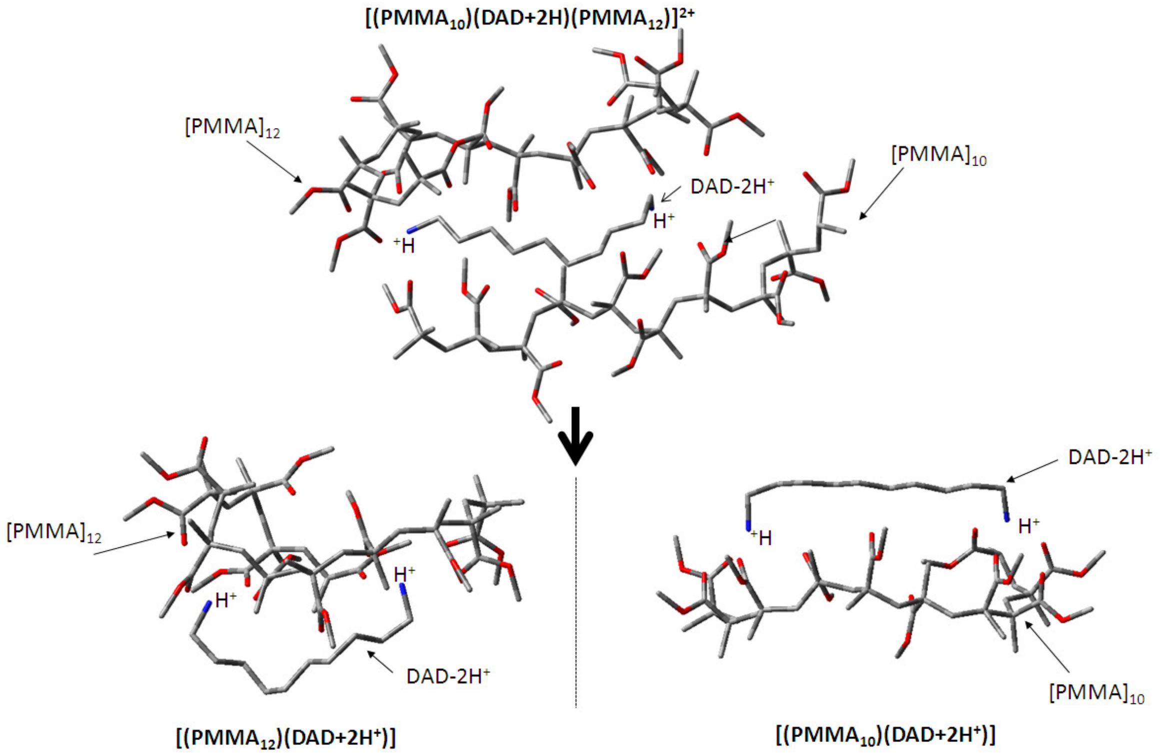

Figure 5-4 Low energy MD structures of $[(PMMA_{10})(DAD+2H)(PMMA_{12})]^{2}$complexes (a) Low energy conformations of $[(PMMA_{10})(DAD+2H)(PMMA_{12})]^{2+}$ obtained by MM/MD-SA. The lowest energy structures were ones in which the di-protonated amine was equally shared by both polymeric species.(b) Low energy conformations of dissociation products possible from both channels.

Other arrangements in which the substrate was not equally shared gave higher MD energies and within the MM/MD-SA simulation would either dissociate or rearrange into the shared substrate arrangement. This suggests that the measured doubly protonated, polyatomic substrates are nearly equally shared between the two polymers. To validate the structures obtained with MM/MD-SA, the collision cross sections of the theoretical structures (Ω_{theo}) were compared to experimental collision cross sections (Ω_{exp}) obtained with travelling wave-ion mobility. For the complex $[(PMMA_{10})(DAB+2H)(PMMA_{12})]^{2+}$ shown in Figure 5-3, the Ω_{theo} is 414 ± 7 Å^{2} and the Ω_{exp} is 411 ± 14 Å^{2}. The lowest energy structure for $[(PMMA_{10})(DAD+2H)(PMMA_{12})]^{2+}$ shown in Figure 5-4 was found to have a Ω_{theo} of 448 ± 12 Å^{2} and a Ω_{exp} of 435 ± 15 Å^{2}. This comparison is not absolutely definitive as small conformational differences could lead to a Ω_{exp} within this range but it does provide a certain degree of experimental validation to the computationally obtained structures.

Predicting the presence of a reverse activation barrier

One of the main assumptions of the kinetic method is the lack of a reverse activation barrier. The presence of multiple charges could greatly affect the viability of the kinetic method depending on the type of dissociation pathway present. In a theoretical complex containing two charges, partitioning of the charges among the different dissociation products will typically give rise to a reverse activation barrier (E_{rev}), as was previously shown by Fenselau who investigated the gas-phase basicity of protonated bradykinin with the kinetic method using doubly protonated complexes that consisted of a peptide and a reference base [21].

In this study, $[(PMMA_a)(DAA+2H)(PMMA_b)]^{2+}$, when activated by CID, loses a neutral polymer oligomer. Fenselau [21] demonstrated that when the dissociation pathway involved loss of a neutral reference base, leaving a doubly protonated peptide, no noticeable effects of peak broadening (that would arise from a reverse activation barrier) were observed in kinetic energy release spectra. Examination of the reactant complex structure and product structures suggests that there is no significant structural rearrangement is required for dissociation suggesting a lack of, or modest reverse activation barrier. Therefore, the relative activation energies of the two dissociating channels should relate to the relative binding energies of the double protonated diaminoalkane substrates to the PMMA oligomers.

The evaluation of $\Delta(\Delta S^{\ddagger})$

In systems where reference compounds with known thermochemical affinity values for a substrate are available, extended versions of the kinetic method can be used to provide entropic corrections to the measured ($\Delta H_1^{\ddagger}$ -$\Delta H_2^{\ddagger}$) term. When there are no suitable reference compounds available this is not possible, and therefore it is critical that either $\Delta(\Delta S^{\ddagger}) \approx 0$ or can be independently calculated. If reliable details about the structure of the reactant ion complex and product complexes are known, it is possible to assess if the transition pathway for dissociation of the non-covalent complex requires significant rearrangement. In Chapter 3, structures of dimeric $[(DAA+2H)(PMMA_n)]^{2+}$ ions generated via ESI-MS were determined using MM/MD-SA and validated with ESI-IMS-MS [33]. Shown in Figure 5-5 are the arrival time distributions of a number of ESI-MS generated $[(PMMA_n)(DAA+2H)]^{2+}$ (Figure 5-5a) complexes as well as $[(PMMA_b)(DAA+2H)]^{2+}$ (Figure 5-5b) complexes generated after CID of the reactant trimeric complex (where n = b).

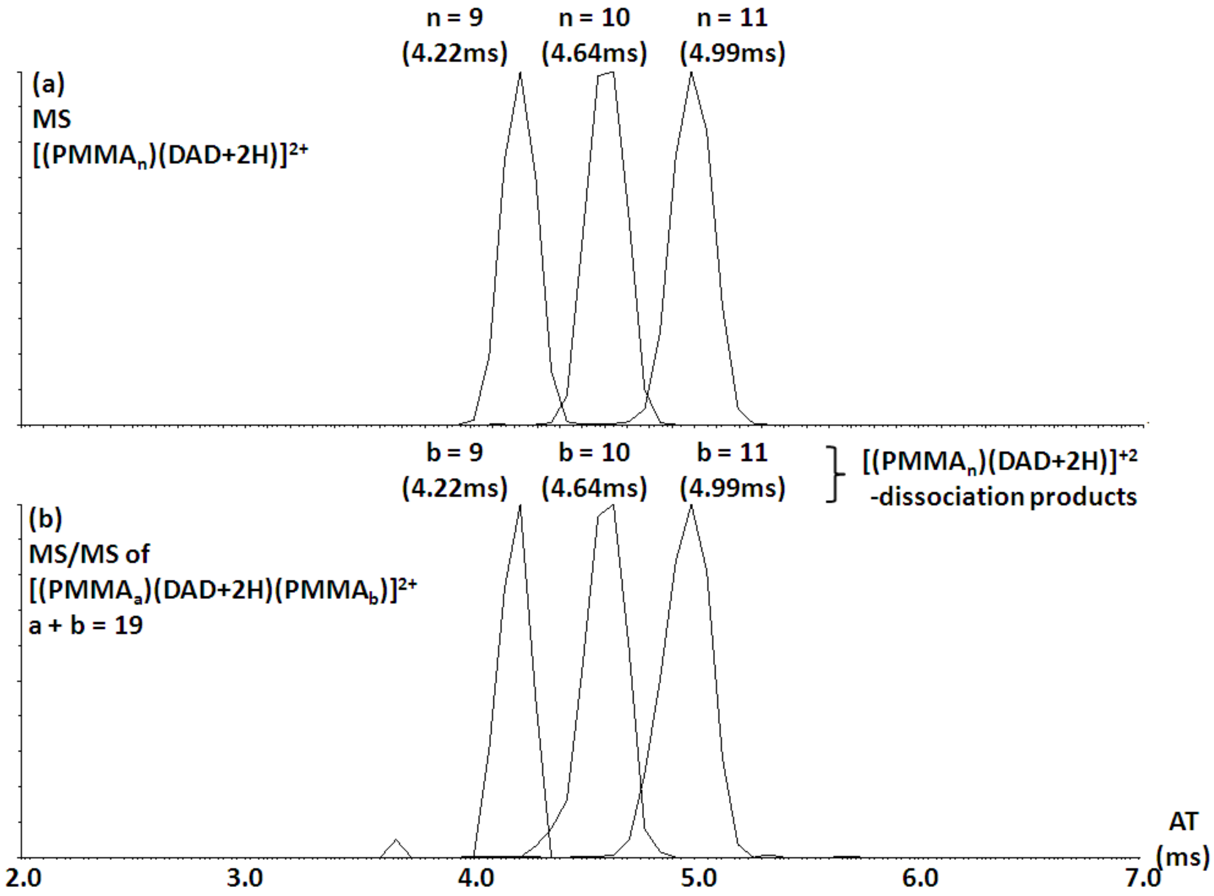

Figure 5-5 Drift times of $[(PMMA_n)(DAD+2H)]^{2+}$ reactant and product ions

a) Drift times of $[(PMMA_n)(DAD+2H)]^{2+}$ arising from ESI-MS (b) drift times of the $[(PMMA_b)(DAD+2H)]^{2+}$ dissociation products from MS/MS of $[(PMMA_a)(DAD+2H)(PMMA_b)]^{2+}$ prior to the ion mobility cell

For the example in Figure 5-5, as these two species are identical in terms of composition, any difference in drift time would presumably be a result of different conformations. For the complexes investigated in this study the Ω_{exp} are identical regardless if the originate from ESI-MS or ESI-MS/MS, suggesting a similar conformation. This comparison does not provide absolute proof of that there are no major rearrangements occurring during the dissociation, but it does quickly validate that there is no significant difference in the conformations of complexes formed via ESI-MS and ESI-MS/MS and thus the MM/MD $[(PMMA_n)(DAA+2H)]^{2+}$ structures are a valid representation of the dissociation products of $[(PMMA_a)(DAA+2H)(PMMA_b)]^{2+}$. In addition, MM/MD-SA of $[(PMMA_n)(DAA+2H)]^{2+}$ (Figure 5-3, Figure 5-4) result in low energy structures are nearly identical to their arrangement within the reactant trimeric complex $[(PMMA_a)(DAA+2H)(PMMA_b)]^{2+}$. These results strongly suggest that upon dissociation of the $[(PMMA_a)(DAA+2H)(PMMA_b)]^{2+}$ complex, no significant rearrangement takes place and therefore the approximation of $\Delta(\Delta S^{\ddagger}) \approx \Delta(\Delta S)$ is suitable.

Using the structures obtained with MM/MD-SA, and accounting for translational, rotational and vibrational contributions, the $\Delta(\Delta S)$ was calculated for the dissociation of $[(PMMA_a)(DAA+2H)(PMMA_b)]^{2+}$ ($b = a + 1$) for the three different diaminoalkane substrates (Figure 5-6). What is shown is that $\Delta(\Delta S)$ for these competing dissociation channels are zero within the estimated error. Therefore, so long as the approximation of $\Delta(\Delta S^{\ddagger}) \approx \Delta(\Delta S)$ is acceptable, it is possible to eliminate the entropic term of equation 5-5 and relate the branching ratios directly to PMMA affinities for the substrates.

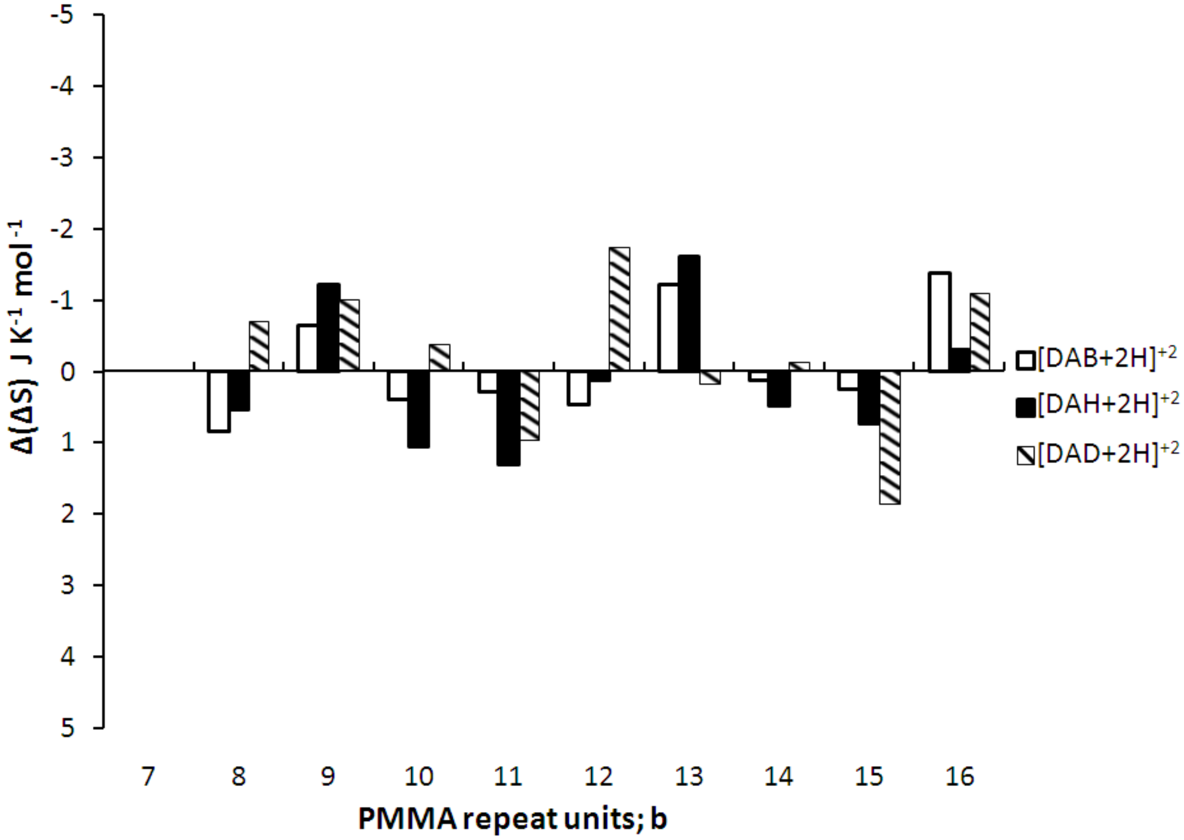

Figure 5-6 $\Delta(\Delta S)$ of competing dissociation channels for $[(PMMA_a)(DAD+2H)(PMMA_b)]^{2+}$ $\Delta(\Delta S)$ of competing dissociation channels for $[(PMMA_a)(DAD+2H)(PMMA_b)]^{2+}$ when b = a + 1 were approximated by means of statistical thermodynamics, where translational, rotational and vibrational contributions were considered. Structures and vibrational frequencies used were obtained using MM/MD-SA from previous work.[33]

Building a relative affinity ladder for different lengths of PMMA for $[DAA+2H]^{+2}$

Figure 5-7 shows an additive plot of the branching ratios for $\ln(I_{PMMAn+1}/I_{PMMAn+1})$. The trends observed here show a continuous and 'smooth' increase in the apparent affinity, with the magnitude of the branching ratio diminishing with increasing size.

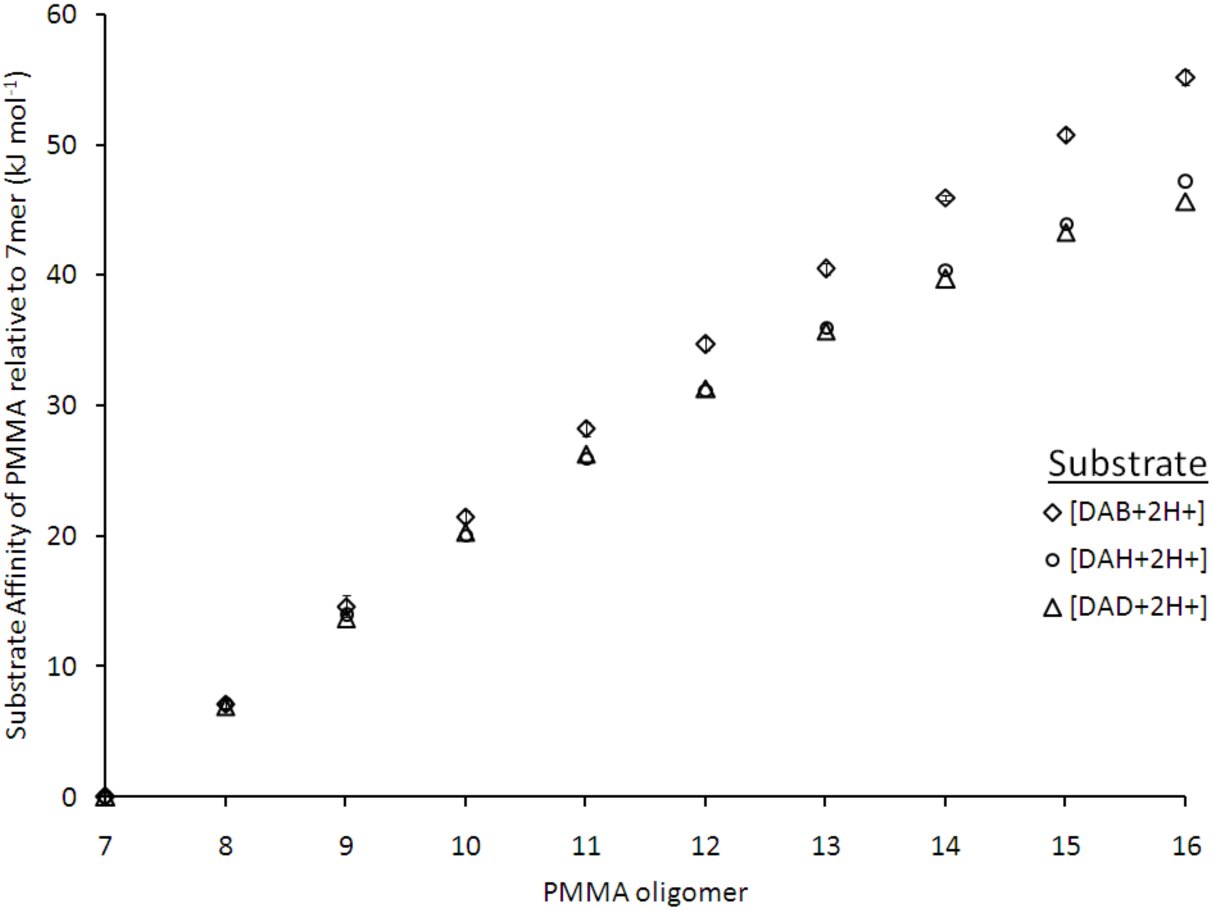

Figure 5-7 Additive plot of branching ratios; $\ln(I_{PMMAn+1}/I_{PMMAn})$
Additive plot of branching ratios; $\ln(I_{PMMAn+1}/I_{PMMAn})$ for substrates $(DAB+2H)^{+2}$, $(DAH+2H)^{+2}$, and $(DAD+2H)^{+2}$. An anchor point of 0 assigned to lowest affinity polymer; $PMMA_7$.

The magnitude of the relative affinity for the smallest substrate, $(DAB+2H)^{+2}$, is larger in comparison with the larger substrates, $(DAH+2H)^{+2}$ and $(DAD+2H)^{+2}$, which are themselves very similar. In some cases, it was possible to obtain branching ratios for $\ln(I_{PMMAn+2}/I_{PMMAn+1})$ which demonstrated good self-consistency of the additive branching ratios (Table 5-1,Table 5-2).

Table 5-1 Relative peak ratios, MM/MD relative binding energies and derived T_{eff} of $(DAB+2H)^{+2}$ to PMMA oligomers

$PMMA_n$	$^{a}\ln(I_{n+1}/I_n)$	$^{b}\ln(I_{n+2}/I_n)$	$^{c}E_{(MM/MD)}$ (kJ mol^{-1})	$^{d}T_{eff}$ (K)
7	0	-	0	-
8	2.9 ± 0.1	-	20 ± 2	854
9	5.9 ± 0.3	-	41 ± 2	812
10	8.6 ± 0.2	-	60 ± 3	859
11	11.3 ± 0.2	-	79 ± 4	835
12	13.9 ± 0.2	-	96 ± 5	801
13	16.2 ± 0.2	16.3 ± 0.3	112 ± 6	797
14	18.4 ± 0.4	18.4 ± 0.2	125 ± 6	715
15	20.4 ± 0.3	20.3 ± 0.4	135 ± 5	623
16	22.1 ± 0.3	22.0 ± 0.3	141 ± 7	463

[a] Additive plot of branching ratios for $[(PMMA_{n+1})(DAB+2H)]^{+2}/[(PMMA_n)(DAB+2H)]^{+2}$

[b] Additive plot of branching ratios for $[(PMMA_{n+2})(DAB+2H)]^{+2}/[(PMMA_n)(DAB+2H)]^{+2}$

[c] Additive relative MM/MD binding energies with curve of best fit applied; potential energy difference of $[(PMMA_n)(DAB+2H)^{+2} + (PMMA_{n+1})] - [(PMMA_{n+1})(DAB+2H)^{+2} + (PMMA_n)]$.

[d] T_{eff} approximation obtained by equation 7

Table 5-2 Relative peak ratios, MM/MD relative binding energies and derived T_{eff} of $(DAD+2H)^{+2}$ to PMMA oligomers

$PMMA_n$	[a]$\ln(I_{n+1}/I_n)$	[b]$\ln(I_{n+2}/I_n)$	[c]$E_{(MM/MD)}$ (kJ mol^{-1})	[d]T_{eff} (K)
7	0	-	0	-
8	2.8 ± 0.3	-	32± 2	1387
9	5.5 ± 0.2	-	58 ± 4	1166
10	8.1 ± 0.2	-	79 ± 5	965
11	10.5 ± 0.3	10.6 ± 0.5	96 ± 6	849
12	12.5 ± 0.2	12.3 ± 0.2	110 ± 7	804
13	14.3 ± 0.2	14.7 ± 0.3	120 ± 8	716
14	15.9 ± 0.3	16.1 ± 0.2	129 ± 8	646
15	17.4 ± 0.2	17.2 ± 0.2	136 ± 7	598
16	18.3 ± 0.4	-	140 ± 9	459

[a] Additive plot of branching ratios for $[(PMMA_{n+1})(DAB+2H)]^{+2}/[(PMMA_n)(DAB+2H)]^{+2}$

[b] Additive plot of branching ratios for $[(PMMA_{n+2})(DAB+2H)]^{+2}/[(PMMA_n)(DAB+2H)]^{+2}$

[c] Additive relative MM/MD binding energies with curve of best fit applied; potential energy difference of $[(PMMA_n)(DAB+2H)^{+2} + (PMMA_{n+1})] - [(PMMA_{n+1})(DAB+2H)^{+2} + (PMMA_n)]$.

[d] T_{eff} approximation obtained by equation 5-7

We have demonstrated that it is appropriate to approximate $\Delta(\Delta S^{\ddagger}) \approx \Delta(\Delta S) \approx 0$ for this system, yet in order to convert branching ratio values into energetic values using equation 5-5, the T_{eff} term must be assessed. This is very difficult given that there is a lack of reference compounds with a known substrate affinity, and of course we would not expect T_{eff} to be constant throughout the range of complexes. An immediate option for smaller systems would be to use quantum computational techniques to approximate binding affinities for select reference compounds which have previously been used in conjunction with the kinetic method [34], but because of the size of the present systems and the existence of many similar yet distinct molecular arrangements, this is not feasible.

In order to best assess the trend in T_{eff}, we have chosen an MM/MD approach. Calculating absolute binding energies this way are approximate at best, and the energy reported is highly dependent upon the force field chosen and empirical simulation settings. However, as we are seeking only the relative affinity, we could minimize the uncertainty by using the relative MM/MD binding energies. All complexes of $[PMMA_n(DAA+2H)]^{+2}$ and neutral $PMMA_n$ for n = 7-16 were equilibrated at 300 K for 5000 ps. The $\Delta E_{MM/MD}$ was calculate as the difference in between $[PMMA_n(DAA+2H)^{+2} + PMMA_{n-1}]$ and $[PMMA_{n-1}(DAA+2H)^{+2} + PMMA_n]$. To obtain insight into the behavior of T_{eff} of these systems under the experimental conditions in this study, equation 5-5 can be an approximate T_{eff} can be determined for each complex (Table 5-1).

$$\mathbf{T_{eff}} = \mathbf{\Delta E_{(MM-MD)}} \Big/ \mathbf{R\ln\left(\frac{I_{n+1}}{I_n}\right)} \qquad \text{Equation 5-7}$$

The T_{eff} term decreases as the size of $[(PMMA_a)(DAA+2H)(PMMA_b)]^{2+}$ increases, which suggests that the population distribution of the dissociating ensemble of complexes gets narrower as the size of the complexes increases.

5.6 Conclusions

In exploring the applicability of the kinetic method in determining relative binding energies of macromolecules for polyatomic substrates, we have identified the following issues:

i) The suitability of the reactant complex arrangement.

In order for the kinetic method to yield results that relate to the affinity of a molecule for a substrate, the trimeric complex must consist of a nearly equally shared substrate, and the two competing molecules should be almost completely interacting with the substrate and not each other. Using MM/MD (validated by IMS) we have shown that for $[(PMMA_a)(DAA+2H)(PMMA_b)]^{2+}$ complexes that this is true.

ii) The potential presence of a reverse activation barrier

If a reverse activation barrier is present, any measurements obtained using the kinetic method would not represent the binding energies, but instead the activation energy required to pass the transition state. The $[(PMMA_a)(DAA+2H)(PMMA_b)]^{2+}$ dissociates exclusively via the loss of a neutral PMMA oligomer and therefore, any coulombic repulsive forces arising from dissociation of two charged products are expected to be absent.

iii) The evaluation of $\Delta(\Delta S^{\ddagger})$

The relationship between $\Delta(\Delta S^{\ddagger})$ and $\Delta(\Delta S)$ was investigated through a careful comparison of the structural arrangement of the trimeric reactant ion complexes and their dissociation products. ESI-IMS was used to compare the drift times of $[(PMMA_n)(DAA+2H)]^{2+}$ arising directly from ESI-MS with complexes arising as dissociation products from $[(PMMA_a)(DAA+2H)(PMMA_b)]^{2+}$. This was followed by a statistical mechanics calculation of the $\Delta(\Delta S)$ term, which was shown to be ≈ 0.

As a function of increasing PMMA length, the affinity of the PMMA for the diaminoalkane substrates increased, with a decreasing magnitude. Lacking reference compounds and T_{eff} terms, the relative binding energies were approximated using MM/MD. These values were then used in conjunction with the measured branching ratios to obtain the trend in T_{eff} which was found to decrease as a function of the size of the trimeric complex, suggesting that the population distribution of the dissociating ensemble of complexes narrows as size increases. The largest obstacle to using the kinetic method on larger complexes is the uncertainty of ion temperature.

5.7 References

1. Szulejko, J. E., McMahon, T. B. A pulsed electron beam, variable temperature, high pressure mass spectrometric re-evaluation of the proton affinity difference between 2-methylpropene and ammonia. Int. J. Mass Spectrom. 109, 5 (1991)
2. Michael Meot-Ner, P. H., Edward P. Hunter, Frank H. Field. Bonding energies in association ions of aromatic compounds. Correlations with ionization energies. J. Am. Chem. Soc. 100, 5 (1978)
3. Price, W. D.; Schnier, P. D., Williams, E. R. Tandem mass spectrometry of large biomolecule ions by blackbody infrared radiative dissociation. Analytical chemistry 68, 859-866 (1996)
4. Schnier, P. D.; Price, W. D.; Jockusch, R. A., Williams, E. R. Blackbody infrared radiative dissociation of bradykinin and its analogues: Energetics, dynamics, and evidence for salt-bridge structures in the gas phase. Journal of the American Chemical Society 118, 7178-7189 (1996)
5. Kitova, E. N.; Bundle, D. R., Klassen, J. S. Thermal Dissociation of Protein−Oligosaccharide Complexes in the Gas Phase: Mapping the Intrinsic Intermolecular Interactions. J. Am. Chem. Soc. 124, 11 (2002)
6. Dunbar, R. C., McMahon, T. B. Activation of Unimolecular Reactions by Ambient Blackbody Radiation. Science 279, 3 (1998)
7. Drahos, L., Vékey, K. How Closely Related are the Effective and the Real Temperature. J. Mass Spectrom. 34, 5 (1999)
8. Greco, F.; Liguori, A.; Sindona, G., Uccella, N. Gas-phase proton affinity of deoxyribonucleosides and related nucleobases by fast atom bombardment tandem mass spectrometry. J. Am. Chem. Soc. 112, 4 (1990)
9. Fenselau, Z. W. a. C. Proton affinity of arginine measured by the kinetic approach. Rapd Commun. Mass Spectrom. 6, 2 (1992)
10. Holmes, J. L.; Aubry, C., Mayer, P. M. Proton Affinities of Primary Alkanols: An Appraisal of the Kinetic Method. J. Phys. Chem A 103, 4 (1999)
11. Eberlin, M. N.; Kotiaho, T.; Shay, B. J.; Yang, S. S., Cooks, R. G. Gas-Phase Cl^+ Affinities of Pyridines Determined by the Kinetic Method Using Multiple Stage (MS3) Mass Spectrometry J. Am. Chem. Soc. 116, 8 (1994)
12. Yang, S. S.; Chen, G.; Ma, S.; Cooks, R. G.; C.Gozzo, F., Eberlin, M. N. Relative carbonyl isocyanate cation $[OCNCO]^+$ affinities of pyridines determined by the kinetic method using multiple-stage (MS3) mass spectrometry. J. Mass Spectrom. 30, 9 (1995)

13. Cheng, X.; Wu, Z., Fenselau, C. Collision energy dependence of proton-bound dimer dissociation: entropy effects, proton affinities, and intramolecular hydrogen-bonding in protonated peptides. J. Am. Chem. Soc. 115, 4 (1993)

14. Wu, Z., Fenselau, C. Gas-phase basicities and proton affinities of lysine and histidine measured from the dissociation of proton-bound dimers. Rapid Commun. Mass Spectrom. 8, 3 (1994)

15. Cerda, B. A.; Hoyau, S.; Ohanessian, G., Wesdemiotis, C. Na^+ Binding to Cyclic and Linear Dipeptides. Bond Energies, Entropies of Na+ Complexation, and Attachment Sites from the Dissociation of Na^+-Bound Heterodimers and ab Initio Calculations. J. Am. Chem. Soc. 120, 11 (1998)

16. Nold, M. J.; Cerda, B. A., Wesdemiotis, C. Proton affinities of the N- and C-terminal segments arising upon the dissociation of the amide bond in protonated peptides. J. Am. Soc. Mass Spectrom. 10, 8 (1999)

17. Armentrout, P. B. Entropy Measurements and the Kinetic Method: A Statistically Meaningful Approach. J. Am. Soc. Mass Spectrom. 11, 8 (2000)

18. Hahn, I.-S., Wesdemiotis, C. Protonation thermochemistry of beta-alanine An evaluation of proton affinities and entropies determined by the extended kinetic method. Int. J. Mass Spectrom. 14 (2003)

19. Grabowy, J. A. D., Mayer, P. M. Entropy Changes in the Dissociation of Proton-Bound Complexes: A Variational RRKM Study. J. Phys. Chem A 108, 6 (2004)

20. Wu, Z., Fenselau, C. Proton affinities of polyglycines assessed by using the kinetic method. J. Am. Soc. Mass Spectrom. 3, 3 (1992)

21. Kaltashov, I. A.; Fabris, D., Fenselau", C. C. Assessment of Gas Phase Basicities of Protonated Peptides by the Kinetic Method. J. Phys. Chem. 99, 5 (1995)

22. Ren, J.; Tan, J. P., Harper, R. T. Gas-Phase Acidities of Cysteine-Polyalanine Peptides I: $A_{3,4}$CSH and HSC$A_{3,4}$. J. Phys. Chem A 113, 9 (2009)

23. Morishetti, K. K.; Huang, B. D. S.; Yates, J. M., Ren, J. Gas-Phase Acidities of Cysteine-Polyglycine Peptides: The Effect of the Cysteine Position. J. Am. Soc. Mass Spectrom. 21, 11 (2010)

24. Case, D. A.; Darden, T. A.; III, T. E. C.; Simmerling, C. L.; Wang, J.; Duke, R. E.; Luo, R.; Merz, K. M.; Pearlman, D. A.; Crowley, M.; Walker, R. C.; Zhang, W.; Wang, B.; Hayik, S.; Roitberg, A.; Seabra, G.; Wong, K. F.; Paesani, F.; Wu, X.; Brozell, S.; Tsui, V.; Gohlke, H.; Yang, L.; Tan, C.; Mongan, J.; Hornak, V.; Cui, G.; Beroza, P.; Mathews, D. H.; Schafmeister, C.; Ross, W. S., Kollman, P. A. AMBER 9. University of California, San Francisco, CA (2006)

25. Wang, J.; Wolf, R. M.; Caldwell, J. W.; Kollman, P. A., Case, D. E. Development and Testing of a General Amber Force Field. J. Comput. Chem. 25, 17 (2004)

26. Wilson, S. R., Cui, W. Applications of Simulated Annealing to Peptides. Biopolymers 29, 10 (1990)

27. Mesleh, M. F.; Hunter, J. M.; Shvartsburg, A. A.; Schatz, G. C., Jarrold, M. F. Structural Information from Ion Mobility Measurements: Effects of the Long-Range Potential. J. Phys. Chem. 100, 4 (1996)

28. Jarrold, M. F., http://www.indiana.edu/~nano/Software.html

29. Casey, J.; Alhazmi, A., Mayer, P. M. Conformation effects on the dissociation of ionized polymers. Eur. J. Mass Spectrom. 11, 6 (2005)

30. Montaudo, G., Lattimer, R. P., *Mass spectrometry of polymers*, CRC Press, 2002.

31. Alhazmi, A. M., Mayer, P. M. Protonating Polymer Oligomers in the Gas Phase to Change Fragmentation Pathways. J. Am. Soc. Mass Spectrom. 20, 6 (2009)

32. Mayer, P. M., Martineau, E. Gas-phase binding energies for non-covalent Aβ-40 peptide/small molecule complexes from CID mass spectrometry and RRKM theory. PCCP 13, 8 (2011)

33. Renaud, J. B.; Martineau, E.; Mironov, G. G.; Berezovski, M. V., Mayer, P. M. The collaborative role of molecular conformation and energetics in the binding of gas-phase non-covalent polymer/amine complexes. PCCP 14, 7 (2012)

34. Mayeux, C.; Jean-FrancoisGal; Charles, L.; Massi, L.; Maria, P.-C.; Tammiku-Taul, J.; Lohu, E.-L., Burk, P. A study of the cesium cation bonding to carboxylate anions by the kinetic method and quantum chemical calculations. J. Mass. Spectrom. 45, 7 (2010)

Chapter 6: Efficient RRKM fitting of multi-channel dissociations using branching relationships

$$\boxed{ln\left(\frac{I_A}{I_B}\right) \propto \frac{-\left(\Delta H_A^{\ddagger} - \Delta H_B^{\ddagger}\right)}{R} \cdot \frac{1}{T_i + \alpha \cdot E_{com}} + \frac{\left(\Delta S^{\ddagger}(A) - \Delta S^{\ddagger}(B)\right)}{R}}$$

6.1 Objectives

- Introduce branching relationships as constraints when fitting breakdown diagrams with RRKM theory
- Determine an empirical approach to express all dissociation channels as a function of the most intense dissociation channel
- Validate the E_0 and $\Delta S^{\ddagger}$ obtained for the dissociation of anthracene radical cation using RRKM modelling with values obtained from iPEPICO experiments.

6.2 Chapter acknowledgements

J.B Renaud thanks:

- Brandi West for sharing of iPEPICO data for the dissociation of ionized anthracene
- Sabria Mohammed and Alicia Sit for collecting and sharing experimental APCI-MS/MS data

6.3 Introduction

A common bottleneck of using computational modelling is the length of time required to complete the calculations. The RRKM fitting method that has been introduced in chapter 3 [1] contains temperature (T_i) and α variables that are altered in order to best model the effective temperature (T_{eff}) of the reactant ion as a function of collision energy (E_{com})

$$\mathbf{T_{eff} = T_i + \alpha \cdot E_{com}} \qquad \text{Equation 6-1}$$

The RRKM model also describes each dissociation channel by the entropy of activation ($\Delta S^{\ddagger}$) and the critical activation energy (E_0). Modelling a dissociation reaction with one channel will therefore have four variables that can be altered in order to obtain a theoretical breakdown curve that most closely matches an experimental breakdown diagram. Often, dissociation of an ion will occur through more than one primary channel with each channel having a unique E_0 and $\Delta S^{\ddagger}$. An increase in the total number of primary dissociation channels will therefore increase the total number of variables that can be altered to fit a breakdown diagram. This drastically increases the computational time of the calculation and introduces greater uncertainty.

As shown in chapter 5, the ratio of fragment ion intensities is related to differences in their dissociation energetics. When an ion has two competing dissociation channels: A and B, the intensity (I) of product ions from those two channels can be related to their respective rate constants (k) by:

$$\mathbf{\frac{I_A}{I_B} \approx \frac{k_A}{k_B}} \qquad \text{Equation 6-2}$$

This relationship can be substituted into the Eyring-Polanyi equation as:

$$\mathbf{\ln\left(\frac{I_A}{I_B}\right) \approx \frac{-\left(\Delta H_A^{\ddagger} - \Delta H_B^{\ddagger}\right)}{R} \cdot \frac{1}{T} + \frac{\left(\Delta S_A^{\ddagger} - \Delta S_B^{\ddagger}\right)}{R}} \qquad \text{(Equation 6-3)}$$

$\Delta H^{\ddagger}$ is the enthalpy of activation, $\Delta S^{\ddagger}$ is the entropy of activation, T is the temperature and R is the gas constant.

Equation 6-3 is similar to the simple kinetic method and can be used to determine the affinity differences of two compounds for a substrate as long as the $\Delta S^{\ddagger}$ of both compounds are equivalent. As discussed in Chapter 5, the temperature of an ion is not easily described [2] and presents the greatest uncertainty into gaining meaningful thermochemical values directly.

In conventional collision induced dissociation (CID), by acknowledging that applying greater E_{com} would increase the T_{eff} of the ion ($T_{eff} \propto E_{com}$), equation 6-3 becomes:

$$\mathbf{ln}\left(\frac{\mathbf{I_A}}{\mathbf{I_B}}\right) \propto \frac{-\left(\Delta \mathbf{H}^{\ddagger}_{\mathbf{A}} - \Delta \mathbf{H}^{\ddagger}_{\mathbf{B}}\right)}{\mathbf{R}} \cdot \frac{\mathbf{1}}{\mathbf{E_{com}}} + \frac{\left(\Delta \mathbf{S}^{\ddagger}_{\mathbf{A}} - \Delta \mathbf{S}^{\ddagger}_{\mathbf{B}}\right)}{\mathbf{R}} \qquad \text{Equation 6-4}$$

Furthermore, this can be made combined with equation 6-1 to yield:

$$\mathbf{ln}\left(\frac{\mathbf{I_A}}{\mathbf{I_B}}\right) \propto \frac{-\left(\Delta \mathbf{H}^{\ddagger}_{\mathbf{A}} - \Delta \mathbf{H}^{\ddagger}_{\mathbf{B}}\right)}{\mathbf{R}} \cdot \frac{\mathbf{1}}{\mathbf{T_i} + \alpha \cdot \mathbf{E_{com}}} + \frac{\left(\Delta \mathbf{S}^{\ddagger}(\mathbf{A}) - \Delta \mathbf{S}^{\ddagger}(\mathbf{B})\right)}{\mathbf{R}} \qquad \text{Equation 6-5}$$

$T_i + \alpha E_{com}$ is equal to the T_{eff}.

A branching ratio is obtained by measuring the ratio of fragment ion intensities at a single collision energy. Here we introduce the term, ‘branching relationship’ which is obtained by plotting the ratios of fragment ion intensities of competing primary dissociation channels as a function of $(T_i + \alpha E_{com})^{-1}$.”

Equation 6-5 proposes that the sign of the branching relationship slope and intercept would give the relative ranking of $\Delta H^{\ddagger}$ and $\Delta S^{\ddagger}$ respectively for the two competing dissociation channels. Due to the nature of the approximations made in equation 6-1 and 6-5, a branching relationship plot does not allow for the determination of relative energetic values directly.

West et al. investigated the dissociation of the anthracene radical cation with imaging photoelectron photoion conincidence spectroscopy (iPEPICO) and measured the E_0 and $\Delta S^{\ddagger}$ for two primary dissociation channels; loss of hydrogen (-H) and loss of acetylene (-C_2H_2). Ionized anthracene is not a non-covalent complex, but it has experimentally determined dissociation energetics, and RRKM calculations can be done quickly because of its small size. In order to investigate the appropriateness of equation 6- 5, a breakdown diagram and branching relationship plot of the anthracene radical cation dissociation was accomplished and results compared with those measured using iPEPICO

6.4 Materials and methods

Anthracene was purchased from Sigma Aldrich (St. Louis) and mixed with chloroform to a concentration of 0.1 mg mL^{-1}. A Micromass Quattro LC (Waters Micromass, Manchester, UK) triple quadrupole mass spectrometer equipped with a Z-spray source was used to carry out the atmospheric pressure chemical ionization - tandem mass spectrometry (APCI-MS/MS). 30 μL of sample solutions were introduced via Rheodyne syringe into a chloroform mobile phase with a flow rate of 300 μL min^{-1}. The source block and probe were held at temperatures of 150°C and 400°C respectively. The corona needle and sample cone voltage was set to 3.4 kV and 30 V respectively. CID was carried out with argon at a gas pressure of 3.2×10^{-3} mbar and laboratory frame collision energies (E_{lab}) were recorded for 30 seconds at each collision energy step. The resolution of the first quadrupole was set to unit mass resolution (17 in the Masslynx software) for all experiments. The resolution of the final quadrupole was held constant at 12 to increase the sensitivity of the APCI-MS/MS experiments.

Obtaining qualitative energetic values using branching relationships

The APCI-MS/MS breakdown diagram of anthracene$^{+\cdot}$ showed three competing, primary pathways:

Table 6-1 Primary Dissociation channels of $C_{14}H_{10}^{\cdot+}$ and iPEPICO measured dissociation energetics

Channel	Dissociation	E_0 (eV) [3]	$\Delta S^{\ddagger}$ (J K^{-1}) [3]
A	$C_{14}H_{10}^{+} \rightarrow C_{14}H_9^{+} + H$	4.28 ± 0.29	12 ± 15
B	$C_{14}H_{10}^{+} \rightarrow C_{12}H_8^{+} + C_2H_2$	4.19 ± 0.3	7 ± 10
C	$C_{14}H_{10}^{+} \rightarrow C_{10}H_8^{+} + C_4H_2$	not observed	not observed

As determined with iPEPICO [3] the loss of hydrogen has a higher E_0 than loss of acetylene but is more entropically favorable (Table 6-1). The sensitivity and resolution of the APCI-MS/MS experiment vis à vis iPEPICO also allowed for a third primary channel representing the loss of C_4H_2 to be detected (Figure 6-1).

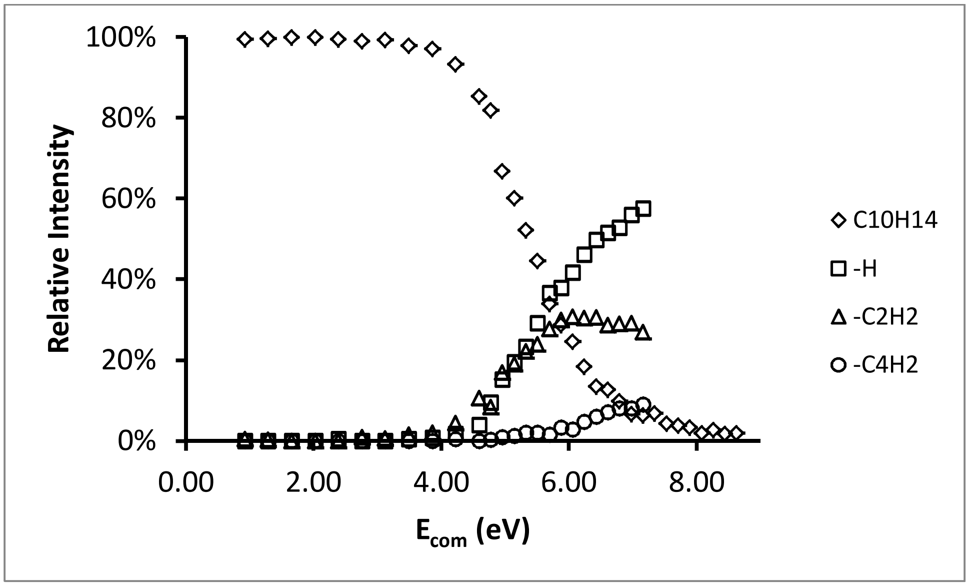

Figure 6-1 APCI-CID Breakdown diagram of $C_{10}H_{14}^{\cdot+}$
The three primary dissociation pathways involved loss of hydrogen (-H), acetylene ($-C_2H_2$) or diacetylene ($-C_4H_2$).

Figure 6-1 was converted to a branching relationship using equation 6-5 (T_i =400, α = 400) in order to compare both $–C_2H_2$ and $-C_4H_2$ channels relative to -H. The branching relationship was only taken at E_{com} ranges with sufficient fragment ion intensity

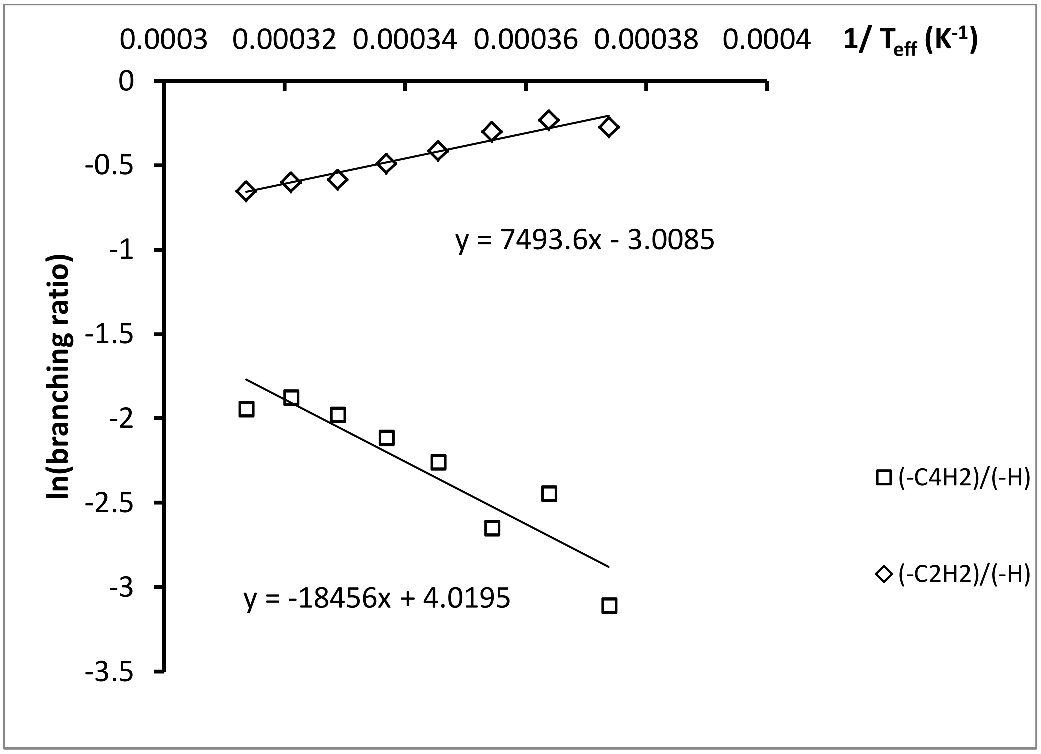

Figure 6-2 Branching relationship of $–C_2H_2$/-H and $–C_4H_2$/-H loss of $C_{14}H_{10}^{\cdot+}$ dissociation

The branching relationship shown at the top in Figure 6-2 compares the loss of acetylene with the loss of hydrogen. Based on equation 6-5, the slope of the branching relationship is described as:

$$\mathbf{slope} \propto \frac{-\left(\Delta H^{\ddagger}_{(-C_2H_2)} - \Delta H^{\ddagger}_{(-H)}\right)}{R} \qquad \text{Equation 6-6}$$

Therefore, the positive slope found in Figure 6-2 would correspond to a $\Delta H^{\ddagger}$ for the loss of hydrogen that is greater than the $\Delta H^{\ddagger}$ for the loss of acetylene which qualitatively agrees with iPEPICO data (Table 6-1).

The intercept from the branching ratio found in Figure 6-2 is negative and based on equation 6-5 relates to:

$$\mathbf{intercept} \propto \frac{\left(\Delta S^{\ddagger}_{(-C_2H_2)} - \Delta S^{\ddagger}_{(-H)}\right)}{R} \qquad \text{Equation 6-7}$$

Therefore, the negative intercept indicates the $\Delta S^{\ddagger}$ of H loss that is greater than the $\Delta S^{\ddagger}$ of acetylene loss which also agrees with iPEPICO measurements (Table 6-1). The sign of the intercept and slope of the branching relationships plotted at reciprocal collision energy allows the entropic and enthalpic terms of two competing channels to be ranked; however, it is not possible to directly measure ΔE_0 and $\Delta(\Delta S^{\ddagger})$. A further point of caution is that West et al. determined that there existed ten equivalent hydrogens on anthracene, while only six feasible sites where acetylene could be lost. This difference would affect the magnitude of the observed slope and intercept found in a branching relationship.

Setting a branching ratio constraint for efficient RRKM – an empirical approach

RRKM fitting of the anthracene breakdown diagram would require exploring combinations of eight variables; Ti and α and E_0 and $\Delta S^{\ddagger}$ for each channel. If a fitting constraint were introduced that required that the branching relationships of theoretical RRKM breakdown curves match the experimental branching relationship (Figure 6-2), it would be possible to describe all dissociation channels as a function of a single channel.

Table 6-2 Experimental branching relationship of $C_{14}H_{10}^{\cdot+}$ dissociation channels

Competitive pathway ratios	Slope $\Delta(\Delta H^{\ddagger})$ (eV)	Intercept $\Delta(\Delta S^{\ddagger})$ (J K^{-1})
$(-C_2H_2)/(-H)$	-0.65 eV	-25 J K^{-1}
$(-C_4H_2)/(-H)$	1.60 eV	33 J K^{-1}

The experimental branching relationships taken at Ti = 400K and α = 400 are shown in Table 6-2. It is not possible to directly compare these $\Delta H^{\ddagger}$ values to the E_0 values of West et al. due to approximations made in equation 6-1 as well as uncertainty in ion temperature. In order to empirically define the effects of the RRKM values of E_0 and $\Delta S^{\ddagger}$ upon the branching relationships of the theoretical RRKM curves, different combinations ΔE_0 and $\Delta(\Delta S^{\ddagger})$ were explored. The E_0 and $\Delta S^{\ddagger}$ of the primary channel (loss of H) was set at the values obtained by West et al [3].

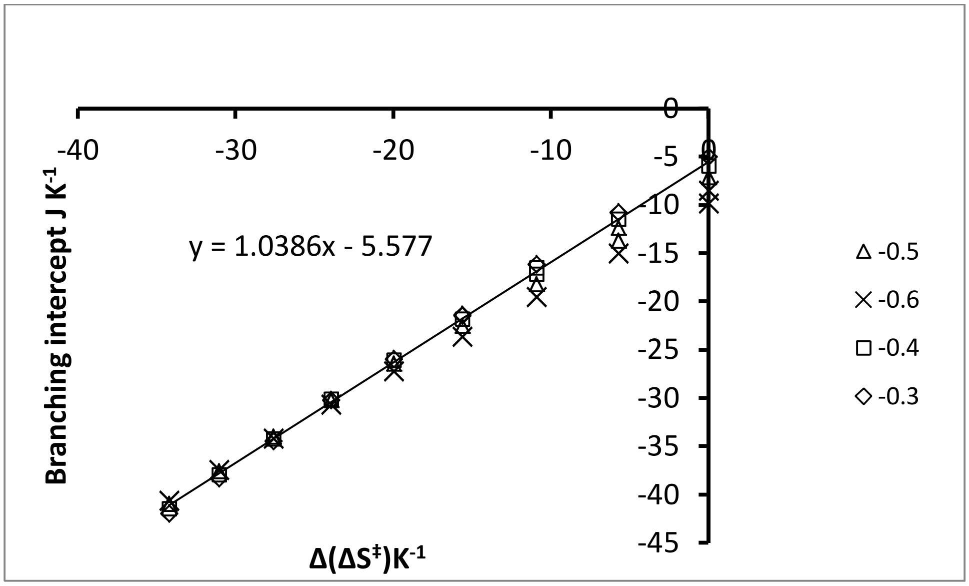

Figure 6-3 $\Delta S^{\ddagger}$(RRKM) vs branching intercept (RRKM) of $C_{14}H_{10}^{\bullet +}$ dissociation channels

Figure 6-3 shows the relationship between the RRKM $\Delta(\Delta S^{\ddagger})$ and the intercept of the branching ratio obtained from the theoretical RRKM breakdown diagrams. The relationships shown in Figure 6-3 are linear and inputting the experimental branching ratio intercept of -25 J K^{-1} into their linear solutions allows for the RRKM $\Delta(\Delta S^{\ddagger})$ that yields the correct branching ratio intercept to be obtained at each ΔE_0. Although the branching relationship intercept is not strongly influenced by the $\Delta(E_0)$, a slight parabolic relationship between the $\Delta(E_0)$ and the correct $\Delta(\Delta S^{\ddagger})$ can be defined (Figure 6-4):

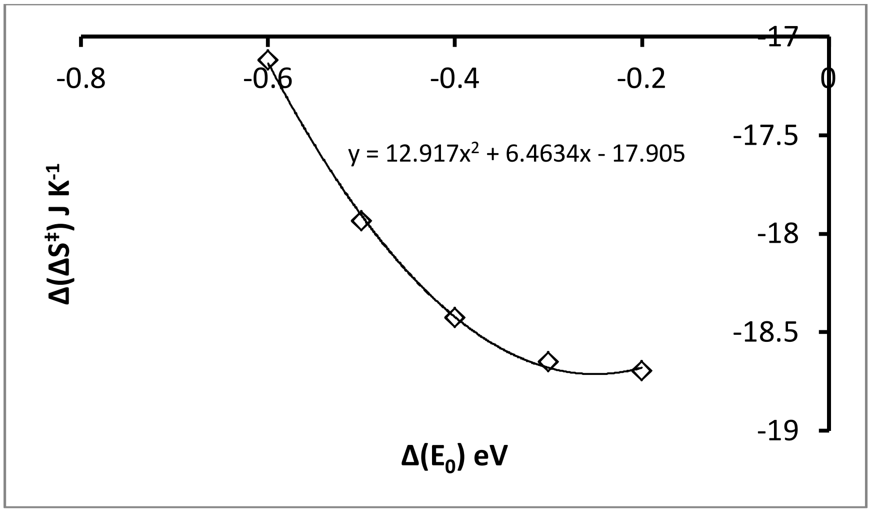

Figure 6-4 $\Delta(\Delta S^{\ddagger})$ as a function of $\Delta(E_0)$ for $C_{14}H_{10}^{\cdot+}$ dissociation channels ($-C_2H_2$/-H)

The empirical relationship between the RRKM $\Delta(\Delta S^{\ddagger})$ that gives a branching relationship with the correct intercept at different $\Delta(E_0)$ and can be described mathematically:

$$\Delta(\Delta \mathbf{S}^{\ddagger})_{\mathbf{intercept}} = \mathbf{12.92} \cdot \Delta(\mathbf{RRKM\ E_0})^{\mathbf{2}} + \mathbf{6.46} \cdot \Delta(\mathbf{RRKM\ E_0}) - \mathbf{17.9} \quad \text{Equation 6-8}$$

The second factor of the branching relationship is the slope which is related to the enthalpics of the dissociation (Equation 6-6). Different RRKM values of $\Delta(E_0)$ were explored to determine their relationship with the branching ratio slopes. The $\Delta(\Delta S^{\ddagger})$ of each theoretical curve generated in Figure 6-5 was calculated with equation 6-8 so that regardless of slope, the intercept would match with the experimental branching relationship intercept.

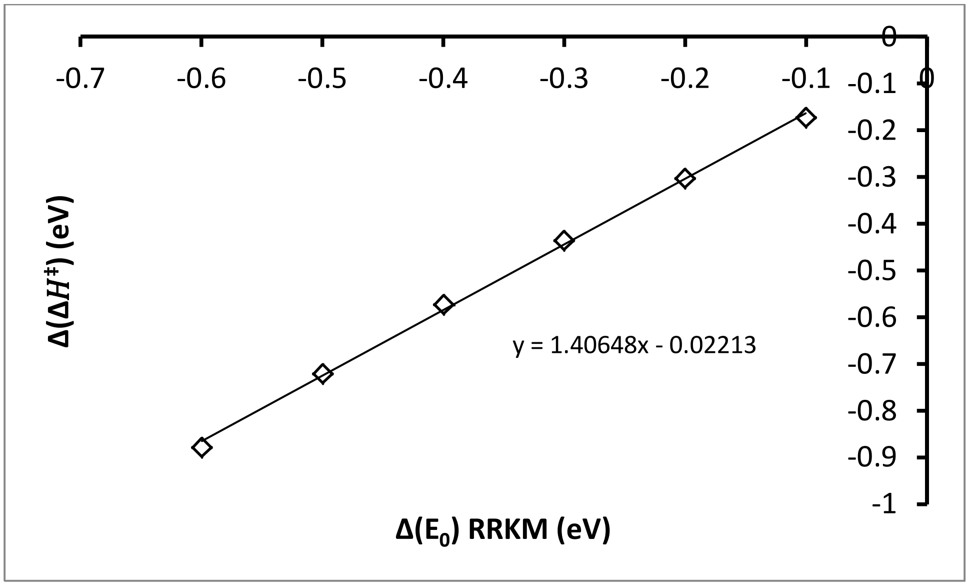

Figure 6-5 Relationship of Δ(E_0) RRKM and branching relationship slope

The relationship outlined in Figure 6-5 is linear and can be described mathematically by:

$$\Delta(\Delta\mathbf{H}^{\ddagger})_{\mathbf{slope}} = \mathbf{1.41} \cdot \Delta(\mathbf{RRKM\ E_0}) - \mathbf{0.022} \quad \text{Equation 6-9}$$

Inputting the experimental branching relationship values into equations 6-8 and 6-9, a theoretical RRKM breakdown diagram with a branching relationship that matches experimental will be obtained. For the loss of acetylene relative to hydrogen loss, the Δ(E_0) and Δ($\Delta S^{\ddagger}$) will be -0.455 eV and -18.69 J K^{-1} respectively in order to obtain a theoretical breakdown curve that has a branching relationship equivalent to that measured experimentally.

The same approach was applied to compare the loss of C_4H_2 to H loss and the RRKM Δ(E_0) and Δ($\Delta S^{\ddagger}$) must be +0.915 eV and +32.31 J K^{-1} respectively. Using these values will give a theoretical curve with the correct branching relationships regardless if the overall fit is appropriate (Figure 6-6). Equations 6-8and 6-9 will only be valid for α=400 and T_i = 400K.

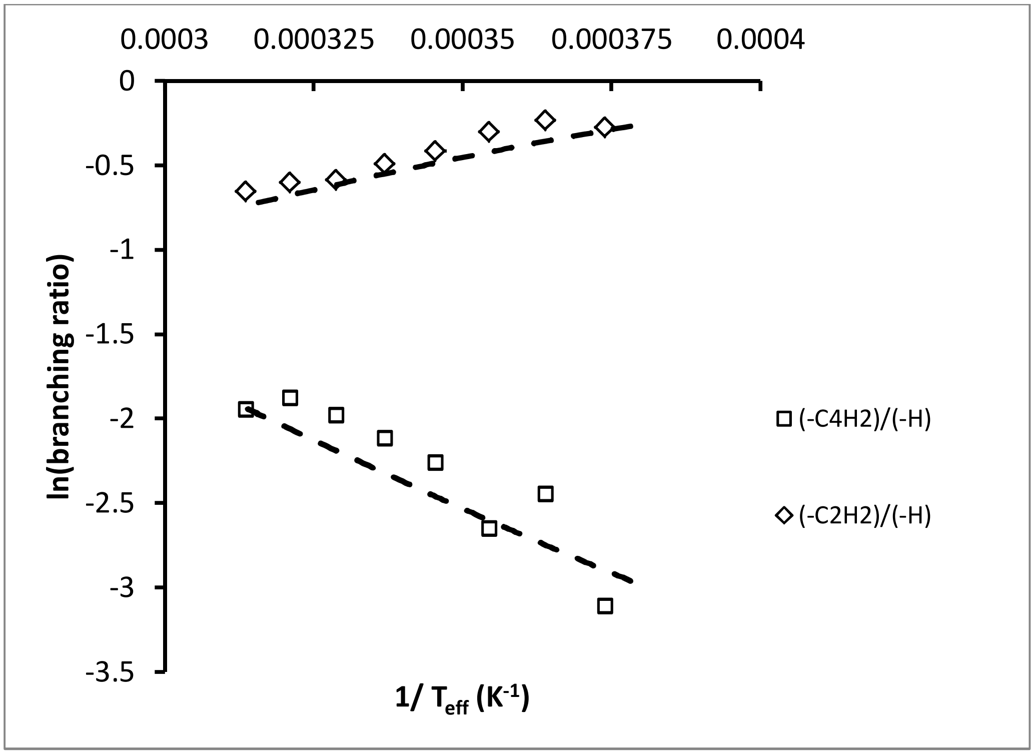

Figure 6-6 Branching relationships of experimental and RRKM (-C_2H_2/-H) and (-C_4H_2/-H) dissociation channels
T_{eff} obtained from equation 6-1, α,T_i = 400. Symbols represent experimental values. Dashed lined obtained from RRKM theoretical breakdown curve.

The $\Delta(E_0)$ and $\Delta(\Delta S^{\ddagger})$ were solved for different α and T_i values. As expected, α greatly affects the $\Delta(E_0)$ and $\Delta(\Delta S^{\ddagger})$ that give the correct branching relationship, but surprisingly T_i has limited effect (Figure 6-7, Figure 6-8).

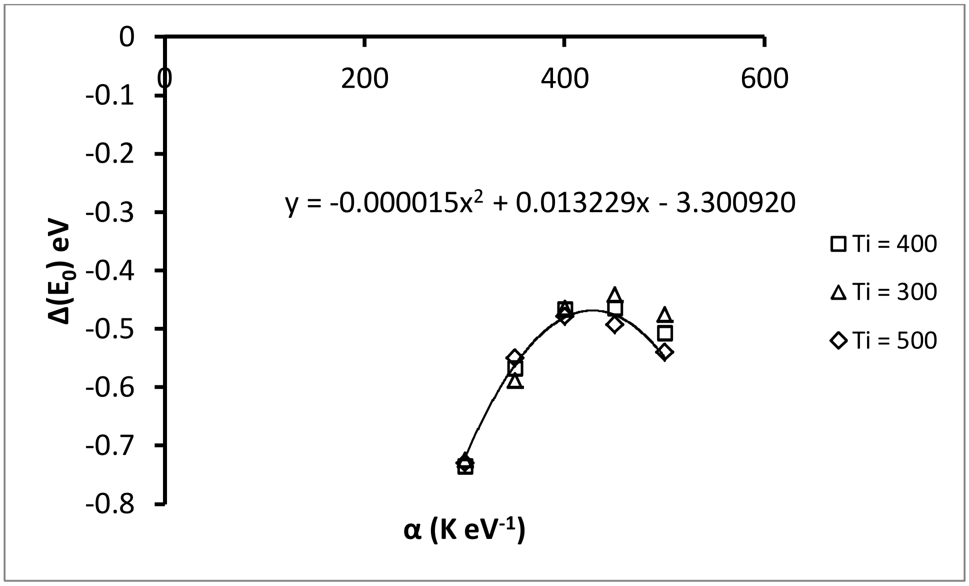

Figure 6-7 Relationship of the RRKM Δ(E_0) and correct branching relationship as a function of α.

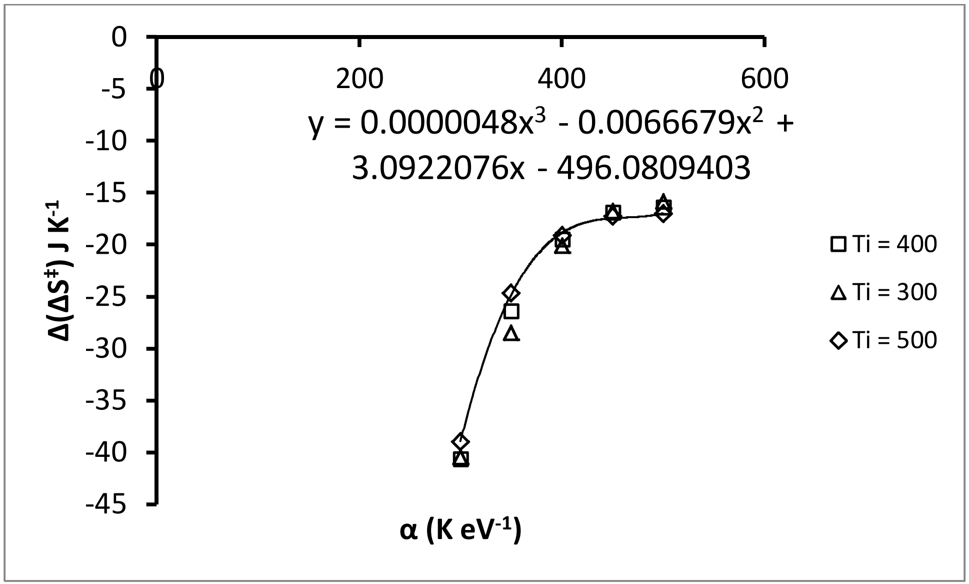

Figure 6-8 Relationship of the RRKM Δ($\Delta S^{\ddagger}$) and correct branching relationship as a function of α.

Derived from Figure 6-7 and Figure 6-8 are master equations that describes the correct Δ(E_0) and Δ($\Delta S^{\ddagger}$) across different α values that would results in an acceptable branching relationship.

$-C_2H_2 = f(-H)$

$$\mathbf{E_0(-C_2H_2) = E_0(-H) - 0.00001483\alpha^2 + 0.01299\alpha - 3.295}$$ Equation 6-10

$$\mathbf{\Delta S^{\ddagger}(-C_2H_2) = \Delta S^{\ddagger}(H) + 0.000003561\alpha^3 - 0.005182\alpha^2 + 2.522\alpha - 426.96}$$
Equation 6-11

$-C_4H_2 = f(-H)$

$$\mathbf{E_0(-C_4H_2) = E_0(-H) + 0.00004031\alpha^2 - 0.034976\alpha + 8.634}$$
Equation 6-12

$$\mathbf{\Delta S^{\ddagger}(-C_2H_2) = \Delta S^{\ddagger}(H) + 0.000006202\alpha^3 - 0.007281\alpha^2 + 2.699\alpha - 269.74}$$
Equation 6-13

Total RRKM Fitting

Combinations of T_i, α, E_0 and $\Delta S^‡$ values within the following ranges were explored to determine which combinations would result in a theoretical breakdown curve that best overall fit of experimental data (Table 6-3) . Combinations of E_0 and $\Delta S^‡$ were only explored for the hydrogen loss channel, while E_0 and $\Delta S^‡$ for the acetylene and diacetylene loss dissociation channels were determined using master equations 6-9 through 6-13 and expressed relative to the H loss channel.

Table 6-3 Ranges of fitting variables scanned for RRKM modelling

	Minimum	Maximum	Step
Ti (K)	300	600	100
α (K eV^{-1})	300	600	25
E_0 (-H) (eV)	4.00	5.11	0.02
$\Delta S^‡$ (-H) (J K^{-1})	-30	40	2

In total, the ranges of variables outlined in Table 6-3 resulted in 100,100 possible theoretical breakdown diagrams. Had the branching relationships not been used, 3.71×10^{11} combinations would have been necessary. The error of the fit was measured as the absolute difference between the relative intensities of the experimental and theoretical breakdown diagram. All fits with an error less than 5% / point were deemed appropriate and averaged together Table 6-4.

Table 6-4 Dissociation energetics of $C_{14}H_{10}^{\cdot+}$ calculated with RRKM/multi-channel fitting

Channel	Dissociation Channel	E_0 (eV)	$\Delta S^‡$ (J K^{-1})
A	$C_{14}H_{10}^+ \rightarrow C_{14}H_9^+ + H$	4.69 ± 0.29	-3 ± 17
B	$C_{14}H_{10}^+ \rightarrow C12H_8^+ + C_2H_2$	4.21 ± 0.29	-19 ± 15
C	$C_{14}H_{10}^+ \rightarrow C_{10}H_8^+ + C_4H_2$	5.81 ± 0.29	36 ± 22
T_i	503 ± 68 K	α	428 ± 40 K eV^{-1}

The best combinations of variables shows excellent agreement between the experimental and theoretical breakdown curves Figure 6-9. Every combination of variables maintained the correct branching relationship, regardless of the overall suitability of the fit (Figure 6-10).

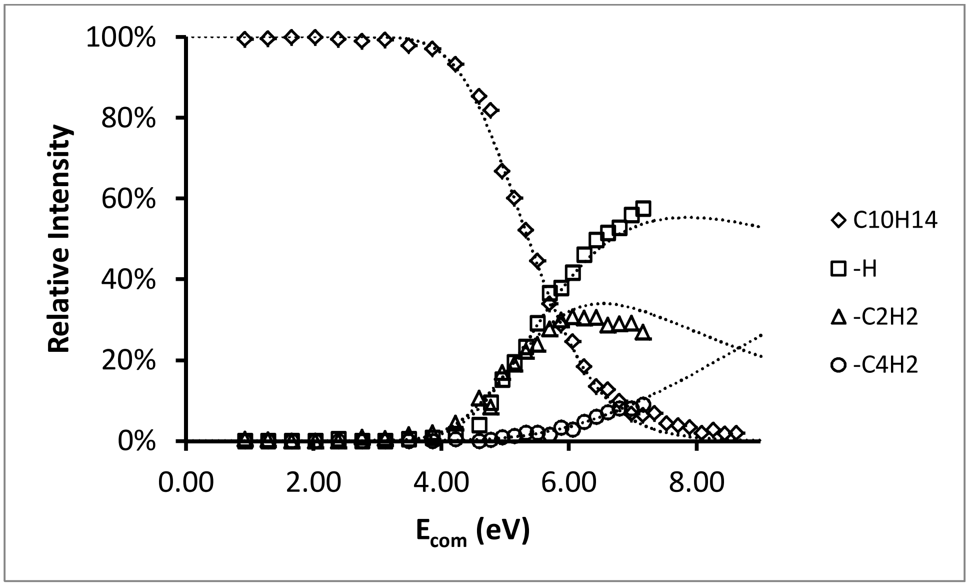

Figure 6-9 RRKM fitted breakdown diagram of $C_{10}H_{14}^{\cdot+}$

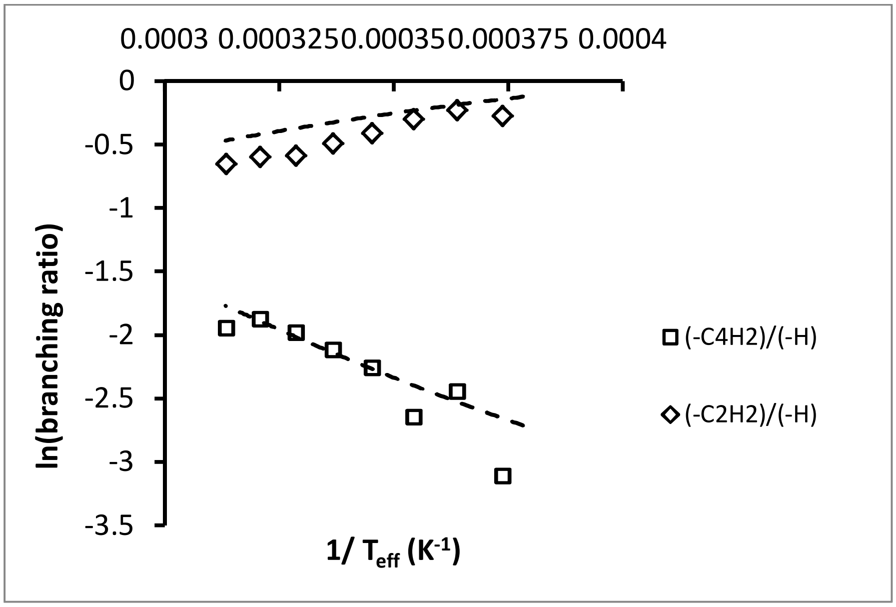

Figure 6-10 Experimental branching relationships and branching relationship of best RRKM fit (Figure 6-9)

The E_0 and $\Delta S^{\ddagger}$ for the loss of H and C_2H_2 obtained via iPEPICO and RRKM are within experimental error of each other with the exception of the $\Delta S^{\ddagger}$ of acetylene loss (Figure 6-12).

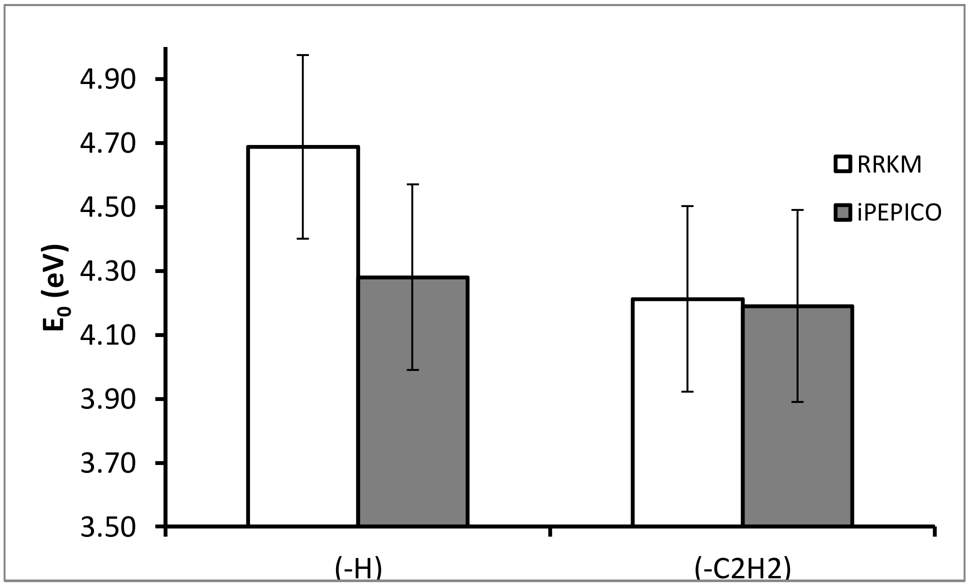

Figure 6-11 Comparison of E_0 obtained by RRKM fitting of APCI-MS/MS and iPEPICO of $C_{14}H_{10}^{\cdot+}$ dissociation channels

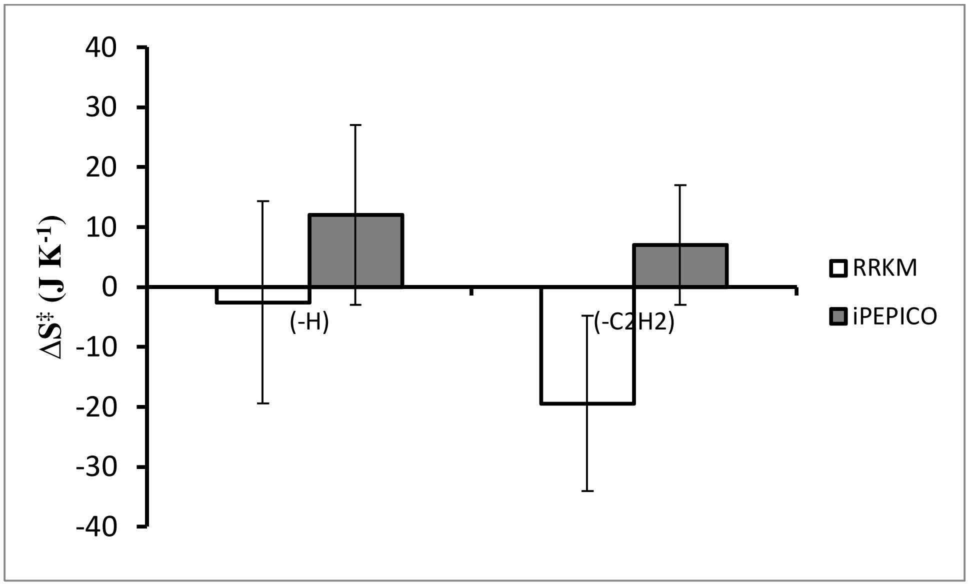

Figure 6-12 Comparison of $\Delta S^{\ddagger}$ obtained by RRKM fitting of APCI-MS/MS and iPEPICO of $C_{14}H_{10}^{\cdot+}$ dissociation channels

The good overall agreement between iPEPICO and RRKM measurements is surprising since the E_{com} range of the breakdown diagram is ~ 8.0 eV, and therefore the approximation that the relationship between T_{eff} and E_{com} is linear is almost certainly incorrect. Secondly, the APCI source makes it unlikely the internal energy of the reactant ion are in a Boltzmann distribution or even similar.

Notwithstanding, the purpose of this chapter was to develop a RRKM multi-channel fitting method for non-covalent complex dissociation channels where the shortcomings listed should be less pronounced for large or intermediate sized systems due to the smaller range of E_{com} values.

6.6 Conclusions

RRKM modelling of ion dissociations involving multiple channels offer a large number of possible thermochemical combinations to explore. The relationship between the appropriate ΔE_0 and the $\Delta(\Delta S^{\ddagger})$ variables used for RRKM fitting of competing dissociation channels are related to the slope and intercept of the experimental branching relationship. This allows for all primary dissociation channels to be described empirically in relation to a single primary channel. Introducing a constraint in that all theoretical RRKM breakdown diagrams explored have a branching ratio that matches experimental, the calculation time is drastically reduced and the confidence of the results are increased. The RRKM derived critical energies and entropies of activation for the dissociation of the anthracene radical cation are within or near the values obtained using iPEPICO.

6.7 References

1. Renaud, J. B.; Martineau, E.; Mironov, G. G.; Berezovski, M. V., Mayer, P. M. The collaborative role of molecular conformation and energetics in the binding of gas-phase non-covalent polymer/amine complexes. Physical Chemistry Chemical Physics 14, 165-172 (2012)
2. Drahos, L., Vékey, K. How closely related are the effective and the real temperature. Journal of Mass Spectrometry 34, 79-84 (1999)
3. West, B.; Sit, A.; Mohamed, S.; Blanchet, V.; Bodi, A., Mayer, P. M. Dissociation of the Anthracene Radical Cation: A Comparative Look at iPEPICO and Collision-Induced Dissociation Mass Spectrometry Results. unpublished (2014)

Chapter 7: A structure and energetic proposal to explain the uneven dissociation of ammoniated triacylglycerides

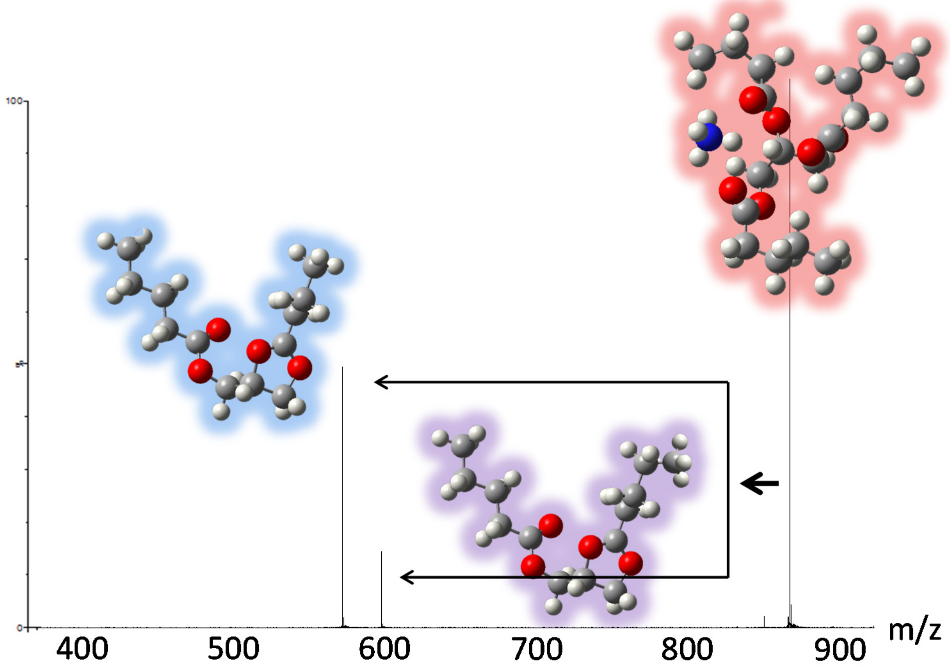

7.1 Objectives

- Provide an energetic and structural explanation of the uneven dissociation channels of ammoniated triacylglycerides

7.2 Chapter acknowledgements

J.B Renaud thanks:

- Sean Overton for experimental assistance, insightful discussions and sharing his passion of all things mass spectrometry
- Hajer Trabelsi, Moufida Welasti, Najla Benaahmed for introducing the author to the importance of triacylglycerol characterization and the current shortcomings
- Shane Byrne for assistance in checking the validity of the mathematical expressions

7.3 Introduction

Fatty acids (FAs) are indispensable compounds of living systems and are necessary for a diverse number of biological processes. They are commonly ingested by an organism in the form of triacylglycerides (TAG); therefore, efficient characterization of TAGs is significant for the assessment of nutritional value of foods and food ingredients. TAGs consist of three FAs chains esterified to a glycerol backbone, yet this simple initial structure masks a high level of complexity which presents challenges to their characterization. When analyzed with mass spectrometry (MS), the mass-to-charge ratio (m/z) of a TAG ion can be measured and the elemental composition of the TAG can be determined; however, one TAG elemental composition could correspond to a number of isobaric species. For example, a TAG with a certain elemental composition could include a mixture of isomers that differ in the combination of FAs present and the location of double bonds within each FA. Different FAs could lead to highly dissimilar metabolic pathways and therefore knowing which are present in a TAG sample is important. It is also important in the assessment of the quality of plant oil for nutritional value and for the detection of plant oil adulteration.

In traditional characterization procedures, triacylglyceride samples were hydrolyzed releasing the free FAs which could then be chemically modified and analyzed using GC or GC-MS [1]. This technique can determine the identities and abundances of the FAs in the sample; however, information regarding their original attachment within a TAG is lost. GC-MS of complete TAG molecules is possible; however, the high temperatures required for the volatilization of some TAG can result in chemical degradation. Moreover, electron impact ionization (EI) with the typical 70 eV electron energy is not a ‘soft’ ionization, and the major

TAG ions observed are fragment ions arising from co-eluting TAGs containing the same carbon number [2].

With the advance of other ionization techniques, such as atmospheric pressure chemical ionization (APCI), and electrospray ionization (ESI) [3], it has become feasible to ionize intact TAGs and preserve their structural integrity into the gas phase [4]. Electrospray ionization-tandem mass spectrometry (ESI-MS/MS) has been a key to extending the characterization of TAGs with mass spectrometry as it allows for the intact TAGs to be preserved into the gas phase and for TAGs to be isolated and fragmented.

In ESI-MS and ESI-MS/MS, the charge can be provided to the TAG molecule by forming a non-covalent complex with small cations including Na^+ [5], Li^+ [6-9], Ag^+ [10] and NH_4^+ [11]. Collision-induced dissociation (CID) of ammoniated TAGs often produces di-glyceride fragment cations (DAG^+) as the most intense fragment ions. The DAG^+ fragments arise from the loss of a neutral FA; R_nCOOH and NH_3 [11]. All of the three FA chains are capable of dissociating as a neutral, so there will be three competing fragmentation pathways (Figure 7-1).

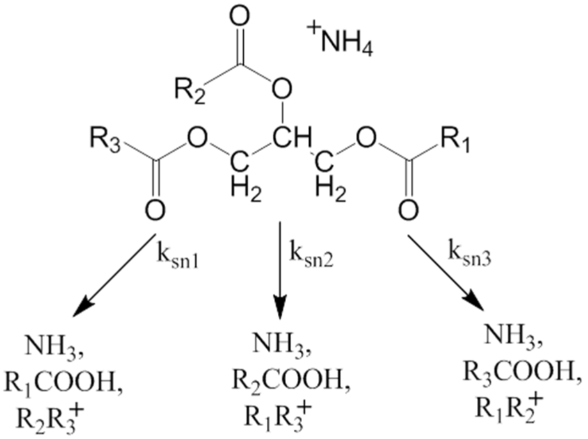

Figure 7-1 Competing dissociation pathways of $[NH_4^+][TAG]$

The mass of the FAs that constitute the TAG are determined by the neutral mass loss observed from the reactant ion. This allows for the carbon number and the number of double bonds of each FA chain to be determined, but not the location and orientation of the double bonds. The protonated TAG molecule $[TAG+H]^+$ that would arise from the loss of NH_3 is often observed only in low abundance and in the case of a completely saturated TAG, not at all [12].

Another layer of structural complexity arises from the position of each FA on the glycerol backbone: the terminal sn-1 or sn-3 positions or the internal sn-2 position. Positional identity of the TAG might prove vital in detecting adulteration of oils and could even influence the biological effect upon an organism [13]. Some studies have discerned the position of each FA based on the relative intensities of the DAG^+ fragments arising from CID of an isomerically pure TAG molecule complexed with a small cation. In most cases, the losses of the terminal FAs are more favorable than the loss of the internal FA. Several researchers have taken advantage of these uneven rates of FA cleavage in order to provide some level of positional isomer quantification [5, 11, 14-16]. Previous explanations of this uneven fragment ion intensity have been based on the postulations of different possible transition states, or even different product ion structures after a terminal or internal FA loss. McAnoy et al. [17] shed light on the mechanism of the dissociation of $[TAG+NH_4]^+$ by using deuterium labelling and suggested different DAG^+ fragment structures as the basis for the different positional fragmentation. However, MS^3 studies [11, 18] have suggested that regardless of the position of FA lost, the final DAG^+ ion product rearranges to an equivalent structure.

Aside from the position of a FA on the glycerol backbone, the relative amount of DAG^+ fragments produced by the three dissociation processes is influenced by the identity of the FA. Evans and co-workers [12, 19, 20] undertook a massive three part study looking at the fragment ion intensities from CID of a variety of ammoniated TAGs. Their results showed: a) the length of the FA chain has some positive correlation to increase the ability of the FA to dissociate as a neutral, b) FA with more double bonds is more likely to dissociate as a neutral and c) the proximity of the double bonds on the FA to the glycerol portion of the TAG has a strong influence on the likelihood of that FA dissociating as a neutral.

MS/MS of an ion at a single collision energy provides a ‘snapshot’ of the fragmentation process. MS/MS at a range of collision energies can provide much more insight into the energetics of the fragmentation process. The link between ion structure and energetics is inherent and govern its fragmentation properties. As shown in chapter 6; “Efficient RRKM fitting of multi-channel dissociations using branching relationships”, qualitative clues into the nature of the dissociation can be uncovered by varying the collision energy in MS/MS and plotting the natural logarithm of the relative intensities of fragment ions from two competing channels as a function of $1/E_{com}$. As depicted in Figure 7-1, MS/MS of $[TAG+NH_4]^+$ leads to three competing dissociation pathways. Many triacylglycerides can contain 2 identical FAs located at the sn-1 and sn-3 position and are written here in the form ‘ABA’. CID of $[ABA+NH_4]^+$ could result in either AB^+, BA^+ and $A\text{-}A^+$ fragment ions, with AB^+ and BA^+ being m/z, and presumably energetically, equivalent. Therefore, equation 6-1 becomes:

$$\frac{\mathbf{I_{AB+}}}{\mathbf{I_{AA+}}} \approx \frac{\mathbf{k_{sn1}+k_{sn3}}}{\mathbf{k_{sn2}}} \approx \frac{\mathbf{2k_{sn1}}}{\mathbf{k_{sn2}}} \qquad \text{Equation 7-1}$$

and combining equation 7-1with 6-4 results in:

$$\mathbf{ln}\left(\frac{\mathbf{I_{AB+}}}{\mathbf{I_{AA+}}}\right) - \mathbf{ln(2)} \propto \frac{-\left(\Delta \mathbf{H^{\ddagger}_{sn1}} - \Delta \mathbf{H^{\ddagger}_{sn2}}\right)}{\mathbf{R}} \cdot \frac{\mathbf{1}}{\mathbf{E_{com}}} + \left[\frac{\left(\Delta \mathbf{S^{\ddagger}_{sn1}} - \Delta \mathbf{S^{\ddagger}_{sn2}}\right)}{\mathbf{R}}\right] \qquad \text{Equation 7-2}$$

By examining the fragmentation of $[TAG+NH_4]^+$ at different collision energies, insight into the energetic factors that determine the dissociation behaviour of TAGs can be obtained. To our knowledge an accurate energetic based explanation for this uneven fragmentation phenomenon based on theory and experiment is not available and would be valuable to the efficient characterization of TAGs. The purpose of this study is to identify the factors responsible for this phenomenon based on structure and energetics and suggest a model in which previous observations of $[TAG+NH_4]^+$ fragmentation found in literature can coalesce.

7.4 Materials and methods

Materials

Triacylglyceride standards: 1,3-dipalmitoyl-2-oleoylglycerol ≥99% (POP), 1,3-dioleoyl-2-palmitoylglycerol ≥99% (OPO) and 1-palmitoyl-2-oleoyl-3-linoleoyl-rac-glycerol ≥98% (POL) were purchased from Sigma Aldrich (St. Louis). Each solution contained 200 µM ammonium acetate and 100 µM triacylglyceride dissolved in a 60:40 HPLC grade methanol: HPLC grade tetrahydrofuran solution purchased from Sigma Aldrich (St. Louis). 1,10-diaminodecane purchased from Sigma Aldrich (St. Louis) was used at a concentration of 200 µM in place of ammonium acetate to generate doubly protonated complexes with triacylglycerides.

ESI-MS/MS

MS/MS was acquired in positive mode electrospray ionization on a Waters Synapt G1 Mass spectrometer in 'V' resolution mode and sample introduced via syringe pump at 10 µL min^{-1}. The capillary, sample cone and extracting cone voltages were held constant at 2.8 kV, 40 V, and 5 V respectively. CID was accomplished within the trap cell at an argon flow rate of 4.0 mL min^{-1} beginning with lab frame collision energy of 3 eV and increasing in increments of 1eV until the reactant ion was below 1% relative intensity. Ion mobility mode was used with a nitrogen flow rate of 28 mL min^{-1}, wave height of 6.5 V and speed of 150 m/s. The ratios of DAG$^+$ fragment ions were measured while the reactant ion was between 85% and 15% relative abundance.

RRKM breakdown curve fitting

The description of RRKM fitting of experimental breakdown curves is described in detail elsewhere [21, 22]. Vibrational frequencies of the $[TAG+NH_4]^+$ molecules were calculated at the AM1 level [23] in the Gaussian 09 program suite [24]. Using these frequencies, reactant densities of states and transition state sums-of-states were calculated by direct count according to the algorithm of Beyer and Swinehart [25, 26].

By altering the E_0 and scaling the 8 lowest vibrational frequencies the transition state ion (which changes the $\Delta S^{\ddagger}$) thousands of theoretical curves were obtained. Each combination which fit the experimental data with less than 4% error per data point was averaged together. Due to the similarity of the ions of this study, the relationship between effective ion temperature and centre of mass collision energy was set as :

$$\mathbf{T_{eff} = 400K + 180KeV^{-1} \cdot (E_{com})} \qquad \text{Equation 7-3}$$

This provides an estimated value for the $\Delta S^{\ddagger}$ and E_0 for the systems of this study and allows for different molecules to be compared. Uncertainties of E_0 and $\Delta S^{\ddagger}$ listed within this study represent uncertainties in the calculated values and based on equation 7-3. Since this technique is semi-quantitative in nature, a much larger uncertainty is expected in the assignment of absolute values. Given the similarity of the molecules of this study, the energetic values obtained will allow for meaningful comparisons.

The E_0 and $\Delta S^{\ddagger}$ of the sn-1 and sn-3 channels were expressed as a function of the sn-2 values using a branching relationship constraint (Chapter 6)

Computational analysis

Structures including and originating from ammoniated glyceryl tributyrate ($[BBB+NH_4]^+$) were optimized and frequencies obtained using B3LYP [27, 28] at the 6-311+g(d,p) level of theory in Gaussian 09 program [24]. The AMBER9[29] program suite using the generalized AMBER force field (GAFF) [30] was used to study low energy conformations of $[POP+NH_4]^+$. Minimized energy conformations of the ammoniated TAG were briefly equilibrated for 20 ps (time step 1 fs) at 300 K before undergoing 2000, 10 ps cycles of 400 K equilibration at a 0.5 fs time step. The low energy structure of each cycle was minimized and stored and used as the starting structure for the subsequent equilibration cycle.

For brevity, ammoniated triacylglycerides, protonated triacylglycerides, neutral FA fragments and diacylglyceride cation fragments will be expressed as $[TAG+NH_4]^+$, $[TAG+H]^+$, R_nCOOH and DAG^+ respectively. Palmitic (C16:0), oleic (C18:1) and linoleic (C18:2) are expressed as P, O and L respectively.

Variable collision energies of POP, OPO and POL to separate energetic terms

Evans et al. chose a single collision energy for MS/MS of a vast number of ammoniated TAG molecules and stated that the relative ion intensities were not ultra-sensitive to collision energies within the range they examined [19]. Based on equation 7-2, the limited effect of collision energy on fragment ratios suggests that the uneven loss of a neutral FA from different positions on the glycerol backbone is not driven by different E_0 values, but by differences in the $\Delta S^{\ddagger}$ of the competing channels. After obtaining MS/MS spectra at a wider range of collision energies, it was evident that the relative ratios of the competing DAG^+ fragments within this study were sensitive to collision energies.

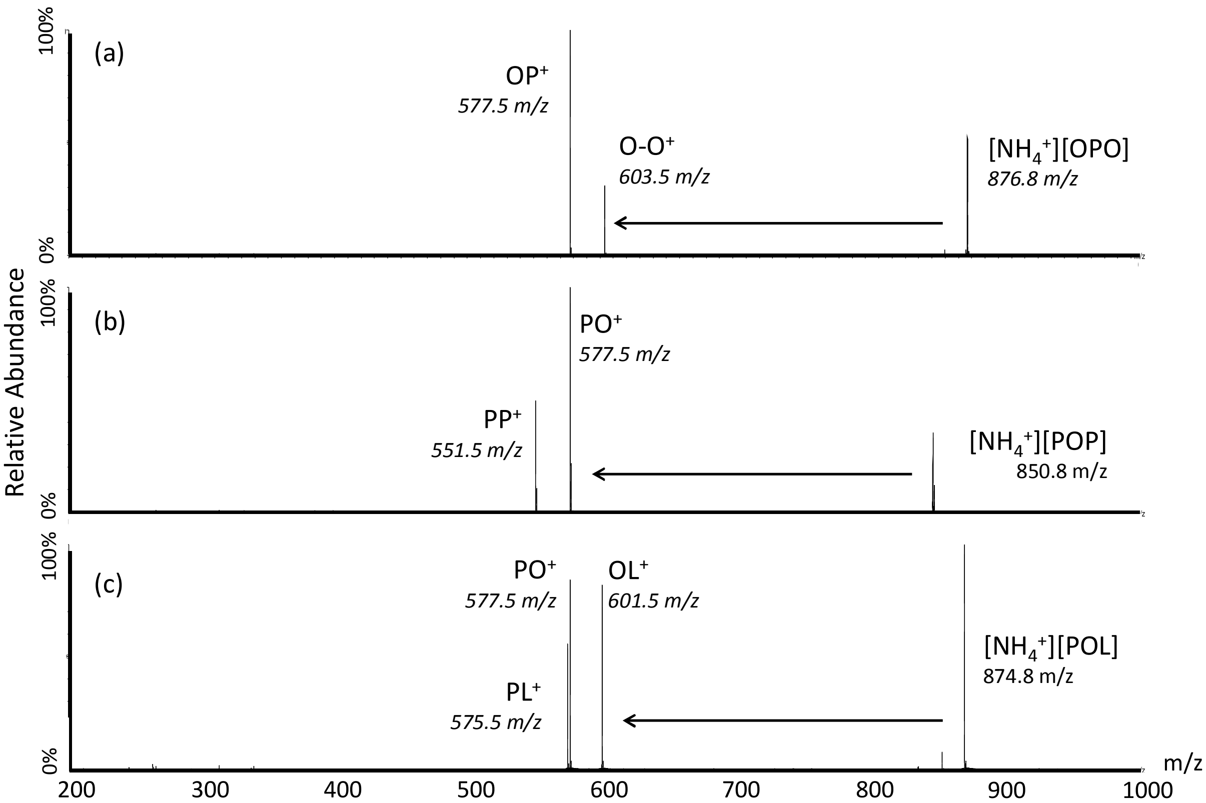

Figure 7-2 MS/MS of $[NH_4^+]$[TAG] at 24eV lab frame collision energy
MS/MS of: (a) $[NH_4^+]$[OPO], (b) $[NH_4^+]$[POP], (c) $[NH_4^+]$[POL] at a lab frame collision energy of 24eV. The main fragments are DAG$^+$ obtained from the loss of NH_3 and a neutral FA. In small abundance, 17 m/z units below the reactant ion is the $[TAG+H]^+$ ion.

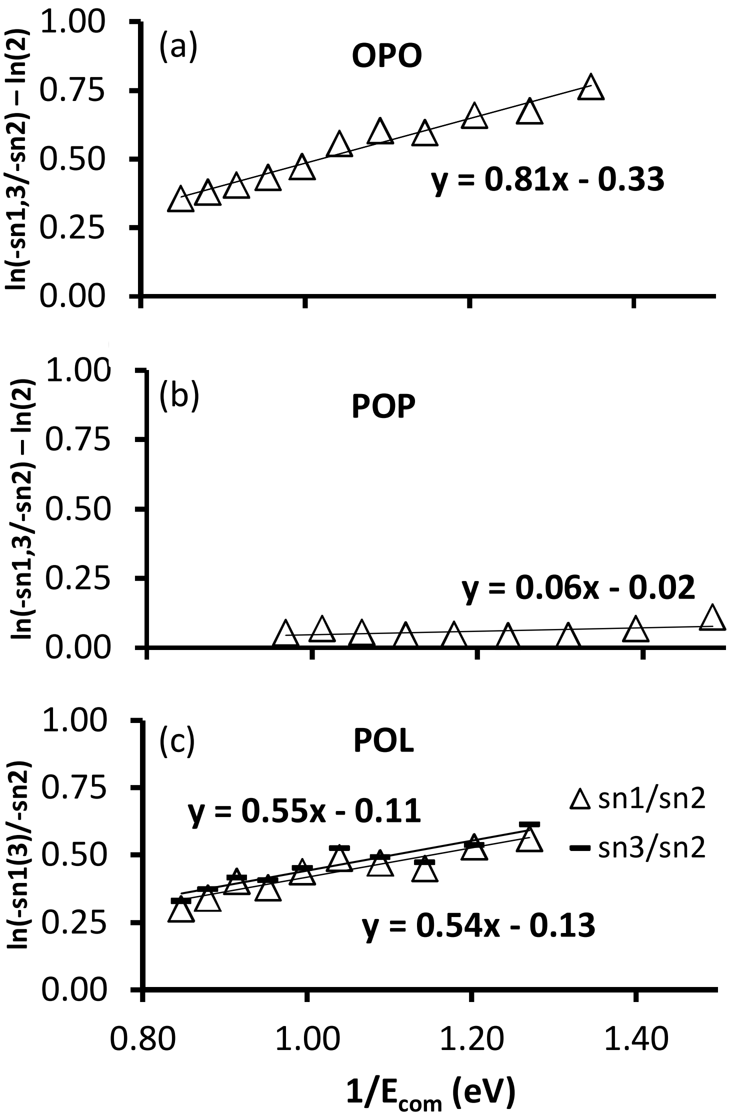

Figure 7-3 ln of DAG$^+$ fragment ion ratios as a function of reciprocal centre of mass collision energy

The natural ln of DAG$^+$ fragment ion ratios (y), are plotted as a function of reciprocal centre of mass collision energy (x) resulting and a linear best fit is applied (y = mx + b). (a) [NH_4^+][OPO]; (Δ) ln(OP$^+$/OO$^+$) ions - ln(2) as two equivalent pathways can result in the OP$^+$ ion. (b) [NH_4^+][POP]; (Δ)ln(PO$^+$/PP$^+$) ions - ln(2). (c) [NH_4^+][POL]; (-)ln(PO$^+$/PL$^+$) and (Δ) ln(OL$^+$/PL$^+$). All slopes are positive to varying degrees, all intercepts ware negative to varying degrees.

Figure 7-2a shows that the dominant peak from CID of [OPO+NH_4]$^+$ is the DAG$^+$ ion, OP$^+$, which results from the loss of either the sn-1 or sn-3 neutral oleic acid. Figure 7-3a is obtained by measuring the relative intensities of OP^+/OO^+ at different collision energies of 0.81eV units and an intercept of -0.33. The qualitative indication is that loss of sn-1(3) is enthalpically less demanding than the loss of the sn-2 palmitic acid. The negative intercept ($\Delta S^{\ddagger}_{sn1} - \Delta S^{\ddagger}_{sn2}$) < 0, suggests that the loss of the sn-2 FA is more entropically favorable than the loss of the sn-1 or sn-3 position. Therefore, the enthalpic and entropic terms are favoring different dissociation pathways.

Applying the same experimental treatment to $[POP+NH_4]^+$, a somewhat different picture develops. In Figure 7-2b, the dominant peak from CID of $[POP+NH_4]^+$ is the a DAG^+ fragment, PO^+, which results from the neutral loss of the palmitic acid at either the sn-1 or sn-3 position. The slope of the fragment ratios (PO^+/PP^+) in Figure 7-3b is only slightly positive, meaning that loss of the sn-1(3) palmitic acids are only slightly less enthalpically demanding than the loss of the sn-2 oleic acid. The intercept is -0.02, meaning that the loss of the sn-2 position is only slightly entropically more favorable than the loss of the terminal positions. The presence of a double bond on the sn-2 position makes up for the preference of sn-1(3) position loss nearly to the point of equality and this reinforces previous observations that a double bond on the FA chain can positively influence the rate of fragmentation [12, 19, 20]. A different observation of the relative fragment ion intensity for $[POP+NH_4]^+$ was made by Evans and co-workers in which, the PO^+ ion was the most intense peak, and the PP^+ fragment was only 22.6% [12]. This difference might be caused by instrumental factors as the aforementioned study employed an ion trap mass spectrometer or by differences in collision gas.

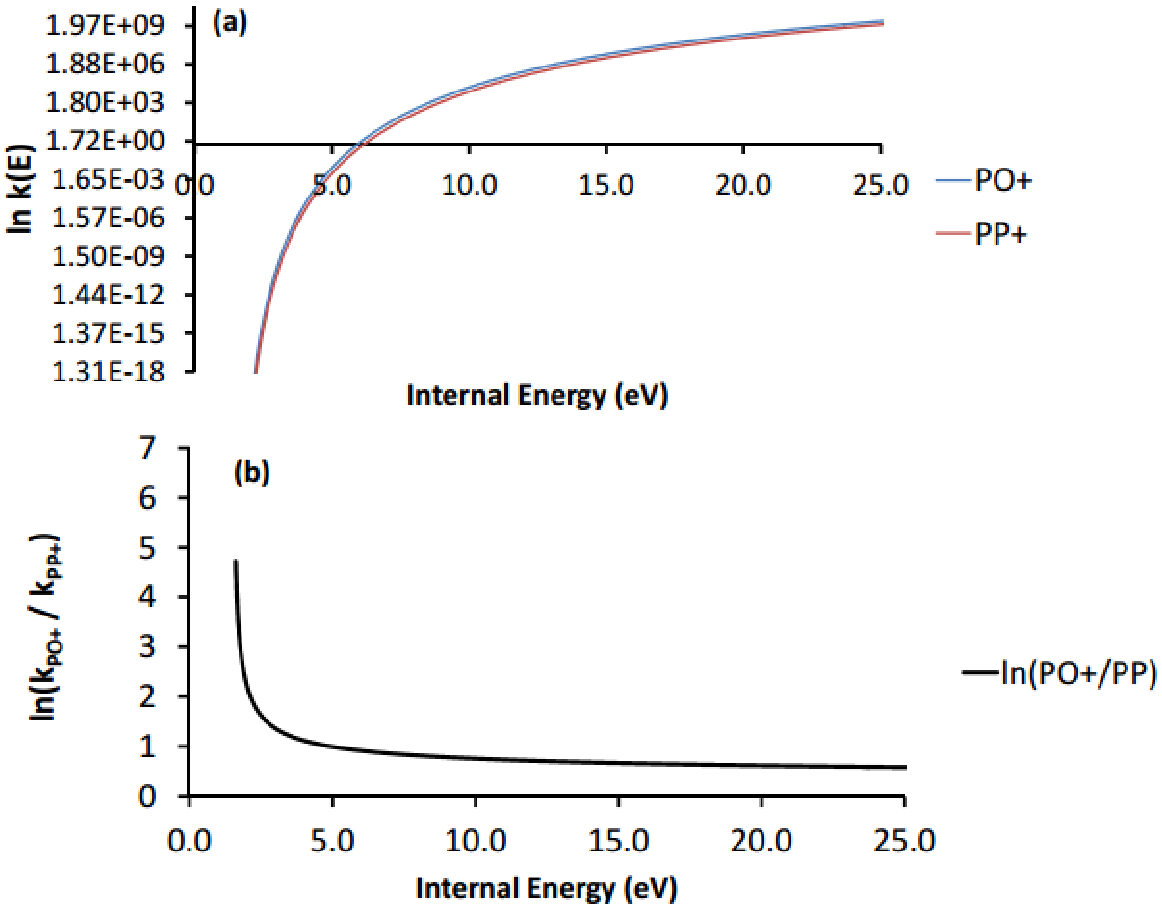

Figure 7-4 (a) The rate constants as a function of internal energy for dissociation of [TAG+NH4] + into DAG+ ions where calculated with RRKM theory. (b) The natural logarithm of the ratio of rate constants that produce PO+ and PP+ show that as internal energy increases, the ratio decreases.

Ion trap mass spectrometers generally involve longer dissociation times and multiple, low energy collisions. Therefore, in order to be observed in the time frame of the dissociation reaction, the internal energy of the parent ion can be less than what would be required for instruments with shorter dissociation time frames. Figure 7-4 shows that lower internal energies, the differences in rate constants between to competing channels is greater than at higher internal energies, which would account for the larger differences in fragment ion intensities observed by Evans and co-workers.

The connectivity of the three dissociation pathways is evident from the CID of $[POL+NH_4]^+$. The intensities of fragment ions arising from neutral loss of sn-1 P and sn-3 L are nearly the same intensity and both, as expected, are greater than the signal arising from the loss of the sn-2 O (Figure 7-2c). When this is compared with the ratio of sn-1 to sn-2 loss (OL^+/PL^+) and sn-3 to sn-2 loss (PO^+/PL^+) (Figure 7-3c), we see in both cases a positive slope and a negative intercept is obtained again. This signifies that the loss of the sn-2 position FA is more enthalpically demanding yet more entropically favorable.

In the three examples of $[OPO+NH_4]^+$, $[POP+NH_4]^+$ and $[POL+NH_4]^+$, the relative intensity ratios of the fragment ions did change with increasing collision energy and the loss of the sn-2 position FA had a higher activation energy than the loss of a FA from the terminal positions. This goes significantly further in describing the positional based effect in competing fragmentation processes by separating energetic and entropic terms. The key point is the determination that loss of the FA from the sn-2 position is entropically more favorable than loss from the sn-1 and sn-3 positions.

RRKM fitting of breakdown curves to estimate energetics

Variable energy analysis can be used quickly to obtain qualitative insight into the different energetic terms that drive (or impede) competing dissociation pathways. RRKM fitting was employed to compare values among distinct yet similar chemical systems [21, 22]. This involved combining different values of $\Delta S^{\ddagger}$ and critical energies of activation (E_0) to generate thousands of theoretical breakdown diagrams which were scored against the experimental breakdown diagrams (Figure 7-5).

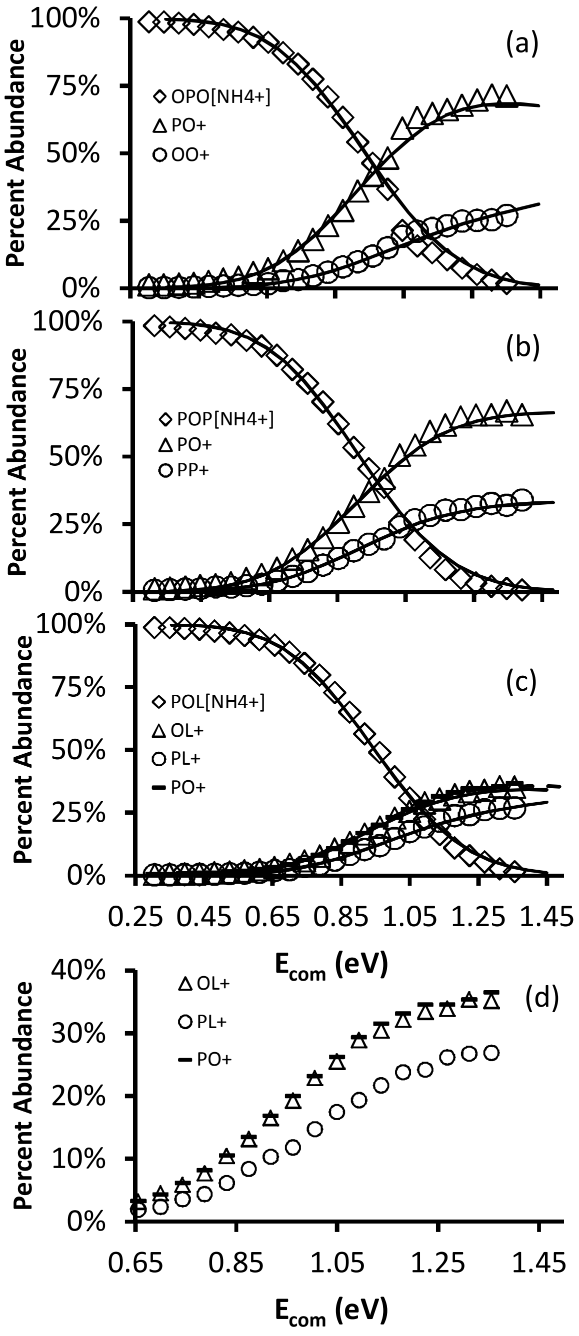

Figure 7-5 RRKM fitted breakdown diagrams for[NH_4^+][TAG]
RRKM fitted breakdown diagrams for (a) [NH_4^+][OPO], (b) [NH_4^+][POP], (c) [NH_4^+][POL].
(d) is the enhancement of (c) for clarity

The best breakdown fits obtained confirmed that for all three $[TAG+NH_4]^+$ molecules, the loss of the sn-2 FAs have higher activation energies (Figure 7-6a) but are more entropically favorable (Figure 7-6b) than dissociation of FA chains at the sn-1 and sn-3 glycerol position.

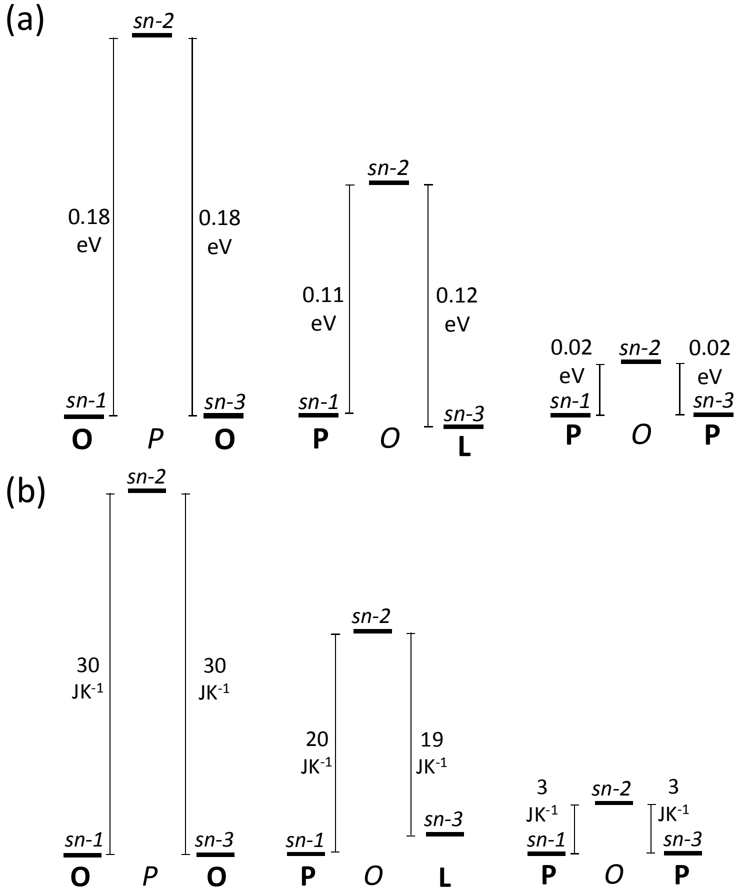

Figure 7-6 RRKM derived E_0 of dissociation channels
RRKM derived (a) ΔE_0 of sn-1(3) loss relative to sn-2 and (b) $\Delta S^\ddagger$ of sn-1(3) loss relative to sn-2. All examples show a higher E_0 value for the loss of the sn-2 FA than the terminal fatty acids. All examples show a higher $\Delta S^\ddagger$ value for the loss of the sn-2 FA than the terminal fatty acids.

The critical energy for the loss of the sn-1(3) position for all examples was found to be similar regardless of the identity of the FA: ≈ 1.52 eV (Table 7-1).

Table 7-1 RRKM derived critical E_0 and $\Delta S^\ddagger$ of dissociation for $[TAG+NH_4]^+$

	- sn-1		- sn-2		- sn-3	
	E_0 (eV)	$\Delta S^\ddagger$ ($J \cdot K^{-1}$)	E_0 (eV)	$\Delta S^\ddagger$ ($J \cdot K^{-1}$)	E_0 (eV)	$\Delta S^\ddagger$ ($J \cdot K^{-1}$)
OPO	1.52 ± 0.05	49 ± 10	1.70 ± 0.06	79 ± 11	-	-
POP	1.50 ± 0.05	46 ± 11	1.52 ± 0.05	49 ± 11	-	-
POL	1.52 ± 0.05	47 ± 9	1.64 ± 0.04	67 ± 9	1.51 ± 0.05	48 ± 9

The position that is most affected by the identity of the FA chain is the sn-2 position. In this study, the loss of the sn-2 palmitic acid in OPO had the highest activation energy; 1.70 eV, followed by oleic in POL with 1.64 eV and oleic in POP with 1.52 eV. Since the sn-2 oleic acid within POP and POL have very different activation energies, it suggests that not only does the identity and position of the FA chain of a triacylglyceride affect its dissociation energetics, but also the neighbouring FAs esterified to the backbone. Therefore any model used to predict the relative intensities of DAG^+ fragments must not only take into account the position and identity of the FA, but also the influence of other FAs within the TAG.

The dissociation pathway of the NH_3 and RnCOOH neutral fragments.

With the exception of highly unsaturated ammoniated TAGs, the DAG^+ ions which arise from the loss of NH_3 and R_nCOOH are often the most abundant fragmentation products observed [12, 19, 20]. If the loss of NH_3 and R_nCOOH occurred in a stepwise fashion, the neutral fragments NH_3 and R_nCOOH would leave as independent fragments (although this is difficult to demonstrate experimentally because both are lost as neutrals and thus not instrumentally observable). In order to illuminate the neutral side of this dissociation process, 1,10-diaminodecane (DAD) was used in place of NH_4^+ as a cationizing agent to form a doubly-protonated complex with the TAGs. CID of the resulting $[(DAD+2H)(TAG)]^{2+}$ complexes produces the charge-separated products $[DAD+H]^+$ and $[TAG+H]^+$ related fragments (Figure 7-7).

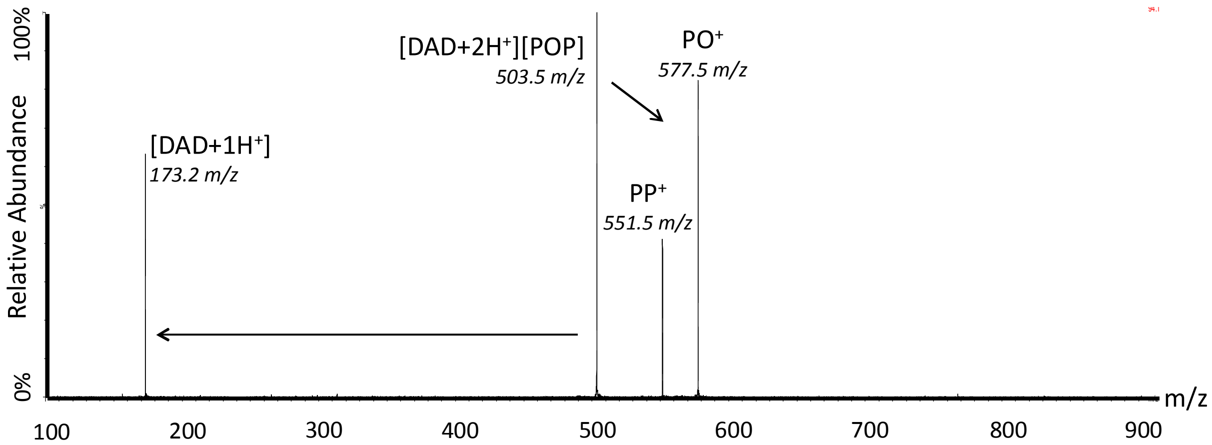

Figure 7-7 MS/MS of $[DAD+2H^{+2}][POP]$

MS/MS of $[DAD+2H^{+2}][POP]$ undertaken at a collision energy of 17 eV lab frame. The 2 charges are partitioned among the fragment ions; $[DAD+1H^+]$ and DAG^+. No signals were observed that would correspond to $[DAD+1H^+]$ and a neutral FA.

What is not observed in the mid-mass range of Figure 7-7 are any ion signals that could correspond to a complex between $[DAD+H]^+$ and an R_nCOOH, which strongly supports that the two fragments leave independently and most likely in a stepwise process.

The nature of the deamination step

The reason that $[TAG+H]^+$ is not usually observed in great amounts could be that the energy barrier for the loss of NH_3 sits near or above the energy required for loss of R_nCOOH. Therefore, the loss of NH_3 could in some cases be the rate determining step for dissociation and the $[TAG+H]^+$ produced quickly dissociates into DAG^+ ions and R_nCOOH neutrals.

An ammoniated glyceryl tributyrate $[BBB+NH_4]^+$ was optimized at the B3LYP/6-311+g(d,p) level of theory.

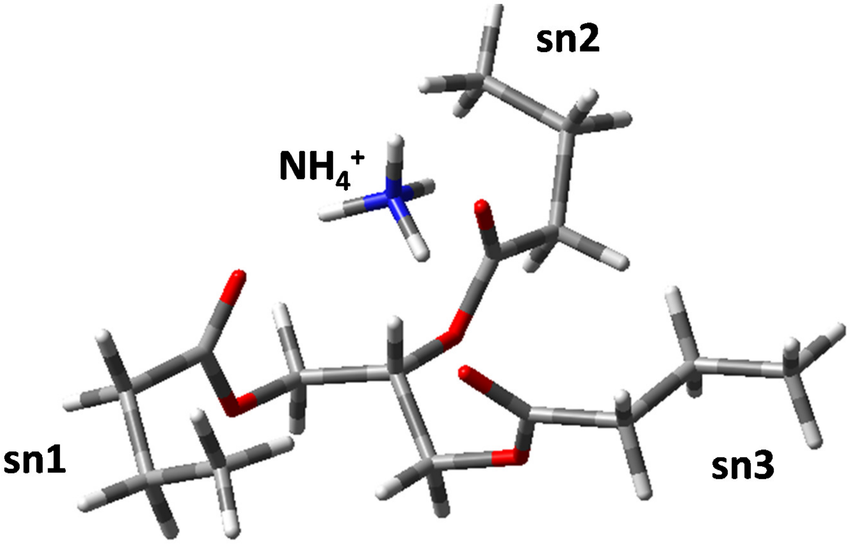

Figure 7-8 DFT optimized structure for ammoniated glyceryl tributyrate
Ammoniated glyceryl tributyrate showing NH_4^+ interaction with the carbonyl oxygens of the triglyceride.

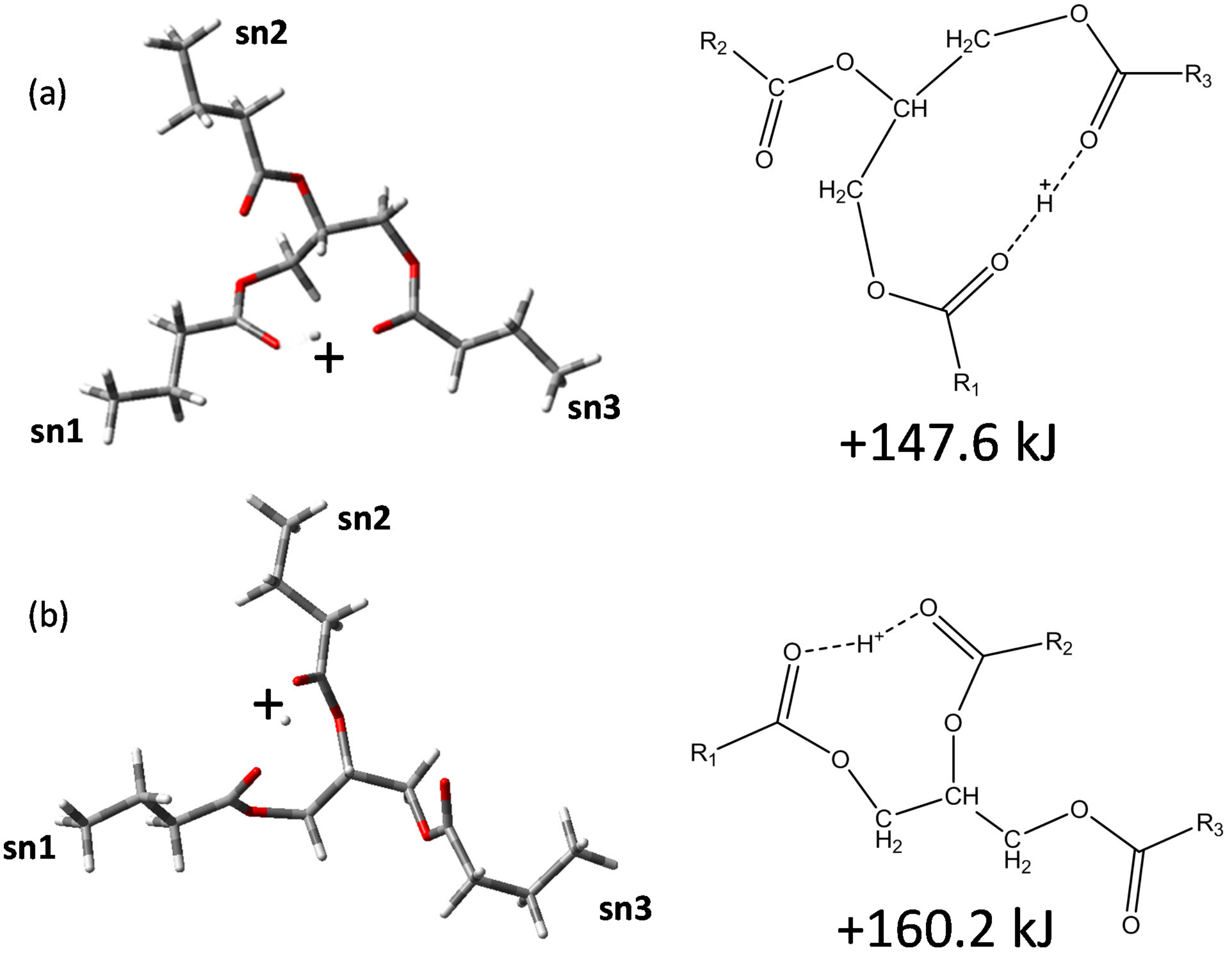

Figure 7-9 DFT optimized protonated, glyceryl tributyrate structures
Two protonated, glyceryl tributyrate structures were obtained using B3LYP 6-311g(d,p) optimization. (a) The Distal isomer; proton bridge formed between the sn-1 and sn-3 carbonyl oxygens is +147.6 kJ relative to ammoniated TAG and (b) Proximal isomer; proton bridge formed between either the sn-1 or sn-3 and the sn-2 carbonyl oxygens is +160.2 kJ relative to ammoniated TAG.

From this optimized structure, NH_4^+ was replaced with H^+ and interestingly this could be optimized into two distinct structural arrangements (Figure 7-9). In both structures, the proton will have focused interaction with 2 carbonyl oxygens at once and form a proton bridge. In what is labeled as the distal structure (Figure 7-9a), the proton bridges the sn-1 and sn-3 carbonyl oxygen atoms to form a 10-member ring. In the proximal structure (Figure 7-9b), the proton bridges the sn-2 carbonyl oxygen with either the sn-1 or sn-3 carbonyl oxygen in a 9-member ring. The optimized distal and proximal structures were found to be 147.6 kJ and 160.2 kJ above the ammoniated TAG respectively (Figure 7-9). These two $[TAG+H]^+$ structures would strongly corroborate the measured energetic values and dissociation behaviour of $[TAG+NH_4]^+$ if the loss of NH_3 from a saturated TAG is the rate determining step. Based on published deuterium labelling experiments [17], it is known that the neutral RCOOH obtains a proton that originates on the NH_4^+. Therefore the loss of the sn-2 FA would only proceed via the proximal $[TAG+H]^+$ intermediate which is higher in energy (+12.6 kJ) than the distal $[TAG+H]^+$. However, the proximal $[TAG+H]^+$ intermediate has a smaller ring and therefore 'freezes out' one fewer rotors than the distal intermediate which could account for the greater entropic favourability of the proximal $[TAG+H]^+$ ion structure.

The possible DAG+ fragment ion structure and its implications

For the saturated model proposed herein, whereby the loss of NH_3 from $[TAG+NH_4]^+$ is the rate-determining step, the subsequent DAG^+ fragments formed must be at or below this activation barrier.

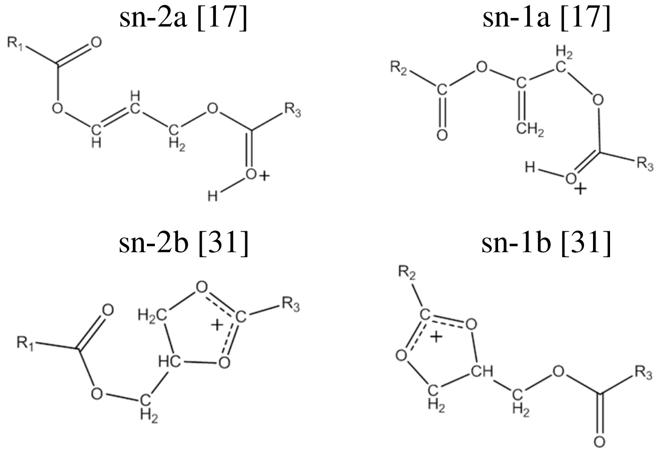

Figure 7-10 Proposed DAG^+ fragment structures found in literature

While a variety of DAG^+ structures have been proposed, none to our knowledge have been subjected to detailed computational analysis. DAG^+ structures were derived from those proposed by McAnoy and co-workers [17], and Lauer and co-workers [31] (Figure 7-10) and a relative energy diagram involving the distal and proximal $[TAG+H]^+$ structures was generated (Figure 7-11).

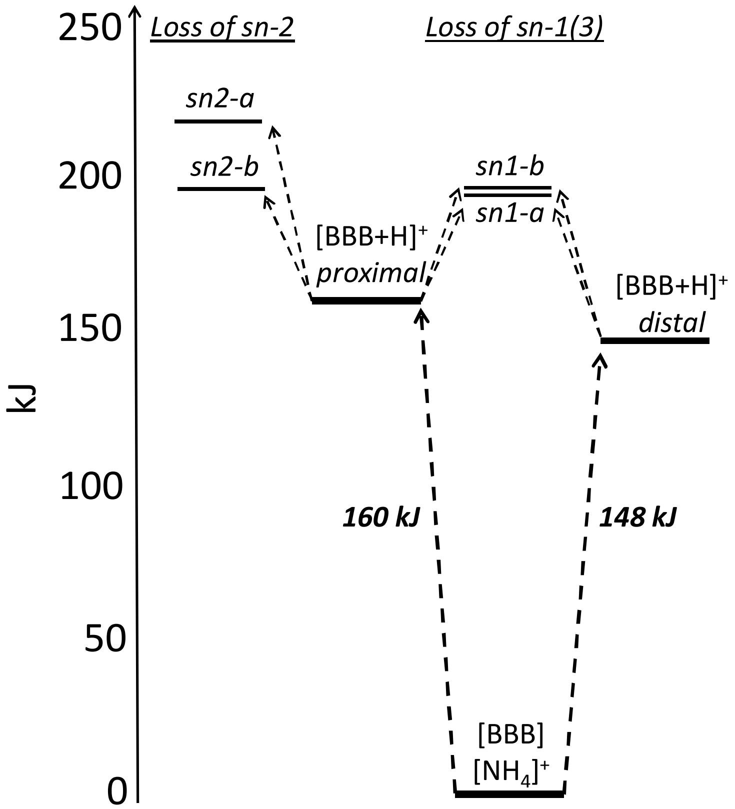

Figure 7-11 Relative energy ladder of [TAG][NH_4^+] dissociation pathways
Relative energy ladder obtained for the optimized B3LYP 6-311g(d,p) structures for ammoniated glyceryl tributyrate, to protonated glyceryl tributyrate, to proposed DAG^+ fragments shown in Figure 7-10.

Although the DAG^+ structures proposed by Lauer et al. [31] were fragments produced by electron impact of TAGs, they could potentially be produced by CID from electrosprayed TAGs and have also been proposed by Marzilli et al. [18] and thus were included in the study.

In structures proposed by McAnoy and co-workers [17] which fit with deuterium labelling experiments, the loss of R_nCOOH occurs with hydrogen shifts that result in a DAG^+ with a double bond in the glycerol backbone. Depending on if the sn-2 or a sn-1(3) RCOOH is lost, the DAG^+ ion will be structurally different (Figure 7-10: sn1a, sn2a). Another DAG^+ structure involves the formation of DAG^+ containing a 5-member 1,3-dioxolane substructure (Figure 7-10:

sn1b, sn2b). This structure, however, produces an equivalent DAG^+ final product regardless if an sn-1(3) or sn-2 position is lost (when all FAs are equivalent).

For DAG^+ ions that contain a double bond on the glycerol backbone (sn1a, sn1b), the structure arising from the less favorable loss of the sn-2 FA is 218 kJ mol^{-1} in energy above the ammoniated structure, and the structure that arises from loss of sn-1(3) sits at 194 kJ mol^{-1}. Although this would explain the favorable loss of the sn-1(3) FAs, they may not agree with MS^3 studies [11, 18] which looked at the fragmentation of the DAG^+ ions and suggest that the final DAG^+ products that occur from loss of either an sn-1(3) or sn-2 FAs are structurally equivalent. 1,3 dioxolane structures generated from TAGs that have lost an sn-1(3) or sn-2 RCOOH and the resulting optimized structure and their calculated energies are nearly equivalent, both sitting at 196 kJ mol^{-1} above the $[TAG+NH_4]^+$ reactant ion. Therefore, the proposed 1,3-dioxolane DAG^+ [18][31] would corroborate the MS^3 results, as the loss of the sn-1(3) or the sn-2 position would result in an equivalent fragment structure. Also, these structures occur at a modest 35 or 48 kJ mol^{-1} above the proximal or distal $[TAG+H]^+$ structures, respectively, and the presence of a reverse activation barrier for the loss of NH_3 could put the deamination step well above the loss of R_nCOOH, explaining why often little or no $[TAG+H]^+$ ions are observed. The structures would also agree with the masses of fragment ions reported in deuterium labelling studies [17].

The effects of double-bonds upon the observed fragmentation

Within the series of TAGs of this study, the closest double bond to the glycerol moiety was at C-9 for both oleic acid and linoleic acid yet the presence of a double bond greatly increased the likelihood of that FA dissociating as a neutral (Table 7-1). MM/MD simulations of $[POP+NH_4]^+$ resulted in low energy structures with the carbonyl oxygens of the FA interacting with NH_4^+ (Figure 7-12 9a,b), similar to that observed with B3LYP/6-311+g(d,p) of glyceryl tributyrate. The alkyl chains of terminal palmitic acids were extended and the alkyl chain of the sn-2 oleic acid adopted a 'horseshoe' structure surrounding the NH_4^+ cation.

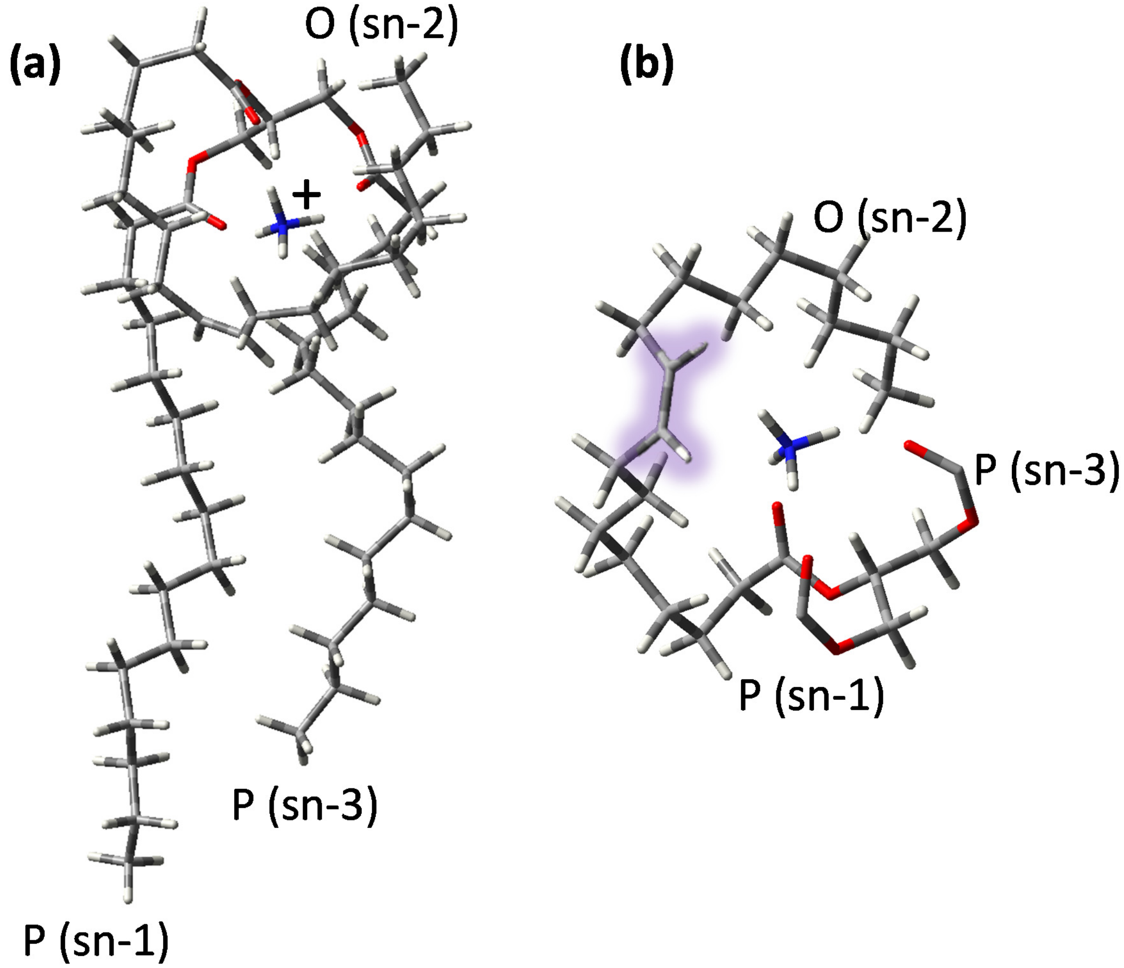

Figure 7-12 Lowest energy MM/MD structure of $[POP+NH_4]^+$

Lowest energy MM/MD structure of (a) $[POP+NH_4]^+$. (b) For clarity, an expansion taken from (a) with the alkyl sn-1 and sn-3 chains removed and oleic acid double bond highlighted.

In general, the proton affinity (PA) of a hydrocarbon is increased by the presence of a double bond. For example the PA of ethane and ethene is 596.3 kJ mol^{-1} and 680.5 kJ mol^{-1} respectively and the PA of propane and propene is 625.7 kJ mol^{-1} and 751.6 kJ mol^{-1} respectively [32]. The number of double bonds can also increase the PA of a hydrocarbon, as seen with trans-butene and 1,3-butadiene which have PA values of 747 and 783.4 kJ mol^{-1} respectively [32]. It is feasible that in addition to the carbonyl oxygens, the double bonds of the FA chains of $[TAG+NH_4]^+$ ions are in sufficient proximity to also interact with the NH_4^+ cation. This would stabilize the NH_4^+ in $[TAG+NH_4]^+$ and potentially, the proton in the $[TAG+H]^+$ intermediate and would lower the potential energy well of that intermediate. Increasing the degree of unsaturation of a TAG increases relative abundance of the $[TAG+H]^+$ ion because the barrier to the loss of NH_3 would now occur at or below the barrier for the loss of the FA. This would cause some of the ion population of $[TAG+H]^+$ to be generated without sufficient energy to be consumed immediately in the formation of DAG^+ products. The positive correlation between the degree of TAG unsaturation and the relative intensity of the $[TAG+H]^+$ has been observed experimentally in a number of molecular systems, most evidently by Evans and co-workers who investigated the relative fragment ion intensities of a series of linoleate and arachidonate TAGs [20]. McAnoy and co-workers observed some charge-remote fragmentation pathways as minor products in deuterium labelling experiments of unsaturated $[TAG+NH_4]^+$ [17]. The increased stability of the NH_4^+ caused by TAG unsaturation leading to an increased potential energy well depth could allow for some of these higher energy, charge remote fragmentation pathways to begin to be observed. This model also explains how a double bond(s) would affect the ratio of DAG^+ ions observed. Referring back to the MS/MS of POP, the E_0 values for the loss of palmitic acid and oleic acid are nearly identical (Table 7-1), which indicates that regardless of position, the influence of the oleic acid double bond is significant. If the dissociation of each of the three FAs on the glycerol backbone were independent, competing events, we would expect that MS/MS of POL would again show the sn-1 palmitic and sn-2 oleic to have similar energetics of dissociation and the dissociation of sn-3 linoleic to be the most favorable due to not only having the advantage of double bonds but also being at the sn-3 position. This is not the case, as seen in the breakdown diagram Figure 7-5c,d which shows that the terminal palmitic and linoleic acid loss occurs in an almost equivalent manner, both doing so in a much more favorable amount than the loss of sn-2 oleic acid. It should be noted that the pathway leading to the loss of sn-3 linoleic was slightly more intense then the pathway leading to the loss of sn-1 palmitic. The fact that a double bond in the sn-3 position FA has such an influence on the dissociation of the sn-1 FA strongly points to there being a shared pathway. The double bond on the linoleic acid stabilizes the proton and lowers the barrier to the distal $[TAG+H]^+$ intermediate. From the distal intermediate, the sn-1 palmitic acid and the sn-3 linoleic acid can dissociate as a neutral in proportions that can still be affected in some way by the double bond. It should also be mentioned that the relative intensity of the sn-1 and sn-3 loss DAG^+ ions began to deviate greatly at higher energies, but this occurs in conjunction with the appearance and growth of lower mass fragment ions that are derived from the DAG^+ fragments.

7.6 Conclusions

Based on MS/MS of $[TAG+NH_4]^+$ at multiple collision energies and computational analysis, the reasons for the enhanced loss of FAs at the sn-1 or sn-3 position are provided. An energetically more stable $[TAG+H]^+$ structure occurs for a proton being shared by the sn-1 and sn-3 carbonyl oxygen (distal intermediate) than a proton bridging a terminal carbonyl oxygen and sn-2 carbonyl oxygen (proximal intermediate). This is countered by the higher entropy of the proximal intermediate. In the absence of double bonds, the barrier to generate $[TAG+H]^+$ from $[TAG+NH_4]^+$ lies at or above that required for a FA to dissociate as a neutral. Based on a shared dissociation pathway for the loss of sn-1 and sn-3, the propensity of a neutral FA to dissociate from a protonated triacylglyceride is not only based on its backbone position or identity, but also upon the other FAs that make up the triacylglyceride.

7.7 References

1. Christie, W. W., Lipid analysis, Vol. 338, Pergamon Press Oxford, 1982.
2. Murata, T., Takahashi, S. Analysis of triglyceride mixtures by gas chromatography-mass spectrometry. Analytical chemistry 45, 1816-1823 (1973)
3. Fenn, J. B.; Mann, M.; Meng, C. K.; Wong, S. F., Whitehouse, C. M. Electrospray ionization for mass spectrometry of large biomolecules. Science 246, 64-71 (1989)
4. Duffin, K. L.; Henion, J. D., Shieh, J. Electrospray and tandem mass spectrometric characterization of acylglycerol mixtures that are dissolved in nonpolar solvents. Analytical chemistry 63, 1781-1788 (1991)
5. Herrera, L. C.; Potvin, M. A., Melanson, J. E. Quantitative analysis of positional isomers of triacylglycerols via electrospray ionization tandem mass spectrometry of sodiated adducts. Rapid communications in mass spectrometry 24, 2745-2752 (2010)
6. Han, X.; Abendschein, D. R.; Kelley, J. G., Gross, R. W. Diabetes-induced changes in specific lipid molecular species in rat myocardium. Biochemical Journal 352, 79 (2000)
7. Hsu, F.-F., Turk, J. Structural characterization of triacylglycerols as lithiated adducts by electrospray ionization mass spectrometry using low-energy collisionally activated dissociation on a triple stage quadrupole instrument. Journal of the American Society for Mass Spectrometry 10, 587-599 (1999)
8. Herrera, L. C.; Ramaley, L.; Potvin, M. A., Melanson, J. E. A method for determining regioisomer abundances of polyunsaturated triacylglycerols in omega-3 enriched fish oils using reversed-phase liquid chromatography and triple-stage mass spectrometry. Food Chemistry (2013)
9. Lin, J.-T., Arcinas, A. Analysis of Regiospecific Triacylglycerols by Electrospray Ionization− Mass Spectrometry3 of Lithiated Adducts. Journal of agricultural and food chemistry 56, 4909-4915 (2008)
10. Lévêque, N. L.; Héron, S., Tchapla, A. Regioisomer characterization of triacylglycerols by non-aqueous reversed-phase liquid chromatography/electrospray ionization mass spectrometry using silver nitrate as a postcolumn reagent. Journal of Mass Spectrometry 45, 284-296 (2010)
11. Byrdwell, W., Neff, W. E. Dual parallel electrospray ionization and atmospheric pressure chemical ionization mass spectrometry (MS), MS/MS and MS/MS/MS for the analysis of triacylglycerols and triacylglycerol oxidation products. Rapid communications in mass spectrometry 16, 300-319 (2002)

12. Li, X.; Collins, E. J., Evans, J. J. Examining the collision-induced decomposition spectra of ammoniated triglycerides as a function of fatty acid chain length and degree of unsaturation. II. The PXP/YPY series. Rapid communications in mass spectrometry 20, 171-177 (2006)

13. Lien, E. L.; Boyle, F. G.; Yuhas, R.; Tomarelli, R. M., Quinlan, P. The effect of triglyceride positional distribution on fatty acid absorption in rats. Journal of pediatric gastroenterology and nutrition 25, 167-174 (1997)

14. Malone, M., Evans, J. Determining the relative amounts of positional isomers in complex mixtures of triglycerides using reversed-phase high-performance liquid chromatography-tandem mass spectrometry. Lipids 39, 273-284 (2004)

15. Mottram, H. R.; Woodbury, S. E., Evershed, R. P. Identification of triacylglycerol positional isomers present in vegetable oils by high performance liquid chromatography/atmospheric pressure chemical ionization mass spectrometry. Rapid communications in mass spectrometry 11, 1240-1252 (1997)

16. Mottram, H. R., Evershed, R. P. Structure analysis of triacylglycerol positional isomers using atmospheric pressure chemical ionisation mass spectrometry. Tetrahedron letters 37, 8593-8596 (1996)

17. McAnoy, A. M.; Wu, C. C., Murphy, R. C. Direct qualitative analysis of triacylglycerols by electrospray mass spectrometry using a linear ion trap. Journal of the American Society for Mass Spectrometry 16, 1498-1509 (2005)

18. Marzilli, L. A.; Fay, L. B.; Dionisi, F., Vouros, P. Structural characterization of triacylglycerols using electrospray ionization-MSn ion-trap MS. Journal of the American Oil Chemists' Society 80, 195-202 (2003)

19. Li, X., Evans, J. J. Examining the collision-induced decomposition spectra of ammoniated triglycerides as a function of fatty acid chain length and degree of unsaturation. I. The OXO/YOY series. Rapid communications in mass spectrometry 19, 2528-2538 (2005)

20. Gakwaya, R.; Li, X.; Wong, Y. L.; Chivukula, S.; Collins, E. J., Evans, J. J. Examining the collision-induced decomposition spectra of ammoniated triglycerides. III. The linoleate and arachidonate series. Rapid communications in mass spectrometry 21, 3262-3268 (2007)

21. Mayer, P. M., Martineau, E. Gas-phase binding energies for non-covalent Aβ-40 peptide/small molecule complexes from CID mass spectrometry and RRKM theory. Physical Chemistry Chemical Physics 13, 5178-5186 (2011)

22. Renaud, J. B.; Martineau, E.; Mironov, G. G.; Berezovski, M. V., Mayer, P. M. The collaborative role of molecular conformation and energetics in the binding of gas-phase non-covalent polymer/amine complexes. Physical Chemistry Chemical Physics 14, 165-172 (2012)
23. Dewar, M. J.; Zoebisch, E. G.; Healy, E. F., Stewart, J. J. Development and use of quantum mechanical molecular models. 76. AM1: a new general purpose quantum mechanical molecular model. Journal of the American Chemical Society 107, 3902-3909 (1985)
24. Frisch, M. J.; Trucks, G. W.; Schlegel, H. B.; Scuseria, G. E.; Robb, M. A.; Cheeseman, J. R.; Scalmani, G.; Barone, V.; Mennucci, B.; Petersson, G. A.; Nakatsuji, H.; Caricato, M.; Li, X.; Hratchian, H. P.; Izmaylov, A. F.; Bloino, J.; Zheng, G.; Sonnenberg, J. L.; Hada, M.; Ehara, M.; Toyota, K.; Fukuda, R.; Hasegawa, J.; Ishida, M.; Nakajima, T.; Honda, Y.; Kitao, O.; Nakai, H.; Vreven, T.; Montgomery, J. A.; Peralta, J. E.; Ogliaro, F.; Bearpark, M.; Heyd, J. J.; Brothers, E.; Kudin, K. N.; Staroverov, V. N.; Kobayashi, R.; Normand, J.; Raghavachari, K.; Rendell, A.; Burant, J. C.; Iyengar, S. S.; Tomasi, J.; Cossi, M.; Rega, N.; Millam, J. M.; Klene, M.; Knox, J. E.; Cross, J. B.; Bakken, V.; Adamo, C.; Jaramillo, J.; Gomperts, R.; Stratmann, R. E.; Yazyev, O.; Austin, A. J.; Cammi, R.; Pomelli, C.; Ochterski, J. W.; Martin, R. L.; Morokuma, K.; Zakrzewski, V. G.; Voth, G. A.; Salvador, P.; Dannenberg, J. J.; Dapprich, S.; Daniels, A. D.; Farkas, Ö.; Foresman, J. B.; Ortiz, J. V.; Cioslowski, J., Fox, D. J. Gaussian 09. Inc., Wallingford, CT (2009)
25. Beyer, T., Swinehart, D. Algorithm 448: number of multiply-restricted partitions. Communications of the ACM 16, 379 (1973)
26. Baer, T., Mayer, P. M. Statistical Rice-Ramsperger-Kassel-Marcus quasiequilibrium theory calculations in mass spectrometry. Journal of the American Society for Mass Spectrometry 8, 103-115 (1997)
27. Becke, A. D. Density-functional thermochemistry. III. The role of exact exchange. The Journal of Chemical Physics 98, 5648 (1993)
28. Stephens, P. J.; Devlin, F. J.; Chabalowski, C. F., Frisch, M. J. Ab Initio Calculation of Vibrational Absorption and Circular Dichroism Spectra Using Density Functional Force Fields. The Journal of Physical Chemistry 98, 11623-11627 (1994)
29. Case, D. A.; Darden, T. A.; III, T. E. C.; Simmerling, C. L.; Wang, J.; Duke, R. E.; Luo, R.; Merz, K. M.; Pearlman, D. A.; Crowley, M.; Walker, R. C.; Zhang, W.; Wang, B.; Hayik, S.; Roitberg, A.; Seabra, G.; Wong, K. F.; Paesani, F.; Wu, X.; Brozell, S.; Tsui, V.; Gohlke, H.; Yang, L.; Tan, C.; Mongan, J.; Hornak, V.; Cui, G.; Beroza, P.; Mathews, D. H.; Schafmeister, C.; Ross, W. S., Kollman, P. A. AMBER 9. University of California, San Francisco, CA (2006)

30. Wang, J.; Wolf, R. M.; Caldwell, J. W.; Kollman, P. A., Case, D. E. Development and Testing of a General Amber Force Field. Journal of Computational Chemistry 25, 17 (2004)
31. Lauer, W.; Aasen, A.; Graff, G., Holman, R. Mass spectrometry of triglycerides: I. Structural effects. Lipids 5, 861-868 (1970)
32. Hunter, E. P., Lias, S. G. Evaluated Gas Phase Basicities and Proton Affinities of Molecules: An Update,. J. Phys. Chem. Ref. Data 27, 413-656 (1998)

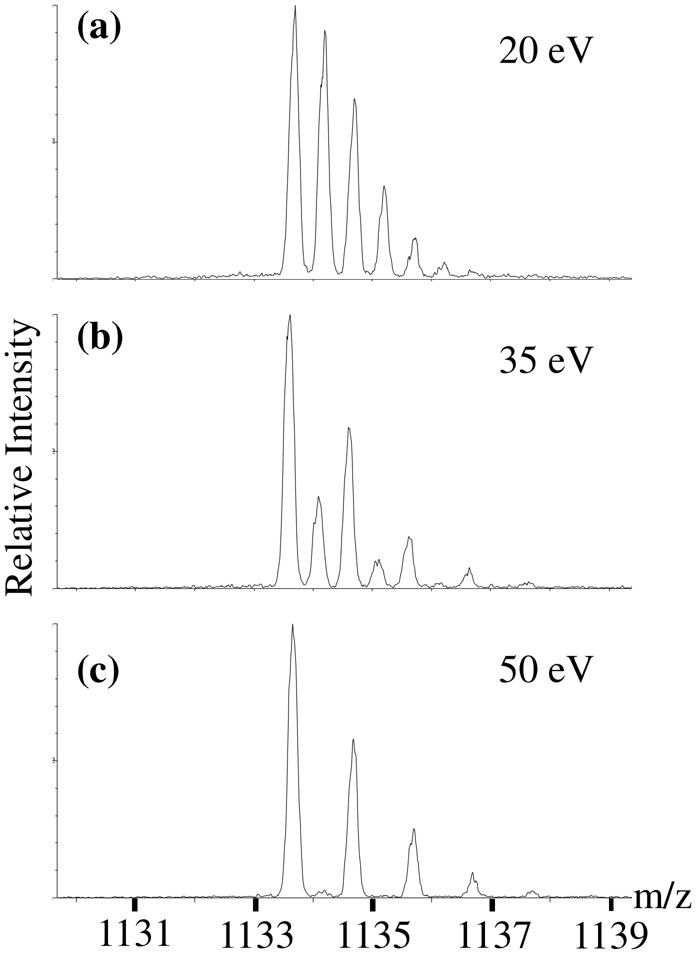
(a)
20 eV
(b)
35 eV
(c)
50 eV
Relative Intensity
m/z
1131
1133
1135
1137
1139

8.1 Objectives

- Utilize IMS before CID to generate breakdown diagrams of overlapping, multimeric complexes
- Generate breakdown diagrams for dissociations where reactant and product ions have identical m/z

8.2 Chapter acknowledgements

J. B. Renaud thanks

- Kevin Berland for assistance in obtaining experimental data
- Gleb Mironov for insightful discussion

8.3 Introduction

Cyclodextrins (CD) are well known to form non-covalent complexes with substrates as well as multimeric aggregates [1, 2]. Solution phase interactions between CD and some substrates are believed to driven primarily by 'hydrophobic' interactions [3] when a substrate is capable of fitting into the inner cavity of the CD host. This interaction is often modelled in a 1:1 host:substrate manner [4], however this is possibly an over simplification of the global interactions taking place [5]. For example, ^{1}H-NOESY experiments have shown the existence of two binding modes between CD and cinchona alkaloids in solution [6] which has been interpreted by Wen and co-workers [7] as evidence for both a 1:1 and 2:1 CD–substrate molecular interaction. Using molecular modelling and phase solubility diagrams, Wen proposed the formation of 'sandwich-type' inclusion complexes of two CD and a cinchonine, but it is possible that an even wider variety of binding stoichiometries are present.

Electrospray ionization (ESI) mass spectrometry (MS) of certain chemical species is often able to detect a rich variety of multimeric complexes, clusters and aggregates that could be present in solution as well as formed by the ESI process. One method used to investigate the energetics at play within non-covalent complexes is tandem mass spectrometry (MS/MS) followed by RRKM modelling of breakdown diagrams in order to obtain critical energies (E_0) and entropies of activation ($\Delta S^{\ddagger}$) for each dissociation channel.

MS/MS is used to generate breakdown diagrams by measuring the relative intensity of the reactant and fragment ions as a function of collision energy. However, generating a breakdown diagram of some multimeric complexes can be complicated when the reactant ion m/z is overlapped with other compounds. This readily occurs when studying compounds such as CD that have a propensity to form aggregates. For example, a singly deprotonated CD monomer

($[M\text{-}H^+]^{-1}$) will have the same monoisotopic m/z as a doubly deprotonated CD dimer ($[(M)_2\text{-}2H^+]^{-2}$), a triply deprotonated CD trimer ($[(M)_3\text{-}3H^+]^{-3}$), and so forth. With sufficient mass resolution, the existence of overlapping multimeric complexes can be detected based on the observed isotopic distributions. The mass difference between a ^{12}C and a ^{13}C isotope is 1.00 Da and therefore the m/z separation between isotopic peaks would be 1.0 m/z and 0.50 m/z for singly and doubly charged compounds respectively.

Kralj, Šmidovnik and Kobe used a combination of ESI-IMS-MS, ESI-MS and ESI-MS/MS to explore interactions between α or β-CD with positional isomers of coumaric acid [8]. Using ESI-MS, they identified the established 1:1 complex, $[CD\text{+substrate-}H^+]^{-1}$, as well as significant signals for multimeric complexes including $[(CD)_2\text{-}2H^+]^{-2}$, $[(CD)_2\text{+substrate-}2H^+]^{-2}$ and $[(CD)_2\text{+substrate-}H^+)_2]^{-2}$. The fragmentation pathways of the multimeric CD complexes were identified using ESI-MS/MS of a combined dimer/monomer m/z signal. Although the monoisotopic m/z of related multimeric complexes can be identical, their experimental collision cross sections (Ω_{exp}) and charge are often sufficiently different to give distinct arrival time distributions using ion mobility spectrometry (IMS). Kralj, Šmidovnik and Kobe showed that ESI-IMS is able to separate overlapping mass spectral signals of deprotonated CD monomers and dimers.

In this work, we have developed an approach to investigate the gas phase energetics of overlapping multimeric complexes using combinations of IMS and MS/MS that allow for breakdown diagrams to be generated and modelled. Furthermore, when fragment ions possess the same monoisotopic m/z as the reactant ion, we demonstrate how the percentage of complex dissociation can be obtained by monitoring changes in the isotope profile. Based on the findings of Kralj, Šmidovnik and Kobe that identified the presence of CD multimeric complexes in ESI-

MS and ability of IMS to separated overlapping signals, β-CD was chosen as a model system. The energetics of β-CD dimeric complexes alone and with two different organic substrates were investigated by using IMS to mobility separate different molecular species with identical monoisotopic m/z followed by MS/MS. The breakdown diagrams were modelled with RRKM unimolecular rate theory and the results connected with structural data obtained with IMS.

Materials

β-Cyclodextrin (β-CD), 4,4'-(propane-1,3-diyl) dibenzoic acid (PDDA) and Ibuprofen (Ibu) were purchased from Sigma-Aldrich (St. Louis). 40 μM solutions of β-CD were prepared in 90:10, HPLC grade methanol:water. Substrate/ β-CD mixtures contained 40 μM β-CD and 20 μM substrate prepared in 90:10, HPLC grade methanol:water.

ESI-MS

MS was acquired in negative mode ESI on a Waters Synapt G1 Mass spectrometer in 'V' resolution mode and the sample was introduced via syringe pump at 10μL min^{-1}. The capillary, sample cone and extracting cone voltages were held constant at 3.0 kV, 40 V, and 4 V respectively and the source and desolvation temperatures were 100°C and 200 °C respectively. Ω_{exp} measurements were derived from IMS drift times using a α,ω-dicarboxy polystyrene [9] and decathymidine standards [10] according to procedure outlined by Smith et al. [11] IMS buffer gas was N_2 at a flow rate of 24 mL min^{-1}. The reported Ω_{exp} are averages obtained from 4 different combinations of wave height and wave velocities: 20V-1250 m/s, 20V-1050 m/s, 15V-1050 m/s and 13V-850m/s. Ω_{exp} uncertainties reported are standard deviations of the Ω_{exp} values measured at different mobility settings, while absolute uncertainties resulting from uncertainties in the calibration curve are ~8%. Ions were mass selected at a LM and HM resolution of 5.0 and 7.0 on the Masslynx 4.0 software to transmit the complete isotope profile through the quadrupole. CID was accomplished post-IMS in the transfer cell with an argon flow rate of 1.0 mL min^{-1} at collision energy intervals of 1.0 eV for 1.0 min acquisition at each collision energy.

Breakdown diagrams were generated by plotting the relative intensities of the reactant and fragment ions as a function of center-of-mass collision energy (E_{com}).

Theoretical breakdown curves

The description of our RRKM fitting of experimental breakdown curves is described in detail in chapters 3 and 4 [12, 13]. Vibrational frequencies of $[\beta\text{-CD-H}^+]^{-1}$ and neutral substrate molecules were calculated at the AM1 level [14] in the Gaussian 09 program suite [15]. Using these frequencies, reactant densities of states and transition state sums-of-states were calculated by direct count according to the algorithm of Beyer and Swinehart [16, 17]. The effective temperature (T_{eff}) of the reactant ions at E_{com} is approximated by:

$$\mathbf{T_{eff} = 400K + \alpha\, KeV^{-1} \cdot (E_{com})} \qquad \text{Equation 8-1}$$

The α value represents a linear approximation between the T_{eff} and E_{com} and 400K is an approximation of the initial temperature. A critical oscillator was removed and thousands of theoretical breakdown curves were automatically generated by altering the E_0 and the eight lowest vibrational frequencies of the transition state. The approximate nature of the assigned post-collision internal energy distribution of the dissociating ions means that the values for $\Delta S^{\ddagger}$ and E_0 derived herein must be taken as approximate only. However, due to the structural similarity of the relative values of these quantities should be reliable for comparison. Uncertainties of E_0 and $\Delta S^{\ddagger}$ listed within this study represent uncertainties of the theoretical fit only and do not reflect the absolute uncertainly due to the approximate nature of equation 8-1. For complexes with greater than one dissociation channel, the E_0 and $\Delta S^{\ddagger}$ of all channels were expressed in relation to the most dominant channel in order to obtain a suitable branching relationship (See Chapter 6).

ESI-MS of β-CD and organic substrate solutions

ESI-MS of a 40 µM β-CD solution under the conditions described yields a prominent signal at 1133.4 m/z (Figure 8-1). Close examination of the 1133.4 m/z signal shows a staggered isotopic profile; major isotope peaks separated by 1 m/z and interposed minor peaks separated by 0.5 m/z (Figure 8-1b). The singly deprotonated monomer, $[\beta\text{-CD-H}^+]^{-1}$ has the same monoisotopic m/z of the doubly deprotonated dimer, $[(\beta\text{-CD})_2\text{-2H}^+]^{-2}$ and the co-occurrence of both species is evident by differences in ^{13}C isotope separation. Under the experimental conditions used, many other β-CD containing compounds were observed in the mass spectrum including 562.2 m/z, $[\beta\text{-CD-2H}^+]^{-2}$; 1169.4 m/z, $[\beta\text{-CD+Cl}^-]^{-1}$ / $[(\beta\text{-CD})_2\text{ +2Cl}^-]^{-2}$; 1179.4 m/z, $[\beta\text{-CD+HCO}_2^-]^{-1}$; 1700.5 m/z, $[(\beta\text{-CD})_3\text{-2H}^+]^{-2}$ and 2267.7, $[(\beta\text{-CD})_2\text{-H}^+]^{-1}$.

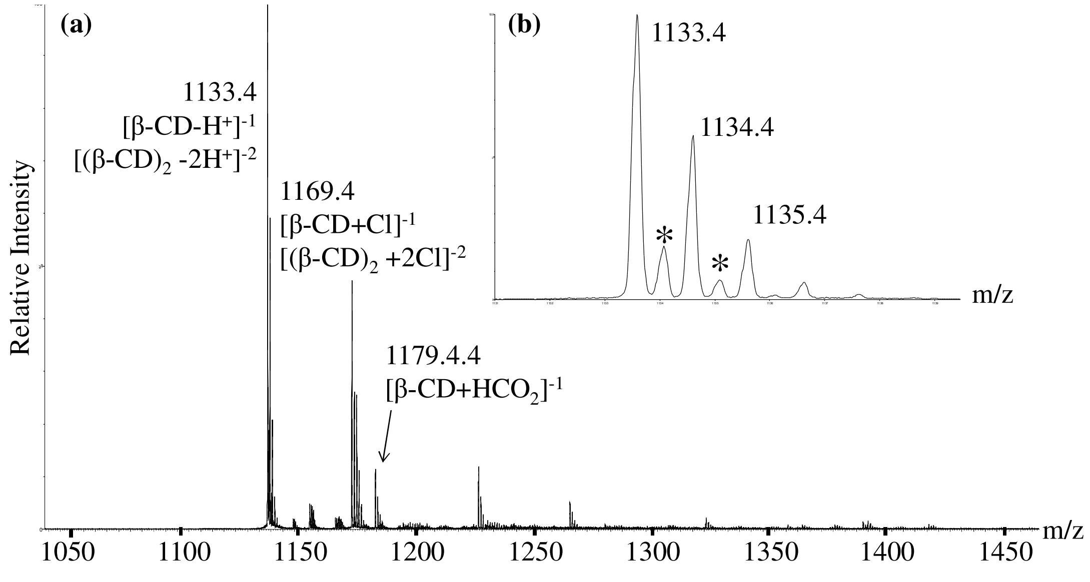

Figure 8-1 ESI-MS of 40 µM β-CD solution
(a) ESI-MS of 40 µM β-CD solution. Multiple adducts β-CD and multimeric complexes are observed and (b) the most prominent peak at 1133.4 m/z is a combination of $[(\beta\text{-CD})_2\text{ -2H}^+]^{-2}$ and $[\beta\text{-CD-H}^+]^{-1}$(*)as seen by the staggered isotope distribution

β-CD was mixed in a 2:1 molar ratio with either Ibu or PDDA in order to favour the complexation of multiple β-CD with a single organic substrate (Figure 8-2)

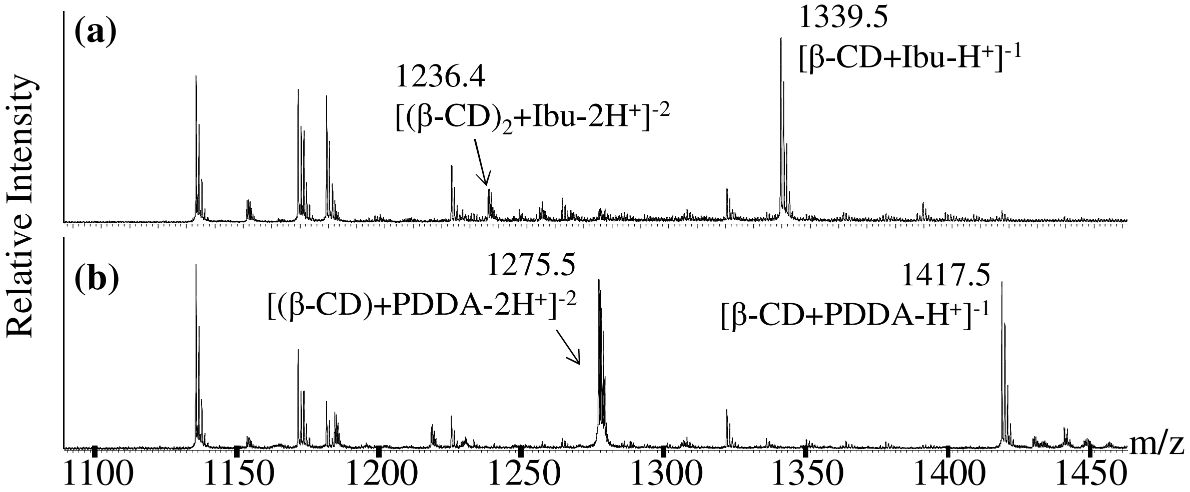

Figure 8-2 ESI-MS of 40 µM β-CD with 20 µM (a) Ibu and (b) PDDA $[\beta\text{-CD+substrate-H}^+]^{-1}$ and $[(\beta\text{-CD})_2\text{+substrate-2H}^+]^{-2}$ are observed for both compounds.

Ibu and PDDA were used as substrates primarily because they have similar reported gas phase E_0 of dissociation in a 1:1 β-CD complex [18], yet differ in length and number of carboxylic groups. ESI-MS of the β-CD-Ibu solution resulted in signals for $[\beta\text{-CD+Ibu-H}^+]^{-1}$ as well as a signals that corresponded to $[(\beta\text{-CD})_2\text{+Ibu-2H}^+]^{-2}$ and $[(\beta\text{-CD+Ibu-H}^+)_2]^{-2}$ (Figure 8-2a). The summed isotope intensity of the dimer species $[(\beta\text{-CD})_2\text{+Ibu-H}^+]^{-2}$ was 30% of the intensity of the monomer species $[\beta\text{-CD+Ibu-H}^+]^{-1}$. In comparison, under the same experimental conditions the summed isotope intensity of $[(\beta\text{-CD})_2\text{+PDDA-2H}^+]^{-2}$ was 183% greater than the 1:1 bound complex of $[\beta\text{-CD+PDDA-H}^+]^{-1}$ (Figure 8-2b), suggesting a greater ability for PDDA to form multimeric complexes with β-CD. In solution studies, Peña determined that a 2:1 CD complex formation was favoured for a pyrene substrate because pyrene is not able to be completely enveloped by a single CD, leaving a portion of the substrate available for a secondary association [19]. PDDA is not only longer than Ibu, it contains a secondary carboxylic acid group which could allow it to more easily form electrostatic interactions with two CD molecules.

ESI-IMS separation of $[\beta\text{-CD-H}^+]^{-1}$ and $[(\beta\text{-CD})_2\text{-2H}^+]^{-2}$

The monomer $[\beta\text{-CD-H}^+]^{-1}$ and dimer $[(\beta\text{-CD})_2\text{-2H}^+]^{-2}$ have an identical monoisotopic m/z of 1133.4. ESI-IMS-MS of m/z 1133.4 shows two distinct arrival time distributions (ATD) (Figure 8-3a).

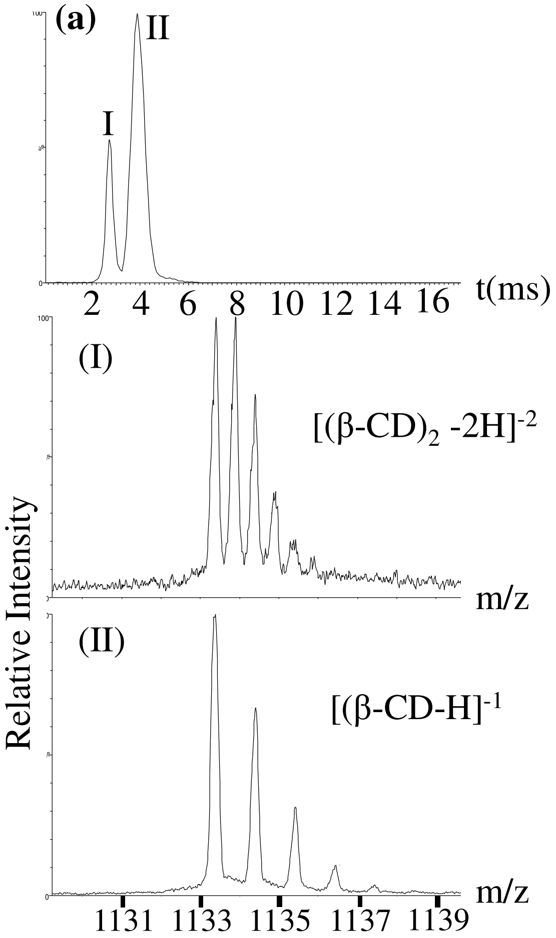

Figure 8-3 Arrival time distribution of mass selected 1130-1340 m/z
Arrival time distribution of mass selected 1130-1340 m/z showing two distributions. The fastest arrival distribution I corresponds to $[(\beta\text{-CD})_2\text{ -2H}^+]^{-2}$ and arrival distribution II corresponds to $[\beta\text{-CD-H}^+]^{-1}$

The mass spectrum of the fastest IMS ATD (I) has isotopic separations of 0.50 m/z which corresponds to the dimer $[(\beta\text{-CD})_2\text{-}2H^+]^{-2}$ (Figure 8-3I). The slower ATD (II) has an isotopic profile separated by 1.00 m/z, which corresponds to the monomer $[\beta\text{-CD-}H^+]^{-1}$ (Figure 8-3II). Generating a breakdown diagram of $[(\beta\text{-CD})_2\text{-}2H^+]^{-2}$ with MS/MS alone would not be possible because of spectral overlap. Using IMS as a filter prior to MS/MS in the transfer cell would allow for a pure signal to be obtained which could then be fragmented at varying collision energies to obtain a breakdown diagram.

Determining proportion of $[(\beta\text{-CD})_2\text{-}2H^+]^{-2}$ dissociation by monitoring changes in isotopic profile

Generating a breakdown diagram for the singly charged dimer; $[(\beta\text{-CD})_2\text{-}H^+]^{-1}$ (2267.8 m/z) is straightforward as it dissociates by the loss of neutral $[(\beta\text{-CD}]^0$ to give a single $[\beta\text{-CD-}H^+]^{-1}$ product ion at m/z 1133.4. Generating a breakdown diagram of $[(\beta\text{-CD})_2\text{-}2H^+]^{-2}$ is not straightforward. The reactant ion; $[(\beta\text{-CD})_2\text{-}2H^+]^{-2}$ and product ions; $[\beta\text{-CD-}H^+]^{-1}$ have the same monoisotopic mass and the main evidence of a dissociation taking place is the transformation of the isotopic profile by increasing collision energy (Figure 8-4).

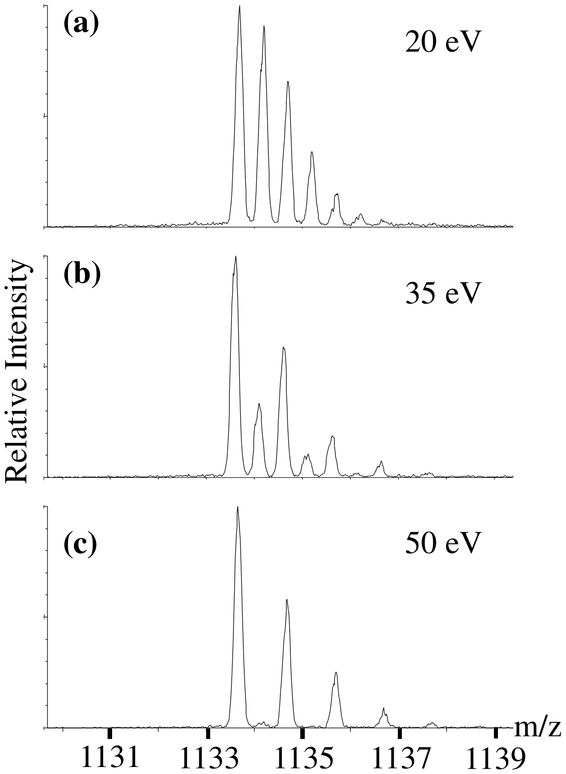

Figure 8-4 Change in isotope profile during MS/MS of $[(\beta\text{-CD})_2\ \text{-}2H^+]^{-2}$ post IMS separation Change in isotope profile during MS/MS of $[(\beta\text{-CD})_2\ \text{-}2H^+]^{-2}$ post IMS separation. (a) at E_{lab} of 20 eV, signal is exclusively $[(\beta\text{-CD})_2\ \text{-}2H^+]^{-2}$ (b) E_{lab} of 35 eV is a mixture of $[(\beta\text{-CD})_2\ \text{-}2H^+]^{-2}$ and $[\beta\text{-CD}\ \text{–}H^+]^{-2}$ and (c) E_{lab} of 50 eV results in complete dissociation of $[(\beta\text{-CD})_2\ \text{-}2H^+]^{-2}$.

In Figure 8-4 only $[(\beta\text{-CD})_2\text{-}2H^+]^{-2}$ is present at a E_{lab} of 20eV, while at 35 eV an interspersed isotope profile is characteristic of the co-presence of $[(\beta\text{-CD})_2\text{-}2H^+]^{-2}$ and $[\beta\text{-CD-}H^+]^{-1}$. At an E_{lab} 50 eV the absence of 0.5 m/z separated isotope peaks shows that the signal is almost exclusively $[\beta\text{-CD-}H^+]^{-1}$.

In order to generate a breakdown diagram of $[(\beta\text{-CD})_2\text{-}2H^+]^{-2}$, the relative amounts of reactant ion, $[(\beta\text{-CD})_2\text{-}2H^+]^{-2}$ and fragment ion; $[\beta\text{-CD-}H^+]^{-1}$ were calculated based on changes in the isotopic profile. Only isotopic contributions from 0-2 m/z units above the reactant ion were considered. The observed natural abundance (NA) of each isotope (i) was obtained from the IMS resolved monomer and dimer at 3eV lab frame collision energy.

$$\mathbf{NA_i} = \frac{\mathbf{NA_i}}{\mathbf{NA_{0m/z}+NA_{+0.5m/z}+NA_{+1m/z}+NA_{+1.5m/z}+NA_{+2m/z}}} \qquad \text{Equation 8-2}$$

The proportion of dimer (D) within the co-presence of monomer (M) was defined as x,

$$\mathbf{x} = \frac{\mathbf{[D]}}{\mathbf{[D+M]}} \quad \text{Equation 8-3}$$

The observed experimentally abundance (OA) of each isotope (i) at a given collision energy was defined as:

$$\mathbf{OA_i} = \frac{\mathbf{OA_i}}{\mathbf{OA_{+0m/z}+OA_{+0.5m/z}+OA_{+1m/z}+OA{+}_{1.5m/z}+OA_{+2m/z}}} \qquad \text{Equation 8-4}$$

The proportion of dimer (x), can be mathematically determined using any of the isotope peaks, or as in this case the average of 5 isotopic peaks;

$$\mathbf{x} = \frac{\mathbf{OA_{0m/z}-NA.M_{0m/z}}}{\mathbf{NA.D_{0m/z}-NA.M_{0m/z}}} \qquad \text{Equation 8-5}$$

$$\mathbf{x} = \frac{\mathbf{OA_{+0.5m/z}}}{\mathbf{NA.D_{0m/z}}} \qquad \text{Equation 8-6}$$

$$\mathbf{x} = \frac{\mathbf{OA}_{+1m/z} - \mathbf{NA.M}_{+1m/z}}{\mathbf{NA.D}_{+1m/z} - \mathbf{NA.M}_{+1m/z}} \qquad \text{Equation 8-7}$$

$$\mathbf{x} = \frac{\mathbf{OA}_{+1.5m/z}}{\mathbf{NA.D}_{+1.5m/z}} \qquad \text{Equation 8-8}$$

$$\mathbf{x} = \frac{\mathbf{OA}_{+2m/z} - \mathbf{NA.M}_{+2m/z}}{\mathbf{NA.D}_{+2m/z} - \mathbf{NA.M}_{+2m/z}} \qquad \text{Equation 8-9}$$

$$\bar{\mathbf{x}} = \frac{\mathbf{x}_{+0m/z} + \mathbf{x}_{+0.5m/z} + \mathbf{x}_{+1m/z} + \mathbf{x}_{+1.5m/z} + \mathbf{x}_{+2.0m/z}}{\mathbf{5}} \qquad \text{Equation 8-10}$$

The final consideration is that a doubly charged dimer will produce two singly charged monomers which over represents the extent of dissociation of the reactant ion. Therefore, the percentage of dimer survival at a given collision energy is:

$$\%\textbf{Survival Dimer} = \frac{\bar{\mathbf{x}}}{\mathbf{0.5}(\mathbf{1} + \bar{\mathbf{x}})} \qquad \text{Equation 8-11}$$

This method was used to generate the breakdown diagram for $[(\beta\text{-CD})_2\text{-}2\text{H}^+]^{-2}$ in Figure 8-5.

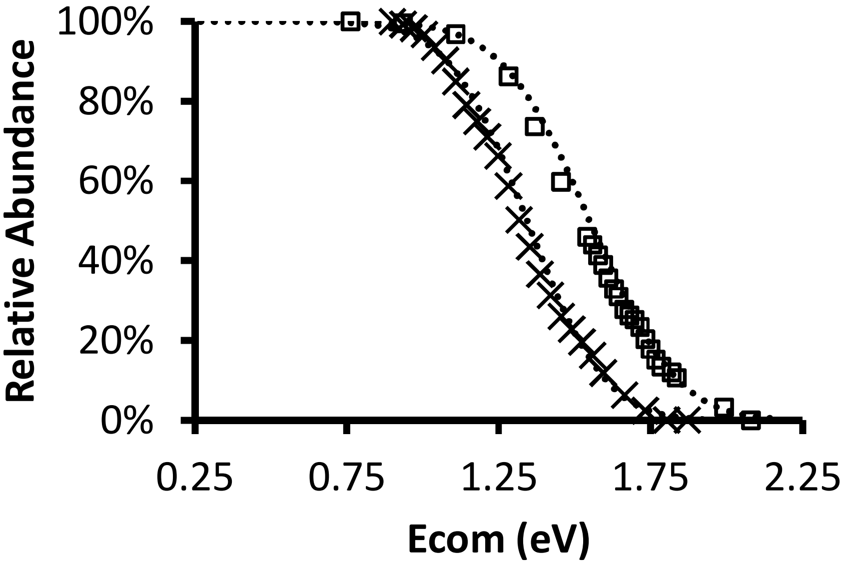

Figure 8-5 Experimental breakdown diagrams for -1 and -2 $(\beta\text{-CD})_2$
Experimental breakdown diagrams for (a) $[(\beta\text{-CD})_2\ \text{-}2\text{H}^+]^{-2}$ (×)and $[(\beta\text{-CD})_2\ \text{-H}^+]^{-1}$ (□).

Modelling the breakdown diagrams with RRKM theory allowed for the approximation of the critical energy, E_0, and $\Delta S^\ddagger$ for the dissociation of the complexes and which provides insight into dissociation process. In Figure 8-5a, it can be seen that the doubly charged ion; $[(\beta\text{-CD})_2\text{-}2H^+]^{-2}$ is less kinetically stable than the singly charged complex; $[\beta\text{-CD-}H^+]^{-1}$ as it dissociates at lower collision energy than the singly charged dimer. Accordingly, the best RRKM fits for the β-CD dimers gave E_0 values of 1.85 ± 0.11eV and 1.79 ± 0.09 for $[(\beta\text{-CD})_2\text{-}H^+]^{-1}$ and $[(\beta\text{-CD})_2\text{-}2H^+]^{-2}$, respectively. The entropics for this dissociation were nearly equivalent at 53 ± 16 and 54 ± 19 J K^{-1}. The $\Delta S^\ddagger$ for dissociation of this complexes are positive that suggests that given the rigid nature of the compounds, limited conformational reorganization is required. The slightly lower E_0 for the doubly charged complex suggests that the dimer is slightly less stable due to coulombic repulsive forces.

Table 8-1 RRKM derived E_0 and $\Delta S^\ddagger$ values for the dissociation of $[(\beta\text{-CD})_2 - nH^+]^{-n}$

Parent Ion	Dissociation Pathway	E_0 (eV)	$\Delta S^\ddagger$ (J K^{-1})
$[(\beta\text{-CD})_2\text{-}H^+]^{-1}$	$-[\beta\text{-CD}]^0$	1.85 ± 0.11	53 ± 16
$[(\beta\text{-CD})_2\text{-}2H^+]^{-2}$	$-[\beta\text{-CD}]^{-1}$	1.79 ± 0.09	54 ± 19

Generating breakdown diagrams of [(β-CD)$_2$+substrate-2H$^+$]$^{-2}$ complexes

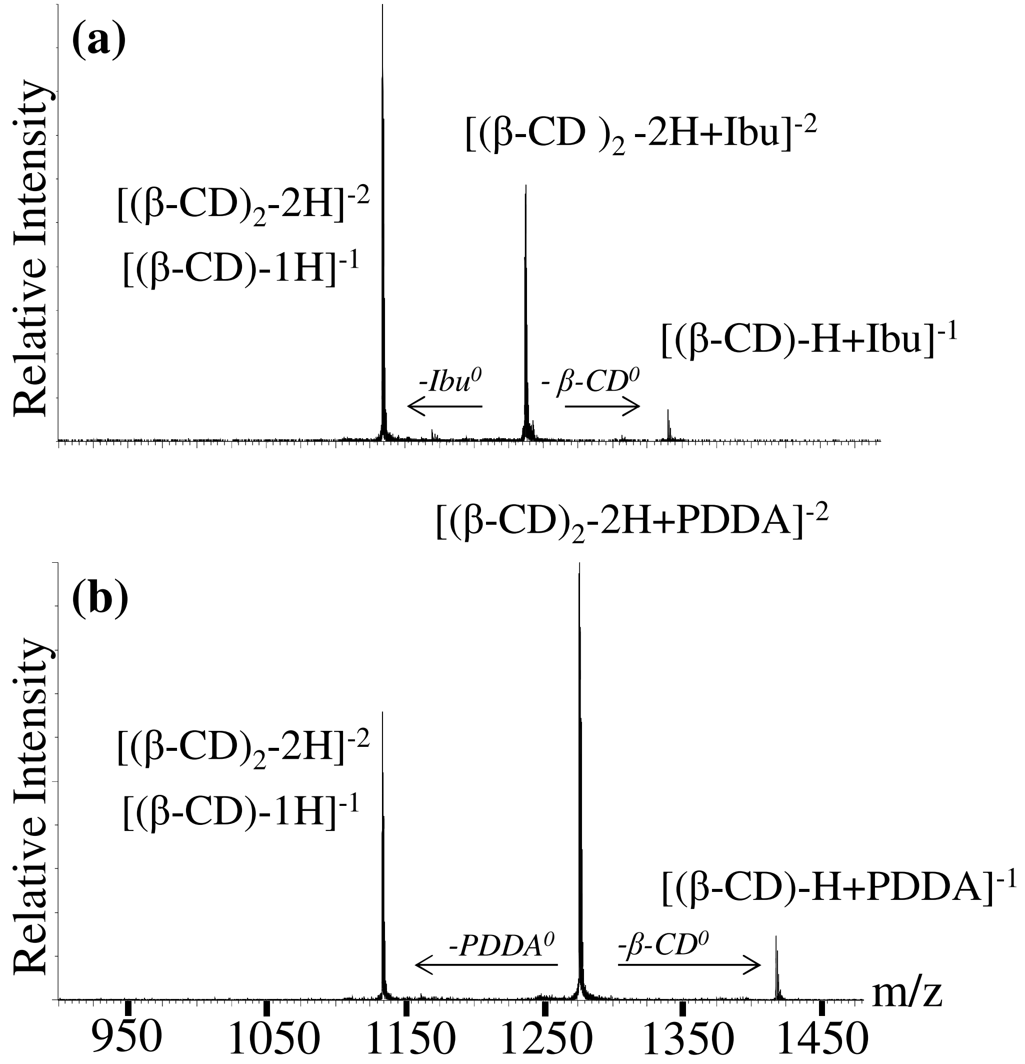

Figure 8-6 ESI-MS/MS of [(β-CD)$_2$ + substrate-2H$^+$]$^{-2$}
ESI-MS/MS of [(β-CD)$_2$-2H+substrate]$^{-2}$ for (a) Ibu and (b) PDDA at E_{lab} 20 eV. Main fragmentation path is the loss of neutral substrate yielding [(β-CD)$_2$ -2H]$^{-2}$ and minor pathway is the loss of [β-CD –H$^+$]$^{-1}$ yielding [β-CD –H + substrate]$^{-1}$

Unlike MS/MS of $[(\beta\text{-CD})_2\text{-}2H^+]^{-2}$, $[(\beta\text{-CD})_2\text{+substrate-}2H^+]^{-2}$ signals contained far less m/z overlap with other species, however there were two major dissociation pathways which produced different fragment ions with identical m/z (Figure 8-6).

Pathway (1) - The loss of a neutral substrate to give the single product ion $[(\beta\text{-CD})_2\text{-}2H^+]^{-2}$ at m/z 1133.4 and,

Pathway (2) - Charge separation producing $[\beta\text{-CD-}H^+]^{-1}$ (m/z 1133.4) and $[\beta\text{-CD+substrate–}H^+]^{-1}$.

Both dissociation pathways resulted in product ions with m/z 1133.4 and thus obtaining the relative intensities of each pathway was not straight forward. The intensity of fragment ions of pathway 2 were obtained from the summed ion intensity of $[\beta\text{-CD+substrate–}H^+]^{-1}$.The $[\beta\text{-CD +substrate–}H^+]^{-1}$ signal of pathway 2 will produce an equivalent signal at 1133.4 m/z for $[\beta\text{-CD-}H^+]^{-1}$. Therefore, the intensity of $[(\beta\text{-CD})_2\text{-}2H]^{-2}$ originating from pathway (1) was obtained by subtracting the summed isotope intensity of $[\beta\text{-CD +substrate–}H^+]^{-1}$ from summed isotope intensity of m/z 1133.4 according to equation 8-12:

$$\mathbf{I}_{\mathbf{Pathway\ 1}} = \mathbf{I}_{\mathbf{1133.4}} - \mathbf{I}_{[\mathbf{CD+substrate-H^+}]^{-1}} \qquad \text{Equation 8-12}$$

With this, it was possible to obtain breakdown diagrams for both $[(\beta\text{-CD})_2\text{+Ibu–}2H^+]^{-2}$ and $[(\beta\text{-CD})_2\text{+PDDA–}2H^+]^{-2}$

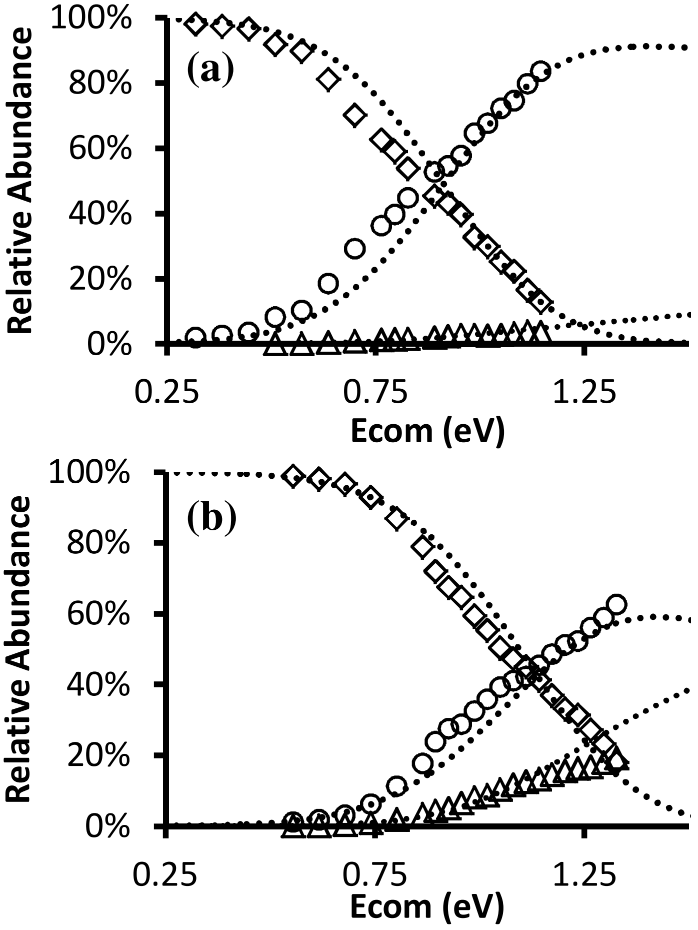

Figure 8-7 RRKM fitted breakdown diagrams of $[(\beta\text{-CD})_2 + \text{substrate-}2\text{H}^+]^{-2}$
The two possible dissociation pathways for (b) $[(\beta\text{-CD})_2\text{+Ibu-}2\text{H}^+]^{-2}$ and $[(\beta\text{-CD})_2\text{+PDDA-}2\text{H}^+]^{-2}$ are the neutral loss of substrate (○) or loss of $[\beta\text{-CD -H}^+]^{-1}$ (Δ). Dashed lines indicate best RRKM fit to data.

It can be seen directly from the breakdown diagrams (Figure 8-7a,b) that the onset of dissociation of $[(\beta\text{-CD})_2\text{–}2\text{H+Ibu}]^{-2}$ is earlier than $[(\beta\text{-CD})_2\text{+PDDA–}2\text{H}^+]^{-2}$. For both $[(\beta\text{-CD})_2\text{+Ibu–}2\text{H}^+]^{-2}$ and $[(\beta\text{-CD})_2\text{+PDDA–}2\text{H}^+]^{-2}$, the dominant pathway is the loss of the neutral substrate, indicating a stronger binding between both β-CD than the binding between β-CD and the substrate.

The loss of $[\text{Ibu}]^0$ and $[\text{PDDA}]^0$ from the reactant complex had similar critical energies of 1.12 ± 0.05 and 1.11 ± 0.05, respectively (Table 8-2). The PDDA containing complex is more kinetically stable due to an entropic effect. The $\Delta S^{\ddagger}$ for loss of $[Ibu]^0$ and [PDDA] were approximated to be 0 ± 11 and -18 ± 10, respectively. This suggests that the transition state for the loss of PDDA requires a tighter conformational re-organization than the loss of Ibu and connects with IMS measurements that show the $[\beta\text{-CD+PDDA–2H}^+]^{-2}$ being more compact than $[\beta\text{-CD+Ibu–2H}^+]^{-2}$. The minor pathway whereby $[\beta\text{-CD–H}^+]^{-1}$ dissociates from the reactant ion complex is the most closely related to the dissociation of the β-CD dimer. The E_0 for this channel is 1.39 ± 0.09 eV and 1.46 ± 0.05 eV for Ibu and PDDA, respectively, while the $\Delta S^{\ddagger}$ is 25 ± 10 and 38 ± 9 J K^{-1}. This means that binding of Ibu or PDDA to $[(\beta\text{-CD})_2\text{–2H}^+]^{-2}$ significantly lowers the binding between the two β-CD by 0.33 and 0.40 eV respectively, again pointing to an inclusion complex in the substrate-bound dimer.

Table 8-2 RRKM derived energetic values for the dissociation of $[(\beta\text{-CD})_2\text{+substrate-2H}^+]$ complexes

Parent Ion	Dissociation Pathway	E_0 (eV)	$\Delta S^{\ddagger}$ (J K^{-1})
$[(\beta\text{-CD})_2\text{+Ibu-2H}^+]^{-2}$	$-[\beta\text{-CD}]^{-1}$	1.39 ± 0.09	25 ± 10
$[(\beta\text{-CD})_2\text{+Ibu-2H}^+]^{-2}$	$-[Ibu]^0$	1.12 ± 0.05	0 ± 11
$[(\beta\text{-CD})_2\text{+PDDA-2H}^+]^{-2}$	$-[\beta\text{-CD}]^{-1}$	1.46 ± 0.05	38 ± 9
$[(\beta\text{-CD})_2\text{+PDDA-2H}^+]^{-2}$	$-[PDDA]^0$	1.11 ± 0.05	-18 ± 10

Determination of Ω_{exp} using IMS

Using IMS in conjunction with CID allows for the generation of breakdown diagrams from overlapping m/z signals and also, the determination of Ω_{exp} which provides a structural facet to explain energetic observations. The Ω_{exp} was calculated as an average value from four different instrumental combinations of wave velocity and wave height. The Ω_{exp} of $[\beta\text{-CD-H}^+]^{-1}$ and $[(\beta\text{-CD})_2\text{-2H}^+]^{-2}$ were found to be 199 ± 2 Å^2 and 355 ± 2 Å^2 respectively (Table 8-3).

Table 8-3 Ω_{exp} of β-CD and (β-CD +substrate) complexes measured with TWIMS Error represents standard deviation between four combinations of travelling wave velocity and height. Absolute error is 8%.

Complex	Ω_{exp} (Å^2)
$[\beta\text{-CD-H}^+]^{-1}$	199 ± 2
$[\beta\text{-CD+Ibu-H}^+]^{-1}$	220 ± 5
$[\beta\text{-CD+PDDA-H}^+]^{-1}$	223 ± 5
$[(\beta\text{-CD})_2\text{-2H}^+]^{-2}$	355 ± 2
$[(\beta\text{-CD})_2\text{+Ibu-2H}^+]^{-2}$	370 ± 3
$[(\beta\text{-CD})_2\text{+PDDA-2H}^+]^{-2}$	366 ± 3

In order to investigate the effects of the substrate upon the overall conformation of the multimeric complexes, the Ω_{exp} of β-CD monomers and dimers bound to Ibu or PDDA were measured (Table 8-3). Figure 8-8 shows the ATD of Ibu and PDDA containing complexes; the central distribution (*) corresponds to $[\beta\text{-CD-H}^+]^{-1}$ which is present in both solutions and has the same ATD indicating that the instrumental conditions were equivalent.

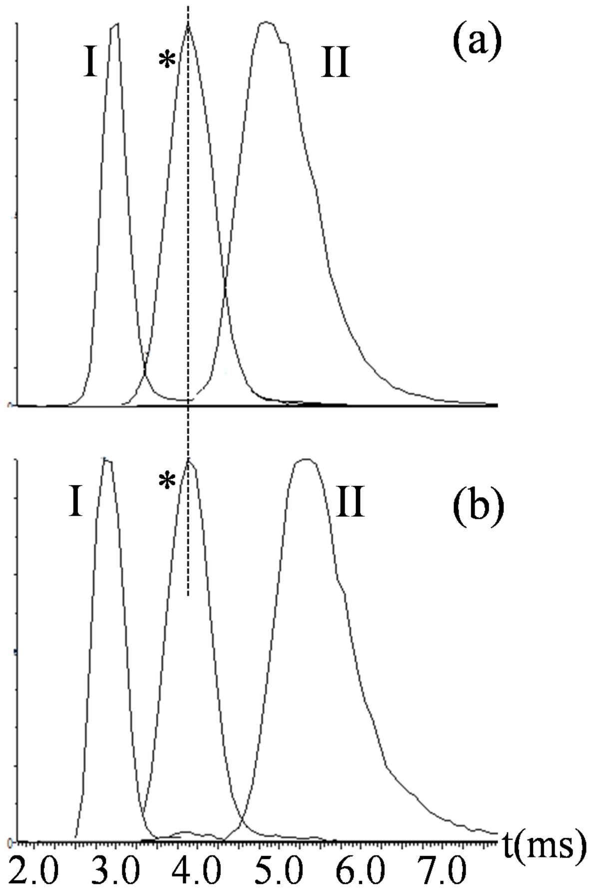

Figure 8-8. Extracted arrival time distributions from β-CD mixed with ibu or PDDA Extracted arrival time distributions from β-CD mixed with (a) ibuprofen and (b) PDDA. The $[\beta\text{-CD-H}^+]^{-1}$ arrival times in both solutions were identical (3.88 ms). ATD of I $[(\beta\text{-CD})_2 + \text{substrate-2H}^+]^{-2}$ is 3.16 and 2.98ms for Ibu and PDDA, respectively (*). ATD of II $[\beta\text{-CD} + \text{substrate-H}^+]^{-1}$ is 5.14 and 5.16 ms for Ibu and PDDA respectively

Peak II in Figure 8-8a,b correspond to $[\beta\text{-CD+Ibu–H}^+]^{-1}$ and $[\beta\text{-CD+PDDA–H}^+]^{-1}$, respectively. $[\beta\text{-CD+Ibu–H}^+]^{-1}$ has a faster drift time than $[\beta\text{-CD+PDDA–H}^+]^{-1}$ which is reflected by their Ω_{exp} of 220 ± 5 Å^2 and 223 ± 5 Å^2, respectively. Although the difference is only 3 Å^2, a larger Ω_{exp} for the PDDA complex is consistently obtained at different IMS settings. The difference in the Ω_{exp} of the substrate bound complexes to the unbound $[\beta\text{-CD–H}^+]^{-1}$ is defined here as the $\Delta\Omega_{exp}$ and corresponds to the increase in Ω_{exp} caused by the substrate and/or induced conformational changes by complexation. The $\Delta\Omega_{exp}$ of Ibu and PDDA are +21 Å^2 and

+24 Å^2, respectively. This suggests that Ibu and PDDA are not completely contained within the inner cavity of β-CD.

In contrast to the 1:1 complexes, the drift time of $[(\beta\text{-CD})_2\text{+Ibu–2H}^+]^{-2}$ is consistently slower than that of $[(\beta\text{-CD})_2\text{+PDDA–2H}^+]^{-2}$ (Figure 8-8, peak I) even though PDDA is a longer molecule than Ibu. This is reflected in the Ω_{exp} of 370 ± 3 Å^2 and 366 ± 3 Å^2 for $[(\beta\text{-CD})_2\text{–2H+Ibu}]^{-2}$ and $[(\beta\text{-CD})_2\text{–2H+PDDA}]^{-2}$, respectively (Table 8-3). The $\Delta\Omega_{exp}$ between the bound to the unbound $(\beta\text{-CD})_2$ is therefore a modest 15 Å^{2}and 11 Å^2 for Ibu and PDDA, respectively. This suggests that the substrates are less exposed than when they are bound to a single β-CD. A major structural difference between Ibu and PDDA is the additional carboxylic acid of PDDA. Substrate interactions with CD in the gas phase are driven predominately through electrostatic interactions, and both carboxylic group of PDDA are likely forming hydrogen bonds with each β-CD, resulting in a slighter tighter conformation.

8.6 Conclusion

β-CD dimers alone and in complex with PDDA or Ibu were studied in order to develop an approach generate breakdown diagrams when there is m/z overlap of the reactant ion or fragment ions.

ESI-IMS was used to prior to CID in order to deconvolute m/z spectral overlap that occurs in the dissociation of doubly deprotonated dimers $[(\beta\text{-CD})_2\text{-2H}]^{-2}$. When the fragment ions have identical m/z as the reactant ion, breakdown diagrams were generated by monitoring the relative abundance of fragment ions through changes in the isotopic profile. This allowed for RRKM fitting of the breakdown diagram and the E_0 and $\Delta S^{\ddagger}$ values for the dissociation to be obtained, providing insight into the different dissociation reactions. The RRKM derived E_0 for dissociation of $[(\beta\text{-CD})_2\text{-H}^+]^{-1}$ and $[(\beta\text{-CD})_2\text{-2H}^+]^{-2}$ corresponded to a slight decrease in complex stability due to increased charge-charge repulsion in the dianion. The E_0 for the loss of a β-CD from the $[(\beta\text{-CD})_2\text{+substrate-2H}^+]^{-2}$ complex was 1.39 ± 0.09 eV and 1.46 ± 0.09 eV for Ibu and PDDA respectively, which suggests that substrate binding decreases the (β-CD)-(β-CD) binding within the complex. Ω_{exp} values were derived from ion mobility arrival time distributions using calibrants. The increase of Ω_{exp} upon binding of Ibu and PDDA to $[\beta\text{-CD-H}^+]^{-1}$ was 21 $Å^2$ and 24 $Å^2$. Ibu and PDDA binding to $[(\beta\text{-CD})_2\text{-2H}^+]^{-2}$ resulted in a very modest increase in Ω 15 $Å^2$ and 11 $Å^2$, respectively, suggesting that the neutral drugs are indeed bound as inclusion complexes within both β-CD moieties.

8.7 References

1. Gabelica, V.; Galic, N., De Pauw, E. On the specificity of cyclodextrin complexes detected by electrospray mass spectrometry. Journal of the American Society for Mass Spectrometry 13, 946-953 (2002)
2. Gabelica, V.; Galic, N.; Rosu, F.; Houssier, C., De Pauw, E. Influence of response factors on determining equilibrium association constants of non-covalent complexes by electrospray ionization mass spectrometry. Journal of Mass Spectrometry 38, 491-501 (2003)
3. Lebrilla, C. B. The gas-phase chemistry of cyclodextrin inclusion complexes. Accounts of Chemical Research 34, 653-661 (2001)
4. Li, Z.; Couzijn, E. P., Zhang, X. Intrinsic properties of α-cyclodextrin complexes with benzoate derivatives in the gas phase: An experimental and theoretical study. The Journal of Physical Chemistry B 116, 943-950 (2012)
5. Loftsson, T.; Masson, M., Brewster, M. E. Self-association of cyclodextrins and cyclodextrin complexes. Journal of pharmaceutical sciences 93, 1091-1099 (2004)
6. Liu, Y.; Li, L.; Zhang, H.-Y.; Fan, Z., Guan, X.-D. Selective binding of chiral molecules of cinchona alkaloid by β-and γ-cyclodextrins and organoselenium-bridged bis (β-cyclodextrin) s. Bioorganic chemistry 31, 11-23 (2003)
7. Wen, X.; Liu, Z.; Zhu, T.; Zhu, M.; Jiang, K., Huang, Q. Evidence for the 2: 1 molecular recognition and inclusion behaviour between β-and γ-cyclodextrins and cinchonine. Bioorganic chemistry 32, 223-233 (2004)
8. Kralj, B.; Šmidovnik, A., Kobe, J. Mass spectrometric investigations of α- and β-cyclodextrin complexes with ortho-, meta-and para-coumaric acids by negative mode electrospray ionization. Rapid Communications in Mass Spectrometry 23, 171-180 (2009)
9. Hamilton, J. V.; Renaud, J. B., Mayer, P. M. Experiment and theory combine to produce a practical negative ion calibration set for collision cross-section determinations by travelling-wave ion-mobility mass spectrometry. Rapid Communications in Mass Spectrometry 26, 1591-1595 (2012)

10. Hoaglund, C. S.; Liu, Y.; Ellington, A. D.; Pagel, M., Clemmer, D. E. Gas-phase DNA: oligothymidine ion conformers. Journal of the American Chemical Society 119, 9051-9052 (1997)

11. Smith, D. P.; Knapman, T. W.; Campuzano, I.; Malham, R. W.; Berryman, J. T.; Radforda, S. E., Ashcrofta, A. E. Deciphering drift time measurements from travelling wave ion mobility spectrometry-mass spectrometry studies. Eur. J. Mass Spectrom. 15, 113-130 (2009)

12. Mayer, P. M., Martineau, E. Gas-phase binding energies for non-covalent Aβ-40 peptide/small molecule complexes from CID mass spectrometry and RRKM theory. Physical Chemistry Chemical Physics 13, 5178-5186 (2011)

13. Renaud, J. B.; Martineau, E.; Mironov, G. G.; Berezovski, M. V., Mayer, P. M. The collaborative role of molecular conformation and energetics in the binding of gas-phase non-covalent polymer/amine complexes. Physical Chemistry Chemical Physics 14, 165-172 (2012)

14. Dewar, M. J.; Zoebisch, E. G.; Healy, E. F., Stewart, J. J. Development and use of quantum mechanical molecular models. 76. AM1: a new general purpose quantum mechanical molecular model. Journal of the American Chemical Society 107, 3902-3909 (1985)

15. Frisch, M. J.; Trucks, G. W.; Schlegel, H. B.; Scuseria, G. E.; Robb, M. A.; Cheeseman, J. R.; Scalmani, G.; Barone, V.; Mennucci, B.; Petersson, G. A.; Nakatsuji, H.; Caricato, M.; Li, X.; Hratchian, H. P.; Izmaylov, A. F.; Bloino, J.; Zheng, G.; Sonnenberg, J. L.; Hada, M.; Ehara, M.; Toyota, K.; Fukuda, R.; Hasegawa, J.; Ishida, M.; Nakajima, T.; Honda, Y.; Kitao, O.; Nakai, H.; Vreven, T.; Montgomery, J. A.; Peralta, J. E.; Ogliaro, F.; Bearpark, M.; Heyd, J. J.; Brothers, E.; Kudin, K. N.; Staroverov, V. N.; Kobayashi, R.; Normand, J.; Raghavachari, K.; Rendell, A.; Burant, J. C.; Iyengar, S. S.; Tomasi, J.; Cossi, M.; Rega, N.; Millam, J. M.; Klene, M.; Knox, J. E.; Cross, J. B.; Bakken, V.; Adamo, C.; Jaramillo, J.; Gomperts, R.; Stratmann, R. E.; Yazyev, O.; Austin, A. J.; Cammi, R.; Pomelli, C.; Ochterski, J. W.; Martin, R. L.; Morokuma, K.; Zakrzewski, V. G.; Voth, G. A.; Salvador, P.; Dannenberg, J. J.; Dapprich, S.; Daniels, A. D.; Farkas, Ö.; Foresman, J. B.; Ortiz, J. V.; Cioslowski, J., Fox, D. J. Gaussian 09. Inc., Wallingford, CT (2009)

16. Beyer, T., Swinehart, D. Algorithm 448: number of multiply-restricted partitions. Communications of the ACM 16, 379 (1973)
17. Baer, T., Mayer, P. M. Statistical Rice-Ramsperger-Kassel-Marcus quasiequilibrium theory calculations in mass spectrometry. Journal of the American Society for Mass Spectrometry 8, 103-115 (1997)
18. Mironov, G. G.; Logie, J.; Okhonin, V.; Renaud, J. B.; Mayer, P. M., Berezovski, M. V. Comparative study of three methods for affinity measurements: Capillary electrophoresis coupled with UV detection and mass spectrometry, and direct infusion mass spectrometry. Journal of the American Society for Mass Spectrometry 23, 1232-1240 (2012)
19. Muñoz De La Peña, A.; Ndou, T.; Zung, J., Warner, I. Stoichiometry and formation constants of pyrene inclusion complexes with. β -and γ-cyclodextrin. The Journal of Physical Chemistry 95, 3330-3334 (1991)

Chapter 9: Conclusions

In this work, dissociation energetics and structure of a variety of non-covalent complexes were analyzed. RRKM unimolecular rate modelling of MS/MS dissociation channels approximated the critical energy of activation (E_0) and entropy of activation ($\Delta S^{\ddagger}$). Ion mobility spectrometry (IMS) in conjunction with computational techniques provided structural information about the reactant and often product ions resulting from a dissociation event.

For PMMA, diamine non-covalent complexes, the minimization of coulombic repulsion between charges is the most important factor in determining the overall interaction energetics and structure of the non-covalent complex. This finding was independently obtained based on structural and energetic experiments.

The absolute values obtained with RRKM fitting of MS/MS breakdown diagrams are approximate, however this approach is able to measure small differences in binding between a small protonated peptide and isomeric tetra-saccharides and can corroborated independently with experimental and theoretical structural analysis.

In cases where RRKM fitting of MS/MS breakdown diagrams is not possible, the simple kinetic method can provide insight into the relative affinity of intermediate molecules for polyatomic substrates. Careful MM/MD and IMS analysis can allow for predictions of a reverse activation barrier and $\Delta(\Delta S^{\ddagger})$ to be taken however, the greatest potential for errors arises from the uncertainty in effective temperature of the ion.

Plotting the ratio of competing fragment ions across reciprocal collision energy, allows for multiple dissociation channels to be expressed as a function of a single dissociation channel. This greatly decreases the calculation time of the RRKM fitting. This was applied to ionized anthracene and the RRKM results were within experimental range of values obtained using iPEPICO (with 1 exception).

The relative intensities of fragment ions from MS/MS of ammoniated triacylglycerides allows for the positional identity of the fatty acids on the glycerol backbone to be determined. Using RRKM fitting and computational methods, we proposed that the rate determining step is often the initial loss of NH_3 from the non-covalent complex, giving two possible intermediate structures that fragment unevenly into product ions.

Breakdown diagrams were obtained for $[(\beta\text{-CD})_2\text{-}2H^+]^{-2}$ by filtering out ions with the same m/z using IMS. The product ions arising from MS/MS of $[(\beta\text{-CD})_2\text{-}2H^+]^{-2}$ have the same m/z as the reactant ion and therefore, changes in the isotopic profile can be used to monitor the extent of fragmentation across a range of collision energies.

Overall, we have shown that in it difficult to apply a single method or workflow to investigate non-covalent complexes with a structure and energetic approach. Each system of interest is unique and offers its own challenges. We have shown here that a general method of either explaining dissociation energetics based on ion structure or using insight from dissociation energetics to uncover dissociation mechanisms and structures is possible through careful use of a number of complementary techniques.

Claims to original research

1) Energetic and structural data of polymer/diamine complexes were obtained by RRKM modelling of MS/MS breakdown diagrams and IMS coupled to MM/MD. Both the structural and energetic approach was able to identify the same trends of complex size, diamine size and charge state. The driving force that influences the dissociation energetics and the structures of these complexes is the minimization of coulombic repulsion by maximizing the distance between charges.

   The same approach was used on saccharide peptide complexes which also showed that structure and energetic data obtained independently could help explain the same experimental trends.

2) The applicability of the kinetic method for obtaining the affinities of synthetic polymers to amines was explored. It is possible to obtain relative values using the simple kinetic method; however, the lack of reference compounds and the uncertainty of effective temperature make it difficult for the simple kinetic method to be used to obtain absolute values.

3) An explanation of why ammoniated triacylglycerides dissociate in an uneven fashion is provided. The loss of NH_3 from the ammoniated complex is frequently not observed in the MS/MS spectra however, it is often the rate determining step of the dissociation.

4) RRKM breakdown diagrams are obtained on multimeric structures that are overlapped in the ESI-MS by compounds with the same m/z or result in MS/MS fragments with the same m/z as the reactant complex.

List of publications

Justin B. Renaud, Sean Overton, Paul M. Mayer. “Energy and entropy at play in competitive dissociations: the case of uneven dissociation of ionized triglycerides.” **(2013)** Intl J. Mass Spectrom. 352(15) 77-86

Justin B. Renaud, Paul M. Mayer. *Review; “The applicability of the kinetic method for measuring relative affinities of macromolecules for polyatomic substrates*.” Intl. J. Mass Spectrom. **(2012)** Eur. J. Mass Spectrom. **18(2)** 223-34

Jenna V. Hamilton, Justin B. Renaud, Paul M. Mayer “*Experiment and theory combine to produce a practical negative ion calibration set for collision cross-section determinations by travelling-wave ion-mobility mass spectrometry*”. **(2012)** Rapid. Comm. Mass Spectrom. **26**, 1591-1595

J. B. Renaud, E. Martineau, G.G. Mironov, M. Berezovski and P.M. Mayer, “*The collaborative role of molecular conformation and energetics in the binding of gas-phase non-covalent polymer/amine complexes*” .**(2012)** Phys. Chem. Chem. Phys. **14** 165-172

S. Curtis, J. DiMuzio, A. Mungham, J. Roy, D. Hassan, J. Renaud and P. M Mayer, *“Reactions of Atomic Metal Anions in the Gas Phase: Competition between Electron Transfer, Proton Abstraction and Bond Activation*” **(2011)** J. Phys Chem A. 115 14006-14012

Amanda N.Comeau, Justin B. Renaud, Gleb G. Mironov, Maxim V. Berezovski, Paul M. Mayer. “*Investigating the relationship between the gas-phase conformations and dissociation energetics of gas-phase specific, peptide–saccharide complexes*.” Eur. J. Mass Spectrom. **(2011)** Intl. J. Mass Spectrom.,**(316-318)** 31-39

S. Curtis, J. Renaud, J. L. Holmes and P. M. Mayer, “*Old Acid, New Chemistry. “Negative Metal Anions Generated from Alkali Metal Oxalates and Others”* **(2010)** J. Am. Soc. Mass Spectrom. **21** 1944-1946.

J. Renaud, A. M. Alhazmi and P. M. Mayer, “*Comparing the fragmentation chemistry of gas-phase adducts of poly(dimethylsiloxane) oligomers with metal and organic ions*” **(2009)** Can. J. Chem. **87** 453-459.

Analytical Chemistry, Food Chemistry

Moufida Oueslati Arfaouia, Justin Renaud, Hanen Ghazghazi, Sadok Boukhchina & Paul Mayer. *“Variation in oil content, fatty acid and phytosterols profile of Onopordum acanthium L. during seed development.”* **(2014)** Natural Product Research . DOI:10.1080/14786419.2014.940944

Hajer Trabelsi, Justin Renaud, Wahid Herchi, Mohamed L. Khouja, Sadok Boukhchina, Paul Mayer. *“LC–ESI–QTOF–MS, MS/MS Analysis of Glycerophospholipid Species in Three Tunisian Pistacia lentiscus Fruit Populations*.**”** **(2013)** J. Am. Oil Chem. Soc, 90, 5, 611-618

N. Tlili, H. Trabelsi, J. Renaud, A. Khaldi, P. M. Mayer, S. Triki, "*Triacylglycerols and Phospholipids of Caper Seeds (Capparis spinosa)*." **(2012)** J. Am. Oil Chem. Soc. **88** 1787-1793

Hajer Trabelsi, Faouzi Sakouhi, Justin Renaud, Pierre Villeneuve, Mohamed L. Khouja, Paul Mayer, Sadok Boukhchina. "*Fatty acids, 4-desmethylsterols, and triterpene alcohols from Tunisian lentisc (Pistacia lentiscus) fruits*" **(2012)** Eur. J. Lip. Sci. and Tech. **114,** 968-973

Gleb G. Mironov, Jennifer Logie, Victor Okhonin, Justin Renaud, Paul M. Mayer and Maxim V. Berezovski. "*Comparative Study of Three Methods for Affinity Measurement: Kinetic Capillary Electrophoresis Coupled with UV Detection and Mass Spectrometry, and Direct Infusion Mass Spectrometry*". J. Am. Soc. Mass Spectrom. **(2012)** *JASMS.* **23,** 1232-1240

H. Trabelsi, O. Aicha Cherif, F. Sakouhi, P. Villeneuve, J. Renaud, N. Barouh, S. Boukhchina, P. M. Mayer, "*Total lipid content, fatty acids and 4-desmethylsterols accumulation in developing fruit of Pistacia lentiscus L. growing wild in Tunisia*", **(2012)** Food Chemistry. **131** 434-440